Final Report

Multiazimuth Seismic Diffraction Imaging for Fracture Characterization in Low-Permeability Gas Formations

08122.53.final

March 25, 2014

Principal Investigators: Dr. Sergey Fomel, Professor & Dr. Peter Eichhubl, Research Scientist
Bureau of Economic Geology
Jackson School of Geosciences
The University of Texas at Austin
Austin, TX 78758

Other Authors: Alexander Klokov, Jon Olson, Farrokh Sheibani,
Stephen E. Laubach, Tobias Weisenberger, John N. Hooker, Andràs Fall

LEGAL NOTICE

This report was prepared by *Bureau of Economic Geology, University of Texas at Austin* as an account of work sponsored by the Research Partnership to Secure Energy for America, RPSEA. Neither RPSEA members of RPSEA, the National Energy Technology Laboratory, the U.S. Department of Energy, nor any person acting on behalf of any of the entities:

a. MAKES ANY WARRANTY OR REPRESENTATION, EXPRESS OR IMPLIED WITH RESPECT TO ACCURACY, COMPLETENESS, OR USEFULNESS OF THE INFORMATION CONTAINED IN THIS DOCUMENT, OR THAT THE USE OF ANY INFORMATION, APPARATUS, METHOD, OR PROCESS DISCLOSED IN THIS DOCUMENT MAY NOT INFRINGE PRIVATELY OWNED RIGHTS, OR

b. ASSUMES ANY LIABILITY WITH RESPECT TO THE USE OF, OR FOR ANY AND ALL DAMAGES RESULTING FROM THE USE OF, ANY INFORMATION, APPARATUS, METHOD, OR PROCESS DISCLOSED IN THIS DOCUMENT.

THIS IS A FINAL REPORT. THE DATA, CALCULATIONS, INFORMATION, CONCLUSIONS, AND/OR RECOMMENDATIONS REPORTED HEREIN ARE THE PROPERTY OF THE U.S. DEPARTMENT OF ENERGY.

REFERENCE TO TRADE NAMES OR SPECIFIC COMMERCIAL PRODUCTS, COMMODITIES, OR SERVICES IN THIS REPORT DOES NOT REPRESENT OR CONSTIITUTE AND ENDORSEMENT, RECOMMENDATION, OR FAVORING BY RPSEA OR ITS CONTRACTORS OF THE SPECIFIC COMMERCIAL PRODUCT, COMMODITY, OR SERVICE.

THIS PAGE INTENTIONALLY LEFT BLANK

TABLE OF CONTENTS

LIST OF FIGURES

SECTION 2.2

SECTION 2.3

CHAPTER 3

LIST OF TABLES

Page

CHAPTER 2

SECTION 2.3

EXECUTIVE SUMMARY

Fluid flow in fractured rock is an increasingly central issue in recovering water and hydrocarbon supplies and geothermal energy, in predicting flow of pollutants underground, in engineering structures, and in understanding large-scale crustal behavior. Successful imaging and prediction of open fractures is essential to gas production from low-permeability reservoirs. The objective of this research project was to develop advanced technologies and techniques that improve detection, characterization, and production prediction from low-permeability gas accumulations through both new seismic diffraction imaging technology and improved wireline-conveyed sidewall core analysis of structural diagenetic fracture surrogates. Fractures significant to production are generally considered below the detection limit of conventional reflection seismic techniques. We approached this limitation along four lines of research: 1. Investigate novel techniques in diffraction seismic techniques that may provide the opportunity to shrink the observation gap between conventional seismic techniques and fracture size distributions that can be observed in core and image logs; 2. Develop new approaches to fracture network modeling; 3. Investigate proxy techniques that allow predictions of fracture occurrence based on characteristics of the fracture population that can be observed using seismic techniques; and 4. Investigate aspects of fracture populations that make them more or less conducive to detection by seismic techniques.

Seismic methods offer the promise of measuring key fracture attributes away from borehole samples. Our goal in developing a new seismic imaging technology was to overcome limitations of the commonly practiced seismic analysis tools. We have developed a novel approach to seismic diffraction imaging based on diffraction separation migration in dip-angle common-image gathers. Using theoretical and experimental studies, we have shown that, the appearance of diffraction events in the dip-angle domain differs significantly in shape from reflections. The shape difference can be used as a criterion for reflection/diffraction separation. The Hybrid Radon Transform, a tool that extracts events that fit the diffraction model, can successfully separate diffractions. Input for this procedure is migrated dip-angle gathers, possibly after preliminary plane-wave destruction in the data domain. After the separation, integration of extracted diffraction events along dip angles provides a diffraction image, which is a seismic image of small but important geologic objects that are often invisible after conventional seismic processing. Unlike reflections, diffractions are always significantly affected by velocity errors. They can be used in applications to efficient migration-velocity analysis, which requires only a single offset (such as zero offset) as input, making it favorable for velocity-model construction.

Stress intensity factor (SIF) determination plays a central role in linearly elastic fracture mechanics problems. Numerical methods are necessary for the SIF evaluation of 3-D planar cracks because analytical solutions are limited to simple geometries with special boundary conditions. We have examined the capability of Displacement Discontinuity Method (DDM) using constant rectangular discontinuity elements for modeling cracks with simple geometry.

The accuracy of the model was shown to be excellent for rectangular and square shaped cracks. The stepwise shape of the mesh boundary when representing elliptical or penny-shaped cracks introduces more error in to the calculation, but the minimum and maximum SIF values can be accurately computed. Results of our numerical studies show that joint orientation is dependent on its vertical position with respect to the normal fault. Mechanical properties significantly affect the pattern of tensile stress distribution. While high value of Poisson's ratio increases the magnitude of both fault-parallel and fault-perpendicular tension around the tip-lines, low values completely changes fault-perpendicular tensile stress distribution pattern in mid-depth along an isolated fault. This situation suggests a mechanism of opening mode fracture extension in a relatively wide area induced by overburden. In general, normal fault can cause regional stress rotation, but the generated tension is not enough to exceed compressive remote horizontal stresses except a small zone very close to the fault tip-line.

We have investigated key aspects controlling seismic detection including fracture clustering and the diagenetic attributes of fractures and hostrock. Our results demonstrate that, while fracture diagenesis is frequently heterogeneous in reservoirs, aspects essential to the reservoir seismic response such as degree of cement infill and fracture cement mineral composition, are predictable using proxy techniques such as the degradation index and applying a fundamental understanding of reservoir diagenetic processes during burial. It is our expectation that the widely applicable techniques that we developed will have an impact on effective targeting of zones of potentially good producibility in tight formations. Core and production data show that fracture attributes such as degree of diagenetic overprint on fractures, leading to locally sealed or partly sealed fractures, can be the difference between productive (economic) wells and dry holes. Such fracture attributes cannot currently be distinguished using currently available seismic techniques even under the most favorable circumstances.

Our integrated approach has the potential for reducing exploration and finding costs, increasing the success of exploration, and overcoming limitations in existing technologies. In addition to anticipated economic benefits, improved technologies in targeting naturally fractured reservoirs may increase the efficiency and reach of hydraulic fracture treatments. Improved targeting technologies can provide direct environmental benefits by, for examples, optimizing water use for hydraulic fracture treatments and reducing the footprint of well sites.

The technology developed in the course of this project has been transferred to the industry through three annual meetings with industry stakeholders, direct interaction with producers, our research web site, presentation and sessions chaired at national meetings, and publication of results in international journals. Industry meetings were held in Austin, TX, and Rochester NY, involving guests from about 20 companies active in exploration of unconventional resources.

CHAPTER 1

SEISMIC DIFFRACTION IMAGING

1.1 Summary

Common-reflection angle migration can produce migrated gathers either in the scattering-angle domain or in the dip-angle domain. The latter reveals a clear distinction between reflection and diffraction events. We derive analytical expressions for events in the dip-angle domain and demonstrate that the shape difference can be used for reflection/diffraction separation. We define reflection and diffraction models in the Radon space. The Radon Transform allows us to isolate diffractions from reflections and noise. The separation procedure can be performed after either time migration or depth migration. Synthetic and real data examples confirm the validity of the proposed technique.

1.2 Introduction

Faults and fractures to a large extent define rock permeability, and their detection and characterization are therefore important for oil and gas exploration and production (Laubach et al., 2000). Conventional seismic is based mainly on reflections from continuous and smooth reflecting boundaries. Energy scattered from small-scale geological objects such as faults and fractures often can get destroyed or suppressed by traditional seismic processing (Khaidukov et al., 2004).

In this report, by diffractions we mean the energy scattered by small subsurface objects or emitted from reflectors edges. The main difficulty in using diffractions is their weakness compared with the strong specular reflection energy present in observed seismic records. The differences between reflections and diffractions can reach several orders of magnitude (Klem-Musatov, 1994). Nevertheless, many attempts to use diffraction energy for finding small-scale subsurface objects have been undertaken. Landa et al. (1987), Kanasewich and Phadke (1988), and Tsingas et al. (2011) proposed a method for diffraction imaging that is based on coherent summation of diffracted events using an appropriate traveltime description in common-offset and common-midpoint domains. Landa and Keydar (1998) used common-diffraction-point sections for imaging of diffraction energy and detection of local heterogeneities. Berkovitch et al. (2009) presented a technique that is based on the multifocusing method. A similar idea was proposed by Dell and Gajewski (2011), who used the common-reflection-surface operator. A number of papers propose diffraction enhancement by modifying prestack Kirchhoff depth migration using appropriate weighting (Kozlov et al., 2004; Moser and Howard, 2008; Koren and Ravve, 2011). A similar approach in the local image matrices domain was presented by Zhu and Wu (2010).

But even in the case of construction operators that stack diffraction events along their actual traveltime curves, residual reflection energy is often strong enough to prevent correct

identification and characterization of scattering objects. Reflection/diffraction separation might therefore be required.

Probably the first attempt to separate reflection and diffraction components of the total wavefield was described by Harlan et al. (1984). Local slant stacks were used to remove reflections of continuous beds and retaining diffractions. Khaidukov et al. (2004) used distinctions in moveout properties of the waves, focused reflected waves to their imaginary source location in the pseudo-depth domain, muted them, and, after defocusing, obtained gathers where reflection events were suppressed. Taner et al. (2006) opened up the possibility of separating reflections and diffractions using constant plane-wave slope sections. In this domain, diffracted waves appear as quasi-hyperbolic-shaped traveltimes. In turn, reflections behave as simply shaped, laterally continuous events. Therefore, the reflection energy can be suppressed by a method known as plane-wave destruction (Claerbout, 1992; Fomel, 2002). Separation and imaging of diffractions using plane-wave destruction in the poststack domain was proposed by Fomel et al. (2007) and extended by Al-Dajani and Fomel (2010) and Burnett and Fomel (2011).

Reflection and diffraction events have different shapes in migrated common-image gathers (CIGs) in the dip-angle domain (Audebert et al., 2002; Landa et al., 2008; Reshef and Landa, 2009). Reflections have concave shapes ("smiles"), with a stationary point at the position of the correct dip value. By contrast, diffractions are flat when the migration velocity is correct and the migrated gather is observed directly at a diffraction point. Away from diffraction points, the diffraction response is a curve that does not have a stationary point.

In this study, we present a procedure for reflection-diffraction separation that is based on the difference between reflection and diffraction shapes in the migrated dip-angle domain. Following Klokov et al. (2010a,b) we adopt for this purpose the Hybrid Radon Transform (Trad et al., 2001).

First, we describe migrated common-image gathers in the dip-angle domain and show how diffraction and reflection events behave in this domain. We demonstrate the ability to use a single offset to generate dip-angle CIGs. We then present, using synthetic and real data examples, the separation and imaging of seismic diffractions and the influence of velocity errors on the appearance of migrated diffractions in the dip-angle domain.

1.3 Theory of reflections and diffractions in migrated dip-angle gathers

Kirchhoff migration can be regarded as integration over all possible reflection opening and reflector dip angles (Xu et al., 2001; Brandsberg-Dahl et al., 2003; Sava and Fomel, 2003). In the 2D case, the summation surface is defined by two angles only – namely, the opening angle θ and the reflector dip α. Integration over α for constant θ produces a conventional common-image

gather in the angle domain. Integration over θ for constant α produces a common-image gather in the dip-angle domain. The gather contains migrated traces that are partial images of a fixed lateral position for different reflector dips.

In the dip-angle domain, there is a significant distinction between reflections and diffractions (Landa et al., 2008). Next we derive analytical expressions for shapes of reflection and diffraction events.

1.3.1 Time-migrated dip-angle domain

Let us start, for simplicity, from the case of 2D zero-offset time migration. A similar analysis can be extended to prestack migration. In the 2D zero-offset and constant-velocity media situation, mapping between model coordinates $\{x,z\}$ and data coordinates $\{y,t\}$ is provided by the following geometrical relationships:

$$y = x + z \tan\alpha_0 , \tag{1}$$

$$t = \frac{2\,z}{v\cos\alpha_0} , \tag{2}$$

where v is the medium velocity and α_0 is the dip angle.

Time-migration amounts to the inverse transformation

$$x_m = y - \frac{v_M\,t}{2}\sin\alpha , \tag{3}$$

$$\tau = t\cos\alpha \tag{4}$$

where v_M is the migration velocity and α is the migration angle.

Let us consider a plane reflector with dip α_0 (Figure 1a), defined by the function

$$z(x) = z_1 + x\tan\alpha_0 . \tag{5}$$

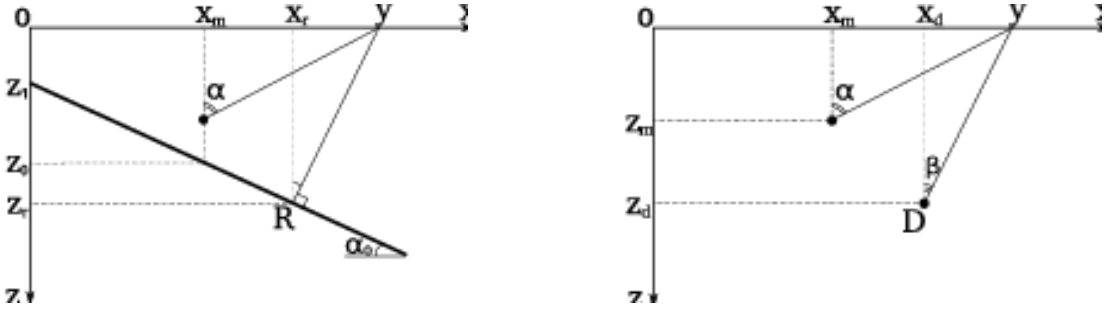

a) b)

Figure 1: (a) Zero-offset reflection and (b) zero-offset diffraction (schemes).

Deriving x from equation 5 and substituting it into equation 1, we obtain an expression that connects depth of the reflector with data coordinates:

$$z(y)=(z_1\cos\alpha_0+y\sin\alpha_0)\cos\alpha_0\,. \tag{6}$$

Substituting equation 6 into equation 2, we define a shape of the reflector response in the data domain:

$$t(y)=\frac{2(z_1\cos\alpha_0+y\sin\alpha_0)}{v}. \tag{7}$$

A time image of the reflector, according to equations 3 and 4, is defined by

$$x_m=-\frac{v_M}{v}z_1\cos\alpha_0\sin\alpha+y\left(1-\frac{v_M}{v}\sin\alpha_0\sin\alpha\right), \tag{8}$$

$$\tau=\frac{2}{v}(z_1\cos\alpha_0+y\sin\alpha_0)\cos\alpha\,. \tag{9}$$

Eliminating y from equations 8 and 9 and substituting $\gamma = v_M/v$, we obtain an image of the plane reflector in the dip-angle coordinates:

$$\tau(x_m,\alpha)=\frac{2\cos\alpha}{v}\,\frac{x_m\sin\alpha_0+z_1\cos\alpha_0}{1-\gamma\sin\alpha_0\sin\alpha}\,. \tag{10}$$

According to equation 5, which defines reflector depth z_0 in the position x_m,

$$x_m\sin\alpha_0+z_1\cos\alpha_0=z_0\cos\alpha_0\,. \tag{11}$$

Substituting equation 11 into equation 10, we obtain a shape of a reflection event on a dip-angle CIG for a fixed lateral position:

$$\tau(\alpha)=\tau_0\frac{\cos\alpha_0\cos\alpha}{1-\gamma\sin\alpha_0\sin\alpha}\,, \tag{12}$$

where $\tau_0 = 2z_0/v$ is the true two-way vertical time for a reflection point.

The event has the shape of a smile with a stationary point. If the migration velocity is correct ($\gamma = 1$), the stationary point occurs at $\alpha = \alpha_0$. It is easy to verify that in this case the derivative at the stationary point,

$$\frac{\partial\tau(\alpha)}{\partial\alpha}=\tau_0\cos\alpha_0\frac{\gamma\sin\alpha_0-\sin\alpha}{(1-\gamma\sin\alpha_0\sin\alpha)^2}, \tag{13}$$

becomes zero and that $\tau(\alpha) = \tau_0$. Summation of the dip-angle gather over the angle then produces a correct image according to the stationary phase principle (Bleistein et al., 2001).

Analysis of equation 12 shows some useful properties of reflection events in the time-migrated dip-angle domain. Particularly if a reflector is horizontal ($\alpha_0 = 0$), the shape does not depend on velocity-model accuracy:

$$\tau(\alpha)|_{\alpha_0=0} = \tau_0 \cos\alpha c \tag{14}$$

Now let us consider a diffraction point with coordinates $\{x_d, z_d\}$ (Figure 1b). It is convenient to parameterize its response in the data by the ray angle β. According to equations 1 and 2, the response is

$$y = x_d + z_d \tan\beta\,, \tag{15}$$

$$t = \frac{2\, z_d}{v \cos\beta}\,. \tag{16}$$

According to equations 3 and 4, the time image of a diffraction point is

$$x_m = x_d + z_d \left(\tan\beta - \frac{v_M}{v}\frac{\sin\alpha}{\cos\beta}\right), \tag{17}$$

$$\tau = \tau_0 \frac{\cos\alpha}{\cos\beta}\,, \tag{18}$$

or, eliminating β and substituting $\gamma = v_M / v$, $\xi = (x_m - x_d) / z_d$,

$$\tau(\alpha) = \tau_0 \cos\alpha \frac{\xi\gamma \sin\alpha + \sqrt{\xi^2 + 1 - \gamma^2 \sin^2\alpha}}{1 - \gamma^2 \sin^2\alpha}. \tag{19}$$

When the migration velocity is correct ($\gamma = 1$) and the dip-angle gather is observed directly at diffraction point ($\xi = 0$), the response is a flat line $\tau(\alpha) = \tau_0$, which corresponds to illuminating the diffractor uniformly from different angles. Otherwise, the response is a curve and may not have a stationary point.

Our theory is tested in Figure 2. The dip-angle gathers were obtained by time migration of the zero-offset section (Figure 3b), which corresponds to the model with two plane reflectors and a diffractor (Figure 3a).

The analytically calculated events (equations 12 and 19) overlap on the gathers. The diffraction response is shown as a dotted curve and appears flat in the dip-angle gather above the diffraction

point when the migration velocity is correct. It becomes curved when the migration velocity changes. Reflections (dashed curves) have the shape of a smile independent of the velocity model accuracy.

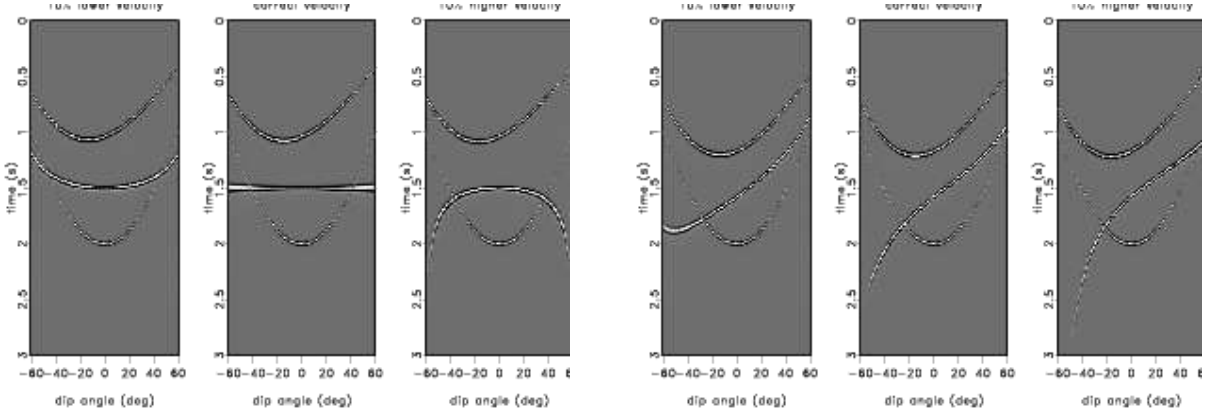

a) b)

Figure 2: Dip-angle gathers for migration with different velocities for position (a) above the diffractor at 4.0 km and (b) away from the diffractor at 4.5 km.

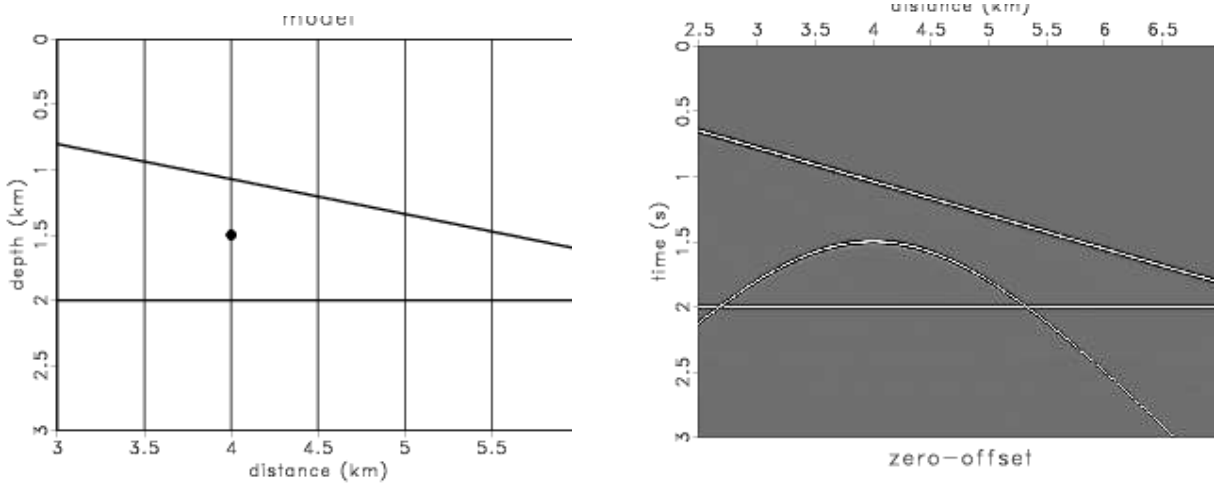

a) b)

Figure 3: (a) Theoretical model with two plane reflectors and one diffractor and (b) zero-offset section corresponding to the model.

1.3.2 Depth-migrated dip-angle domain

Equations 12 and 19 can be easily transformed from time to pseudo-depth. Substituting $\tau(\alpha) = 2z_\alpha / v_M$ and $\tau_0 = 2z_0 / v$, we get expressions for the case of constant-velocity media. A reflection event is described as

$$z(\alpha) = z_0 \gamma \frac{\cos\alpha_0 \cos\alpha}{1 - \gamma \sin\alpha_0 \sin\alpha}, \tag{20}$$

and a diffraction event as

$$z(\alpha) = \gamma\cos\alpha \frac{\rho\gamma\sin\alpha + \sqrt{\rho^2 + z_0^2(1-\gamma^2\sin^2\alpha)}}{1-\gamma^2\sin^2\alpha}. \tag{21}$$

where z_0 is the real depth of the reflection (or diffraction) point and $\rho = x_m - x_d$.

Equations 20 and 21 were derived on the assumption of constant-velocity media. Their application in depth-migrated gathers may appear unfounded. However, the equations do not contain terms describing velocity in the media. The events shape is defined by the velocity-accuracy parameter, which is removed by the correct velocity model.

In order to examine the validity of equations 20 and 21, we performed the following experiment. We put a plane reflector and a scattering point in the velocity field from the Marmousi model (Figure 4a). The modeled zero-offset section (Figure 4b) contains two responses of the considered objects. The diffraction curve is complicated: it is bent and has a number of caustics, and the reflection curve is complicated as well. Because describing the events accurately by any analytical expression is difficult, diffraction analysis in the data domain may present serious challenges.

Figure 5 demonstrates depth-migrated dip-angle gathers corresponding to the position above the scattering point and away from it. We computed the traveltimes by Huygens wavefront-tracing (Sava and Fomel, 2001), which allowed us to deal accurately with multiple arrivals. The gathers are overlain by analytically calculated curves (equations 20 and 21).

In the CIG observed directly at the scattering point, the diffraction event is flat, as expected, and is approximated exactly by the model. For a distance of 100 m, the approximation remains accurate. In far positions, the diffraction event deviates slightly from the analytical curve, especially at steep dips. The reflection event, in turn, has a complex shape; nevertheless, it tends to conform to the analytical expression.

An image of a diffraction object is formed by events whose shape is close to flat. Our experiment demonstrates that effective depth-migrated diffraction events, even in the case of a complicated velocity field, are approximated by equations 20 and 21 with sufficient accuracy.

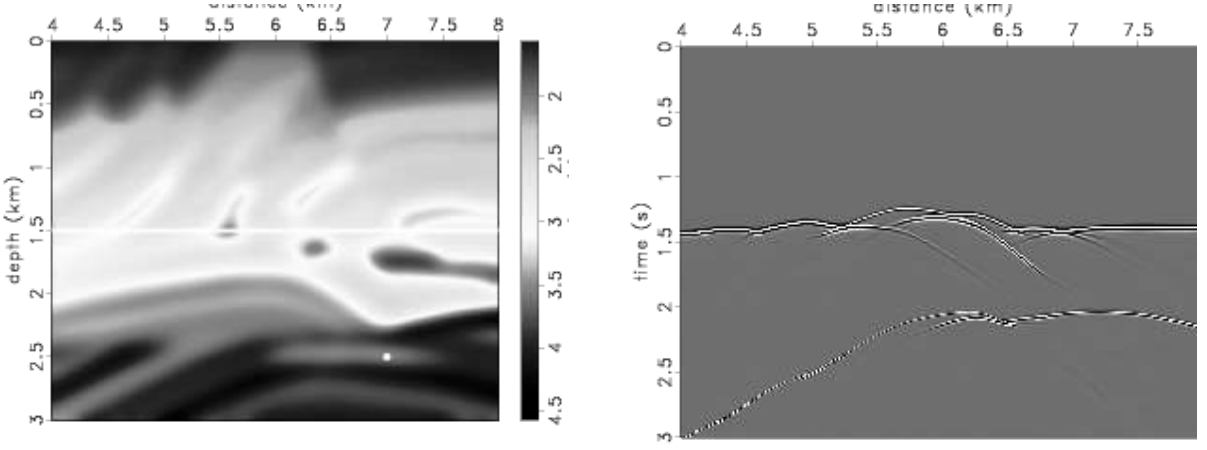

a) b)

Figure 4: (a) Reflector and scattering point dipped into the Marmousi model and (b) corresponding zero-offset section.

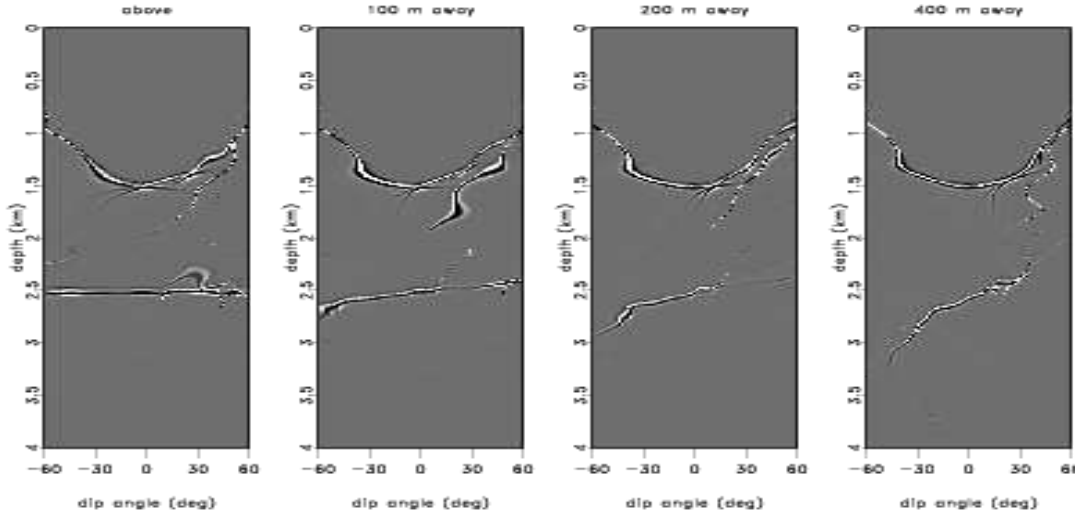

Figure 5: Depth-migrated dip-angle gathers corresponding to different distances with respect to the scattering point.

1.3.3 Three-dimensional migrated domain

Using the same principles, we can derive analytical expressions for a reflection event and a diffraction event in the 3D migrated dip-angle domain. If a plane reflector has two orthogonal dips α_{0y} and α_{0x}, its 3D time-migrated event can be represented as

$$\tau(\alpha_y, \alpha_x) = \frac{\tau_0}{k_0\, k_m - \gamma\, k_1}, \tag{22}$$

where

$$k_0 = \sqrt{1 + tan^2\alpha_{0y} + tan^2\alpha_{0x}}, \tag{23}$$

$$k_m = \sqrt{1 + tan^2\alpha_y + tan^2\alpha_x}\,, \tag{24}$$

$$k_1 = tan\,\alpha_{0y}\,tan\,\alpha_y + tan\,\alpha_{0x}\,tan\,\alpha_x\,. \tag{25}$$

A point diffractor with coordinates $\{y_d, x_d, z_d\}$ produces a 3D diffraction event, which is described by the following expression:

$$\tau(\alpha_y, \alpha_x) = \tau_0 \frac{\gamma k_2 + \sqrt{\gamma^2(k_2^2 - k_t k_\xi) + k_\xi(k_t + 1)}}{1 - (\gamma^2 - 1)k_t}, \tag{26}$$

where

$$k_2 = \xi_y\,tan\,\alpha_y + \xi_x\,tan\,\alpha_x\,, \tag{27}$$

$$k_t = tan^2\alpha_y + tan^2\alpha_x\,, \tag{28}$$

$$k_\xi = \xi_y^2 + \xi_x^2 + 1\,. \tag{29}$$

In the expressions above, α_y and α_x are the orthogonal migration angles, $\xi_y = (y_m - y_d)/z_d$ and $\xi_x = (x_m - x_d)/z_d$.

The reflection event has a concave shape. The stationary point occurs at $\alpha_y = \alpha_{0y}$ and $\alpha_x = \alpha_{0x}$. The diffraction event, in turn, is flat ($\tau(\alpha_y, \alpha_x) = \tau_0$) in the gather observed directly at a diffraction point ($\xi_y = \xi_x = 0$), and after migration with the correct velocity ($\gamma = 1$).

To summarize, reflections and diffractions have quite different shapes in the dip-angle domain. The diffraction-event shape depends on the imaging depth, migration-velocity accuracy, and the lateral distance between the CIG and the scattering point. Reflection events always keep the shape of a smile. We propose using this shape difference as a criterion for separating reflections and diffractions.

1.4 Separation of reflections and diffractions in migrated dip-angle gathers

The Radon Transform can focus different events in the data space on different areas of the model (Radon) space (Maeland, 1998; Bickel, 2000). After focusing, events of different types can be separated. In particular, primaries and multiples having different velocities can be separated in the Radon domain, which is widely used as a demultiple tool (Foster and Mosher, 1992; Landa et al., 1999).

If events are defined by different equations (as reflections and diffractions are in the migrated dip-angle domain), it is more appropriate to focus them using the Hybrid Radon Transform. The transform is called “hybrid” because it operates with several models simultaneously. It was introduced by Trad et al. (2001) as a combination of linear and hyperbolic Radon Transforms.

In applying the Hybrid Radon Transform to diffraction imaging two models are used (Klokov et

al., 2010a). One of them (m_r) defines reflection events, and the other one (m_d) describes diffractions. The models are connected to the data by two different operators. The adjoint operators transfer energy from the data space to the model spaces, and the forward operator moves the energy back to the data space. After the transformation is performed, diffraction events will be focused in the diffraction model, while the energy of reflection events moves to the reflection model. Separate forward modeling provides two different gathers. The first gather contains reflection events, and the second contains diffraction events only.

The transform operators are based on analytical expressions for the separated events. Let us consider the operators for the case of 2D time migration. The reflection response shape is governed by three parameters from equation 12: imaging time τ_α , real reflector dip α_0 , and velocity model accuracy γ . The operator for the adjoint transform (L_r^T) from the data domain to the reflection-model domain is therefore

$$m_r(\gamma, \alpha_0, \tau_0) = \sum_\alpha d[\alpha, \tau_\alpha(\gamma, \alpha_0, \tau_0)], \tag{30}$$

and for the forward transform (L_r) from the reflection model to the reflection data it is

$$d_r(\alpha, \tau_\alpha) = \sum_\gamma \sum_{\alpha_0} m_r[\gamma, \alpha_0, \tau_0(\gamma, \alpha_0, \tau_\alpha)]. \tag{31}$$

Diffraction events are defined by three parameters as well (equation 19): imaging time τ_α , ratio of the lateral distance between the CIG and the scattering point to the scatterer depth ξ , and velocity-model accuracy γ . The operator for the adjoint transform (L_d^T) from the data domain d to the diffraction-model domain m_d and the forward operator (L_d) can be expressed as

$$m_d(\gamma, \xi, \tau_0) = \sum_\alpha d[\alpha, \tau_\alpha(\gamma, \xi, \tau_0)], \tag{32}$$

$$d_d(\alpha, \tau_\alpha) = \sum_\gamma \sum_\xi m_d[\gamma, \xi, \tau_0(\gamma, \xi, \tau_\alpha)]. \tag{33}$$

To find optimal models, we can construct the following objective function:

$$F(m_r, m_d) = \| W_{data}(L_r m_r + L_d m_d - d) \|_2 + \varepsilon_r \| W_r m_r \|_2 + \varepsilon_d \| W_d m_d \|_2. \tag{34}$$

Here, W_{data} stands for the diagonal matrix of data weights, W_r and W_d are model space weights, ϵ_r and ϵ_d are heuristically selected reflection and diffraction measures of sparseness.

The objective function contains two terms. The first defines how well the modeled data fit the original data. The data weights W_{data} allow us to exclude some parts of the CIG from the data-fitting calculation. These can be the data parts that are contaminated by large amounts of noise or the parts where the signal is simply absent. The model space weights W_r and W_d are model dependent. Because the objective function is minimized iteratively, we define the model weights

for current iteration as inverse model values from the previous iteration (Hugonnet et al., 2001):

$$W_r^{(n)} = diag \frac{1}{\sqrt{m_r^{(n-1)}}}, \tag{35}$$

$$W_d^{(n)} = diag \frac{1}{\sqrt{m_d^{(n-1)}}}, \tag{36}$$

where n stands for the current iteration number. Using model weights allows us to increase model sparseness and to transform data fitting and sparseness estimation into one problem (Trad et al., 2003).

We minimize the function F by the quasi-Newton L-BFGS algorithm (Nocedal, 1980). After models m_r and m_d are found, we perform separate modeling and obtain two separate data sets, one of them containing diffraction events only and the other containing reflection events. Stacking of a "diffraction" CIG in the dip-angle direction provides a diffraction image. This image can be used for locating faults/fractures or other small geological objects, which are not clearly visible on a conventional seismic image.

The Hybrid Radon Transform operators can be built for either time-migrated or depth-migrated domains. In the case of 2D time migration, the operators are defined by equations 12 and 19. They describe the events' shape in the dip-angle domain as accurately as equations 3–4 and 15–16 define the events' shape in the data domain. After 2D depth migration, operators can be built on the basis of equations 20 and 21. When the velocity function has a complex distribution, migrated events will deviate from the analytical description. However, they tend to the shape defined by the proposed equations. In CIGs close to the diffraction point, diffraction events are approximated with high accuracy independently of velocity-model complexity. Therefore, the proposed technique is valuable for extraction of diffraction events migrated in depth. The operators working with 3D events may be constructed on the basis of equations 22 and 26.

Note that the reflection operator and the diffraction operator are not orthogonal, and the model spaces partially overlap. Therefore, the diffraction model may contain some part of reflected energy and vice versa. In practice, because of the significant initial differences in magnitude between reflections and diffractions, this partial cross-talk may exceed the diffraction component. In order to reduce the influence of energy leakage, we apply preliminary processing to destroy a part of the reflected energy in the data domain before migration. In common-offset or common-plane sections, reflections are locally plane. Diffractions, in turn, have a hyperbolic appearance (Harlan et al., 1984). Therefore, using plane-wave destruction (Fomel, 2002; Fomel et al., 2007), we can attenuate reflection with minimum distortion of diffraction events. The preprocessed gathers may nevertheless have some remaining reflection energy. However, the residual reflections are comparable in energy to diffractions, and we are able to prevent their penetration

into the diffraction model by using sparseness measures of the objective function (equation 34).

1.5 Synthetic data examples

We applied our diffraction-extraction algorithm on the left side of the Sigsbee 2B model (Figure 6a). This part of the model contains strong artificial point scatterers, as well as a number of faults. Therefore, this experiment is of particular interest for diffraction imaging.

Figure 7a shows a common-image gather for the position 6.1 km — just above the two point scatterers. The CIG contains a number of smiles from reflection boundaries, as well as some diffraction responses. There are two strong horizontal events at times 6.3 s and 8.2 s. A fault is presented by several inclined events at time 5.4 s. The sea bottom is rough and contains discontinuities, which cause some energy appearing above 4 s from the wave diffracted at the bottom.

Because the Sigsbee 2B data were time migrated with the correct velocity, we reduced the models to two planes, corresponding to $\gamma = 1$. The reflection model contained dip angles of from -50 to 50 degrees. The diffraction model described events with parameter ξ in the range of from -0.12 to 0.12.

Because of the strong scattering properties of the Sigsbee 2B model, we were able to avoid the preliminary plane-wave suppression for model-space cross-talk minimization. Instead, we suppressed reflections by detecting and removing reflection-smile apexes, which allowed us to preserve significant parts of reflections and to test reflection energy focusing in the Radon space. The smile-apex-free migrated data were an input for the Hybrid Radon Transform.

The obtained reflection model is presented in Figure 7b. Reflection events are focused near the zero-dip angle. The sea-bottom reflection event has the strongest energy at a time of about 3.9 s. The diffraction model is shown in Figure 7c. The flat events from the scatterers are well focused at the zero distance. The fault response was transformed into several points at different distances. The strong energy diffracted from the sea bottom is also present.

After diffraction modeling, we can find the dip-angle gather that contains desired diffraction events only (Figure 7d). Stacking the gather over the dip angle provides the diffraction image (Figure 6b). The point scatterers and faults appear clearly whereas reflections are suppressed.
Note that a limited acquisition aperture may yield migration noise. Particularly in the dip-angle domain, events tend to become narrower with depth. Stacking of short diffraction events hampers high-resolution diffraction-image construction because the event tails are not stacked destructively. Using the gather decomposition in the Radon space, we are able to mitigate this problem. When modeling the gather, we have the freedom to choose event width. The diffraction gather in Figure 7d contains events that have maximum width. Note that this procedure does not

always preserve true amplitudes.

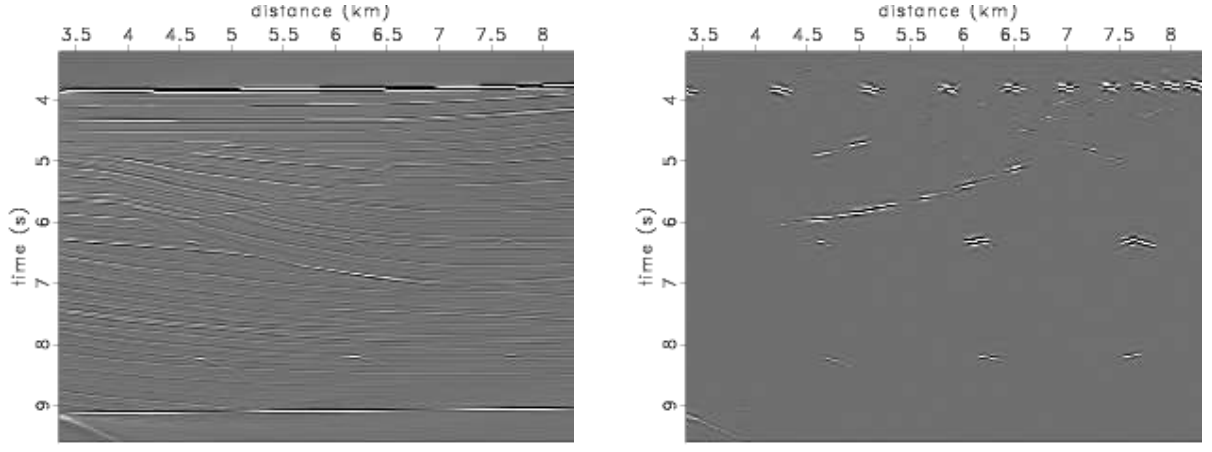

a) b)

Figure 6: (a) Conventional time-migrated image for the Sigsbee 2B model and (b) the diffraction image.

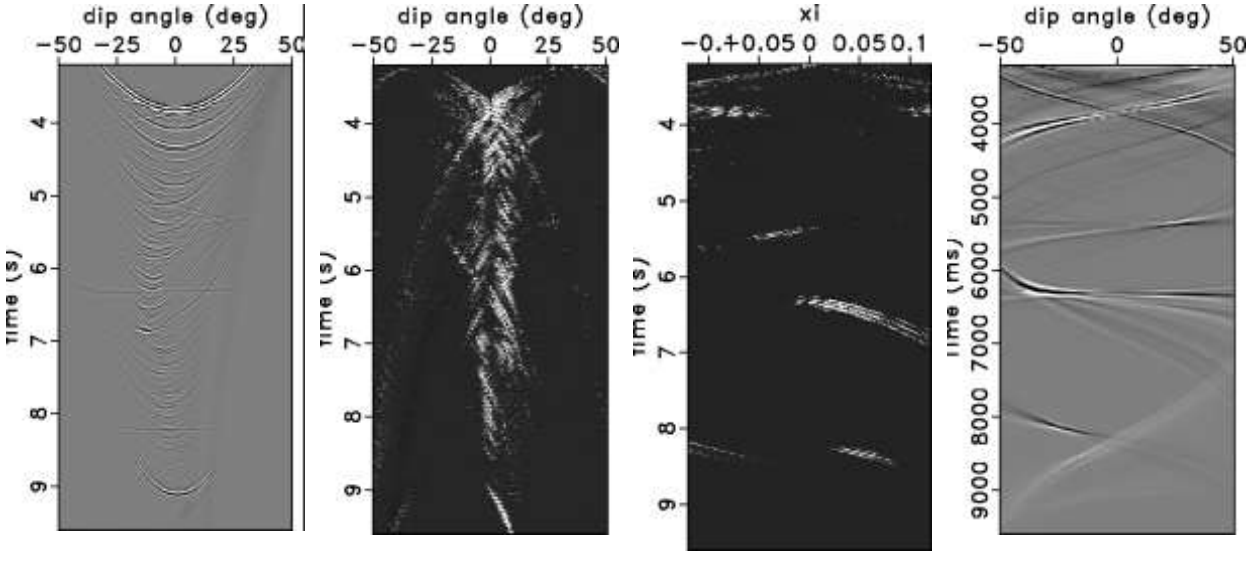

a) b) c) d)

Figure 7: (a) Input common-image gather in the dip-angle domain, (b) reflection and (c) diffraction models in the Radon space, and (d) the gather after diffraction extraction.

We next tested our diffraction imaging technique on the Marmousi data set (Figure 8). The zero-offset section was modeled and depth-migrated with the same velocity model (Figure 4a). Figure 9a shows the depth-migrated dip-angle gather extracted from the 7.4-km position. The reflection events have a complex shape and overwhelm the diffraction component. We applied preliminary reflection suppression in the data domain and remigrated the data. A new common-image gather from 7.4 km is shown in Figure 9b. Reflection smiles have almost disappeared, whereas

diffraction events are easily perceptible. There is an outstanding set of crossing diffraction events, which originate from boundary discontinuities, at a depth level of 0.5 km. At the same time, the gather contains a large amount of migration noise, which has energy comparable to that of diffracted waves. Also, some residual reflection energy is still present.

Integration of the gathers after plane-wave destruction provides an image that has reflection boundaries significantly suppressed (Figure 11a). We can easily identify diffraction objects. Three strong faults can be seen clearly. The top part of the image is filled by points corresponding to discontinuities of reflection boundaries. However, a large number of diffraction objects are masked by residual reflections and noise, especially in the bottom part.

The Hybrid Radon Transform allows us to extract events that fit our diffraction model (Figure 10b). In the Radon space, diffraction energy is well focused at a depth level of up to 1 km. The model becomes more complex as depth increases, and sloping events begin to deviate from the theoretical model. Consequently, their energy gets smeared. Residual reflections and most of the migration noise are concentrated in the reflection model (Figure 10a).

Diffraction modeling yields a common-image gather containing diffraction events only (Figure 9c). An image of diffraction objects is constructed by events whose distance parameter (and, consequently, slope) is close to zero. Steep events are stacked destructively and may generate image artifacts. In order to reduce noise in the diffraction image, we limited the modeled distance interval to 0.2 km, and, thus, the diffraction gather does not contain events whose dips are too steep.

Integration of diffraction gathers provides the diffraction image (Figure 11b). We can identify diffraction objects in the bottom part, where the noise was filtered out. For instance, there is a strong scatterer corresponding to the pinch-out at depth of about 2.5 km and at a distance of 4.8 km.

The Marmousi example demonstrates that our diffraction-imaging technique can be applied after depth migration with a complex velocity. As demonstrated previously (Figure 5), in depth-migrated gathers observed close to a scattering point, a shape of diffraction events can be accurately described by the model. This allows us to focus diffraction energy in the Radon space and to separate diffractions from reflections and migration noise.

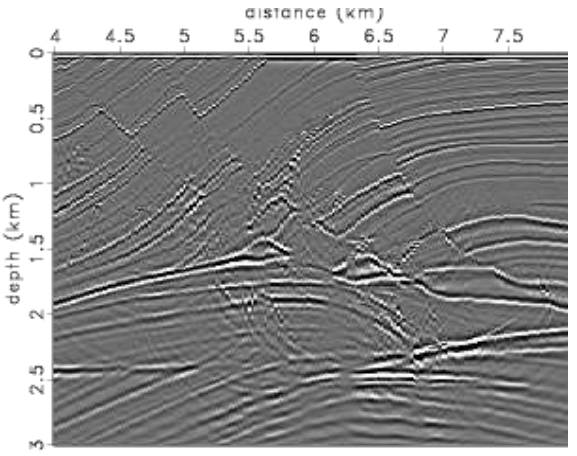

Figure 8: Conventional depth-migrated image for the Marmousi model.

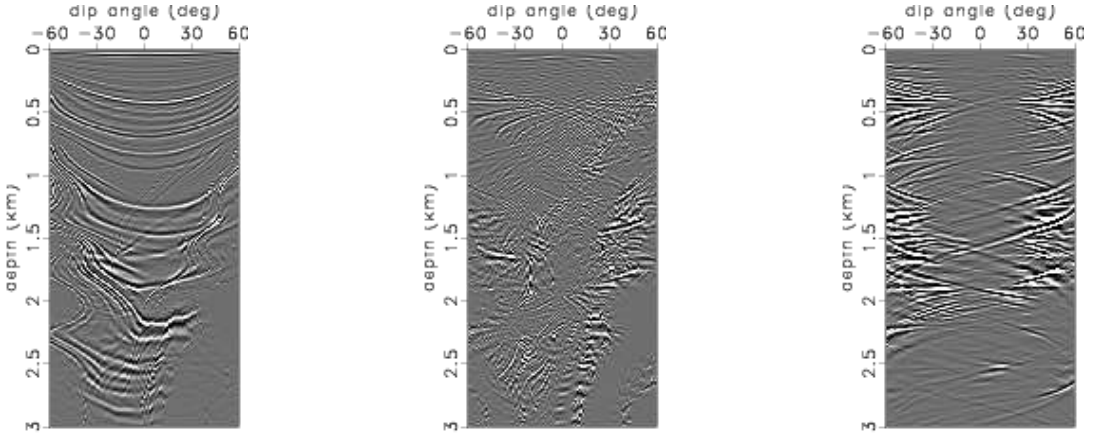

a) b) c)

Figure 9: (a) Input common-image gather in the dip-angle domain, (b) the migrated gather after preliminary plane-wave destruction, and (c) the gather after diffraction extraction.

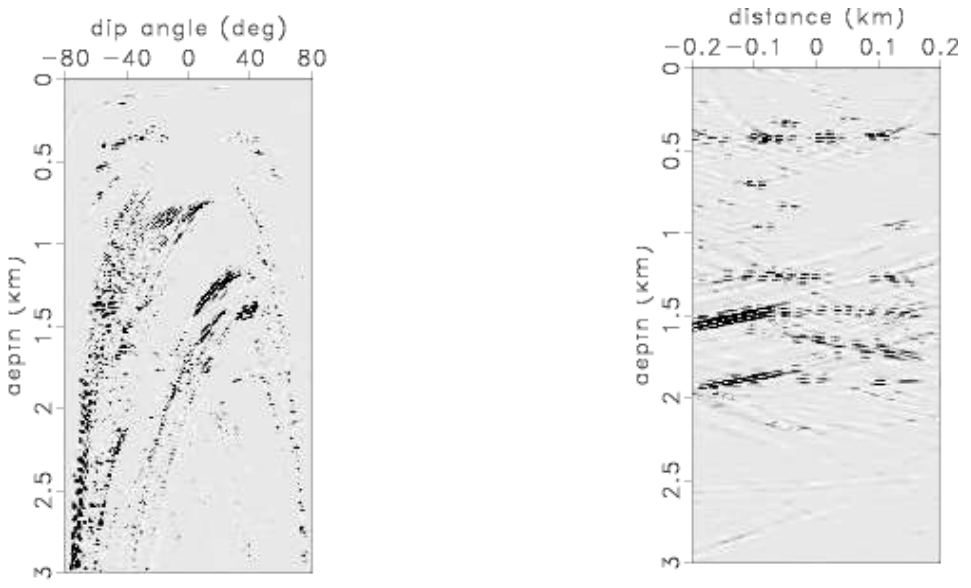

a) b)

Figure 10: (a) Reflection model and (b) diffraction model for the common-image gather from the Marmousi data set.

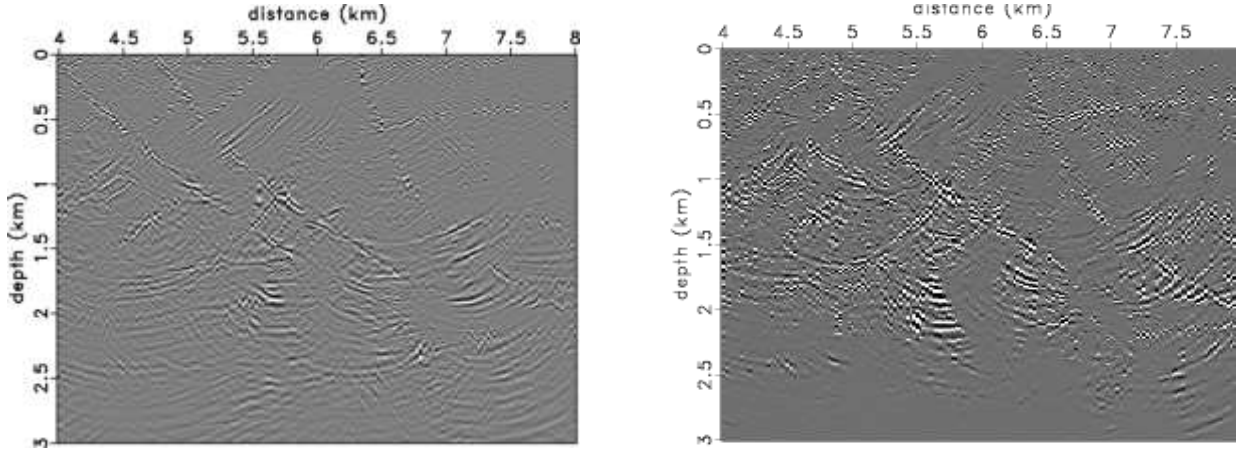

a) b)

Figure 11: (a) Depth-migrated image for the Marmousi model after preliminary plane-wave destruction and (b) diffraction image.

1.6 Field data examples

1.6.1 Viking Graben AVO data set

We applied our method next to a marine data set that was obtained over a structure in the North Sea called the Viking Graben. The data were collected by Mobil Corporation and released in 1994 to support development of seismic processing and inversion methods (Keys and Foster, 1998).

The conventional time-migrated image is shown in Figure 12. With some effort, one can identify a system of faults at a time level of about 1.3 s. Some point scatterers are present in the top part of the image, just below the sea bottom. At a level of about 2 s, we observe the so-called Paleocene anomaly, which can be associated with a class 3 gas sand (Madiba and McMechan, 2003).

Figure 13a shows a migrated dip-angle gather corresponding to a lateral position of 18 km. There are strong diffraction events at about 2 s originating from the amplitude anomaly. The gather is located above a fault at time interval 1.1-1.4 s. The fault is a source of diffracted waves, but the diffraction events are not immediately visible because of the strong, dominating reflection component.

Preliminary plane-wave destruction and migration allow us to detect a number of diffraction events (Figure 13b). However, the gather also retains a significant amount of noise. The reflection-free image (Figure 15a) is noisy, and diffraction objects are not clearly visible.

As in the synthetic examples, the Hybrid Radon Transform isolates diffractions (Figure 13c). Four strong events from the fault are clearly visible. The event at about 1.25 s appears horizontal, indicating that the migration velocity is correct. The strong event at a time level of about 0.65 s corresponds to a discontinuity of a reflection boundary. Note that the gas-sand amplitude anomaly produces diffraction events as well.

Migrated events often do not have an ideal shape. Their unevenness could be a reason for the additional appearance of image noise. The Radon Transform using the sparseness factor brings an event closer to the shape described by the theoretical model. Therefore, inverted events have a more regular shape, which helps to stack them optimally.

Radon-space models are shown in Figure 14. Because plane reflection boundaries were previously suppressed, the reflection model contains residuals, which are not focused well. There are four focusing points in the diffraction model, which stand out at time levels between 1.1 and 1.4 s. These points contain an energy of diffraction events originating from the fault. The

diffracted energy from the amplitude anomaly is focused in several positions around 2 s.

The diffraction image (Figure 15b) can be divided into three parts. In the time interval from 1.1 s to 1.6 s, we can see a strong system of faults, whereas faults are absent outside the layer. This interval may indicate the geological time of the extensive rifting process. The part of the image below 1.6 s corresponds to the Paleocene interval. The Paleocene amplitude anomaly looks strong in the diffraction image. The interval above 1.1 s contains several horizontal lines of point scatterers. The source of the scattering is the sharp boundaries of the covering layers.

Note that the diffraction image helps us detect objects that are subtle in the conventional image, such as the fault at the lateral position of 21.8 km and at the time levels of 1.3 to 1.5 s.

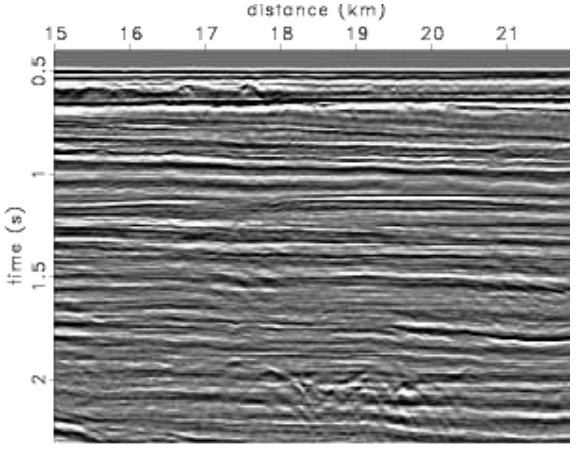

Figure 12: Conventional time-migrated image for the Viking Graben data set.

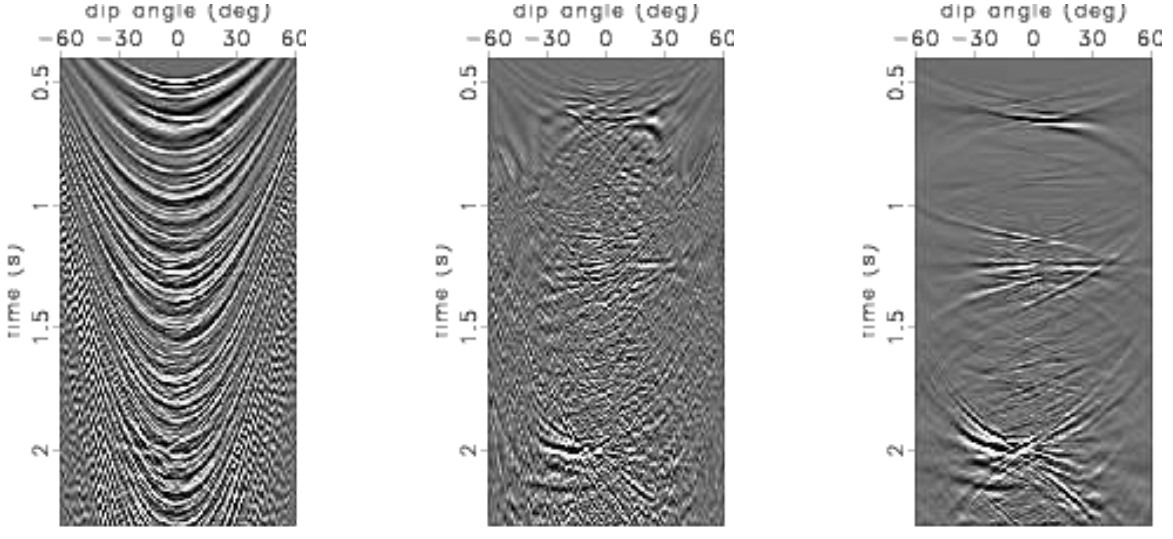

a) b) c)

Figure 13: (a) Input common-image gather in the dip-angle domain, (b) the migrated gather after preliminary plane-wave destruction, and (c) the gather after diffraction extraction.

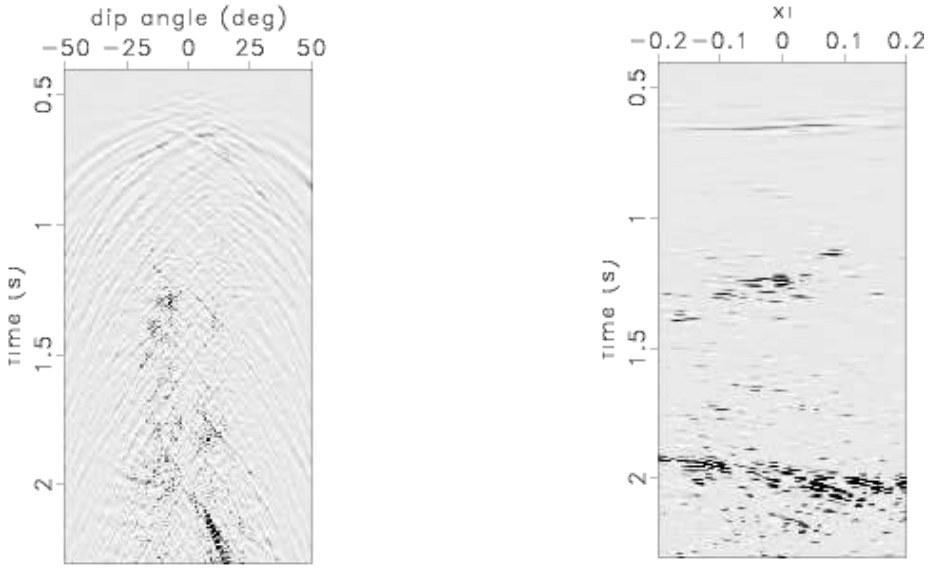

a) b)

Figure 14: (a) Reflection model and (b) diffraction model for the common-image gather from the Viking Graben data.

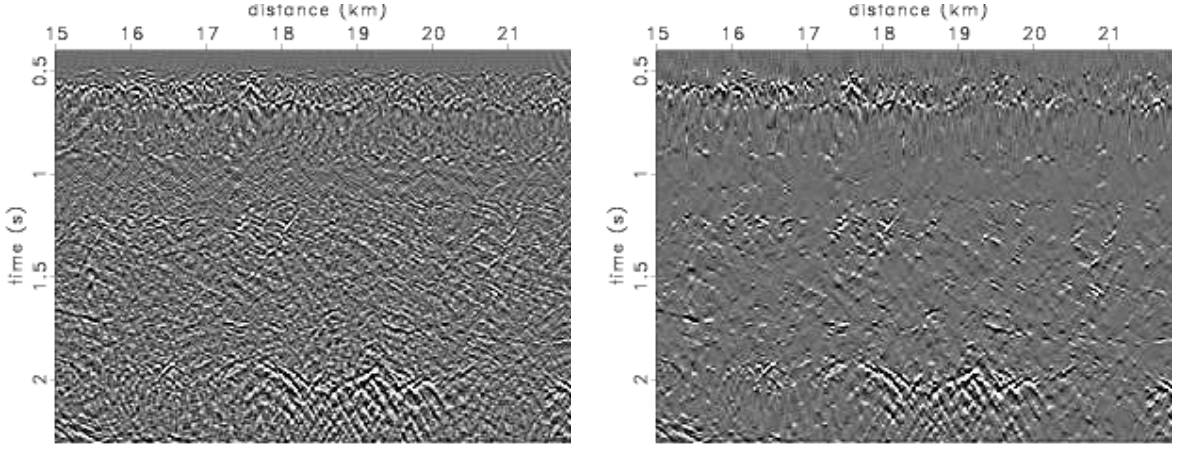

a) b)

Figure 15: (a) Time-migrated image for the Viking Graben data set after preliminary plane-wave destruction and (b) diffraction image.

1.6.2 US East Coast Deep Water line

During 1970's, the U.S. Geological Survey acquired approximately 25000 km of 2D marine seismic data along the U.S. Atlantic Continental Margin, primarily to address hydrocarbon resource potential and stratigraphic history (Hutchinson et al., 1995). We work with line 32 located across the Carolina Trough, which is underlain by narrow rift basins and extensive salt

deposits.

The line extends to 282.2 km. The shots are spaced at 50 m. The near offset trace is 425 m, while far offset trace is 3970 m. The CMP fold of this line is 48. We concentrated on 15 km part of the line. Our imaging target is the layer deposited just beneath the sea bed at time level 4.1 – 5.0 s. Figure 16a shows a time-migrated image of the interest area.

Figure 16b shows a diffraction image. Reflections are well removed and the image reveals a number of diffraction wave sources. There are three parallel lanes of such sources, which correspond to discontinuities of reflection boundaries. The diffraction image shows that our target layer is packed by vertical faults. The magnitude of the diffractions is decreasing from left to right.

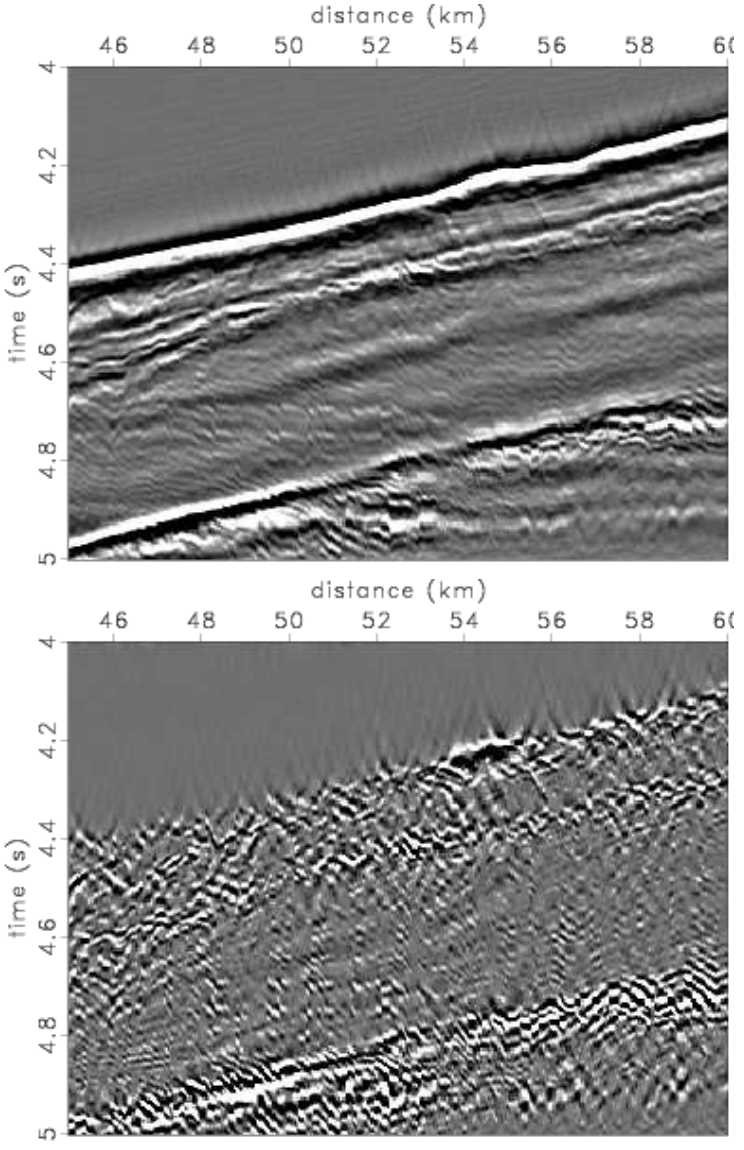

Figure 16: Conventional time-migrated image (above) and diffraction image (below).

We can predict the presence of faults from the conventional image. There are visible amplitude perturbations in the lateral interval 45–52 km. However, fractures detection from the right part of the conventional image is not so trivial.

Dip-angle gathers after diffraction events extraction provide valuable information, which may be used for diffraction image validation. We consider a dip-angle common-image gather from the position 58.75 km. There is a vertical fracture located in this position. The interval of interest for the considered position is 4.3–4.7 s.

Figure 17b shows the dip-angle gather after diffraction isolation. The interval of interest includes a number of flat diffraction events. The gather from the position shifted on 100 m contains the same set of diffraction events, but now they all appear inclined (Figure 18b). This behavior of diffraction events coincides completely with theoretical predictions. This validates that the interval of interest contains real diffraction events, which, in turn, produce real diffraction objects in the image. After conventional migration the diffraction events are not clearly seen (Figures 17a and 18a), because they are masked by strong reflection concave events.

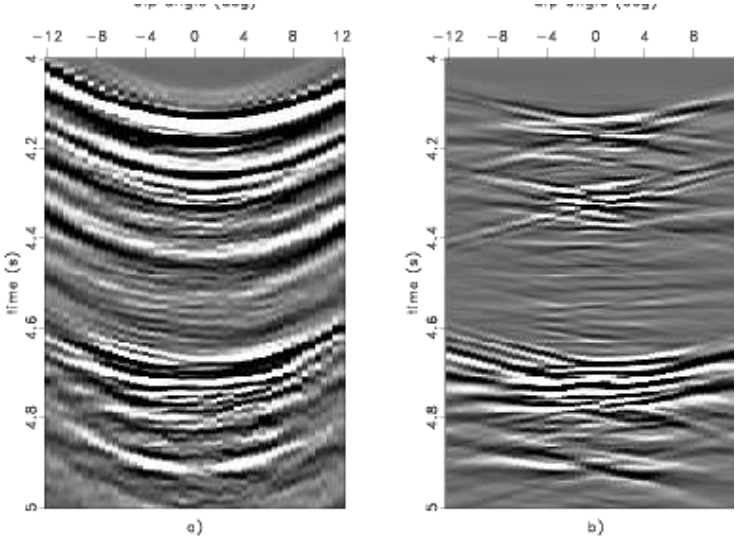

Figure 17: (a) Conventional dip-angle gather from position above a vertical diffraction object and (b) the dip-angle gather after diffraction events extraction.

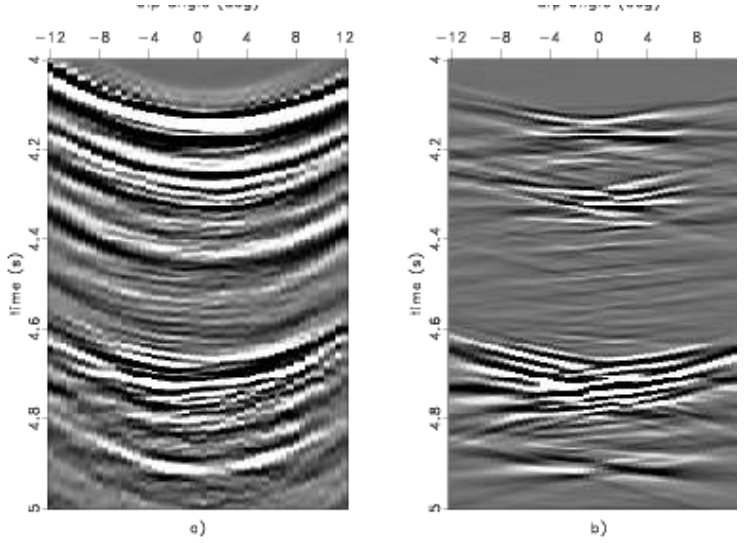

Figure 18: (a) Conventional dip-angle gather from position aside a vertical diffraction object and (b) the dip-angle gather after diffraction events extraction.

1.6.3 Gibson Gulch

We applied our method of diffraction imaging to a field 3D data set obtained from the Piceance Basin area in Colorado, USA. We worked with regular stacked volume. The volume extended to 10 km in the inline direction and 13 km in the crossline direction. The bin size is 33.55 by 33.55 m. The time-migrated image is shown in Figure 19. The image reveals a thick layer in the time interval 0.6-1.2 s. The top and the bottom are consistent: the boundaries are plane and inclined in the crossline direction and are folded along inlines.

Three separate clusters of diffraction objects can be detected. The first one is located in the top part at time interval 0.5-0.8 s (Figure 20). We can identify a number of point-objects evenly distributed. Some of the diffractors are consistent with the reflection boundary starting at 0.8 s in the left of the shown crossline and indicate its sharpness. For comparison we show a conventional image of this part. Several point-objects can be found here as well, but most of diffractors are hidden behind strong reflection boundaries.

The second cluster of diffractions is located in time interval 1.0-1.4 s and is associated with the reservoir bottom. The diffraction image discovers several vertical objects there (Figure 21). The slice indicates that the diffraction objects are well oriented from the north-west to the south-east in opposite to the top level point-objects.

The third cluster is situated between the previous two ones and inside the reservoir. The diffraction objects have vertical features there (Figure 22). They are not as strong and do not

exceed above the level of residual noise too much. This hampers identification of the objects. In the situation like that, the dip-angle gather analysis can be helpful. Figure 23 shows a 3D dip-angle gather from the position where one of the vertical objects is present. The gather contains events extended along the two orthogonal dips. If we take a gather from the position shifted by 20 m along the inline direction, we can recognize the same events with changed slopes in the crossline direction. This behavior is expected theoretically which allows as to consider these events as real diffraction events.

The dip-angle gather analysis can be applied to each diffraction object separately. It is convenient to have some integral attribute for characterization of the whole diffraction image volume. As the attribute one may use diffraction energy stack produced by integration in vertical time windows. Figure 24 shows a set of diffraction energy maps. A time window of 50 ms was used at different time levels. The maps reveal areas rich in diffraction energy as well as areas that are poor in them. One can also trace orientation of diffraction objects – from the north-west to the south-east, which is consistent with the layer bottom features. This kind of attribute may favor fracture corridor mapping.

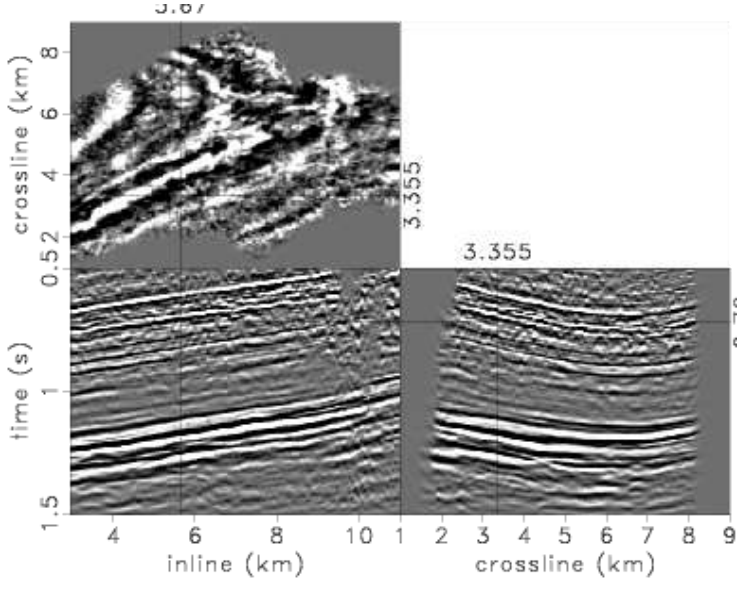

Figure 19: Conventional time-migrated image for Gibson Gulch data set.

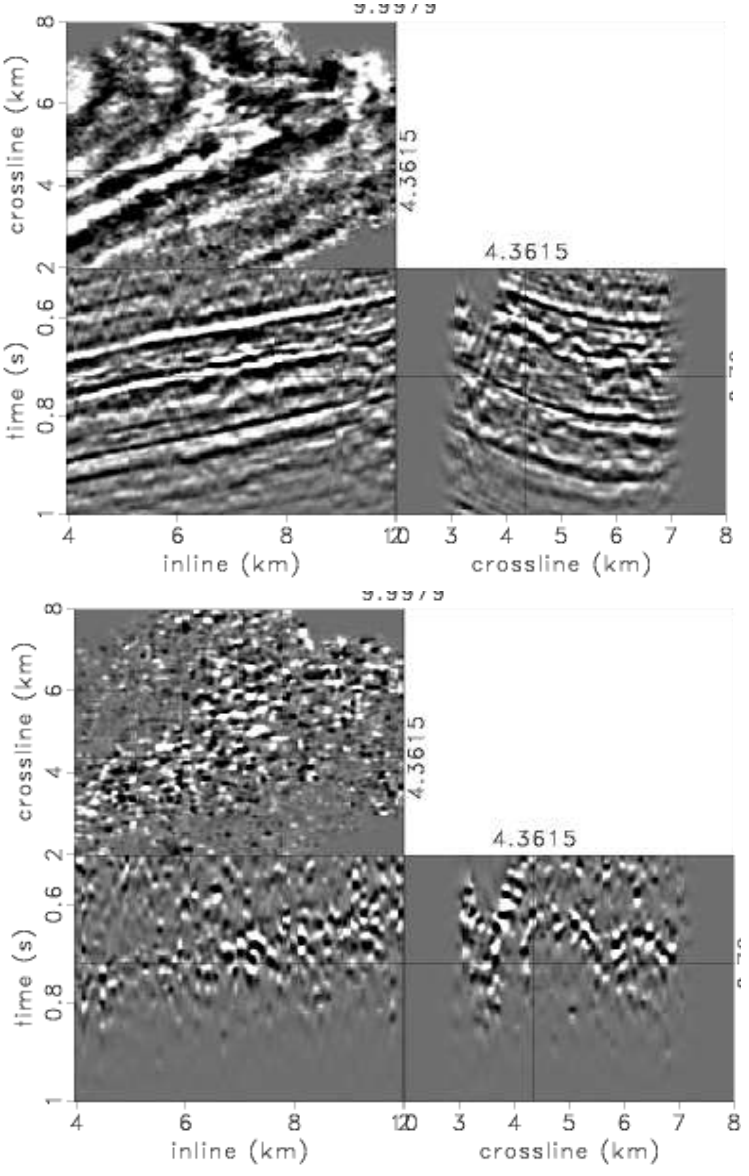

Figure 20: Conventional time-migrated image (above) and diffraction image (below) for the top part of the volume.

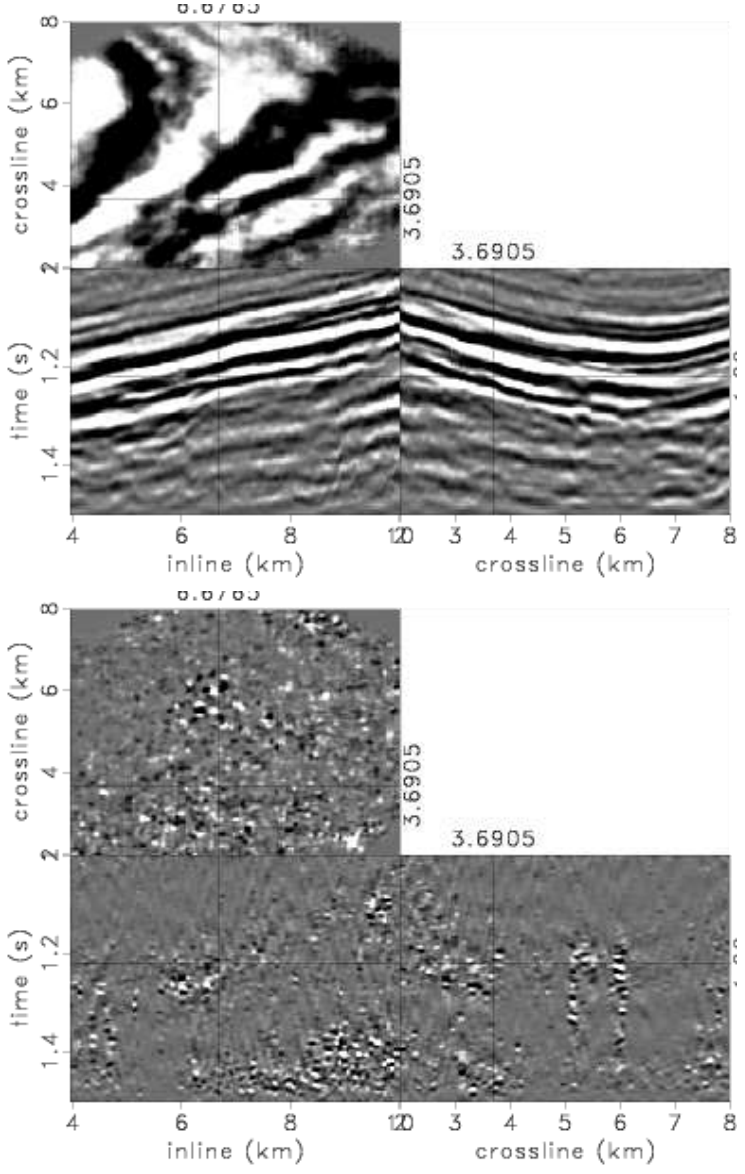

Figure 21: Conventional time-migrated image (above) and diffraction image (below) for the bottom part of the volume.

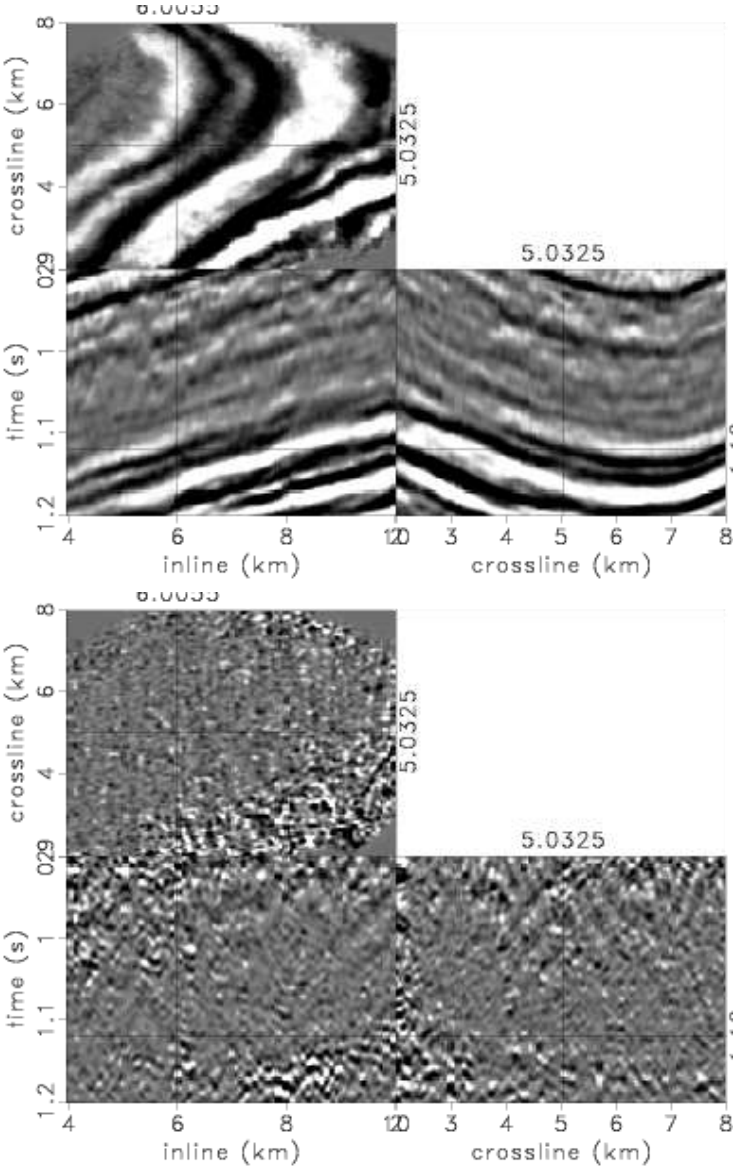

Figure 22: Conventional time-migrated image (above) and diffraction image (below) for the middle part of the volume.

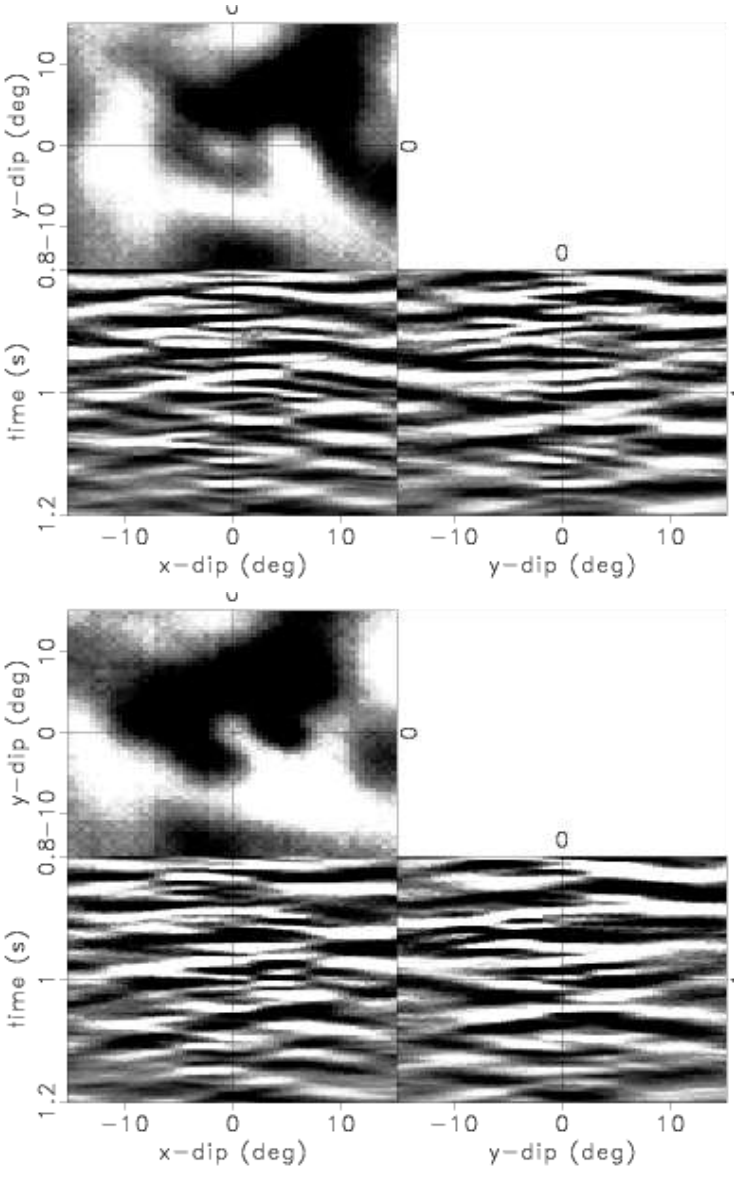

Figure 23: Dip-angle gather after diffraction events extraction from positions y = 5.033 km and x = 6.318 km (above), and dip-angle gather from position shifted on 20 m in x-direction (below).

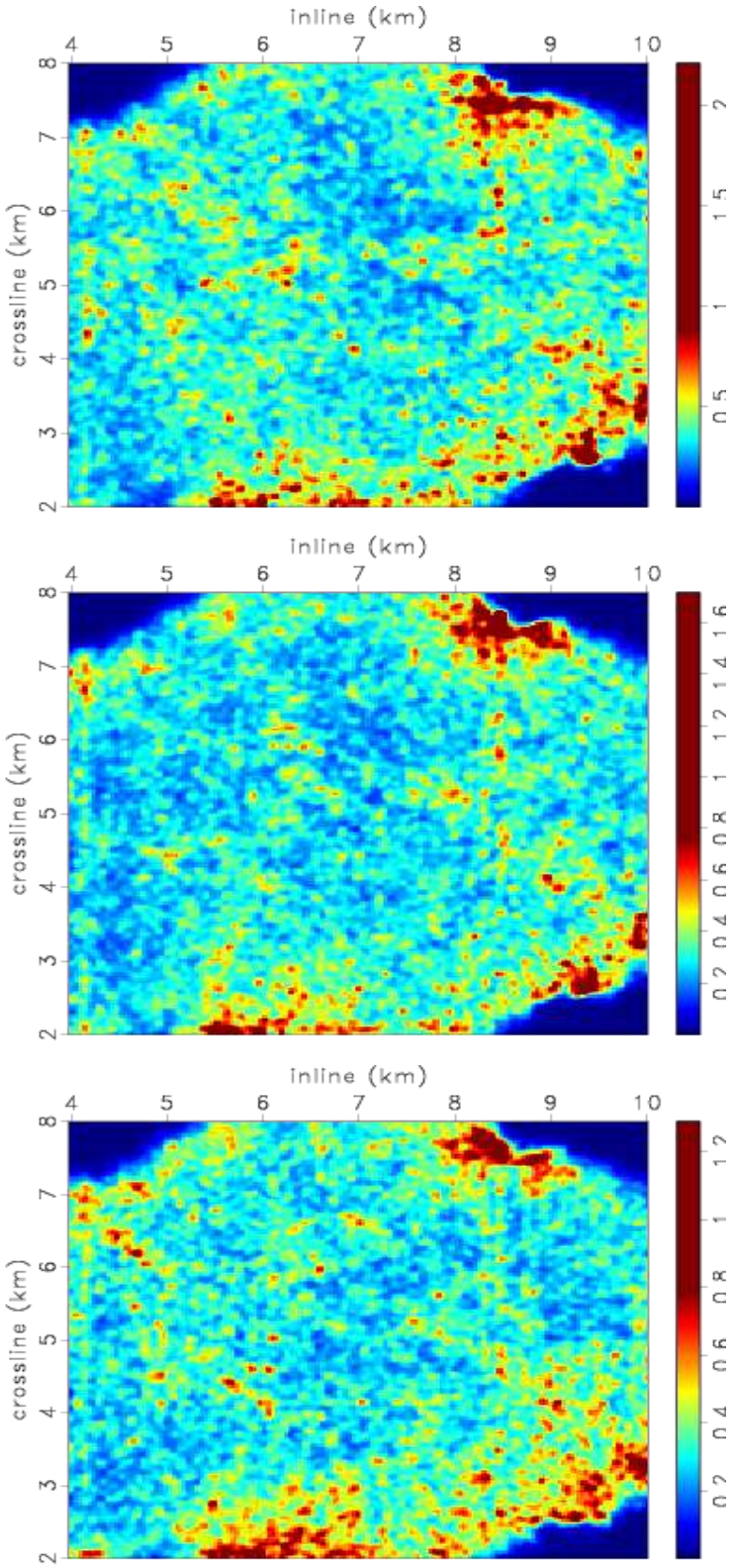

Figure 24: Diffraction energy stacks for different time intervals: 1.00-1.05 s (above), 1.05-1.10 s (middle), and c) 1.10-1.15 s (below).

1.7 Migration velocity analysis

Migration Velocity Analysis using reflection events is usually based on analysis of common-image gathers that represent seismic images obtained from different offsets. Migration with correct velocity produces CIGs with flat events, whereas velocity errors lead to visible differences between common-offset images. Analyzing residual moveout in the CIGs defines velocity-model correction (Deregowski, 1990).

The diffraction component can also be used for estimating velocity-model accuracy (Landa et al., 2008; Reshef and Landa, 2009). Equations 19, 21, and 26 show that in the migrated dip-angle domain, a diffraction-event curvature is described by velocity-model accuracy. By analyzing the curvature, we can detect whether the velocity model is correct and estimate the required correction from the value of γ .

To illustrate this idea, we used the Sigsbee 2B synthetic data. Figure 25a shows a common-image gather for a position of 6.1 km, which was obtained after migration of the zero-offset section with 10% lower velocity. Because the migration velocity is low, the diffraction events are curved, and their branches look like reflections. However, the shape of the diffraction events differs from that of reflection smiles. This difference allows us to extract diffractions from the gather.

To separate reflections and diffractions, in cases when the correct migration velocity is unknown, we extend Radon space models in the velocity-model-accuracy parameter (γ) dimension. Diffraction-event energy is well focused on the plane corresponding to correct migration velocity (Figure 25b). If the velocity model is wrong, diffraction events appear out of focus (Figures 25c and 25d).

This example shows that utilizing focusing power in the Radon space enables, in principle, an estimation of velocity-model corrections. Migration velocity analysis based on diffractions requires a single common-offset section only. This property makes it advantageous for velocity-model construction, particularly in the near surface. In the shallow part, migrated gathers have limited offset, and the conventional MVA, which is based on reflections, suffers from the data shortage.

Diffraction Migration Velocity Analysis should be performed on separate common-offset sections. Accumulation of common-offset sections migrated using an incorrect velocity

may lead to loss of the diffraction component generated by destructive summation.

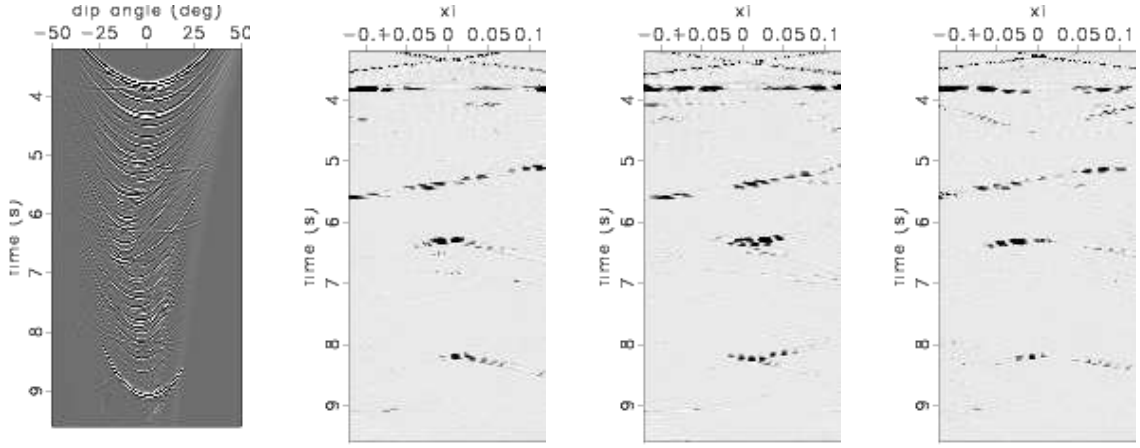

a) b) c) d)

Figure 25: (a) Dip-angle gather for migration with 10% lower velocity; diffraction model planes corresponding to (b) 10% lower velocity, (c) 15% lower velocity, and (d) 5% lower velocity.

1.8 Conclusions

There are two major advantages to migration into dip-angle common-image gathers. First, appearance of data in this domain is the same whether the input data are multi- or single-offset. Second, diffraction events differ significantly in shape from reflections. The shape difference can be used as a criterion for reflection/diffraction separation.

Derived analytical expressions show that a correctly migrated diffraction event is not highly dependent on complexity of the velocity model, and diffractions can be accurately approximated in the depth-migrated domain. Therefore, diffraction analysis in the migrated domain may excel over techniques operating in the data domain.

Diffractions can be separated by the Hybrid Radon Transform, a tool that extracts events that fit the diffraction model. Input for the procedure is a migrated dip-angle gather, possibly after preliminary plane-wave destruction in the data domain. Our examples show that the input may contain significant amounts of noise — either migration noise or migrated data noise. Noise, which is inconsistent with the diffraction model, gets rejected from the output gather by the Hybrid Radon Transform.

Integration of extracted diffraction events along dip angles provides a diffraction image, which is a seismic image of small but important geologic objects that are often invisible after conventional seismic processing.

Unlike reflections, diffractions are always significantly affected by velocity errors. They can be used in applications to efficient migration-velocity analysis, which requires only a single offset (such as zero offset) as input, making it favorable for velocity-model construction in the near surface.

The distinct difference between reflections and diffractions in the migrated dip-angle domain suggests that this domain is advantageous for separating and imaging these two types of waves.

1.9 Acknowledgments

We thank Evgeny Landa for many stimulating discussions. We are also grateful to Igor Ravve for valuable comments and suggestions.

The East Coast line is provided by US Geological Survey. We thank Karl Schleicher for the data preprocessing.

1.10 References

Al-Dajani, A., and S. Fomel, 2010, Fractures detection using multi-azimuth diffractions focusing measure: Is it feasible?: SEG Technical Program Expanded Abstracts, 29, 287–291.

Audebert, F., P. Froidevaux, H. Rakotoarisoa, and J. Svay-Lucas, 2002, Insights into migration in the angle domain: SEG Technical Program Expanded Abstracts, 21, 1188–1191.

Berkovitch, A., I. Belfer, Y. Hassin, and E. Landa, 2009, Diffraction imaging by multifocusing: Geophysics, 74, WCA75.

Bickel, S. H., 2000, Focusing aspects of the hyperbolic radon transform: Geophysics, 65, 652–655.

Bleistein, N., J. Cohen, and W. Stockwell, 2001, Mathematics of multidimensional seismic imaging, migration, and inversion: Springer.

Brandsberg-Dahl, S., M. V. de Hoop, and B. Ursin, 2003, Focusing in dip and AVA compensation on scattering-angle/azimuth common image gathers: Geophysics, 68, 232–254.

Burnett, W., 2011, Multiazimuth velocity analysis using velocity-independent seismic imaging: PhD thesis, The University of Texas at Austin.
Burnett, W., and S. Fomel, 2011, Azimuthally anisotropic 3D velocity continuation: International Journal of Geophysics, 2011.
Claerbout, J., 1992, Earth soundings analysis: Processing versus inversion: Blackwell Scientific Publications, Inc.
Dell, S., and D. Gajewski, 2011, Common-reflection-surface-based workflow for diffraction imaging: Geophysics, 76, S187–S195.
Deregowski, S. M., 1990, Common-offset migrations and velocity analysis: First Break, 8, 225–234.
Fomel, S., 2002, Applications of plane-wave destruction filters: Geophysics, 67, 1946–1960.
Fomel, S., E. Landa, and M. T. Taner, 2007, Poststack velocity analysis by separation and imaging of seismic diffractions: Geophysics, 72, U89–U94.
Foster, D. J., and C. C. Mosher, 1992, Suppression of multiple reflections using the radon transform: Geophysics, 57, 386–395.
Harlan, W. S., J. F. Claerbout, and F. Rocca, 1984, Signal/noise separation and velocity estimation: Geophysics, 49, 1869–1880.
Hugonnet, P., P. Herrmann, and C. Ribeiro, 2001, High resolution radon - a review: 63rd EAGE Conference and Exhibition.
Kanasewich, E. R., and S. M. Phadke, 1988, Imaging discontinuities on seismic sections: Geophysics, 53, 334–345.
Keys, R. G., and D. J. Foster, eds., 1998, Comparison of seismic inversion methods on a single real data set: Society of Exploration Geophysicists.
Khaidukov, V., E. Landa, and T. J. Moser, 2004, Diffraction imaging by focusing-defocusing: An outlook on seismic superresolution: Geophysics, 69, 1478–1490.
Klem-Musatov, K., 1994, Theory of seismic diffractions: Society of Exploration Geophysicists.
Klokov, A., R. Baina, and E. Landa, 2010a, Separation and imaging of seismic diffractions in dip angle domain: 72nd EAGE Conference and Exhibition.
Klokov, A., R. Baina, E. Landa, P. Thore, and I. Tarrass, 2010b, Diffraction imaging for fracture detection: synthetic case study: SEG Technical Program Expanded Abstracts, 29, 3354–3358.
Koren, Z., and I. Ravve, 2011, Full-azimuth subsurface angle domain wavefield decomposition and imaging Part I: Directional and reflection image gathers: Geophysics, 76, S1–S13.
Kozlov, E., N. Barasky, E. Korolev, A. Antonenko, and E. Koshchuk, 2004, Imaging scattering objects masked by specular reflections: SEG Technical Program Expanded Abstracts, 23, 1131–1134.
Landa, E., I. Belfer, and S. Keydar, 1999, Multiple attenuation in the parabolic tau-p domain using wavefront characteristics of multiple generating primaries: Geophysics, 64, 1806–1815.
Landa, E., S. Fomel, and M. Reshef, 2008, Separation, imaging, and velocity analysis of

seismic diffractions using migrated dip-angle gathers: SEG Technical Program Expanded Abstracts, 27, 2176–2180.
Landa, E., and S. Keydar, 1998, Seismic monitoring of diffraction images for detection of local heterogeneities: Geophysics, 63, 1093–1100.
Landa, E., V. Shtivelman, and B. Gelchinsky, 1987, A method for detection of diffracted waves on common-offset sections: Geophysical Prospecting, 35, 359–373.
Laubach, S., R. Marrett, and J. Olson, 2000, New directions in fracture characterization: The Leading Edge, 19, 704–711.
Madiba, G. B., and G. A. McMechan, 2003, Processing, inversion, and interpretation of a 2D seismic data set from the North Viking Graben, North Sea: Geophysics, 68, 837–848.
Maeland, E., 1998, Focusing aspects of the parabolic radon transform: Geophysics, 63, 1708–1715.
Moser, T. J., and C. B. Howard, 2008, Diffraction imaging in depth: Geophysical Prospecting, 56, 627–641.
Nocedal, J., 1980, Updating quasi-newton matrices with limited storage: Mathematics of Computation,, 35, 773–782.
Pranter, M. J., A. I. Ellison, R. D. Cole, and P. E. Patterson, 2007, Analysis and modeling of intermediate-scale reservoir heterogeneity based on a fluvial point-bar outcrop analog, williams fork formation, piceance basin, colorado: AAPG Bulletin, 91, 1025–1051.
Reshef, M., and E. Landa, 2009, Post-stack velocity analysis in the dip-angle domain using diffractions: Geophysical Prospecting, 57, 811–821.
Sava, P., and S. Fomel, 2001, 3-d traveltime computation using huygens wavefront tracing: Geophysics, 66, 883–889.
Sava, P. C., and S. Fomel, 2003, Angle-domain common-image gathers by wavefield continuation methods: Geophysics, 68, 1065–1074.
Taner, M. T., S. Fomel, and E. Landa, 2006, Separation and imaging of seismic diffractions using plane-wave decomposition: SEG Technical Program Expanded Abstracts, 25, 2401–2405.
Trad, D., M. Sacchi, and T. Ulrych, 2001, A hybrid linear-hyperbolic radon transform: Journal of Seismic Exploration, 9, 303–318.
Trad, D., T. Ulrych, and M. Sacchi, 2003, Latest views of the sparse Radon transform: Geophysics, 68, 386–399.
Tsingas, C., B. E. Marhfoul, S. Satti, and A. Dajani, 2011, Diffraction imaging as an interpretation tool: First Break, 29, 57–61.
Xu, S., H. Chauris, G. Lambaré, and M. Noble, 2001, Common-angle migration: A strategy for imaging complex media: Geophysics, 66, 1877–1894.
Zhu, X., and R.-S. Wu, 2010, Imaging diffraction points using the local image matrices generated in prestack migration: Geophysics, 75, S1–S9.

CHAPTER 2

FRACTURE MODELING

2.1 Stress Intensity Factor Determination for Three-Dimensional Cracks Using the Displacement Discontinuity Method[1]

2.1.1 Introduction

Stress intensity factor determination plays a central role in linearly elastic fracture mechanics problems. Fracture propagation is controlled by the stress field near the crack tip. Because the stress field near the crack tip is asymptotic dominant or singular, it is characterized by the stress intensity factor. The real stress distribution at the vicinity of crack tip and the K-field LEFM approximation can be depicted schematically as in Figure 1.1. The stress singularity right at the tip of the crack cannot be experienced in real nature because inelastic deformation prevents the crack tip from being perfectly sharp. However, according to small scale yielding of the process zone immediately around the crack tip in comparison with the K-field region (Figure 1.2), the SIF is the quantity which dictates if/when the crack will propagate. The inaccuracy of the stress field calculation using the SIF based on LEFM is less than 15% of the exact solution over the distance ranging from $r<0.01a$ to $r<0.15a$, where r is the radius of K-field region and a is the half length of the crack (Pollard and Segall 1987).

Since SIF was proposed by Irwin (1957) to express displacements and stresses in the vicinity of crack tip, several analytical techniques have been developed for a variety of common crack configurations; however, these analytical solutions are limited to simple crack geometries and loading conditions. For the case of 3-D planar cracks embedded in a semi-infinite body, there are less available analytical solutions for SIF. These exact analytical solutions provide good insight about fracture problems but they are not usable for general crack propagation modeling where the geometry of simultaneously propagating cracks can be asymmetrical and irregular and the boundary conditions can be complicated.

[1] The material of this section was used for presenting and proceeding in: Sheibani F., J.E. Olson. 2013. Stress intensity factor determination for three-dimensional crack using the displacement discontinuity method with applications to hydraulic fracture height growth and non-planar propagation paths. In The International Conference for Effective and Sustainable Hydraulic Fracturing, Brisbane, Australia, 20-22 May 2013.

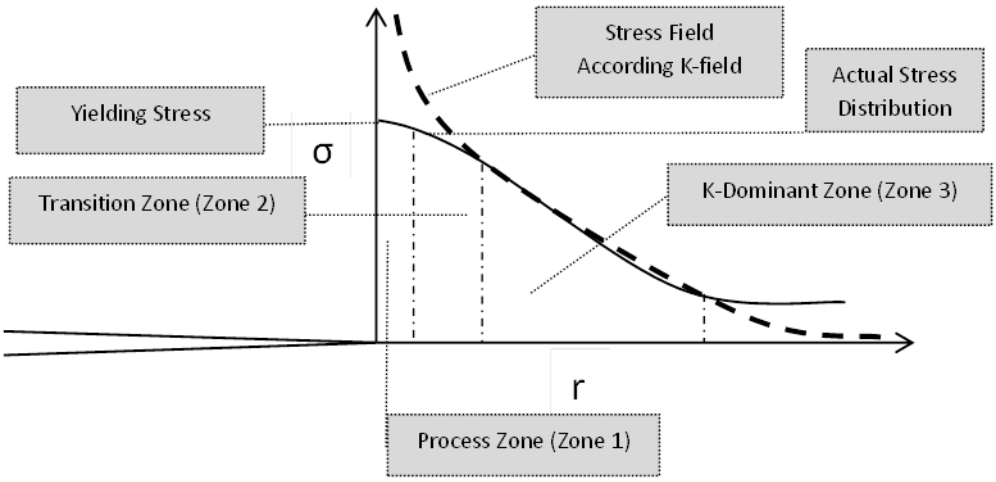

Figure 1.1: Schematic representation of stress distribution around the crack tip. (Chang & Mear, 1995)

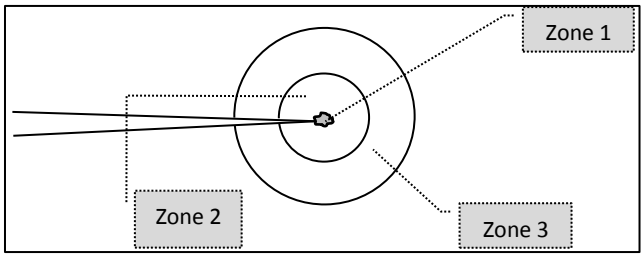

Figure 1.2: Process zone and K-filed representation: Deformation is inelastic within Zone 1. This zone is called "process zone". Elastic deformation occurs within zone 2; however, perturbation induced by process zone causes K-field solution being inaccurate to present the stress field. K-field solution dominates within zone 3 and yields accurate calculation for stress distribution. (Chang & Mear, 1995)

There are four general distinctive numerical methods to model fracture propagation problems:

1- The boundary element method (BEM) requires discretization and calculation only on boundaries of the domain. The stress resolution is higher in comparison with finite element and finite difference methods because the approximation is imposed only on boundaries of the domain, and there is no further approximation on the solution at interior points. Particularly, for some problems where the ratio of boundary surface to volume is high (for instance for large rock masses), BEM can be advantageous because FEM or

other whole-domain-discretizing methods require larger numbers of elements to achieve the same accuracy.

2- The Finite Element Method (FEM) has been widely used in fracture mechanics problems since it was implemented by Chan *et al.* (1970) for SIF calculation. Several modifications have proposed to remove its deficiencies in LEFM problem modeling. Henshell & Shaw (1975) and Barsoum (1976) devised "quarter point element" or "singularity elements" to improve the accuracy of stress and displacement distributions around the crack and SIF evaluation. To overcome the time consuming process of remeshing in fracture propagation problems, Benzley (1974) proposed the Extended Finite Element Method (XFEM). XFEM allows fracture propagation without changing the mesh by adding analytical expressions related to the crack tip field to the conventional FE polynomial approximation in what are called "enriched elements". Further work is being done to address the accuracy and stability of XFEM modeling, especially for multiple crack problems and approaching tip elements called "blending elements" (Trancon et al. 2009 and Jiang et al. 2010).

3- The Finite Difference Method (FDM) requires calculations on a mesh that includes the entire domain. FDM usage in fracture mechanics is mostly limited to dynamic fracture propagation and dynamic SIF calculation (Lin and Ballmann, 1993 and Chen 1975).

4- The Discrete Element Method (DEM) is mostly applied when continuity cannot be assumed in discontinuous, separated domains. The method apply to describe the behavior of discontinuities between bodies with emphasize on the solution of contact and impact between multiple bodies (Pande *et al*. 1990).

Generally, when the geometry of a problem is changing, whole-domain-discretizing methods like FEM, FDM and DEM are more time-consuming than BEM because of the remeshing process around a propagation fracture. However, BEM loses its advantage when the domain is grossly inhomogeneous.

The "Integral equation" approach (also called influence function) and the "displacement discontinuity method" are two types of BEM widely used in LEFM analysis. Both approaches incorporate only boundary data by relating boundary tractions and displacements. In the integral equation technique, superposition of known influence functions (called Green's function) along boundaries generates a system of simultaneous integral equations (Rizzo, 1967). In DDM, unknown boundary values are found from a simple system of algebraic equitation (Crouch, 1976). Generally, DDM has the advantage

over integral equations in being faster, while integral equations can be more accurate for non-linear problems.

SIF values can be obtained from the displacement discontinuity magnitudes at crack tip elements (Crouch & Starfield, 1983). However, according to Crouch (1976), DDM consistently overestimates displacement discontinuities at the tip of the crack (considering element midpoint) by as much as 25%. To improve the accuracy of the solution, some researchers proposed using higher accuracy crack tip element and/or using relatively denser distribution of elements near the crack tip. Crawford & Curran (1982) proposed higher order elements to improve the DDM solution and they used numerical integration to find the fundamental solution of linear and quadratic displacement discontinuities. Scavia (1991) proposed another approach called "hybrid displacement discontinuity method" by using parabolic DD for crack tip elements and constant DD for other elements. He concluded increasing the number of elements more than 8-10 times cannot yield more accurate results and the error in mode I stress intensity factor calculation for a 2-D straight crack with uniform internal pressure, sporadically changes in a range of 1% to about 10% depending on the ratio of parabolic element length to constant element length. However, Yan (2005) used the same combination of DD element and concluded the ratio of crack tip element to constant DD element must be between 1-1.3 to obtain good results with relative error less than 3% in mode II SIF calculation for a straight 2-D crack. Shou & Crouch (1995) presented a new hybrid displacement discontinuity method by using quadratic DD elements and special crack tip elements to show $\sqrt{r}$ variation of displacement near the crack tip. Dong & de-Pater (2001) used the same method with few modifications about the position of collocation points to determine quadratic elemental displacement. They showed the error can be fixed up to 1.5% for Mode I, and about 2% for mode II SIF calculation for a slanted straight crack. Wen *et al.* (1994) took a different approach; instead of direct calculation of stress intensity factors from displacement discontinuities, they proposed an "equivalence transformation method" in which stresses on the crack surface are calculated from displacement discontinuities, and then by using crack line Green's function, the SIF at the crack tip can be obtained from calculated stresses. They implemented the equivalence transformation method to calculate dynamic stress intensity factors for an isolated 2-D crack in an infinite sheet subjected to Heaviside loading. By comparison with the exact solution and using 80 DD elements, they inferred the error in mode I SIF is less than 1% and for mode II doesn't exceed 1.5%.

All of the methods mentioned above including using special crack tip elements or equivalence transformation methods to decrease the error in crack tip element

displacement and corresponding SIF calculation; however, they all need numerical integration and can be more time-consuming than constant elemental DD approximation. Olson (1991) empirically determined the coincidence between DDM modeling and analytical displacement distribution solution of a straight 2-D crack to remove the error. He showed the margin of error is less than 5% even by using only 2 elements in a 2-D crack. His proposed formula has been widely used in geologic fracture problems (Thomas & Pollard, 1993; Kattenhorn, 1998; Willemse & Pollard, 2000; Tuckwell et al, 2003; Olson, 2007). The work presented here extends Olson's method (Olson, 1991) to SIF calculation for 3-D homogenous, isotropic and linearly elastic material problems. Mériaux (2002) followed the method of Olson (1991) but proposed a different constant, which was adopted in some later work (Mutlu & Pollard, 2006; Ritz & Pollard, 2011). In this section we argue that the change does not actually improve SIF accuracy.

According to Murakami & Endo (1983) and Murakami *et al.* (1989) the maximum mode I stress intensity factor appearing at a certain point along the crack front can be estimated by the following equation with less than 10% error for an arbitrary-shaped planar crack:

$$K_{I\,max} = 0.50\sigma\sqrt{\pi\sqrt{area}} \qquad (1.1)$$

where 'area' is the area of crack projected in the direction of the maximum principal stress.

Fortunately, for simple crack geometries like elliptical and circular cracks, there exist analytical formulae for mode I stress intensity factor variation along the crack tip which help us to evaluate the accuracy of the numerical modeling (Irwin, 1962; Nisitni & Murakami, 1974). For rectangular defects there are no analytical formulae, but the accuracy of DDM numerical modeling can be examined by comparing against earlier numerical work using integral equation methods (Weaver, 1976; Kassir, 1982; Isida *et al.* 1991; Wang *et al.* 2001).

2.1.2 Numerical Procedure

2.1.2.1 Displacement Discontinuity Method

The general concept of the displacement discontinuity method proposed by Crouch (1976) is to approximate the distribution of displacement discontinuity of a crack by discretizing it into elements. Knowing the analytical solution for one element, the numerical elastic solution of the whole discontinuity can be calculated by adding up the effect of all subdividing elements.

The 3-D displacement discontinuity used here is based on the analytical elastic solution of normal and shear displacement of a finite rectangular discontinuity in half-space (Figure 1.3-a) proposed by Okada (1992). These equations are closed-form half-space solutions of deformations and deformation derivatives in which most of singularities and mathematical instabilities were removed. For the analytical solution readers are referred to Okada (1992); only a brief explanation is provided here. Direction of coordinates as well as geometry of three different finite rectangular sources used by Okada (1992) are depicted in Figure 1.3-a. δ is dip angle, x axis is taken parallel to the fault strike, z shows the vertical direction and x-y plane is taken parallel to the free surface. Internal displacements, u_x, u_y, u_z are presented in his table 6, x derivative of displacement ($\frac{\delta u_x}{\delta x}, \frac{\delta u_y}{\delta x}, \frac{\delta u_z}{\delta x}$) are presented in his table 7, y derivative of displacement ($\frac{\delta u_x}{\delta y}, \frac{\delta u_y}{\delta y}, \frac{\delta u_z}{\delta y}$) are presented in his table 8, and z derivative of displacement ($\frac{\delta u_x}{\delta z}, \frac{\delta u_y}{\delta z}, \frac{\delta u_z}{\delta z}$) are presented in his table 9. All displacements and displacement derivatives excluding z derivative are expressed by a composition of three parts (A, B, C) which the first part is related to the full-space solution and the next two parts take into account the effect of half-space. Parts A, B and C are tabulated in the 1st,2nd and 3rd rows of each table receptively. Once displacement derivatives are calculated, stress and strain field can be evaluated using Hooke's law for linear isotropic materials and assuming strains are infinitesimal as the following:

$$\varepsilon_{ij} = \frac{1}{2}\left(\frac{\partial u_i}{\partial x_j} + \frac{\partial u_j}{\partial x_i}\right) \quad (1.2\text{-a})$$

$$\sigma_{ij} = \lambda \varepsilon_{kk} \delta_{ij} + 2\mu \varepsilon_{ij} \quad (1.2\text{-b})$$

Where G is the shear modulus, λ is the lame's constant, $i,j=(x,y,z)$ and δ_{ij} is the Kronecker delta.

By placing N unknown constant displacement elements within the boundaries of the region to be analyzed and knowing the boundary conditions on each element (traction or displacement), a system of 3N linear algebraic equations by using the principle of superposition can be set up as the following:

$$\sigma_s^i = \sum_{j=1}^{N} A_{ss}^{ij} D_s^j + \sum_{j=1}^{N} A_{sd}^{ij} D_d^j + \sum_{j=1}^{N} A_{sn}^{ij} D_n^j \quad (1.3\text{-a})$$

$$\sigma_d^i = \sum_{j=1}^{N} A_{ss}^{ij} D_s^j + \sum_{j=1}^{N} A_{sd}^{ij} D_d^j + \sum_{j=1}^{N} A_{sn}^{ij} D_n^j \quad (1.3\text{-b})$$

$$\sigma_n^i = \sum_{j=1}^{N} A_{ns}^{ij} D_s^j + \sum_{j=1}^{N} A_{nd}^{ij} D_d^j + \sum_{j=1}^{N} A_{nn}^{ij} D_n^j \quad (1.3\text{-c})$$

where *N* is the total number of elements, *s*, *d*, *n* are the directions of local coordinates depicted in Figure 1.3-b, D_s^j, D_d^j and D_n^j are unknown strike-slip shear, dip-slip shear and opening displacement discontinuities of the *j*th element, σ_s^i, σ_d^i and σ_n^i are known strike-slip shear, dip-slip shear and normal boundary tractions induced on the *i*th element, and A_{pq}^{ij}(*p*,*q*=*s*,*d*,*n*) is the boundary stress influence coefficients for the problem. For example, A_{sn}^{ij} is the distributed shear force parallel to the local *s* direction and at the center of *i*th element due to unit normal displacement discontinuity over the *j*th element. Influence coefficients are calculated using the analytical solution, stress rotation, and Cauchy's formulae to find element's traction.

If known values are the displacements of one side of the boundary elements, these equations will be modified as Equation 1.4-a,b and c. Displacement boundary condition is useful for some sort of problems, for example to apply far-field displacement instead of remote stresses:

$$u_s^i = \sum_{j=1}^{N} B_{ss}^{ij} D_s^j + \sum_{j=1}^{N} B_{sd}^{ij} D_d^j + \sum_{j=1}^{N} B_{sn}^{ij} D_n^j \quad (1.4\text{-a})$$

$$u_d^i = \sum_{j=1}^{N} B_{sd}^{ij} D_s^j + \sum_{j=1}^{N} B_{dd}^{ij} D_d^j + \sum_{j=1}^{N} B_{dn}^{ij} D_n^j \quad (1.4\text{-b})$$

$$u_n^i = \sum_{j=1}^{N} B_{sn}^{ij} D_s^j + \sum_{j=1}^{N} B_{nd}^{ij} D_d^j + \sum_{j=1}^{N} B_{nn}^{ij} D_n^j \quad (1.4\text{-c})$$

where, u_s^i, u_d^i and u_n^i are known strike-slip and dip-slip shears and opening on the positive (or negative) face of the crack (Figure 1.3), and B_{pq}^{ij}(*p*,*q*=*s*,*d*,*n*) are boundary influence coefficients for displacements. For example, B_{sd}^{ij}means crack wall displacement along the local *d* direction (dip slip movement) over *i*th element due to unit displacement discontinuity parallel to the local *s* direction of the *j*th element (unit strike slip along the *j*th element).

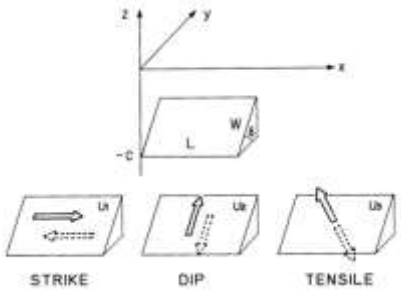

Figure 1.3-a: Direction of coordinates and geometry of three different finite rectangular sources used by Okada (1992)

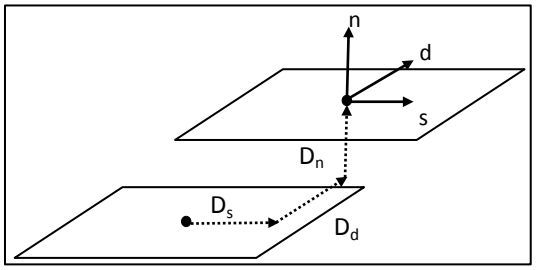

Figure 1.3-b: 3-D displacement Discontinuity Modeling

2.1.2.2 Stress Intensity Factor Computation

Olson (1991) empirically determined that the analytical and numerical solutions for a planar 2-D crack coincide at approximately at $x = (a - \frac{P}{1.3})$, where x is the distance from the center of the crack and a is half length of the crack. He showed by using the empirical constant $C = 0.806$ the margin of error is less than 5% for stress intensity factor calculation of a 2-D crack even when there are only two elements in a crack. The proposed modified constant of $C = 0.798$ by Mériaux *et al.* (2002) changes SIF about

1% which is trivial compared with other factors such as number of elements and does not improve on this accuracy.

Once the crack tip element displacement discontinuities are calculated, K_I, K_{II} and K_{III} can be directly obtained using:

$$K_I = C\frac{D_n E\sqrt{\pi}}{4(1-\nu^2)\sqrt{P}} \quad (1.5\text{-a})$$

$$K_{II} = C\frac{D_s E\sqrt{\pi}}{4(1-\nu^2)\sqrt{P}} \quad (1.5\text{-b})$$

$$K_{III} = C\frac{D_t E\sqrt{\pi}}{4(1+\nu)\sqrt{P}} \quad (1.5\text{-c})$$

where E is modulus of elasticity, ν is Poisson's ratio, P is crack tip element length perpendicular to crack front, D_n is the opening of crack tip element, $D_s$is shear displacement discontinuity perpendicular to $D_n$and the crack front, D_t is front-parallel displacement discontinuity (Figure 1.3) and C is an empirically determined constant that accounts for the discrepancy between the numerical approximation and the analytical solution equals 0.806 (Olson, 1991).

2.1.3 Validation of Numerical Model

2.1.3.1 Rectangular Crack

There is no analytical solution for the stress intensity factor variation along a rectangular crack front. However, rectangular cracks were the subject of several papers where the "Integral Equation" or "Body Force Method" was used to numerically approximate mixed Mode SIF values (Weaver 1977, Kassir 1981 & 1982, Isida et al. 1991, Wang et al. 2001, Noda & Kihara 2002). Results obtained from Isida *et al.* (1991) are in a good agreement with Wang *et al.* (2001) for maximum SIF calculation of rectangular cracks. In addition, Isida *et al.* (1991) investigated how maximum stress intensity factors change in a half-space in terms of crack depth. Because of these reasons, Isida *et al.* (1991) and Wang *et al.* (2001) were selected as reference solutions to which we compare the results from this paper. Studies done by Weaver (1977), Kassir (1981) and Mastrojannis *et al.* (1979) yield relatively different results for $K_{I\,max}$ calculation. These earlier works are

different by about 5% on average (Isida 1991). In addition they cannot be used for stress intensity factor variation along the crack edge. Equation 1 proposed by Murakami *et al.* (1988) is among few studies done to find the maximum stress intensity factor of an arbitrary-shaped crack. Using that formulae and knowing the maximum stress intensity factor for a rectangular discontinuity always is at the middle of longer edge, the maximum stress intensity factor of a rectangular crack can be approximated with adequate accuracy. For instance, they approximated the dimensionless stress intensity factor at the edge-midpoints of a square crack as $F_I = 0.768$, for which the error is about 1%.

Considering a rectangular crack as shown in Figure 1.4, the dimensionless parameter, F_I, represents the dimensionless stress intensity factor along the crack front $y = b$:

$$F_I = \frac{K_I(x,y)|x=x,y=\pm b}{\sigma_n\sqrt{\pi b}} \tag{1.6}$$

The stability of the solution can be examined by investigation of the strain energy variation through increasing the number of elements. The strain energy of a pressurized crack equals the integration of displacement distribution multiply normal traction along fracture surface. For constant elemental displacement discontinuity distribution, uniform pressure distribution and assuming uniform element dimensions, strain energy is proportional to the summation of elemental displacement discontinuities (or fracture volume) which makes it a good criteria for general stability evaluation of the solution of displacement distribution along fracture surface. Figure 1.5-b shows that strain energy (U) linearly varies with $\frac{1}{n}$ and has an asymptotic behavior with respect to *n*, where *n* is the number of elements on each side of the square crack shown in Figure 1.5-b. The area of the square crack is A, and it is loaded with a constant pressure p. Figure 1.5-b shows the result tends to be stabilized as *n* increases which means it aproches the exact solution. Assuming the error in strain energy calculation approaches zero if $n \to \infty$ ($\frac{1}{n} \to 0$), the correct answer for error estimation in the strain energy calculation can be obtained from Figure 1.4. Figure 1.5 shows the error calculation in strain energy. The displacement discontinuity method always overestimates the strain energy (or displacement across the crack surface) but it yields more accurate results closer to the exact solution when the number of elements increases. The error changes from 48.8% using a 3×3 mesh to about 1.99% for a mesh including 71×71 elements. In comparison with the two

dimensional analysis of a straight crack [16], the rate of convergence is faster, but the error in strain energy calculation is higher using the same number of elements to divide one side of a crack.

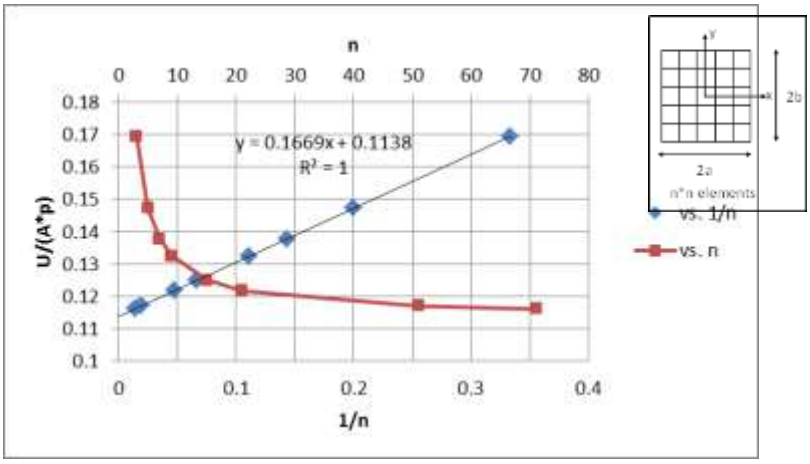

Figure 1.4: Approximation of the solution of strain energy for a square pressurized crack (a=b) as a function of number of displacement discontinuities across each side of the fracture (red points). By plotting of strain energy vs. $\frac{1}{n}$, the stabilized magnitude can be obtained for $n \to \infty$ ($\frac{1}{n} \to 0$).This magnitude was used to generate Figure 1.5.

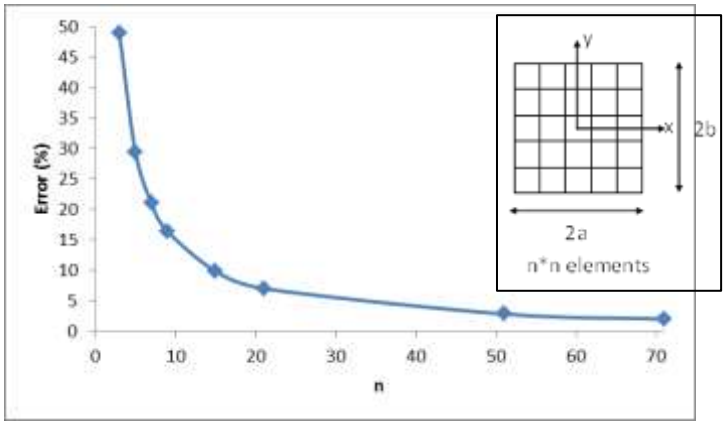

Figure 1.5: Error in strain energy (or fracture volume) calculation as a function of number of elements on each side of a pressurized square crack (a=b)

The error in strain energy calculation is mainly related to the largest error occurring at the corners of the square crack where the displacement gradient is highest. Figure 1.6 shows

the stress intensity factor variation along the half-length of the crack tip using DDM compared with the integral equation solution suggested by Wang *et al.* (2001) mentioned in Table 10 of their paper. The total number of elements used in the simulation was 22×22 to be consistent with the number of colocation points used by Wang *et al.* (2001). The difference between these two solutions is negligible for all elements but the corners (element No. 11). However, the corner elements of rectangular cracks don't play an important role in fracture propagation problems because the level of SIF is the lowest there and unlikely to control the initiation of crack propagation.

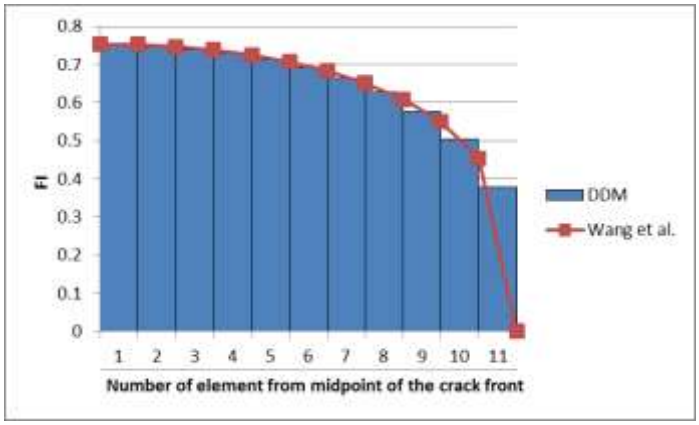

Figure 1.6: Variation of Dimensionless stress intensity factor, F_I, along the half length of a square crack front

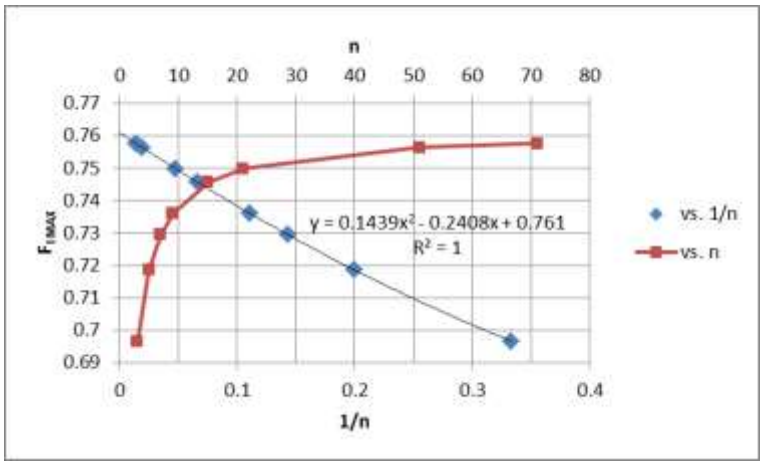

Figure 1.7: Extrapolation of $F_{I\,max}$ for a square crack in an infinite body. n is the number of displacement discontinuities across each side of a square fracture

It is always desirable to use a coarser mesh to save computation time, but the accuracy of DDM depends strongly on mesh refinement. Figure 1.7 shows the extrapolation of maximum dimensionless stress intensity factor, $F_{I\,max}$ (which occurs at side-midpoint of a square crack), as a function of $\frac{1}{n}$. It shows the numerical result of $F_{I\,max}$ is parabolic with the reciprocal of the subdivision number. Figure 1.7 shows that the most reliable value of $F_{I\,max}$ for a square crack is 0.7607, which is slightly different (0.6%) than the value reported by Isida *et al.* (1991) using the body force method.

Figure 1.8 shows the variation of dimensionless stress intensity factor, F_1, along the crack front y=b for various values of $\frac{b}{a}$, using 22×22 elements, a mesh refinement consistent with Wang *et al.* (2001). Figure 2.9 shows the maximum dimensionless stress intensity factor ($F_{I\,max}$) at the location ($x=0, y=b$). When $b/a<1$, the crack tip at $y=b$ represents the longer edge of a rectangular crack, whereas when $b/a>1$ the crack tip at $y=b$ represents the shorter edge. The dimensionless SIF is referenced to the plane strain SIF for a crack with half-length b for all b/a. The results show that at $b/a=0.125$, the maximum SIF (at location $x=0, y=b$) has reached the plane strain value ($F_1=1$). As b/a increases (equivalent to reducing the crack length a relative to b), F_1 is reduced. When $b/a=1.0$, the square crack, $F_1=0.75$. A penny-shaped crack has more restricted opening, and has the ratio of 0.64 to the plane strain SIF (penny-shaped SIF solution will be presented later in Equation 1.9). Reducing a further such that $b/a>1$ makes a the short dimension of the crack and thus the limiting dimension for crack opening and SIF value. The dimensionless SIF at y=b will then go to 0 as $a \rightarrow 0$. In comparing to the solution of Wang et al 2001, it is evident that the distribution of SIF near the $x=a$ crack tip is more accurate when $b/a<1$, but the maximum value of SIF is a good match for all cases. Using higher element density around the rectangular crack front and a coarser mesh at the center was investigated, but we found a uniform mesh yielded more accurate results using fewer elements in comparison with non-uniform mesh.

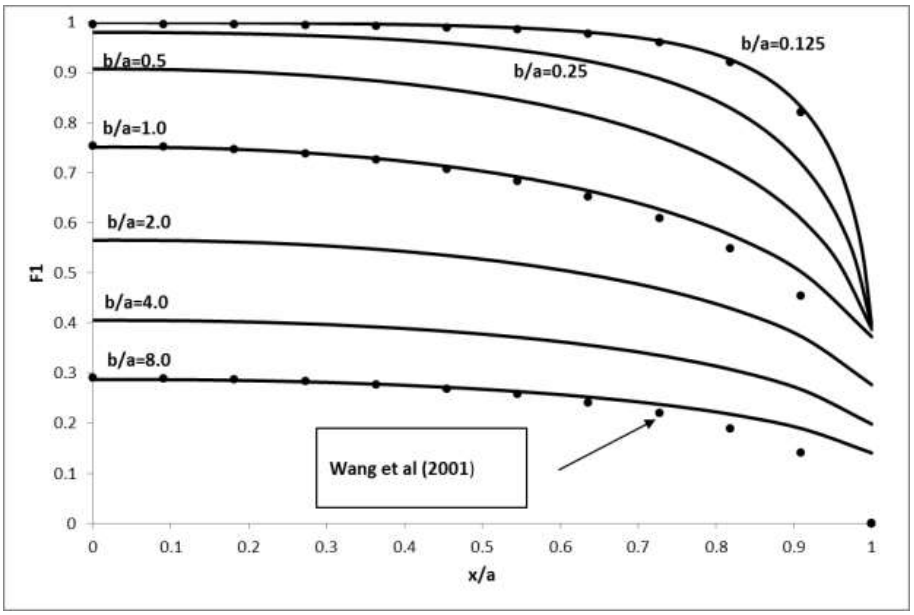

Figure 1.8: Dimensionless stress intensity factor variation along the crack front $\boldsymbol{y = b}$.

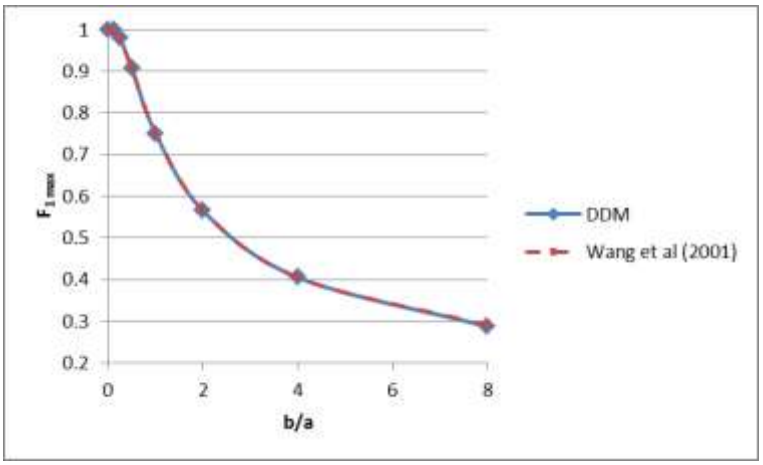

Figure 1.9: Maximum dimensionless stress intensity factor along the crack front $\boldsymbol{y = b}$.The same procedure represented in Figure 1.7 used to estimate $F_{I\,max}$ for different aspect ratio of rectangular fractures

Considering a rectangular vertical crack in a half-space, and assuming $\nu = 0.3$, the dimensionless stress intensity factor at the midpoints of the crack fronts nearest (A_1) and farthest (A_2) from the free surface are presented in Figure 1.10-a and b respectively, as a

function of b/a and b/d. $F_{1\,max}$ and $F_{2\,max}$ are the dimensionless stress intensity factors corresponding to points $A_1$and A_2 respectively and can be defined as the following:

$$F_{1\,max} = \frac{K_I(x,y)|A_1}{\sigma_n\sqrt{\pi b}} \tag{1.7-a}$$

$$F_{2\,max} = \frac{K_I(x,y)|A_2}{\sigma_n\sqrt{\pi b}} \tag{1.7-b}$$

where σ_n is the net pressure at the surface of crack. For every combination of b/a and b/d, the stress intensity factor along the side nearest to the free surface is greater than the side farthest away.

Figure 1.10-a and b show for greater aspect ratio (b/a grater or taller crack) SIF is less affected by the depth. Both $F_{1\,max}$ and $F_{2\,max}$ increase as the crack approaches the surface of solid. The mode I stress intensity factor along the crack fronts of a rectangular discontinuity in an infinite body is independent of Young's modulus (Mear, 2011). Figure 1.11-a and 1.11-b show that Poisson's ratio ν variation has a slight effect on $F_{1\,max}$ and $F_{2\,max}$, but only for cracks close to the free surface.

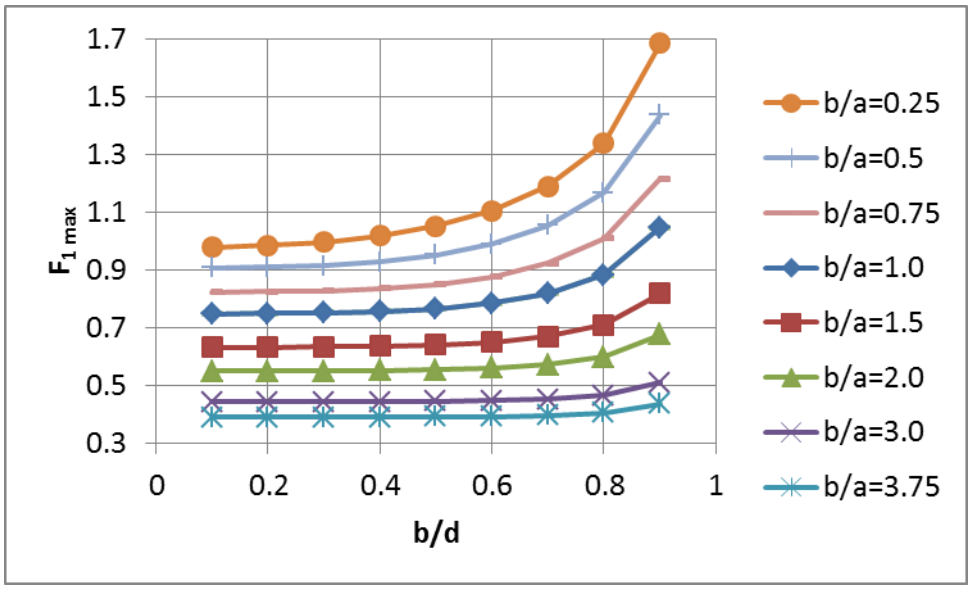

Figure 1.10-a: Dimensionless stress intensity factor, $\boldsymbol{F_{1\,max}}$ at the midpoints of the crack fronts nearest $(\boldsymbol{A_1})$ as a function of b/a and b/d for a rectangular crack in half-space $(\boldsymbol{\nu = 0.3})$

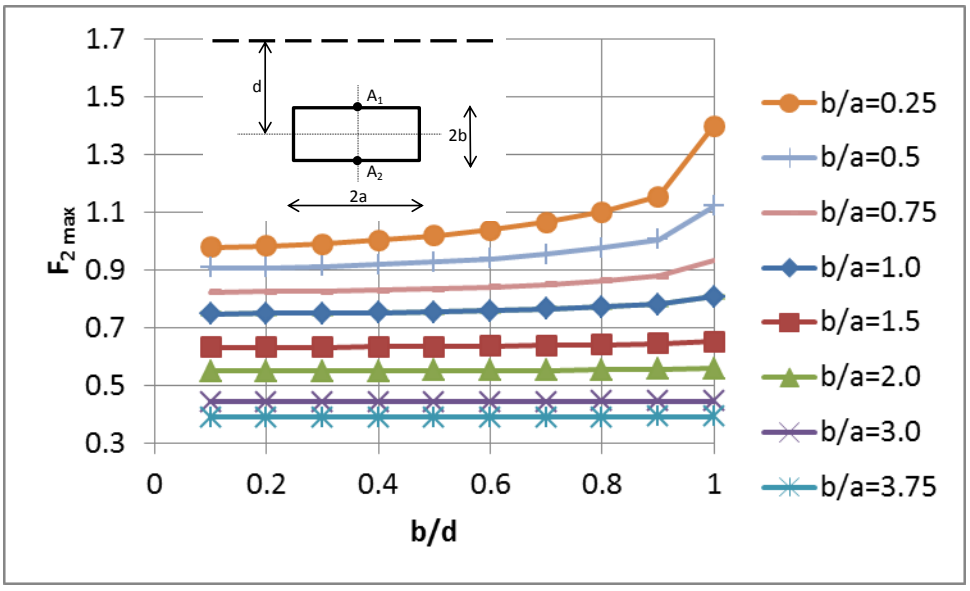

Figure 1.10-b: Dimensionless stress intensity factor $\boldsymbol{F_{2\,max}}$ at the midpoint $\boldsymbol{A_1}$ as a function of b/a and b/d for a rectangular crack in half-space $(\boldsymbol{\nu = 0.3})$

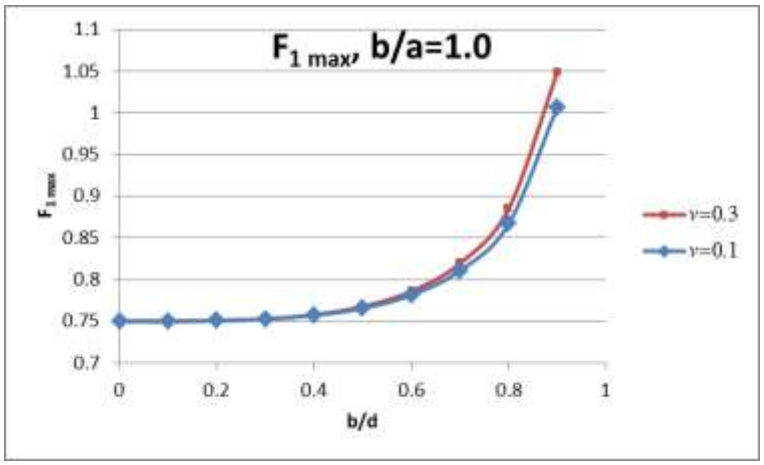

Figure 1.11-a: Effect of Poisson's ratio on dimensionless stress intensity factor, $\boldsymbol{F_{1\,max}}$ for a rectangular crack in half-space

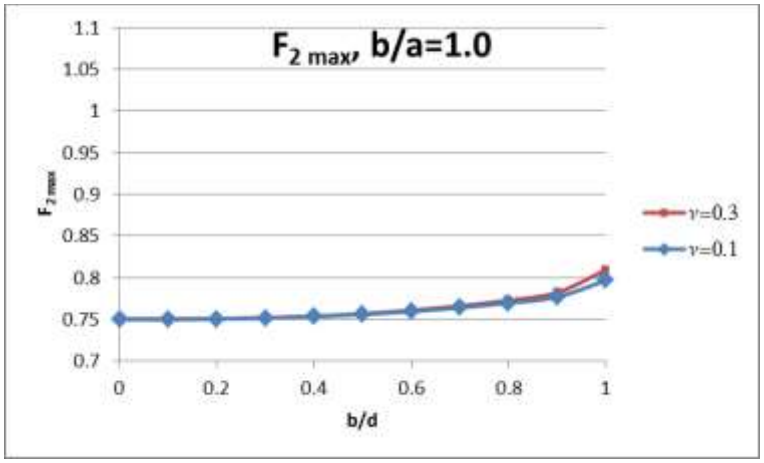

Figure 2.11-b

1.11-b: Effect of Poisson's ratio on dimensionless stress intensity factor $\boldsymbol{F_{2\,max}}$ for a rectangular crack in half-space

In contrast to Mode I, the mode II and III stress intensity factor of a crack in an infinite body is dependent on elastic constants. By defining the dimensionless stress intensity factor for mode II as

$$F_{II} = \frac{K_{II}(x,y)|x=x,y=\pm b}{\tau_{zx}\sqrt{\pi b}}$$

and assuming a frictionless crack surface, Figure 2.13 shows the maximum dimensionless stress intensity factor along the rectangular crack front $y = b$ subject to front-perpendicular shear stress τ_{zx}. The figure shows increasing Poisson's ratio will increase mode II stress intensity factor at
the tip of a rectangular crack embedded in an infinite space. Results compare satisfactorily with Kassir (1982).

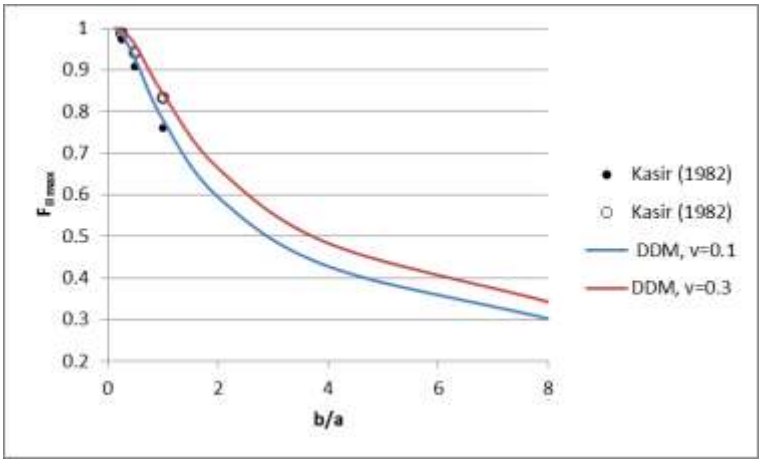

Figure 1.12: Effect of Poisson's ratio on Mode II dimensionless stress intensity factor for a rectangular crack in an infinite space.

2.1.3.2 Elliptical Crack

For an elliptical crack embedded in an infinite body, the stress intensity factor variation along the crack edge can be obtained from the following analytical solution (Nisitani & Murakami, 1974):

$$K_I(\theta) = \frac{\sigma_n(\pi b)^{\frac{1}{2}}}{E(k)}\left(\frac{\sin^2\theta + \frac{b^4}{a^4}\cos^2\theta}{\sin^2\theta + \frac{b^2}{a^2}\cos^2\theta}\right)^{\frac{1}{4}} \tag{1.8}$$

where:

$\theta = \tan^{-1}\frac{y}{x}$, $\frac{x^2}{a^2} + \frac{y^2}{b^2} = 1$ and,

$$E(k) = \int_0^{\frac{\pi}{2}} (1 - k^2 \sin^2\theta) d\theta \quad and \quad k = 1 - \frac{b^2}{a^2}$$

$E(k)$ is the complete elliptical integral of the second kind while a is the major axis and b is the minor axis of ellipse. The maximum and minimum stress intensity factor at the end of minor and major axes, respectively, can be calculated using:

$$(K_I)_{max} = K_I\left(\theta = \frac{\pi}{2}\right) = \frac{\sigma_n \sqrt{\pi b}}{E(k)} \tag{1.9-a}$$

$$(K_I)_{min} = K_I(\theta = 0) = \frac{\sigma_n \sqrt{\pi b}}{E(k)} \sqrt{\frac{b}{a}} \tag{1.9-b}$$

Figure 1.13-a and b show dimensionless stress intensity factor variation along the elliptical crack front using analytical solutions and DDM numerical modeling. There were 154 DD elements used in the model depicted in Figure 1.13-a, and 628 elements in Figure 1.13-b. Whereas SIF is proportional to the area of a planar crack, the area of boundary element mesh in both cases is almost equal to the area of the modeled ellipse. For both models, the aspect ratio of the ellipse is

$\frac{b}{a} = 0.5$ and $F_1 = \frac{K_1(\theta)}{\sigma_n (\pi b)^{\frac{1}{2}}}$.

Both figures show that the trend of stress intensity factor variation can be appropriately modeled by DDM. Oscillation in SIF is because of stepwise mesh boundary used to define the geometry of the ellipse using rectangular elements. However, by using the average of SIF of the neighboring circumferential elements, the accuracy improves for both models and the maximum error decreases from about 24% to 9% for the first model and from 28% to 10% for the second model, as compared to the analytical solution derived by Nisitani & Murakami (1974). Using 20 elements along the major axis and 10 along the minor axis of the ellipse results in good agreement for F1 at $\theta = 0$ and $\frac{\pi}{2}$ (Figure 1.13-a). For $\theta \geq 60^{\circ}$, the rectangular mesh deviates less from the ellipse, and the error in dimensionless stress intensity factor is non-oscillatory and small. Increasing the number of elements doesn't improve the accuracy (Figure 1.13-b). The estimation of maximum SIF presented in Equation 1.1, causes about 4% error compared to $(K_I)_{max} = K_I\left(\theta = \frac{\pi}{2}\right)$ using the analytical solution or numerical modeling.

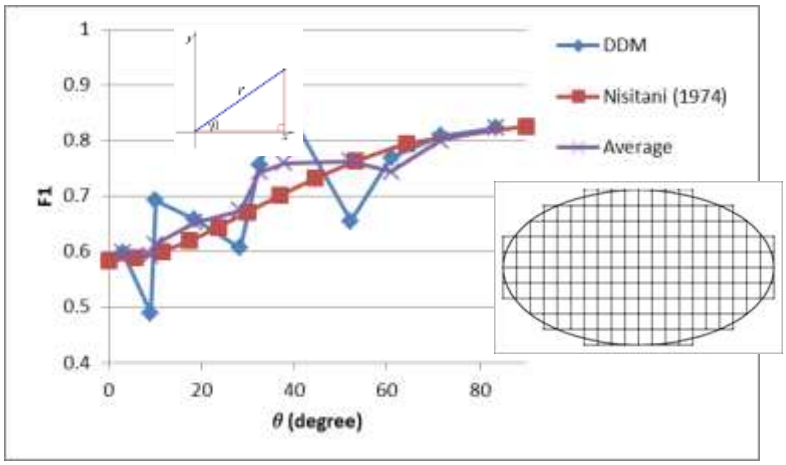

Figure 1.13-a: Dimensionless SIF variation along an elliptical crack front using analytical solution and DDM ($\frac{b}{a} = 0.5$), model No. 1 including 154 elements

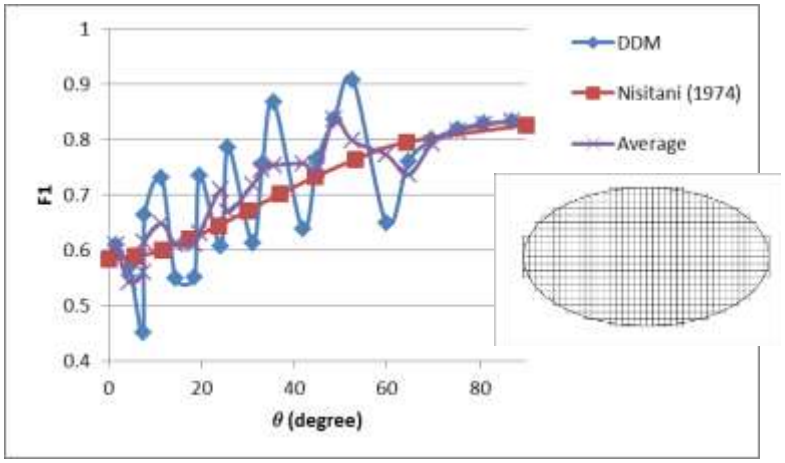

Figure 1.13-b: Dimensionless SIF variation along an elliptical crack front using analytical solution and DDM ($\frac{b}{a} = 0.5$), model No. 2 including 628 elements

2.1.3.3 Penny-shaped crack

The stress intensity factor at the tip of a circular crack of radius a in an infinite solid under uniaxial tension σ_n is (Sneddon, 1946):

$$K_I = \frac{2}{\pi}\sigma_n\sqrt{\pi a} \tag{1.9}$$

Two different size meshes were considered to calculate dimensionless stress intensity factor variation along the tip of a circular crack as depicted in Figures 1.14-a and 14b. The first model includes 76 elements and the second one has 308 elements. According to Figure 1.7, for a rectangular crack using 9×9 elements, the error in stress intensity factor is about 3 percent. For the penny-shaped crack, as with the elliptical crack, the error is a strong function of location. Because of the symmetry, error calculations are shown only for one eighth of the circle. The main reason of error in stress intensity factor along the crack front is jagged geometrical definition of the circle by using rectangular displacement discontinuity elements. The error in SIF can reach up to 20% along the crack front; however, the results are better for $\theta = 0\ or\ \frac{\pi}{2}$ - about 2.5% for the coarser model and almost zero for the finer model. Figure 1.15 compares F_1 variation along the quarter front of the penny-shaped crack for two DD models as well as analytical solution. The figure shows the finer mesh helps to increase the accuracy where the crack front is straight, but is not helpful where the crack front is stepwise. Similar to elliptical cracks, using the average SIF of neighbor circumferential elements considerably increases the accuracy of SIF distribution along the crack front of the penny-shaped discontinuity. The deviation from analytical solution of SIFs (Figures 1.13-a, b and 1.14-a, b) are essentially related to displacement discontinuity calculation and is merely because of the difference between the mesh and the geometry of crack. To overcome the error in crack tip aperture calculation using relatively coarse and constant rectangular DD elements for non-rectangular footprints and avoiding using specialized tip shape function, Pierce & Detournay (2008) suggested special weak form asymptotic solution to correct fracture width at tip element centers based on averaging the volume over a tip element. The suggested weak solution and iterative procedure they used to determine fracture opening and internal fluid pressure was successfully implemented in hydraulic fracturing propagation in a viscos-dominated regime.

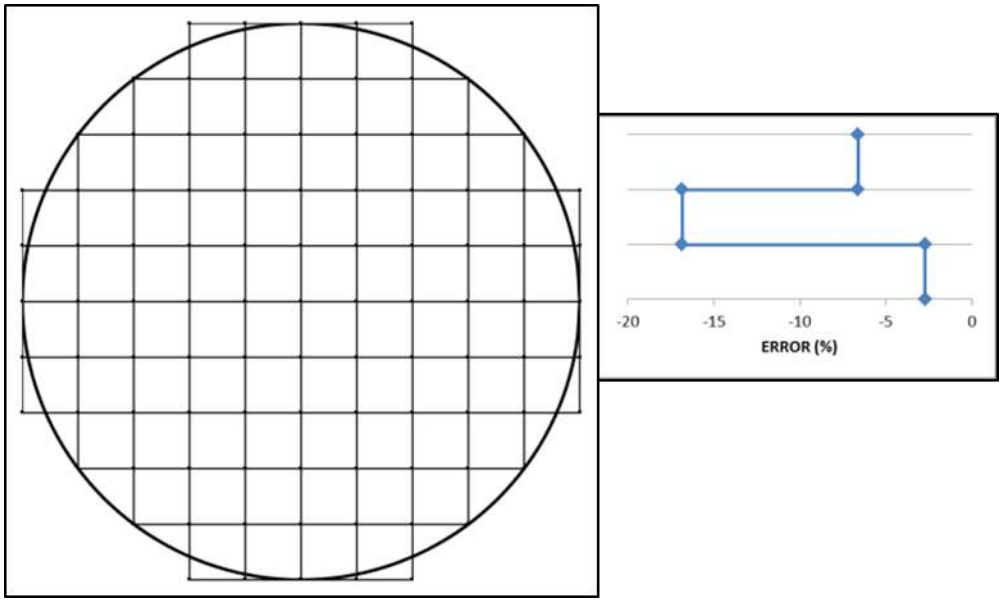

Figure 1.14-a: Error in dimensionless calculation along a penny-shaped crack front, Model 1 including 76 elements

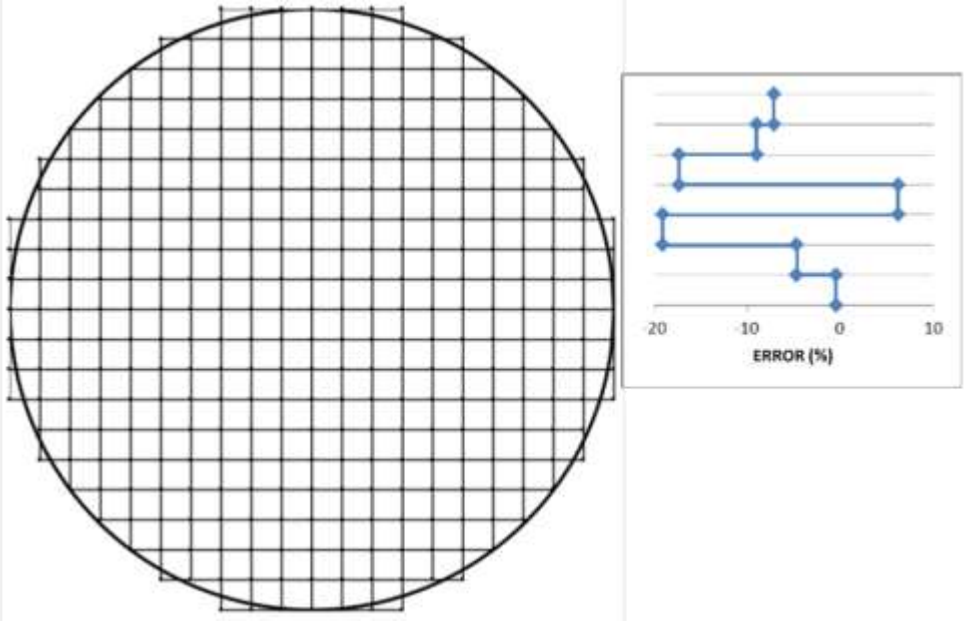

Figure 1.14-b: Error in dimensionless calculation along a penny-shaped crack front, Model 2 containing 308 elements

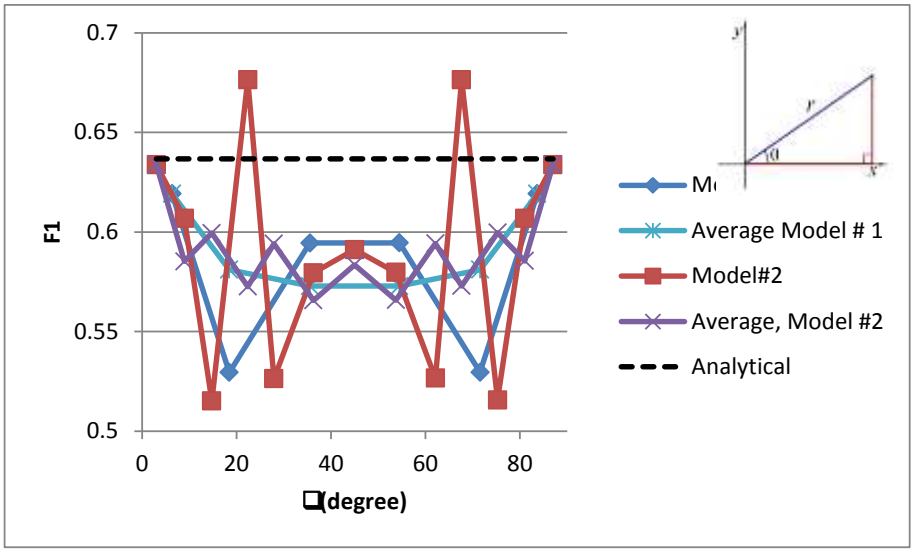

Figure 1.15: Comparison between dimensionless SIF for two DDM models with analytical solution of a penny-shaped crack stress intensity factor

2.1.4 Conclusion

Numerical methods are necessary for the SIF evaluation of 3-D planar cracks because analytical solutions are limited to simple geometries with special boundary conditions. In this section, the capability of DDM using constant rectangular discontinuity elements and considering the empirical constant proposed by Olson (1991) was satisfactory examined for cracks with simple geometry. The accuracy of the model is excellent for rectangular and square shaped cracks while it's computationally inexpensive. The stepwise shape of the mesh boundary when representing elliptical or penny-shaped cracks introduces more error in to the calculation, but the minimum and maximum SIF values can be accurately computed. Oscillation in SIF for curved front of fractures is because of stepwise mesh boundary used to define the geometry of the ellipse or circle using rectangular elements. Because SIF is proportional to displacement discontinuity, that deviation from analytical solution is essentially related to displacement discontinuity calculation and is merely because of the difference between the mesh and the geometry of crack.

2.2 Fracture Path Interpretation: Insights from 3D Displacement Discontinuity Modeling[1]

2.2.1 Overview

Natural or hydraulic fracture attributes such as planarity, path and connectivity affect fluid transport in reservoirs. Although many fracture models are based on two-dimensional, plane strain approximations, accurately predicting fracture propagation geometry requires accounting for the three-dimensional aspects of fractures. In this section, the focus is on the effect of fracture height on lateral propagation of vertical fractures. The 3-D boundary element displacement discontinuity model discussed previously is used to investigate the curving path of overlapping fractures, the angle of intersection for non-parallel fractures and the evolution of stress intensity factor during propagation for different locations around the fracture periphery. The effect of ratio of driving stress to differential remote principal stress and mechanical properties of the fracturing material are also considered.

Results show the curving path of overlapping fractures is strongly influenced by the spacing to height ratio of fractures as well as the differential stress magnitude. In addition, the angle of intersection between two non-coincident but sub-parallel en-echelon fractures is shown to depend strongly on fracture height to spacing ratio, with intersection angles being asymptotic for "tall" fractures (large height to spacing ratios) and nearly orthogonal for "short" fractures.

Fracture height to spacing ratio also affects mode III deformation and twist hackle generation. The effect of mechanical properties on parent fracture path and angle of intersection is minor in comparison with fracture height and differential remote stresses. The degree of mixed mode I-III loading caused by non-planar parent crack propagation is highlighted in addition to the more conventional of spatial or temporal remote stress orientation changes.

[1] The material of this section was used for presenting and proceeding in: Sheibani F., J.E. Olson. 2013. Impact of Fracture Height on Mixed Mode Fracture Propagation: Insights from 3D Displacement Discontinuity Modeling. ARMA, 47th U.S. Rock Mechanics / Geomechanics Symposium, San Francisco, 23-26 June 2013.

2.2.2 Introduction

Fracture mechanics has been successfully applied to model the behavior of geologic structures such as veins, joints, faults, clusters and swarms. Based on field observation, joints are the most common and abundant fractures in the earth's crust (Caputo, 2010). Good knowledge about geometrical and mechanical characteristics of joints, regarding rock deformability and fluid transport, is vital for engineers to design large structures like dams, bridges, power plants, tunnels and nuclear-waste repositories. Moreover, studying joint attributes like planarity, spacing, density, aperture, pattern and connectivity are crucial for oil and gas reservoir engineering. For instance, assessing natural fracture geometry allows for more accurate estimation of porosity and permeability in unconventional gas reservoirs (Pollard & Aydin, 1988). Characterization of the geometry of two parallel interacting joints helps to establish reliable relationship between joint geometry, applied differential remote stress and driving stress during fracture path development (Pollard et al., 1984; Olson & Pollard, 1989). These geometrical characteristics include shape of the overlapping zone and the angle of intersections (in the case linkage happens.)

Geological map data including fracture path, trace geometry, angle of intersection and overstep and/or spacing between fractures contain important information about fracture geometry such as fracture height or confining bedding layer thickness (Wu & Pollard, 1995; Bai *et al*. 2000; Olson, 2004), physical properties of the rock such as permeability (Min *et al.* 2004; Philip *et al.* 2005; Jourde *et al.* 2007) and tectonic loading history during joint formation (Dyer, 1988; Engelder, 1985).

Mechanical interaction between two parallel discontinuities such as geologic structures as well as experimental observations exists at many scales (Figure 2.1). Examples of these geologic structures are two segments of parallel joints, normal faults, and igneous dikes or overlapping spreading centers (OCR) (Pollard & Aydin, 1984). Experimental observation of crack interaction include micro-scale photoelastic studies (Lange, 1968), tensile loading of two parallel cracks in glass (Swain, 1978), and scanning electron microscope observation of stress-induced crack growth (Krantz, 1979). However, as joint interaction is the main purpose of this section, discontinuity dimensions, boundary conditions and mechanical and fracture properties used in this section are compatible with the nature of joints. As joints are primarily opening mode discontinuity, from here on fractures and joints both are used interchangeably.

Dyer (1988) applied superposition of Mode I and Mode III plane crack analytical solution to calculate the stress field around a single, infinitely long crack with a fixed height. Neglecting the effect of interaction between younger and older joints, spacing between older joints and considering the systematic change in orientation of the later joints, he concluded that change in principal stresses near through-going joints is the causative factor for asymptotic vs. orthogonal approaching of younger joints at the vicinity of older joints in Arches national park, Utah. Younger joints do not cut, nor intersect older joints: they are bound between two adjacent older joints. It seems younger joints nucleates in the central region between older set of joints. Trace of younger joints is almost linear in the central region but it starts asymptotic approach close to older through-going joints (Dyer, 1988). Trace of both sets shows the temporal rotation of principal remote stresses equal 30^0. For this angle between trace of older and younger joints, he obtained limits on the ratio of the far-field horizontal stresses for both cases of asymptotic and right angle intersection between younger joints and older through-going joints.

Based on a 2-D displacement discontinuity model for critical propagation, Olson and Pollard (1989) showed how fracture path is sensitive to remote differential stresses and overstepping between initial fractures, and how the internal fluid pressure changes during overlapping stage. They concluded that by implementing the proposed method and using a map of natural fracture traces, the differential stress acted during propagation can be inferred. For an isotropic remote stress, cracks first propagate away from each other before curving in more sharply toward one another when the overstep is small in comparison with their length. Nearly straight crack paths imply remote compressive differential stress. In contrast, tensile crack-parallel differential stress exaggerates the path curvature and results in right angle or T-type intersection.

Using the same numerical method and by comparison with experimentally produced fracture path, Pollard *et al.* (1990) hypothesized that the non-perpendicular intersection obtained from numerical modeling and observed in experiments, should be related to the last increments of fracture growth that couldn't be described by their model. Later experiments and numerical modeling done by Thomas and Pollard (1993) showed that a Mode I fracture can propagate in the vicinity of traction free surface without turning perpendicular to it. They concluded that because of the dominance of stress concentration due to Mode I propagation at points close to the tip of the crack, in comparison with local stress, the effect of free surface condition is little.

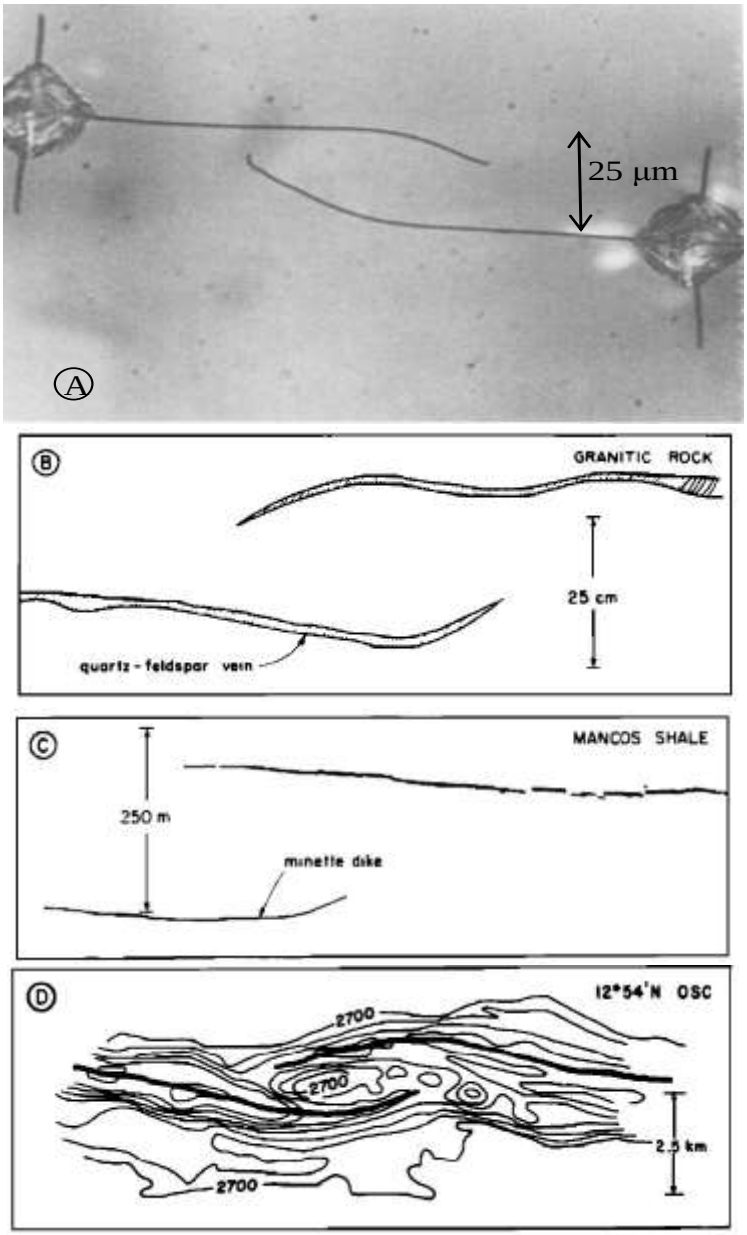

Figure 2.1: Overlapping zones of two interacting fractures in four different scales:

a) Micro crack in glass (Swain, 1978); b) A vein in granite rock; c) A dike d) Overlapping spreading center (Atkinson, 1987); (Modified from Pollard & Aydin, 1984, and Atkinson, 1987.)

Observing the dependency of curvature of interacting fractures on not only far-field differential stresses, but also on local stress field generated around their tips, Cruikshank *et al.* (1991) considered the effect of constant internal fluid pressure on fracture path and

suggested the ratio between the remote differential stress and driving stress to quantify the tendency for straight or curved propagation as:

$$R = \frac{(\sigma_{22}^r - \sigma_{11}^r)}{(p - \sigma_{11}^r)} \tag{2.1}$$

where σ_{22}^r and σ_{11}^r are crack-parallel and crack-perpendicular remote stress respectively and p is internal fluid pressure as depicted in Figure 2.2. He inferred that assuming compressive normal stress is positive, $R < 1$ results in more curved fracture while $R > 1$ implies less interaction between cracks and therefore straighter path.

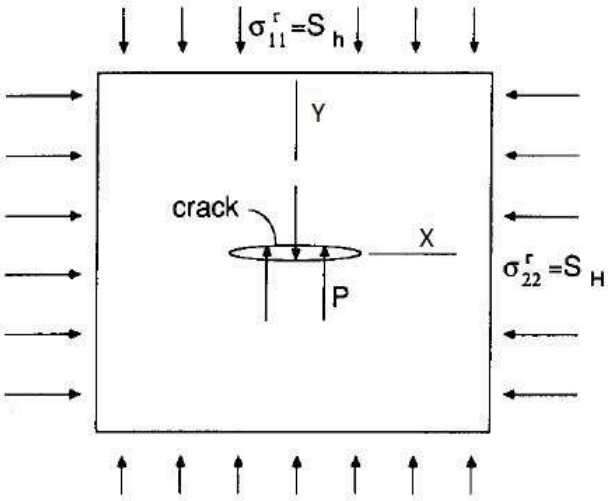

Figure 2.2: Remote stress and boundary condition of a 2-D crack. Compression is positive (from Olson & Pollard, 1989).

Comparing with earlier experimental work and using a 2-D hybridized displacement discontinuity modeling, variation of Mode I stress intensity factor at inner and outer tips of two parallel stepping cracks under far field cracks-perpendicular uniform tension during propagation was calculated by Chan (1991). He found out that after intersection, the Mode I stress intensity factor at the outer tips approaches the 2-D analytical solution of stress intensity factor for a crack of equivalent length equal to horizontal distance between outer tips.

Renshaw & Pollard (1994) considered the effect of subcritical fracture growth and fracture roughness (which was argued by Thomas and Pollard (1993)) on two

mechanically interacting fractures path. They inferred that crack roughness could suppress crack path curving, and straight propagation paths don't necessarily imply the predominance of remote differential stresses.

Works mentioned so far are all based on a 2-D analysis. Therefore, the effect of fracture aspect ratio, or fracture height (if any) on fracture path was not considered. Using a pseudo-three-dimensional model, Qiu (2002) investigated the effect of bed thickness in critical and subcritical growing fracture path. Variation of required internal fluid pressure for critical propagation and change in stress intensity factor for subcritical growth during the propagation were also considered. Although she didn't characterize fracture attributes, based on different bed thickness, she qualitatively concluded fracture height has a major influence on fracture path, and a subcritical fracture growth path is straighter than critical fracture propagation path because of the weaker mechanical interaction. The weaker mechanical interaction is an outgrowth of the fact that subcritical cracks grow at lower stress intensity factor and thus lower driving stress, reducing the ratio, *R*, of remote differential stress to driving stress.

In this section, for crack propagation modeling, a 3-D displacement discontinuity method of boundary element is used to study fracture path and the angle of intersection. The major factors that affect fracture path are joint spacing, joint height and differential remote stresses. Elastic properties and distance from a free surface in half-space problems are also considered as minor effects. Finally, the angle of intersection between approaching en-echelon fractures is examined in detail to explain why sometimes the approach is asymptotic and other times it is near orthogonal (but always less than 90°).

2.2.3 Theoretical Background

Assuming an isotropic, homogenous, linear elastic solid, linear elastic fracture mechanics can be used for fracture propagation. Among different criteria computing the direction of propagation, four are widely used: maximum circumferential stress (Erdogan & Sih, 1963), maximum principal stress, minimum energy release rate (Hussain *et al.* 1974) and maximum strain energy density criteria (Sih, 1974). Here, the maximum circumferential stress criteria suggested by Erdogan and Sih (1963) is used where growth occurs radially from the crack tip in the plane perpendicular to the direction of greatest tension, or along the path of zero shear stress. This criterion can be used for Mode I and combination of

mode I and II propagation modeling and can appropriately model joints propagation as primarily opening mode discontinuity.

Figure 2.3 shows schematic lateral propagation of a vertical joint due to combination of opening (Mode I) and in-plane shear (Mode II). Any contribution of out-of-plane shear (Mode III) was neglected for this example. Assuming fracture height is restricted by the mechanical layer thickness of the formation, only lateral propagation is allowed (fracture height, H, is assumed to be equal to layer thickness, T). The half-space medium containing fractures is homogenous and there is no variation in mechanical properties between layers. The layer boundary is imaginary and is arbitrarily imposed to restrict fracture height. Mixed mode I and II results in kinking of the crack tip, and the angle of crack extension, θ_0, can be calculated using (Cottrell & Rice, 1980):

$$\tan\frac{\theta_0}{2} = \frac{1}{4}\left[\frac{K_I}{K_{II}} - Sgn(K_{II})\sqrt{\left(\frac{K_I}{K_{II}}\right)^2 + 8}\right] \tag{2.2}$$

where $Sgn(K_{II})$ denotes the sign of K_{II}, clockwise kinking assume positive and K_{II} is positive when the positive surface of the crack has positive sliding displacement relative to the negative surface (in X direction, refer to positive direction of strike slip, U_1 in Figure 1.3-a). Using the propagation angle, θ_0, from Equation 2.2, the equivalent opening mode stress intensity factor in the direction of crack extension (K_{eq}) and can be obtained from (Cottrell & Rice, 1980):

$$K_{eq} = K_I \cos^3\frac{\theta_0}{2} - \frac{3}{2}K_{II}\cos\frac{\theta_0}{2}\sin\theta_0 \tag{2.3}$$

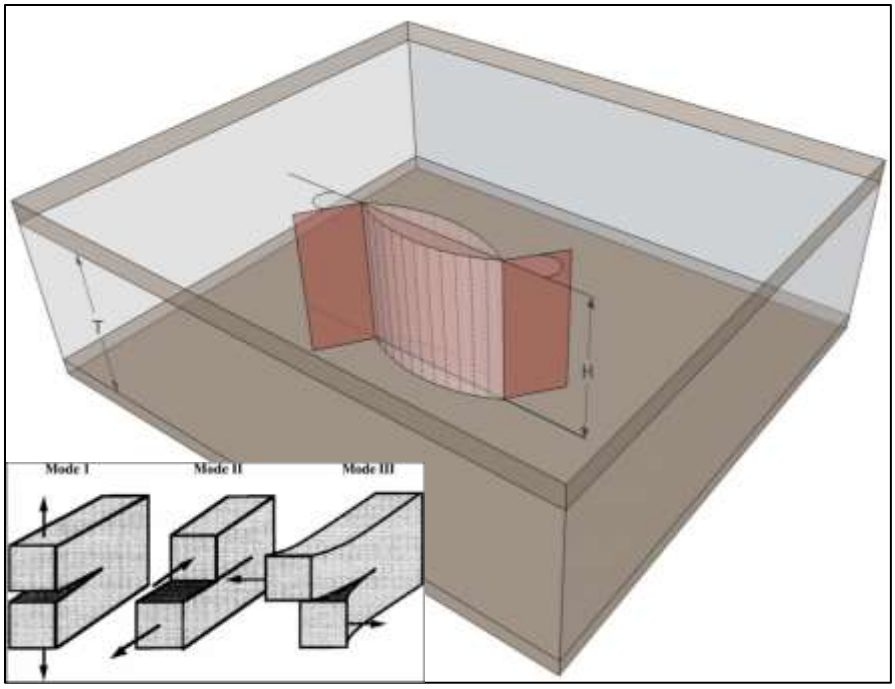

Figure 2.3: Schematic view of Mode I and mixed Modes I & II propagation modeling considered in this section for a vertical joint (Different modes of fractures are represented in the left lower corner.)

K_I and K_{II} in Equations 2.2 and 2.3 are considered as the average opening and in-plane shear stress intensity factors respectively along lateral tip-lines of a rectangular discontinuity.

According to unstable crack growth, a fracture starts to propagate when the stress intensity factor at the tip reaches a critical value, the so-called critical stress intensity factor or fracture toughness, denoted as K_c. Fracture toughness is a material property inferred to be independent of the size of the crack. K_c varies in the range of $0.3\ to\ 3.0\ MPa\sqrt{m}$ depending on rock type at relatively low confining pressure and temperature (Atkinson & Meredith, 1987). Natural hydraulic fractures caused by flowing of ground water into the fracture can be considered as critical crack growth (Secor, 1969). Natural fractures do not propagate continuously but they stop when the net pressure dissipates in the fracture during propagation and start again when enough driving stress is provided by flowing fluid from the matrix into the fracture (Olson, 2003). Therefore, neglecting the dynamic effects due to wave propagation produced by the discontinuity extension is reasonable, and natural fracture growth is considered as

quasi-static. Using maximum circumferential criteria for mixed mode I and II crack propagation, crack extension occurs when $K_{eq} \rightarrow K_c$.

2.2.4 Numerical Modeling of Mixed Mode I+II Fracture Propagation

The overlap region for two interacting fractures can be characterized by 3 parameters, shown in Figure 3.4. In the figure, L and W denote major and minor axis of the circumscribing ellipse, respectively, and β is the angle of intersection between two interacting fractures. Solid lines show the shape of the propagation of two parallel fractures and the elliptical representation of overlapping region is plotted by dash line.

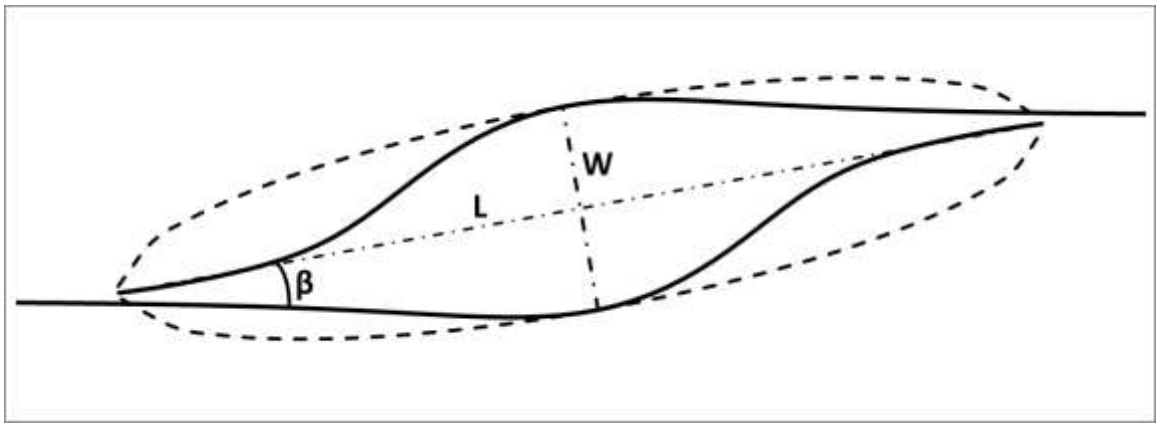

Figure 2.4: Shape of overlapping region after propagation in terms of L, W, and β.

In this section the effect of initial geometric parameters (S and H shown in Figure 2.5) and stress boundary conditions (depicted in Figure 2.2) in terms of differential remote stress, $\Delta\sigma = \sigma_{22}^r - \sigma_{11}^r$ (assuming compression is positive), on final configuration of fracture path and angle of intersection, β, is investigated. Propagation is only allowed at inner vertical tip-lines and the total crack array length, L_0, is kept constant and equal to $20\ m$ in order to impose a fixed length scale on the problem. Propagation can be modeled by adding boundary elements to the inner fracture tips and the internal fluid pressure is updated in each growth increment in such a way that fracture growth stays critical, i.e. $K_{eq} = K_c = 1.5\ MPa\sqrt{m}$. For investigating the effects of initial geometric parameters and remote differential stress on fracture path, $\frac{S}{L_0}$ changes as 0.1, 0.2 and 0.5 and $\frac{S}{H}$ varies in the range of 0.05 to 4.0 assuming $\Delta\sigma = 1.0, 0.0$ and -0.5 MPa. The positive value of $\Delta\sigma$ indicates compressive differential remote stress applied parallel to the initial crack

while the negative value indicates crack-parallel tension. The isotropic condition is defined as $\Delta\sigma = 0.0\ MPa$. The effect of mechanical properties on the problem is examined by comparing fracture path obtained for two different values of Poisson's ratio, $\nu = 0.1$ and 0.3, while Young's modulus, E, is kept constant and equal to 10.0 GPa.

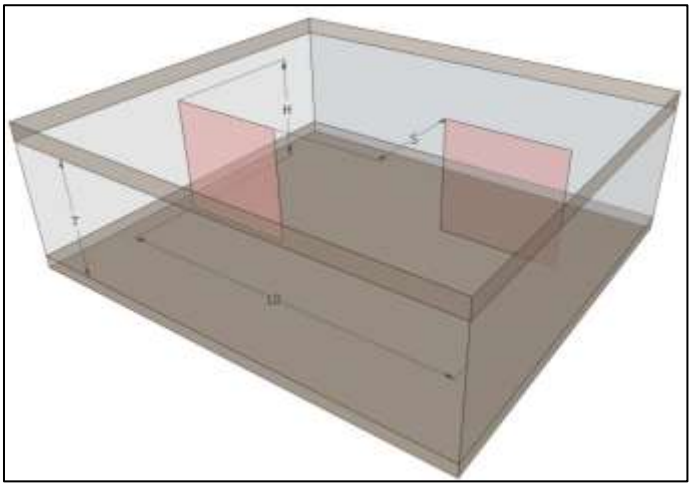

Figure 2.5: Two geometrical parameters that affect fracture path. H is fracture height, S is fracture spacing.

To study fracture path dependency on fracture depth, two extreme cases are considered: joint depth below the free surface is large relative to joint dimensions (resembling a full-space solution), and joint depth is 1.1 times joint height. For both cases, initial crack length is 0.5 m and is divided into 5 equal elements. Based on fracture height, 3 to 7 elements are used to subdivide fracture height. To prevent numerical instability resulting from analytical solution singularity, propagation is stopped when a crack tip comes within *0.1 m* (equal element length) of an existing fracture. In this situation, fracture path characteristics are calculated based on extrapolation of the last five elements representing nodes using quadratic least-square regression until intersection is achieved.

2.2.4.1 Propagation Path and Driving Stress Change

Figures 2.6-a, b and c show crack path and driving pressure for $\frac{S}{L_0}$=0.1, 0.2, and 0.5 ($S = 2.0, 4.0\ and\ 10.0\ m$ respectively). $\frac{S}{H}$ is constant for all four cases and equals $\frac{1}{10}$. The effect of differential remote stress is investigated assuming $\Delta\sigma = 1.0, 0.0$ and -0.5MPa. Figure 2.7 reproduces Figure 2.6 assuming $\frac{S}{H}$ equals 1.0 to see the effect of fracture height on fracture interaction.

Figure 2.6 should be more close to a 2-D modeling because for all three cases $H \gg S$ while Figure 2.7 shows the importance of 3-D modeling where$H = S$. Comparison between 2 figures shows that fracture interaction decreases with increasing S/H ratio. Positive differential stress or relative crack-parallel remote compression inhibits curvature in fracture path and therefore impedes interaction. Negative remote differential stress promotes curving and divergence of crack paths except for the widest spaced case.

The pressure required for critical propagation (Figures 2.6-a,b,c) initially decreases with increasing fracture length until the fractures are about tip-to-tip, then it increases where overlapping inhibits the growth. Although fracture paths show departure from straight direction before overlapping, the effect of this early crack interaction has a negligible effect on the driving stress necessary for critical propagation. The maximum pressure during propagation generally occurs at intersection for those cases following convergent paths. However, in the non-intersecting cases (e.g. Figure 2.6-c and 2.7-c for compressive differential stress) the driving stress decrease at the end of propagation is an artificial effect caused by interaction enhancement due to tensile stress distribution around the outer tip of the other fracture. It's worth mentioning driving pressure is not an accurate indicator to show interaction strength for positive differential remote stress. Compressive differential stress causes increasing in driving stress, but decreases interaction as opposes fracture curvature toward the other crack in the direction of minimum principal remote stress. Using Equation 2.1 to interpret fracture interaction might be sometimes misleading for critical propagation, but in the case of using, it seems the maximum driving pressure should be selected to calculate R factor. Figure 2.8 depicts this maximum for different values of S and ratios of $\frac{S}{H}$ using isotropic differential stress condition. The figure shows, if interaction occurs between fractures, the minimum value of peak driving stress happens at $\frac{S}{H} = 1$. For small value of $\frac{S}{H}$, increasing $\frac{S}{H}$ results in peak pressure decreasing and is due to weakness in fracture interaction while fracture height decreases. However, for $\frac{S}{H} \gg 1$, peak pressure increases by increasing $\frac{S}{H}$ and is related to increasing in fracture compliance due to fracture height shortening. That means for a given bed thickness, the minimum internal fluid pressure is needed for the propagation of overlapping fractures if the spacing between fractures is equal to their height. This is widely accepted idea that fracture spacing in sedimentary rock should be proportional to mechanical thickness for parallel joints; this simulation shows that the notion can be generalized for interacting overlapping non-parallel joints as well.

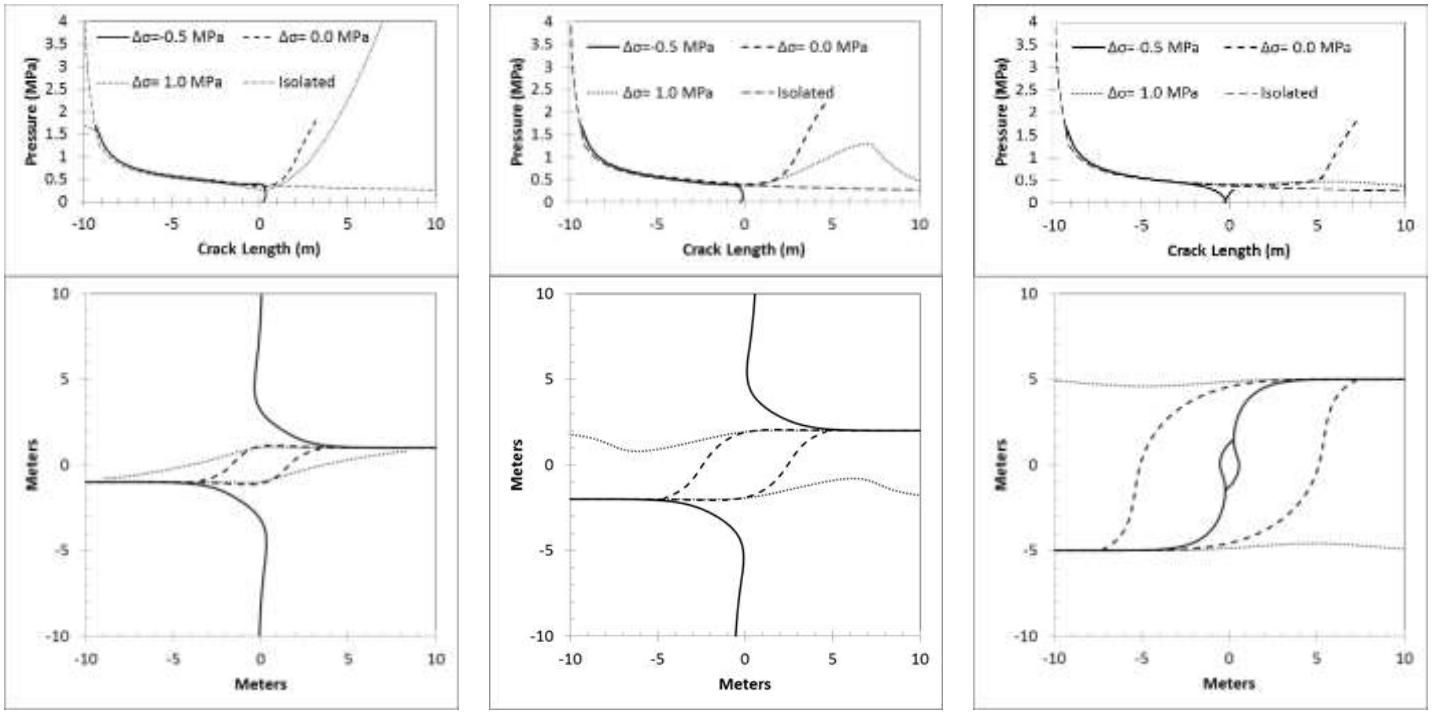

a) $\boldsymbol{S = 2.0\ m}$ ***b)*** $\boldsymbol{S = 4.0\ m}$ ***c)*** $\boldsymbol{S = 10.0\ m}$

Fig 2.6: Fracture path and required pressure for critical growth. The effect of fracture spacing and height as well as remote differential stresses are investigated, $\frac{S}{H} = \frac{1}{10}$

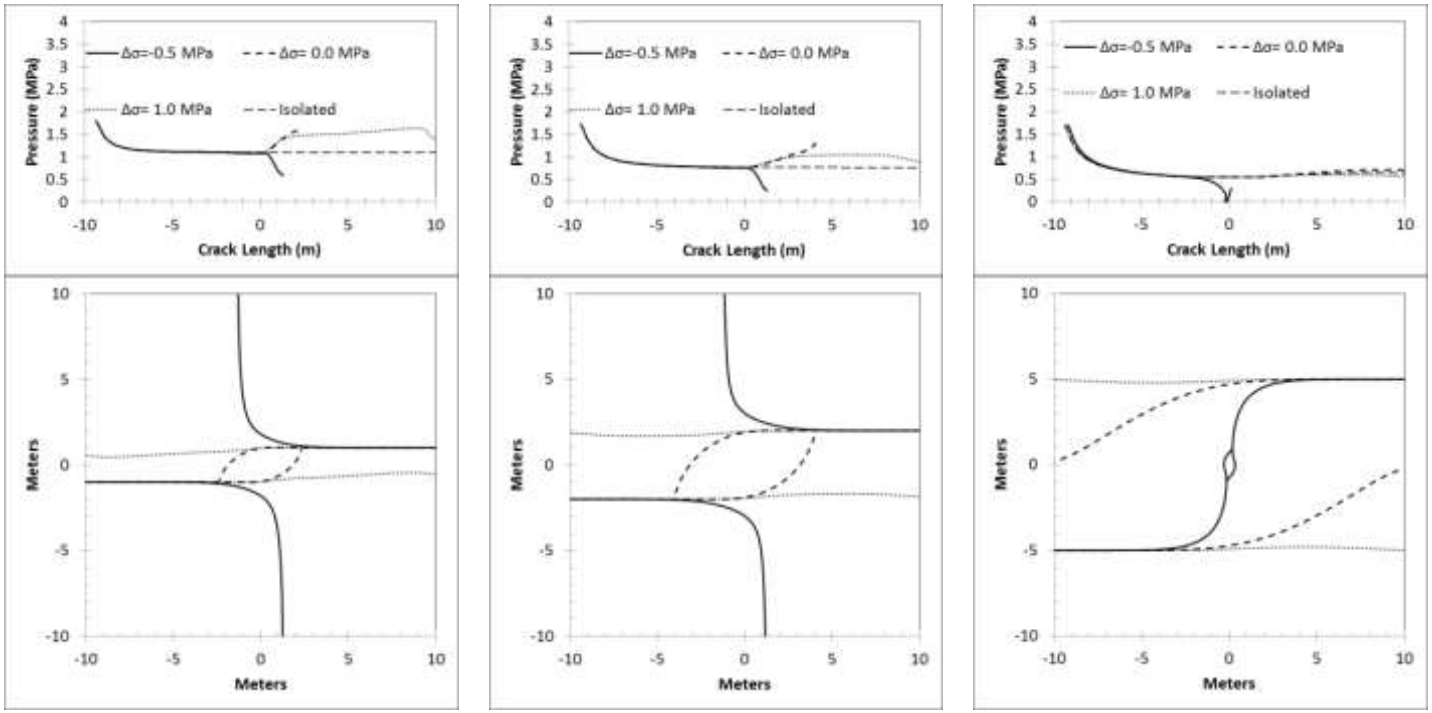

a) $\boldsymbol{S = 2.0\ m}$ ***b)*** $\boldsymbol{S = 4.0\ m}$ ***c)*** $\boldsymbol{S = 10.0\ m}$

Fig 2.7: Fracture path and required pressure for critical growth. The effect of fracture spacing and height as well as remote differential stresses are investigated , $\frac{S}{H} = 1.0$

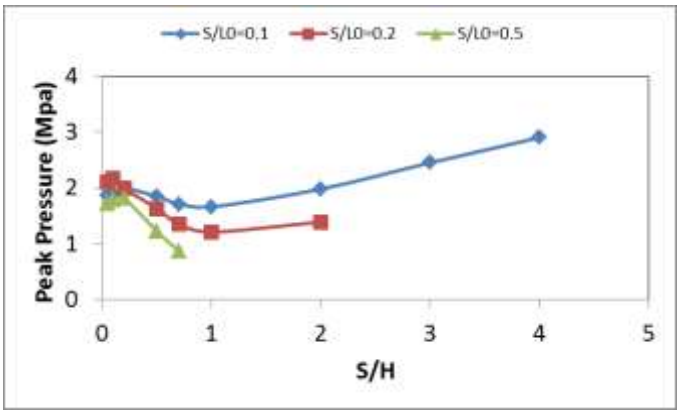

Figure 2.8: Peak driving stress for 2 interacting fractures

In a 2-D analysis, for an isolated plane strain crack of length, L, the driving stress ($\Delta\sigma_I$) for critical growth is calculated by the following equation:

$$\Delta\sigma_I = \frac{K_c}{\sqrt{\pi L/2}} \tag{2.4}$$

which shows required driving stress approaches zero if crack length approaches infinity; However, in 3-D analysis the stress intensity factor and required driving stress for critical propagation is mainly controlled by the smallest dimension, which means for a very long crack, L should be replaced by H in Equation 2.4. Figure 2.9 represents required driving stress for an isolated crack as a function of fracture height when fracture length is 20 m (equal to the total crack array length) which is the stabilized driving pressure in Figure 2.6 and 2.7. The figure shows for $H \geq L_0 = 20.0\ m$, the driving pressure is controlled by fracture length, and the 2-D analysis is a good approximation for a 3-D planar crack.

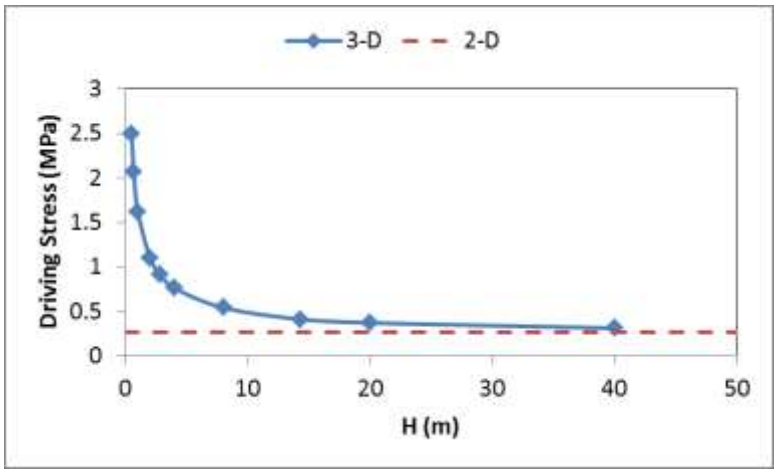

Fig 2.9: Driving Stress for critical propagation of an isolated crack of length, $L_0 = 20.0$ m

Mechanical interaction between fractures controls fracture path. Therefore, to describe fracture path, it is worthwhile to study stress distribution and trajectories around fractures. We examine the case of two interacting, non-propagating parallel cracks to interpret fracture path.

Figure 2.10 shows fracture path for $\frac{S}{H} = 0.05$ ("tall fracture") and 2.0 ("short fracture") assuming isotropic remote differential stress and S=2.0 m. Contours show the magnitude of shear stress, σ_{xy}, normalized by internal fluid pressure , p, and arrows indicate the orientation of the most compressive principal stress. The induced shear stress for the tall fracture case is much greater compared to the shorter fracture, and it is this shear stress that causes the more curved path for the taller fractures. For the lower S/H (thicker bed), the trajectories do the best job of predicting propagation path, but there is still some deviation. That means principal trajectories might be used to predict the fracture path for 2-D plane strain problems with good accuracy, but for 3-D problems, principal trajectories are not accurate enough to predict the fracture path and actual-propagation method is more necessary.

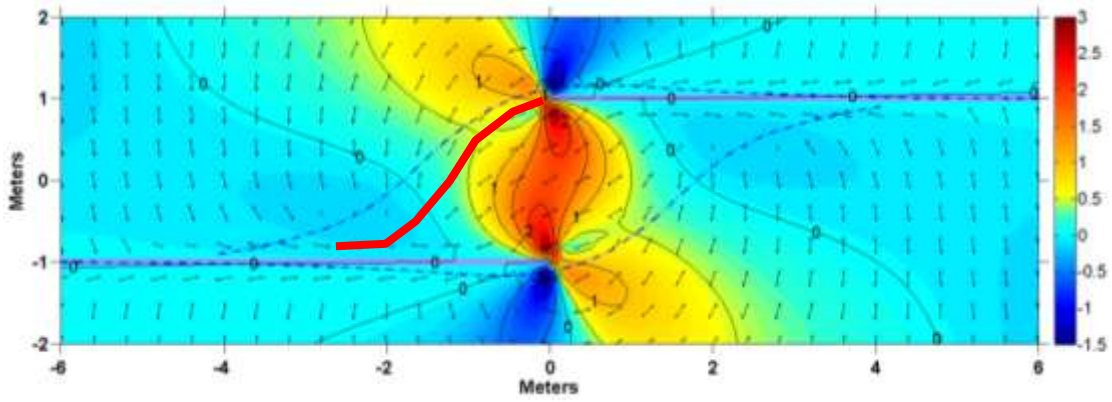

a) $\frac{S}{H} = 0.05$***, zero overlap***

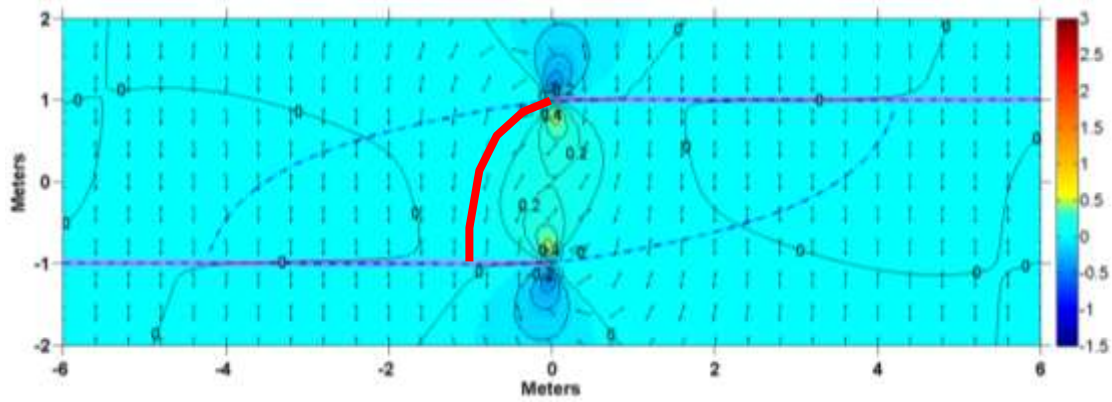

b) $\frac{S}{H} = 2$***, zero overlap***

Fig 2.10: Superimposed plot of fracture path, maximum principal stress trajectories and shear stress induced by opening mode in 2 parallel interacting non-propagating cracks under isotropic remote stress condition. Shear stress contours are normalized by internal pressure. Crack spacing is 2m.

2.2.4.2 Geometrical Features of Interacting Fractures

In this section, the effect of initial geometrical configuration (in terms of $\frac{S}{H}, \frac{S}{L_0}$) angle of intersection (β in Figure 3.4) is investigated. The main focus is on isotropic remote stress condition and a full 3-D analysis assuming a Poisson's ratio of $\nu = 0.3$, but the effect of compressive differential stress ($\Delta\sigma = 1.0\ MPa$), half-space analysis and lower Poisson's ratio ($\nu = 0.1$) is considered as well. Shallow crack refers to the extreme condition where crack depth, $D = 1.1\ H$, and deep crack refers to a full-space condition. The effect of

tensile differential remote stress presented in Figure 2.6 and 2.7 is not considered here, because crack-parallel minimum compressive remote stress condition is rare in the nature.

A distinct difference between 2-D and 3-D modeling of two parallel overlapping fractures is about angle of intersection between fractures. Using 2-D modeling for the isotropic remote stresses, the approach of intersecting fractures always remains asymptotic regardless of their initial overstepping. However, a 3-D analysis shows even for isotropic remote stresses a variety of intersection angles can be obtained based on fracture height and fracture spacing. Based on modeled cases, three different behaviors were seen when a fracture is approaching to another, varying with the ratio of *S/H*: concave, straight, and convex traces as depicted in Figure 2.11.

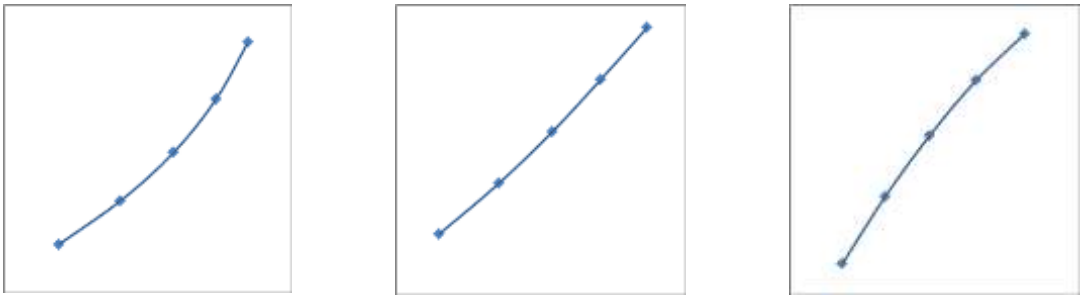

a- Concave for $\frac{S}{H} > 1.0$ ***b- Relatively straight for*** $\frac{S}{H} \cong 1.0$ ***c- Convex for*** $\frac{S}{H} < 1.0$

Figure 2.11: Typical fracture approaches upon intersection in 3-D modeling of two overlapping fractures under isotropic remote stress

The angle of intersection is uniformly increasing until about $\frac{S}{H} \approx 0.5$ (Figure 2.12) which shows the 3-D modeling yields different results in comparison with a 2-D which the approaching is always asymptotic. These figures show that the angle of intersection is more dependent on $\frac{S}{H}$ as all three figures represent the same trend for different value of initial spacing, S. Decreasing fracture height makes the angle of intersection to change from asymptotic to orthogonal. Therefore, for isotropic remote stress condition, a high angle of intersection implies less interaction between fractures. Mechanical property

variation (in terms of Poisson's ratio) and fracture depth have little to no effect on the angle of intersection.

a) $\boldsymbol{S = 2.0\ m}$

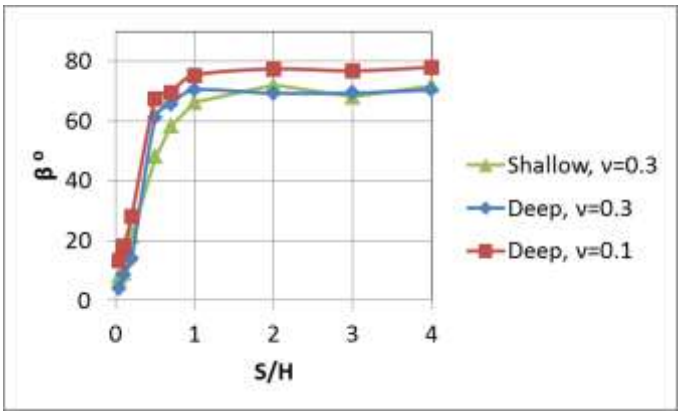

b) $\boldsymbol{S = 4.0\ m}$

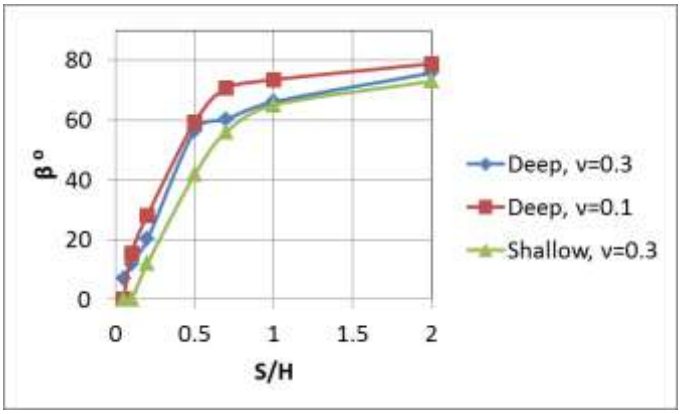

c) $\boldsymbol{S = 10.0\ m}$

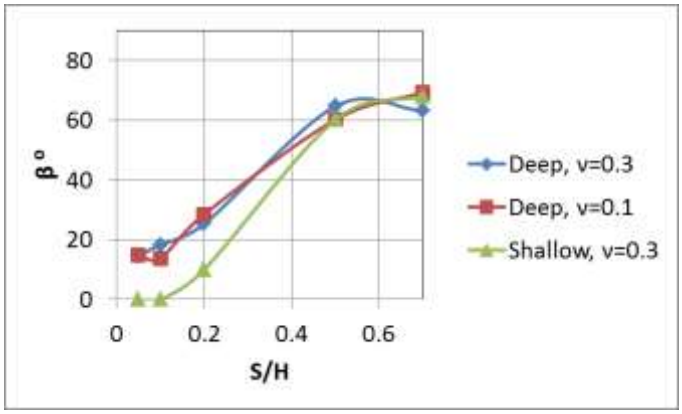

Figure 2.12: Angle of intersection versus $\frac{S}{H}$, a: $\frac{S}{L_0} = 0.1$ b: $\frac{S}{L_0} = 0.2$ and c: $\frac{S}{L_0} = 0.5$. The effect of Poisson's ratio and fracture depth are considered as well.

The change in approach angle with increasing $\frac{S}{H}$ (or decreasing fracture height) can be understood by looking at principal stress trajectories rotation during fractures shortening. Figures 2.13 shows maximum compressive principal stress trajectories (fracture orientation) for two interacting, tip-to-tip parallel fractures and contours of the crack-parallel normal stress (σ_{xx}) magnitude normalized by internal fluid pressure. The actual fracture path is superimposed for each case. Increasing fracture height results in increasing σ_{xx} along the fracture surface, especially in areas close to the inner tip, while according to factures boundary conditions, $\sigma_{yy} = P$ everywhere on fracture surface. For $\frac{S}{H} < 0.25$ (Fig. 2.13-a, b, and c), σ_{xx} exceeds σ_{yy} around the intersection. When *S/H>0.25*, $\sigma_{xx} < \sigma_{yy}$everywhere on fractures surface. The high crack-parallel compression (σ_{xx}) suppresses the propagation of nearby orthogonal cracks, and thus diverts propagation to be asymptotic instead.

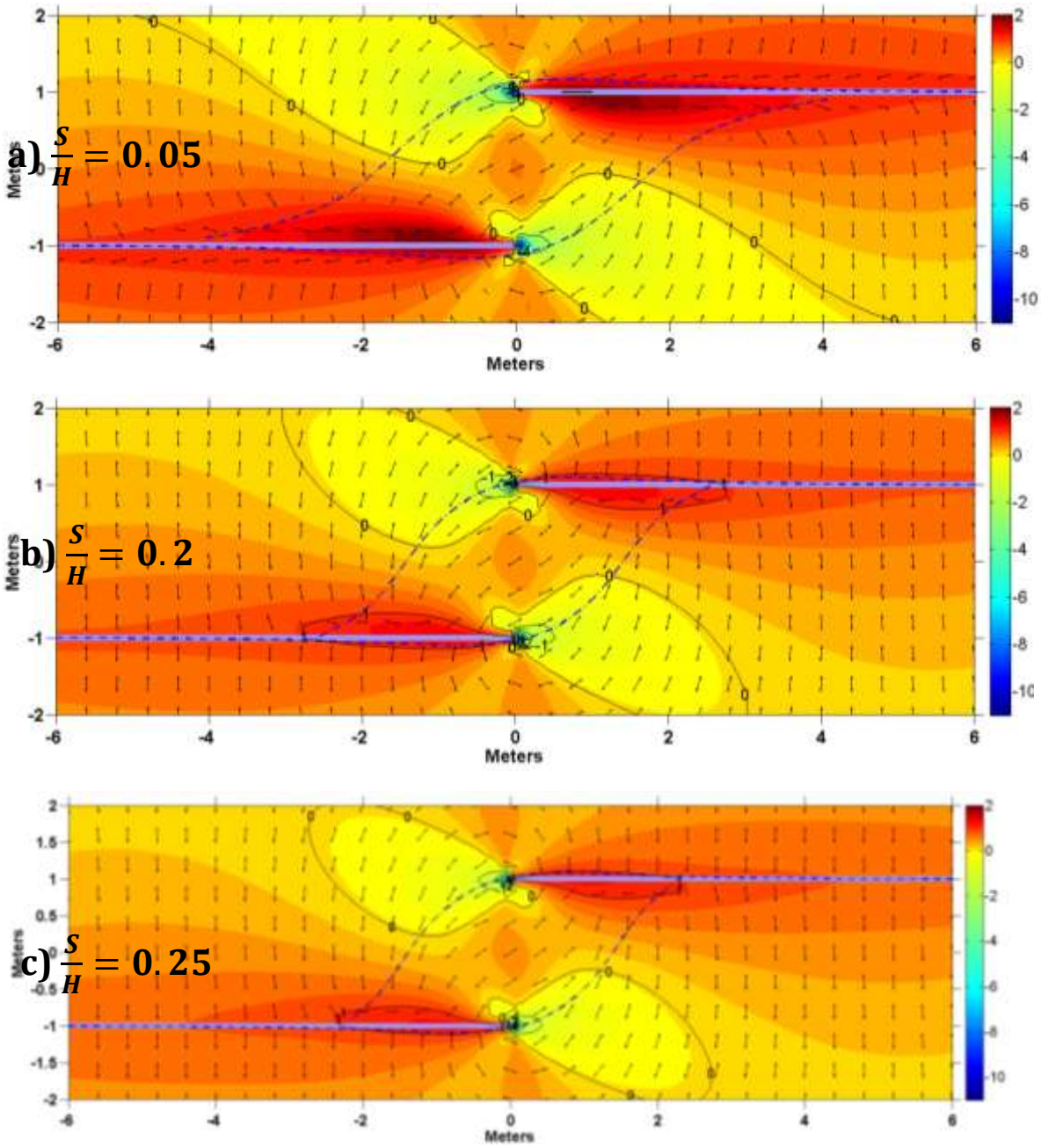

Figure 2.13-a to c: Fracture path superimposed on crack-parallel normal stress distribution of two tip-to-tip parallel interacting fractures, and maximum stress trajectories. Stress contours are normalized by internal pressure.

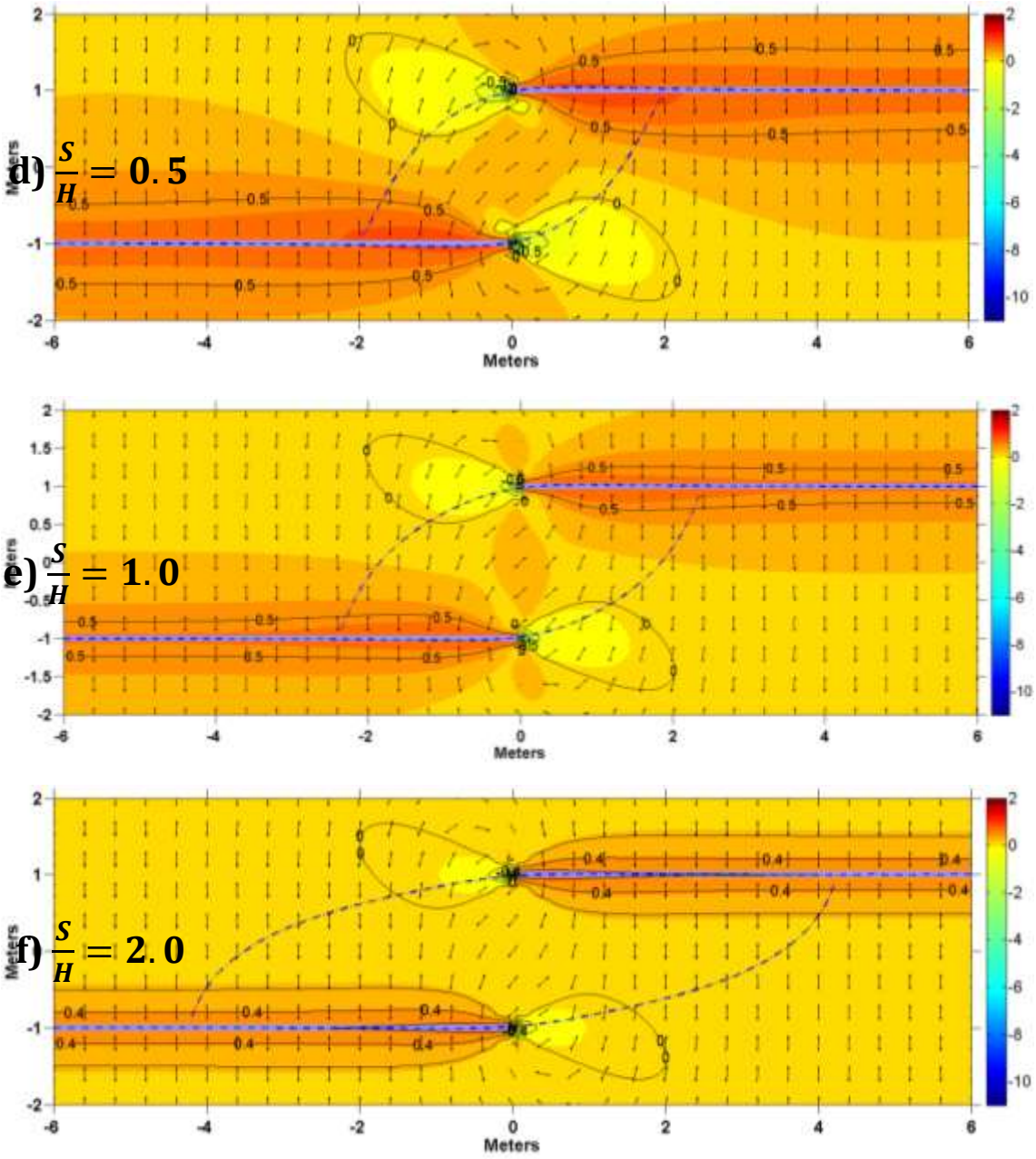

Figure 2.13-d to f: Fracture path superimposed on crack-parallel normal stress distribution of two tip-to-tip parallel interacting fractures, and maximum stress trajectories. Stress contours are normalized by internal pressure.

In the cases in Figure 2.13, fracture "tip to plane" intersection occurs at about 2.0 m from the zero overlap position. Figure 2.14-a shows how $\frac{\sigma_{xx}}{P}$ increases with decreasing $\frac{S}{H}$ for that location. At large *S/H*, the ratio approaches 0.6, but as low *S/H* (the closely spaced case), the ratio is approaching 2. For an isolated crack, the ratio of $\frac{\sigma_{xx}}{P}$ varies with *L/H*, where *L/H << 1* is the plane strain case, and *L/H>>1* is a blade-like (short) crack. In the plane strain case, the maximum possible ratio is achieved at *Sxx/P=1*. The limit for the blade-like case (*L/H>>1*) is 0.6, which is what was found for the 2 crack case for *S/H>>1*. In summary, the interaction between two closely spaced, en echelon fractures increases σ_{xx} in the overlapped area as compared to an isolated crack, which is the probable mechanism for asymptotic intersection.

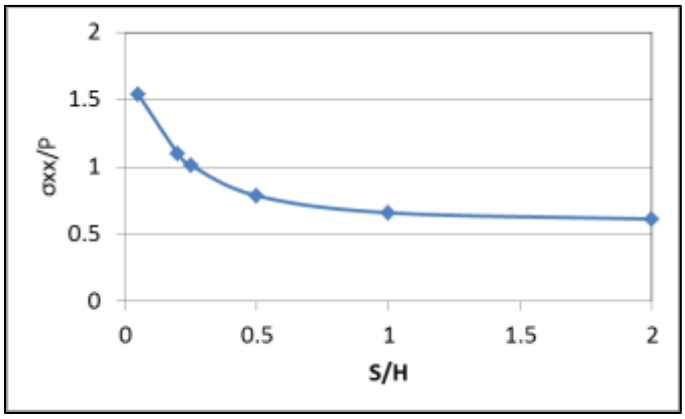

Figure 2.14-a: Two tip-to-tip parallel interacting fractures

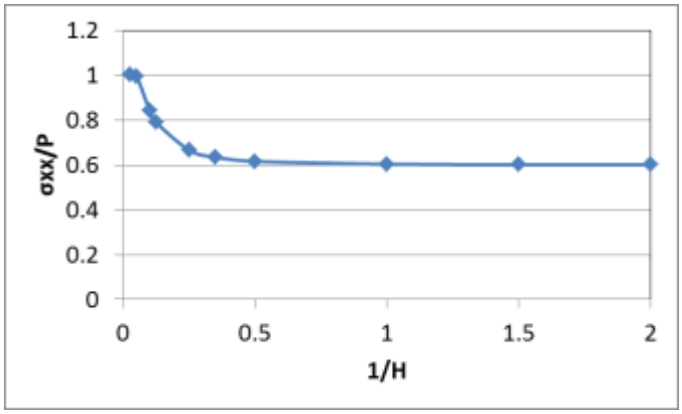

Figure 2.14-: Isolated fracture

Figure 2.14: Crack-parallel normal stress distribution versus Fracture I/H. σ_{xx} is normalized by internal pressure, P.

Differential remote stress also affect angle of intersection. Crack parallel compression impedes perpendicular intersection; however, doesn't affect asymptotic approaching. Figure 2.15 compare angle of intersection based on isotropic differential remote stress and crack-parallel compressive remote stress conditions. The linear variation is observable until *S/H=0.5*, where the angle plateaus.

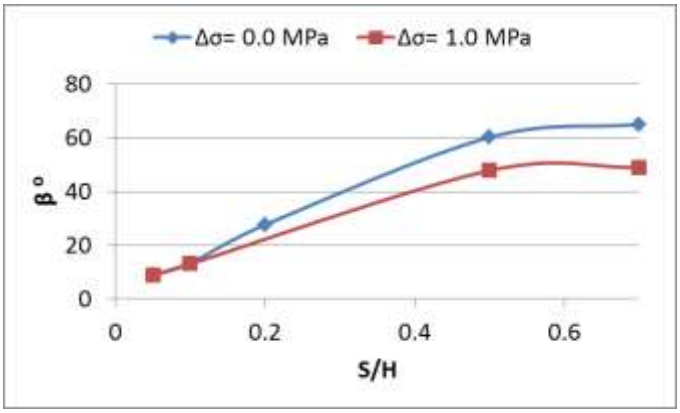

Fig 2.15: Effect of positive differential remote stress (crack-parallel compression) on angle of intersection

Since the fracture surface is free of shear traction, it should be a principal stress plain which implies the fracture is expected to have an asymptotic non-intersecting path or should intersects the free surface at right angle. However, as mentioned before, for the isotropic remote stress condition, intersection angle is something about $60° - 80°$ for short fractures ($\frac{S}{H} \geq 0.5$). Figure 2.22 explains the problem. This approach was used before by Thomas and Pollard (1993) using a 2-D model to explain the non-asymptotic intersecting oblique intersection. The direction of most compressive principal stress is shown by small two-head arrows and its magnitude normalized by internal fluid pressure is depicted by contours. Trajectories and contours are related for the stage of fracture growth shown by solid blue line. The fracture path over next increments is shown by dash line which is about parallel with near trajectories. The figure shows stress perturbation caused by crack tip effect is the reason for changing intersection angle from right angle to something less than $90°$ on area close to the intersected crack surface as by small distance from the crack tip, trajectories are almost perpendicular to the fracture surface.

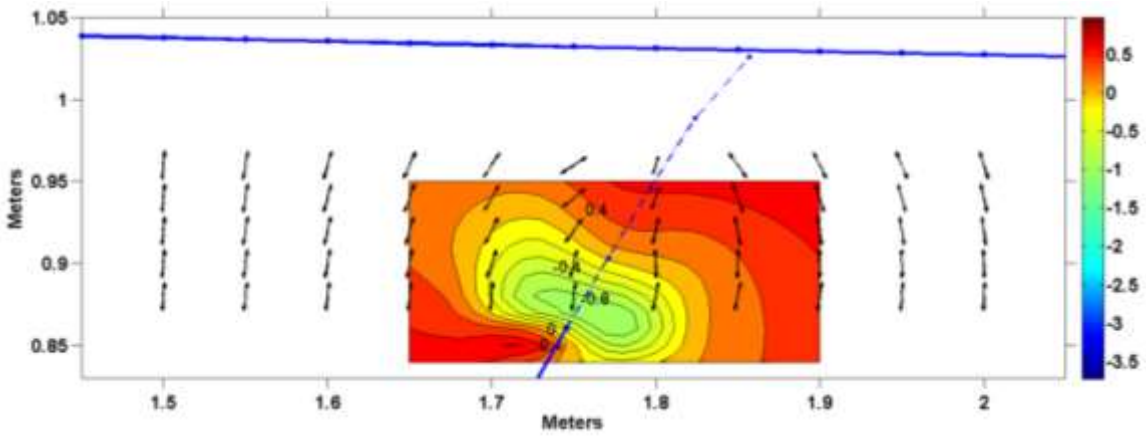

Fig 2.16: Crack tip effect on intersection angle

2.2.5 Overlapping Fractures and Mode III Distribution

In this section, the effect of lateral propagation and fracture interaction on the possibility of fringe crack generation based on mixed mode I+III . Mode III fracture loading occurs when there is shear stress parallel to the fracture front. As a result of mixed mode I+III, the fracture front breaks into several twisted blades called en-echelons, twist hackles or fringe cracks (Cruikshank, 1991). Figure 2.17 shows the schematic parent rectangular fracture propagation due to mixed modes including mixed mode I+II (kinking) and I+III (twisting) loading.

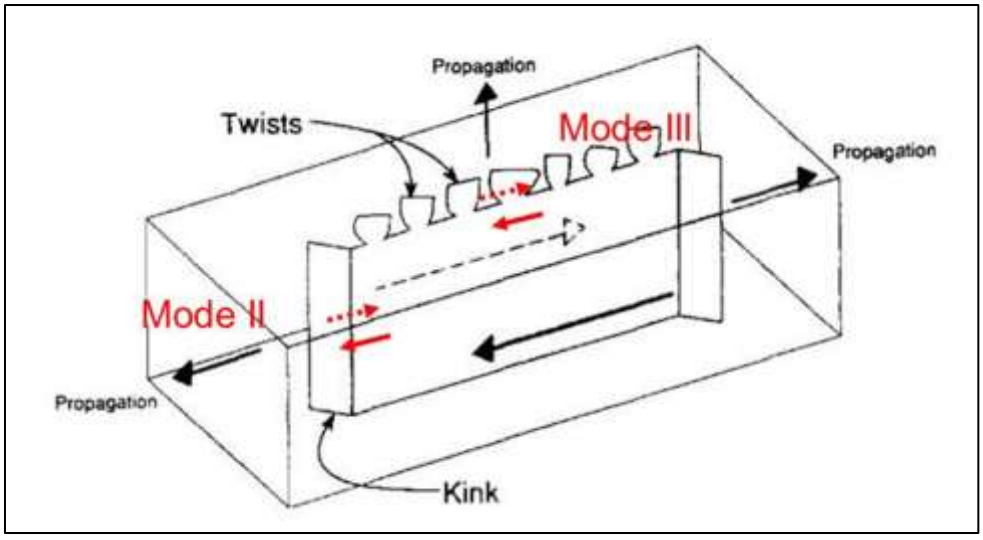

Fig 2.17: Mixed modes Fracture propagation, kinking vs. twisting (Modified from Cruikshank et al. 1991)

In structural geology, fringe cracks conventionally are interpreted as being caused by temporal or spatial reorientation of remote principal stresses (Younes & Engelder, 1999). Fringe crack propagation in the vertical direction might be gradual when the parent crack segmentation is smoothly curved, or it might be abrupt when the breakdown of parent joint is discontinuous as depicted in Figure 2.18. Gradual twist hackles usually grow within the same formation but abrupt fringe cracks are separated from the parent joints by a bed boundary (Younes & Engelder, 1999).

Figure 2.19 shows abrupt fringe generation in Taughannock Falls State Park, NY reported by Younes & Engelder (1999). The twist hackles were generated due to temporal remote stress field rotation and propagated downward into a shale bed from a thin layer of siltstone.

In hydraulic fracturing, fringe crack generation could be an indication of local stress reorientation due to spatial remote stress rotation in the layer above or underneath, or it could be due to any stress perturbation around the hydraulic fracture tip (for example by natural fractures). Experimental simulation of hydraulic fracture interaction with natural fractures done by Bahorich and Olson (2011) demonstrates twist hackle generation around a curving hydraulic fracture front

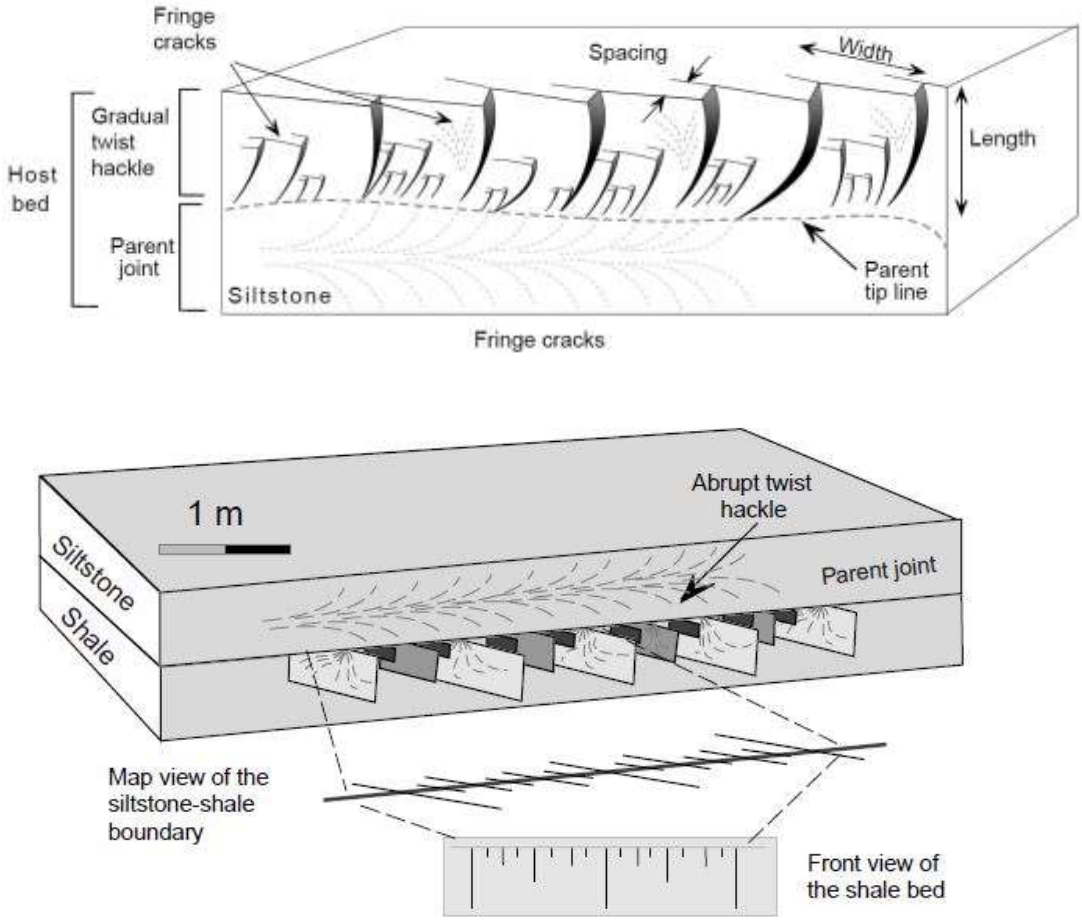

Figure 2.18: Breaking down of parent joint to twist hackles, gradual vs. abrupt (from Younes & Engelder, 1999).

Figure 2.19: Abrupt twist hackles generated from parent joint in siltstone bed into the shale formation underneath in Taughannock Falls State Park, NY (from Younes & Engelder, 1999)

Mixed mode I+III fracture propagation criteria and mechanism is still not fully understood (Lin *et al*. 2010); however, several experimental works (Cooke & Pollard, 1996; Frid *et al*. 2005; Wu, 2006) and field observations (Younes & Engelder, 1999; Belayneh, 2004; Brogi, 2011) support the idea that en-echelons roughly extend perpendicular to local maximum tensile stress. Using this assumption, Pollard *et al.* (1982) derived the analytical solution to estimate angle of twisting for abrupt breakdown as the following:

$$\theta = \frac{1}{2}\tan^{-1}\left[\frac{K_{III}}{K_I\left({}^1/_2 - \nu\right)}\right] \tag{2.5}$$

where θ is the twist angle. Higher values of Mode III SIF (or lower opening mode) result in bigger twisting angle. Similar to twisting angle of abrupt fringes, For gradual fringe cracks propagation, the rate of twisting angle is dependent on mixed mode I+III SIF (Lazarus *et al.* 2001).

For the range of remote stress and internal fluid pressure in the nature, Pollard *et al.* (1982) modified Equation 2.5 and estimated the relation between twist angle of abrupt fringe cracks, θ, and remote stress rotation, α, by the following equation:

$$\theta = 0.5 \tan^{-1}[\frac{\sin 2\alpha}{(0.5+\nu)+(0.5-\nu)\cos 2\alpha}] \quad (2.6)$$

where ν is Poisson's ratio.

When fringe cracks can propagate laterally, they will likely interact mechanically and follow mixed mode I-II paths as discussed for the en echelon crack pair problems earlier in this section. A simulation was performed to represent the parent crack and a large population of fringe cracks as shown in in Figure 2.20. The number of fringe cracks, spacing between them and the initial length upon generation from the tip-line of parent crack were subjects of several papers. Experiments done by Lin *et. al.* (2010) showed a dependency of spacing on twist angle. An approximate solution suggested by Pons & Karma (2010) relates spacing of crack fragments to the ratio of K_I/K_{III} times the process zone size.

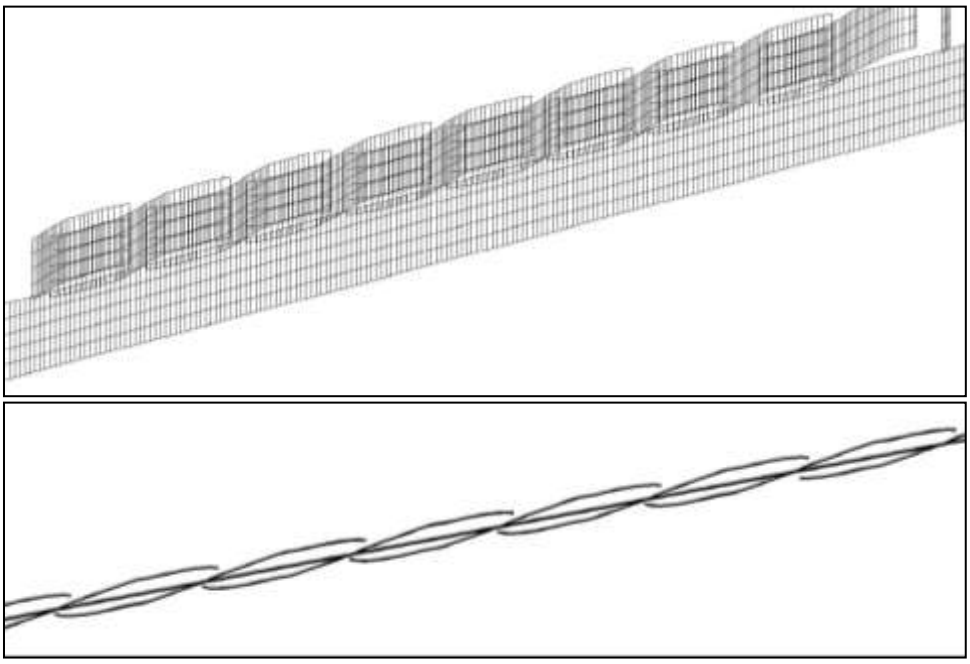

Figure 2.20-a: Hand-shaking or hooked pattern due to strong interaction.

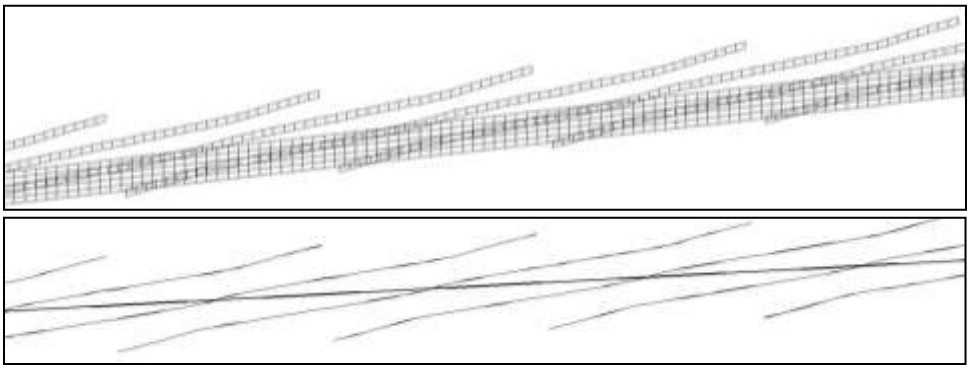

Figure 2.20-b: Parallel pattern due to week interaction

Figure 2.20: Effect of fracture height on lateral propagation of fringe cracks, 3-D visualization and map view.

Figure 2.21 shows how fracture interaction and Mixed mode I+II propagation, or lateral kinking, might cause twist hackle generation. The variation of K_{III} is displayed for the top (and bottom) of the lower left member of two overlapping interacting fractures at different stages of critical lateral propagation ($K_{eq} = K_c = 1.5\ MPa\sqrt{m}$) with $S/H = 0.25$ (Fig. 2.21-a) and 1.0 (Fig. 2.21-b). The magnitude of K_{III} is higher for the more

closely spaced array ($S/H = 0.25$), a product of stronger mechanical interaction as described earlier for the mixed mode I-II propagation examples. The peak value of K_{III} value approaches 50% of K_c in the closely spaced case, whereas it peaks at only about 10% in the wider spacing case (*S/H=1.0*).

The generation of Mode III SIF is simultaneous with deviation of fracture from straight path. The magnitude of Mode III generally increases as fracture overlap increases. Along the curved part of the fracture, K_{III} is almost negligible for the wider spacing case, because of the relatively straighter path compared to the curved part of closely spaced case. For the curved part of closely spaced case, Mode III SIF value is significant, monotonically increasing during the propagation, and has different sign from the straight part of the fracture which is related to the change of direction of fracture path curvature from concave to convex during extension. That says, fringe generation orientation changes from right-lateral in straight part of the fracture to left-lateral along the curved part of closely spaced fractures. Another difference between two graphs is related to the abnormal value of K_{III} on the straight part during the last intervals of propagation upon intersection and around the intersection points. For closely spaced fractures, the other fracture tip approaches almost asymptotically which means the sign of resolved shear by straight part doesn't change – only its value increases around the intersection area; However, for the wider case, the other fracture tip intersects at high angle which causes the sign of resolved shear by the straight part to be different in two sides of intersection point.

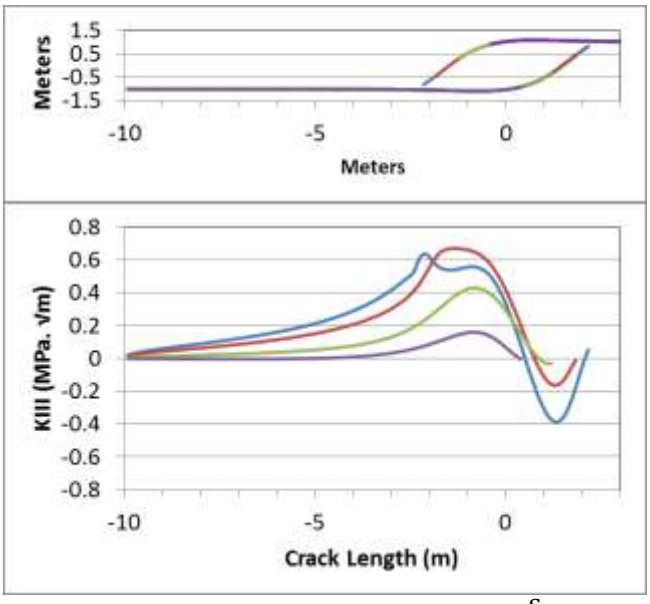

Figure 2.21-a: Closely spaced fractures ($\frac{S}{H} = 0.25$)

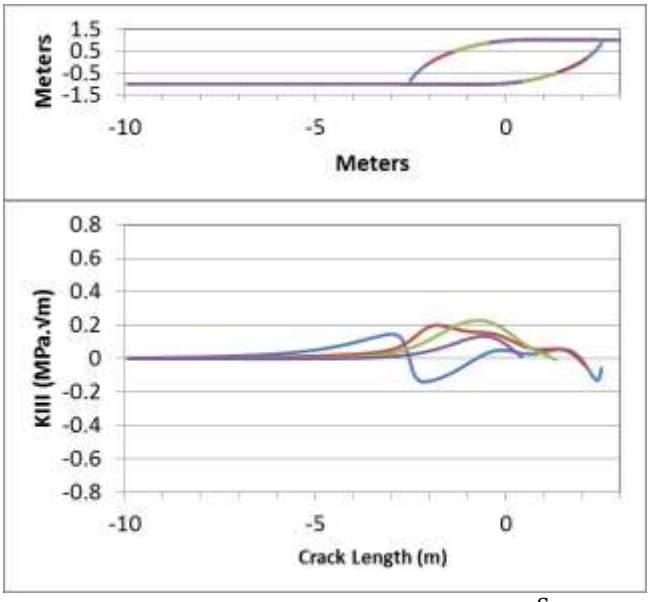

Figure 2.21-b: Widely spaced fractures ($\frac{S}{H} = 1.0$)

Figure 2.21: Evolution of K_{III} distribution (lower graph) and fracture path (upper graph) in different stages of propagation.

2.2.6 Conclusion

The effect of remote differential stress and spacing on crack path of two overlapping fractures was investigated by Olson and Pollard (1989). Using a 2-D boundary element modeling, they found fracture path can be used to infer paleostresses. The previous 2-D work is extended to 3-D to account for fracture height effects and how they might influence fracture propagation pathes. The important dimension in determining the degree of mechanical interaction and fracture path curving is the spacing to height ratio, S/H. Strong interaction happen when fracture is four times od spacing and the result of fracture path when 2-D plane strain approximation is in good agreement with 3-D analysis, while week interaction is seen when $S/H>0.25$ where 2-D analysis is not accurate and three dimensional modeling is necessary. Results showed that fracture height is as important as remote stresses to affect fracture path. In addition to fracture path, the angle of intersection is influence by the *S/H* ratio, with asymptotic approach resulting for $S/H<0.25$ and roughly orthogonal approach for $S/H>=0.5$.

With regard to whether stress trajectories can predict fracture propagation paths, the trajectories do the best job of predicting propagation path for the lower S/H (thicker bed), but there is still some deviation. That means principal trajectories might be used to predict the fracture path for 2-D plane strain problems with good accuracy, but for 3-D problems, principal trajectories are not enough accurate to predict the fracture path and actual-propagation method is more necessary.

Fracture spacing to height ratio also affects value and distribution of Mode III SIF along the top and bottom front of vertical interacting fractures. Fringe cracks generation in either natural fracture or hydraulic fractures would be the result of curved path, fracture interactions or conventional accepted idea of temporal or spatial remote stress rotation.

2.3 Joint Development at the Vicinity of Normal Faults: Perpendicular to Fault Strike versus Parallel

2.3.1 Overview

Most of oil fields include faults, and their tectonic effects perturb the stress field in which secondary structures such as joints have formed. Joint distribution and joint orientation with respect to normal faults provide crucial information for petroleum engineers regarding estimation of porosity and permeability and inferring local and regional principal stresses. While joints are typically vertical or bedding-normal fractures, faults are typically non-vertical and non-orthogonal to bedding. Complicated geometry of successive normal faults and important interactions with the earth's free surface make it necessary to use a three dimensional solution. The purpose of this section is to study the geometrical relationship between genetically related normal faults and joints in various geologic environments through considering a case study of fault-related joints perpendicular to the normal fault strike located in Rough and Rocky Mesa area in the Arches National Park region, Utah. Joint development in the case study is assumed to be due to the normal fault stress field perturbation as well as pore pressure. Results show that induced joint orientation is dependent on vertical position with respect to the normal fault. Normal dip slip on around 50-70 degree faults generate tension mid-depth along an isolated fault only for Poisson's ratios around 0.1 or less than that; two or more faults spaced within 1 fault height increases the magnitude of the tension and widens the area under tension. This area is proportional to fault length and height of the array of normal faults. Calculations represent a more physically reasonable match to measured field data than previously published, and a new mechanism is also identified to explain the driving stress for opening mode fracture propagation upon burial of quasi-elastic rocks.

2.3.2 Introduction

Joints are the most ubiquitous geologic structure in the earth's crust (Pollard and Aydin, 1988). They are common at the vicinity of faults and within fault zones. Joints (as dominantly extensional fractures) and faults (as shear mode discontinuity) are associated

temporally and spatially if they have kinematic or geometric relationship. Joints might develop before, contemporaneous with, or after fault propagation (Peacock, 2001).

Fractures can act as conduits or barriers for subsurface fluid transport. Joint spacing affects general permeability and joint orientation is effective on fluid flow pathway. Joint distributions and orientations determine the direction of horizontal drilling, hydraulic fracturing development, initial production and later injection wells (Fischer, 2000). Faults might be even better conduits for fluid flow compared to joints (Zoback, 2011), because they act as a huge trans-layer discontinuities and their reactivation is likely in depth where joints are more likely to be closed. Faults are the main leakage pathways in geological sequestration of CO_2 (Nicot and Hovarka, 1998; Jordan *et al.* 2011). Injection in hydrocarbon reservoirs to improve production or CO_2 injection for storage might reactivate faults. Fault reactivation and stress-field perturbation might affect joints development. Good knowledge about joint distribution and joint orientation with respect to normal fault leads to successful modeling and development of fractured reservoir (Fischer, 2000; peacock, 2001; Bahat, 2004) and CO_2 sequestration storage (Nicot and Hovarka, 1998; Jordan *et al.* 2011). Furthermore, System of joints and normal fault can be used as paleostress and paleotectonic (Guidi *et al.* 2013). Joints are the best indicator of local minimum stress and fault may help to decipher tectonic history (Bahat, 2004). Inferring local and regional stress from the system of joints and faults is critical for petroleum exploration, and obtaining information about the tectonic history is worthwhile for seismologists to estimate the chance of future earthquake occurrence.

The genetic relation between joints and faults might be inferred from their relative configuration. Figure 3.1 shows common configuration of joints and faults (Blenkinsop, 2008). Figure 3.1-a represents how joint extension, linkage and coalescence might result in a zone of weakness as localized shear mode failure or fault generation (Olson & Pollard, 1991). Figure 3.1-b describes fault formation from linkage of wing-crack or pre-existing joints that subsequently loaded by shear (Horri & Nemat-Naser, 1985).

Synchronized mechanism of fault propagation and joint extension is depicted in Figure 3.1-c, where joints are localized in the process zone of a fault (Vermilye and Scholz, 1998). Joint development due to fault slip are depicted in Figure 3.1-d and 3.1-f (Hancock, 1985; Cruikshank *et al.* 1991; Rawnsley *et al.* 1992; Gross *et al*. 1997; Simon *et al.* 1999; Peacock, 2001; Bahat, 2004; Caputo, 2005; Blenkinsop, 2008), where in the first one, fault slip causes joint generation and internal fluid pressure provides driving stress for further extension, but in the last case, joints propagates only due to slip

movement of the fault. Geologic observation (Gross et al. 1997; Kattenhorn *et al*. 2000; Bahat, 2004) as well as laboratory experiment (Conard & Friedman, 1976; Withjack *et al*. 1990) have established how joints as secondary structures might be created from fault or slip movement on shear weakness plane.

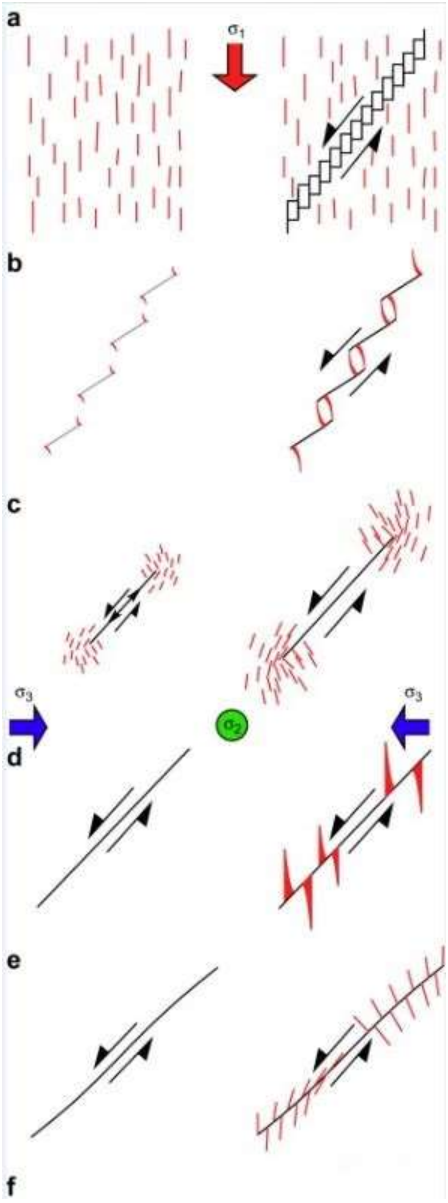

Figure 3.1: Genetic and geometric relationship between different systems of joints and a fault (from Blenkinsop, 2008). Joints are depicted as red lines and faults as black. Refer to the text for the mechanism and their relation.

According to Anderson's theory of faulting, the intermediate principal stress exists in the plane of normal fault and parallel to its strike. Therefore, the least principal compressive stress is perpendicular the strike of normal fault as depicted in Figure 3.2.

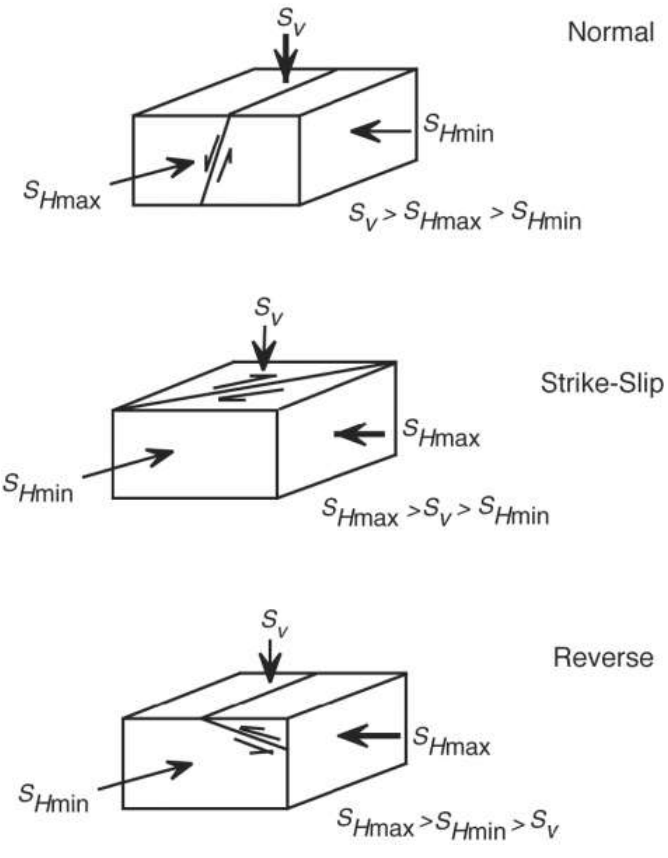

Fault Regime	S_1	S_3
Normal	S_v	$S_{H\min}$
Strike-slip	$S_{H\max}$	$S_{H\min}$
Reverse	$S_{H\max}$	S_v

Figure 3.2: Anderson's fault regimes characterization (from Petrowiki).

Development of joints as "dilatational mode" fracture should be perpendicular to the least principal stress or S_{Hmin} (e.g. Pollard and Aydin, 1988). Therefore, the schematic configuration of joints that post-date normal faults should look likes Figure 3.3-a. This premise suggested by Anderson (1951) is reasonable assuming joints and normal faults

belong to the same kinematic-tectonic event in extending crust perpendicular to their strike. In this situation, if joint density is not considerably modified toward a normal fault, joint orientation reflects regional remote stress pattern at the time of jointing. The assumption doesn't incorporate the effect of normal fault on stress perturbation and local principal stress reorientation due to fault slip and is unable to justify joint growth perpendicular or in high angle to normal fault strike (Figure 3.3-b).

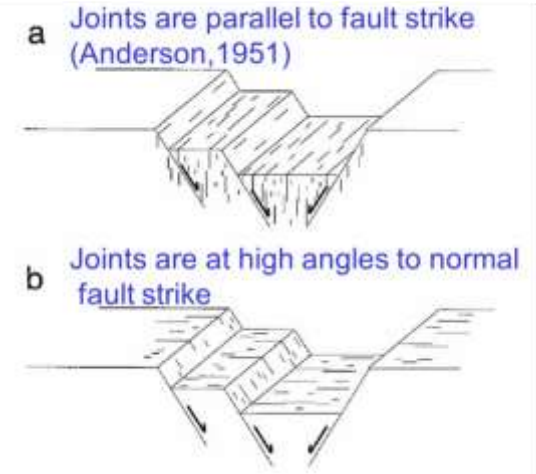

Figure 3.3: Joint arrangements at the vicinity of normal faults (from Kattenhorn et al. 2000).

Geologic observations also support the possibility of joint development at high or right angle to fault strike in response to tensile stress distribution due to dip slip of normal faults. Figure 3.4 shows an outcrop of a normal fault and adjacent fault-parallel joints located in a formation 5 km south of Beer Sheva, Israel reported by Gross *et al.* (1997) and Bahat (2004). They observed two distinct sets of almost vertical joints at the vicinity of the normal fault, one with a mean strike at 55^0N, and another at 326^0N. The fault strikes at 292^0N and dips 45^0N. Based on geometrical configuration of the system of normal fault and two joint sets, they concluded the first set is related to fault kinematics and postdates the normal fault, but the other one have existed prior to faulting and indicates remote stress rotation at the time of faulting.

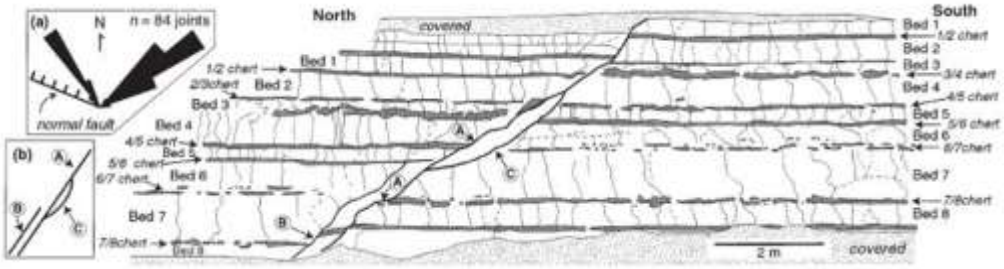

Figure 3.4: Sketch of the outcrop showing a normal fault and two joint sets located 5 km south of Beer Sheva, Israel. Joint set which is genetically related to the normal fault is depicted by solid line and strikes 55^0N, the other set is shown by dash line strikes 326^0N and postdates the fault. Rose diagram is shown above the sketch (from Gross et al.1997).

Figure 3.5 is the map-view sketch of fault-related joints locates in Rough & Rocky Mesa area in the southwest corner of the Arches National Park region, Utah (Kattenhorn *et al.*2000). Geologic structures in Figure 3.5 include parallel successive normal faults, joints with variety of orientations with respect to faults, and deformation bands (Kattenhorn et al. 2000). Arches National Park in Utah provides an ideal opportunity to study deep joints and normal faults in three dimensions because of excellent surface exposure made by erosion as well as existence of several outcrops (Kattenhorn et al. 2000). Different geomechanical and geological aspect of the zone have been the subject of several academic investigations (Dyer, 1983; Cruikshank et al. 1991; Kattenhorn et al. 2000; Rotevan, 2007; Fossen, 2010). The black box in Figure 3.5 shows the area where joints are perpendicular to the normal fault strike which was observed and investigated by Kattenhorn *et al.* (2000). Contrary to the case shown in Figure 3.4, vertical joints in Rough & Rocky Mesa extended for significant distance away from normal faults which indicates other stress components such as pore pressure should be present to provide enough driving stress for joint growth, because stress perturbation and tensile stress distribution induced by normal fault slip dissipates within short distance away from the fault strike.

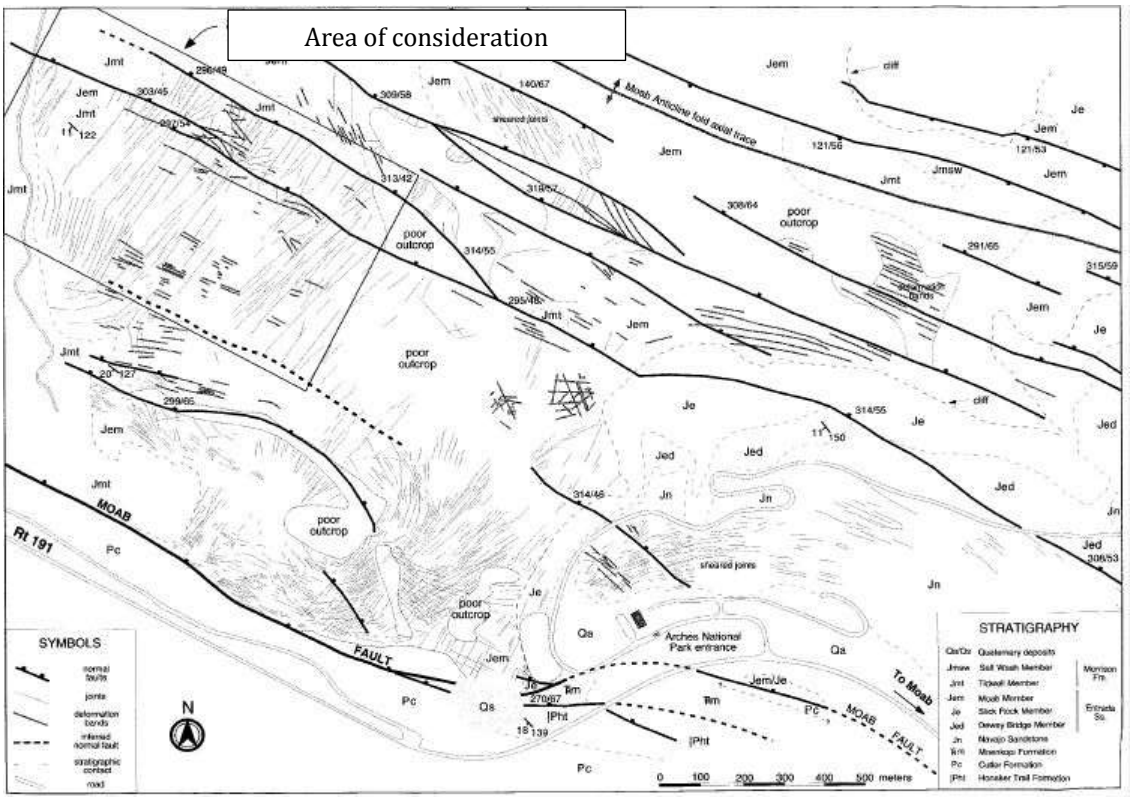

Figure 3.5: Normal faults and joints in Rough and Rocky Mesa. Faults are shown by thick lines and joints are depicted by thin lines. Tick marks shows the direction of slipping (hanging wall), and numbers represent strike and dip angle respectively. Black box shows the area of consideration where joints are perpendicular to normal fault strikes (from Kattenhorn et al. 2000)

Joints are very sensitive to local principal stresses at the time of jointing and therefore, any source that affects the magnitude and direction of minimum stress, affects joint extension as well. Joint propagation is influenced by different source of loadings (Caputo, 2005): gravitational, thermal, pore pressure, tectonics, and diagenetic. Gravitational component is proportional to the rock density and increases with depth. It affects vertical joints propagation through indirect mechanisms such as fault slip induced stresses (will be explained further in the following sections), or bilateral constraint effect and horizontal remote stress distribution from overburden loads. Temporal variation in gravitational force through erosion or deposition also leads to horizontal stress redistribution and may affect joints propagation (Caputo, 2005). The thermal component

is effective through temperature variation in the body of rock. Thermal effects are minor except the case of extreme temperature changing such as lava flows (Delaney & Pollard, 1981). Pore pressure distribution significantly influence joint propagation. Pore-pressure depends on permeability, porosity, depth, fluid density, leak-off, time etc. The reference lower estimation of pore pressure would be hydrostatic pressure; however, transient pressure distribution and low porosity might cause pore pressure exceed lithostatic pressure in deep formations (Engelder and Fischer, 1996). Pore pressure directly affects joint aperture and extension direction by changing net pressure. Neglecting poroelastic effects, pore pressure can be reasonably assumed to be equal to minimum principal stress at the time of jointing (Olson, 1993: Olson, 2007). The tectonic component of stress is another source of loading for joint propagation and is induced by different geologic events in the scale of plate wide to local (Engelder, 1992) such as earthquake, bending, folding etc., but here in this section is specifically used for stress perturbation due to fault slip. Diagenetic effect is another loading component related to rock volumetric change due to chemical of physical process during diagenesis (Laubach *et al*. 2010). This volumetric change in terms of contraction or expansion applies extra strain to the medium and might affect extensional discontinuities.

3D numerical modeling of the mechanical interaction of growing faults (Wilmese *et al.* 1996; Gupta *et al.* 1998; Soliva *et al.* 2006), normal-fault-slip induced heterogeneous stress field (Maerten *et al.* 2002) and the possibility of the development of secondary smaller faults at the vicinity of a larger fault (Maerten *et al.* 2006) have been considered before. However, there have been few endeavors to study the effect of normal fault movement and stress perturbation on extensional fracture propagation at regional scale (Simon *et al.*1999). Contrary to normal faults, strike-slip faults can be modeled using a 2-D plane strain assumption (Rawnsley *et al.* 1992; Homberg *et al.* 1997; Martel and Boger, 1998; Engelder and Peacock, 2001; Wilson *et al.* 2003), because slip movement happens in the horizontal plane; the reason that joint development around strike-slip fault considered more than normal fault in literatures. Katenhorn *et al.* (2000) used a 3-D geomechanical modeling to find the reason of joint propagation at high angle to, and few hundreds of meters away from the normal fault strike (the area which represented by a black box in Figure 3.5). Neglecting pore pressure effects and assuming constant tension perpendicular to fault strike for modeling tectonic slip event on the fault surface, they found except a narrow area extending less than 1% of fault length from the fault strike, slip movement perturbation is not able to generate enough fault-parallel tensile stress to overcome intermediate stress, S_{Hmax}, which was assumed to be equal to vertical compression. They suggested another tensile remote stress parallel to fault strike and 25%

more than fault-perpendicular remote stress is necessary to be superimposed to S_{Hmax} to obtain tensile stresses and fault-perpendicular minimum principal stress trajectories. They justified this assumption by the possibility of regional remote stress rotation, or local fault- parallel stress relaxation due to the effect of other adjacent normal faults. Based on their conclusion, internal fluid pressure was suggested speculatively as an alternative mechanism that might be effective on joint growth, although the notion wasn't considered quantitatively. Disregarding the possibility of remote tensile stress at the burial depth of the modeled fault (i.e. 3.4 km), it is unclear if genetic relation between joints and normal fault was modeled properly as in their model, joint propagation is predominantly controlled by fault-parallel maximum tensile remote stress.

The purpose of this section is to study the geometrical relationship between genetically related normal faults and joints in various geologic environments and to present a more physically reasonable match to measured field data than previously published about long joint development at high angle around normal faults in Rough and Rocky Mesa as depicted in black box in Figure 3.5. The effect of fault dimensions, burial depth, mechanical properties in terms of Poisson's ratio and multiple successive normal faults were considered to increase the area and magnitude of effective distributed tension around the normal fault. Joint development in the case study was assumed to be due to the normal fault stress field perturbation as well as pore pressure. Internal fluid pressure effect on joint propagation was considered artificially by canceling minimum horizontal stress. Calculations were based on isotropic remote stress condition; however, the effect of differential remote compressive stress in removing tension, and the possibility of trajectories rotation were considered as well.

2.3.3 Rough and Rocky Mesa Case Study

2.3.3.1 Tectonic History and General Characteristics of Joints

The sequence of geologic events in Rough and Rocky Mesa is as the following: development of Moab Anticline (refer to Figure 3.5), bending distribution along its axis, generation of deformation band and development of normal faults, and finally, joint propagation due to stress-field perturbed by normal fault slip. According to field reconnaissance, joints don't cross over exposed normal faults indicating they do not pre-date normal faults (Kattenhorn et al. 2000).

Normal fault strikes are relatively parallel and fault dips ranging from 42^0 to 67^0 and their lengths varies from 0.25 to 4.0 km with spacing of 100-400 m (Kattenhorn *et al.* 2000). Joint length varies from region to region, but they extend up to 400 m away from faults in the NW of Rough and Rocky Mesa (Figure 3.5). Joints are relatively vertical and their orientations with respect to the adjacent normal fault strike are sporadic within Rough and Rocky Mesa: from roughly parallel in the south, to almost perpendicular in NW (Figure 3.5). Joint spacing is variable as well, ranging from 10-30 m. Fault and joint height might be inferred from the stratigraphic observation (Figure 3.6). According to Kattenhorn *et al.* (2000), normal faults cut the stratigraphic at least as deep as Wingate Sandstone and as shallow as the Salt Wash Member of the Morrison Formation (shown by a red box in Figure 3.6 which shows 670-875m overall thickness), and Joints extended throughout the layer of the Moab Member (blue box in Figure 3.6, a layer of 27 m thickness). All layers younger than the Brushy Basin Member of the Morrison Formation are assumed eroded in the Rough and Rocky Mesa Region (Kattenhorn *et al.* 2000). Regarding formation layers containing normal faults and joints, extensional fractures are more probable to be developed in layers adjacent to the upper part of the faults.

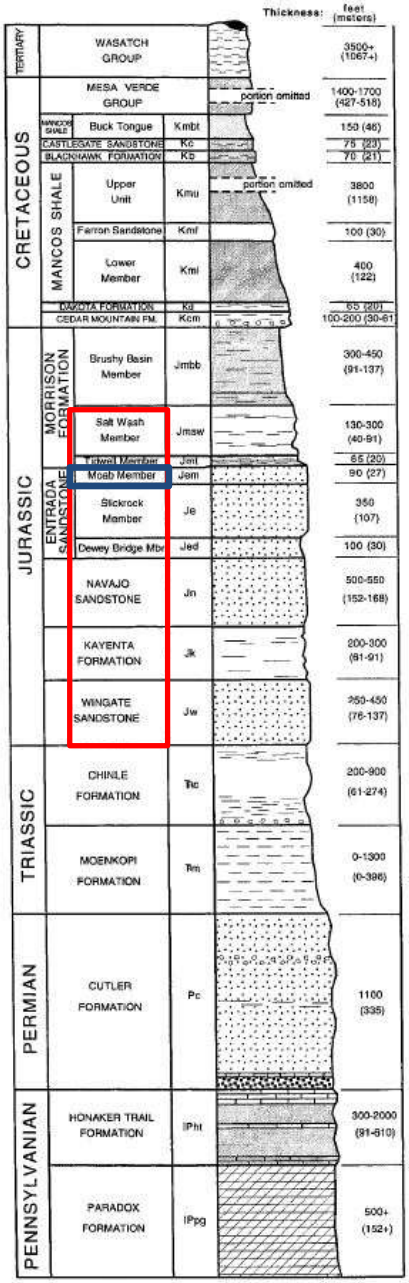

Figure 3.6: Stratigraphic column showing formations in the Rough and Rocky Mesa zone (after Kattenhorn et al. 2000). Layers containing normal faults depicted in Figure 3.5 are shown by a red box, and the layer confining vertical joints is depicted by a blue box.

2.3.3.2 Physical and Mechanical Properties

The following elastic constants and physical property were assumed by Kattenhorn *et al.* 2000 and used in their 3-D modeling for the sandstone: Poisson's ratio, $\nu = 0.25$, shear modulus, $G = 12\ GPa$, and density, $\rho = 2300\ kg/m^3$. In the following section the effect of Poisson's ratio on stress distribution will be examined; Table 3.1 shows the published values of apparent Poisson's ratio ranges from 0.05 to 0.45 with average of 0.25 (Gercek, 2007):

Table 3.1: Recommendation for Poisson's ratio classification (Gercek, 2007)

Very low	$0 \leq \nu < 0.1$
Low	$0.1 \leq \nu < 0.2$
Medium	$0.2 \leq \nu < 0.3$
High	$0.3 \leq \nu < 0.4$
Very high	$0.4 \leq \nu < 0.5$

2.3.3.3 Numerical Method and Model Setup

The 3-D boundary element displacement discontinuity model is used to investigate stress perturbation around normal faults assuming fault geometrical information presented in Table 3.2, rock mechanical properties mentioned in table 3.1, and boundary conditions depicted in Figure 3.7. The effect of fault dimensions, burial depth, mechanical properties, and multiple successive normal faults on tension generation are considered. Different spacing to height ratios were used, but the height to length aspect ratio is kept constant equal to 1. To examine the effect of buried depth on fault slip, a reference case was set at 3.4 km depth (according to stratigraphic column in Figure 3.6) and another case of 6.8 km was analyzed as well. A reference case for Poisson's ratio was used ($\nu = 0.25$), and extreme cases of $\nu = 0.05$, $\nu = 0.1$ and $\nu = 0.4$ were examined as well. Remote total horizontal stresses were assumed to be isotropic equal to pore pressure, which was assumed to be 60% of the total overburden (Davatzes *et al.* 2005). Lithostatic loading as well as horizontal remote stresses were assumed to increase linearly by the depth. Here after, all contour graphs depict effective stress distributions (otherwise

mentioned), so regions which experience effective tensile stress distribution show the possibility of extensional fracture propagation.

Table 3.2: Fault Geometry Information

Shape	Square, Rectangular
Strike length	1000, 2000 m
Height	1000, 2000 m
Dip Angle	50^0
Element Size:	$\mathbf{25 \times 25}$ m

Table 3.3: Mechanical Properties for the Rock

Shear Modulus	12.0 GPa
Poisson's Ratio	0.05, 0.1, 0.25, 0.4
Density	2300 Kg/m3
Coulomb Friction Coefficient	0.6

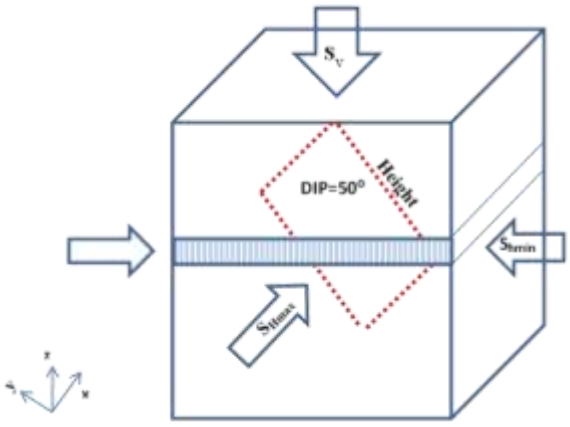

Figure 3.7: Boundary conditions considered for modeling normal faults.

2.3.4 Results and Discussion

2.3.4.1 Effect of Mechanical Properties

Because joints extend about hundreds of meters away from the strike of normal faults in the case study area, the induced stress distribution was calculated on a plane parallel to the fault and 50 meters offset into the hanging wall. Figures 3.8-a and 3.8-b represent the distribution of the fault-strike-parallel stress, σ_{xx}, assuming Poisson's ratio of ν=0.25 and ν=0.1, respectively. Figures 3.9-a and 3.9-b depict the fault-strike-parallel stress, σ_{yy}. Tick marks in figures (3.8 and 3.9) represent the horizontal projection of the direction of maximum compressive stress or minimum tensile stress onto the calculation plane. When the tickmarks on the plot are "vertical", that indicates fault-perpendicular stress is the least compressive (or most tensile). When the tickmarks are horizontal, then the fault-parallel is least compressive (or most tensile). Horizontal thickmarks implies the possibility of fault-strike-parallel joint development and vertical thickmarks implies fault-strike-perpendicular joint development. Figure 3.8-a shows that normal slip causes tensile fault-parallel stress above 3800 ft (the middle depth of the fault) and compressive stress below in hanging-wall. It is only at the depth corresponding to the very top of the fault that the stress change is enough for the tickmarks to become strike-parallel. Lowering Poisson's ratio from 0.25 to 0.1 significantly decreases the magnitude of the fault parallel stress, but there is still enough stress change to cause the trajectories to roll over. However, Fault-strike-perpendicular stress distribution is slightly affected by mechanical properties as depicted in Figures 3.9-a and 3.9-b. Both Figures 3.8 and 3.9 show joint orientation is dependent on its vertical position with respect to the fault. During the next 6 figures, the effect of Poisson's ratio on the possibility and orientation of joint development will be considered by representing stress distribution on horizontal observation plane cutting the fault in different depths.

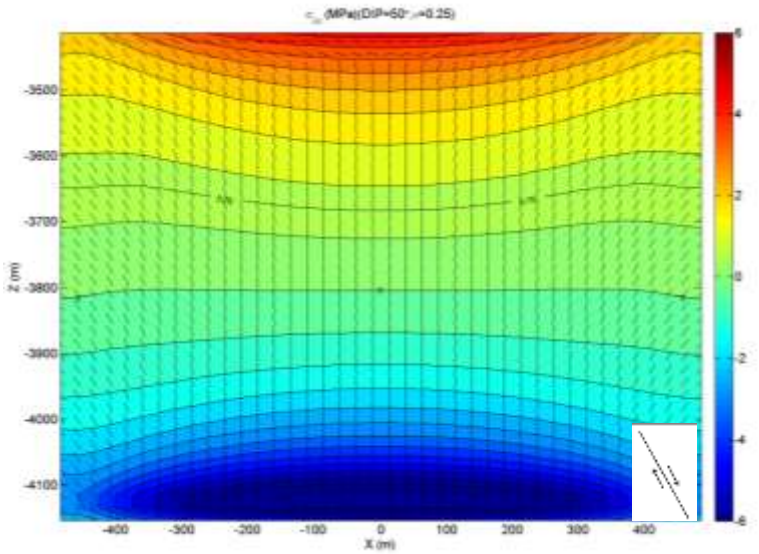

3.8-a: v=0.25

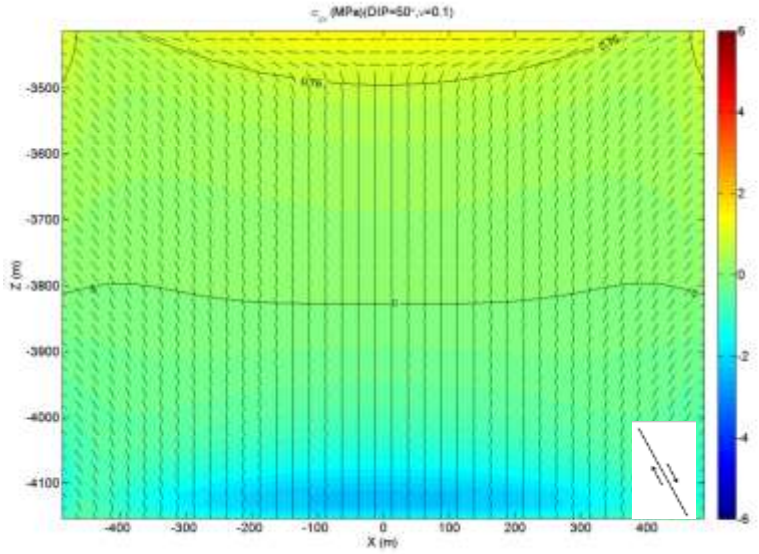

3.8-b: v=0.1

Figure 3.8: Effect of mechanical properties on fault-strike-parallel stress distribution on a plane parallel to the fault and 50 meters offset into the hanging wall

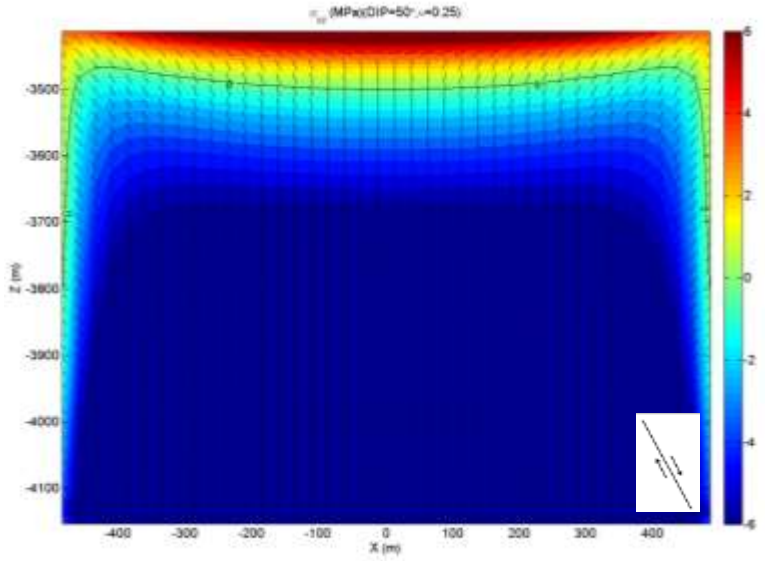

3.9-a: v=0.25

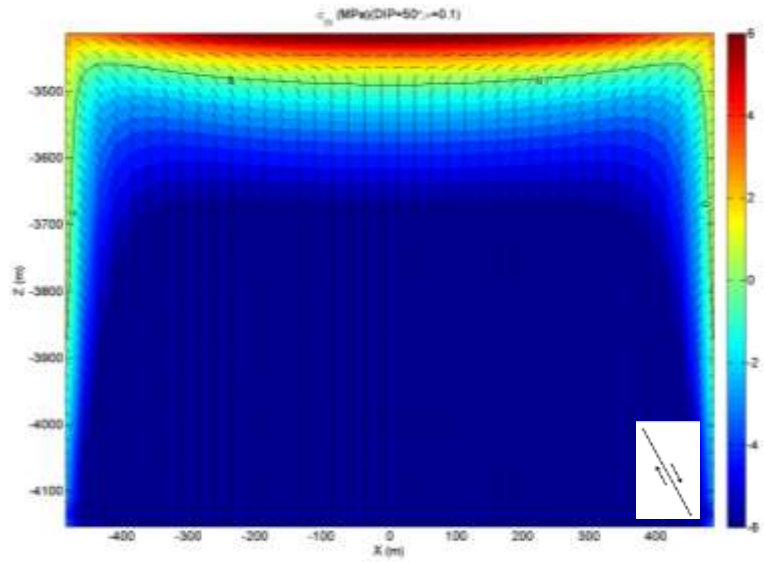

3.9-b: v=0.1

Figure 3.9: Effect of mechanical properties on fault-strike-perpendicular stress distribution on a plane parallel to the fault and 50 meters offset into the hanging wall

Figures 3.10-a & b depict map-view of fault-strike-parallel stress distribution, σ_{xx}, and projection of trajectories on the horizontal plane of observation 100 meters below the upper tip-line, *Z=-3500 m*, assuming $\nu = 0.4$ and 0.25 respectively. Horizontal ticmarks represent joint strike would form perpendicular to the fault strike and vertical ticmarks shows the possibility of fault-strike-parallel joint development. Figures show the possibility of joint extension a few hundreds of meters away from the fault with orientation perpendicular to the fault strike, especially for greater the value of Poisson's ratio (Figure 3.10-a). This relatively thick zone is adjacent to the upper part of the fault in hanging-wall (or lower part of the fault in footwall) and locates below the narrow zone of stress concentration which joints development would form parallel to fault strike. Figures 3.11-a,b depict fault-strike-perpendicular stress σ_{yy}. Figures 3.10 and 3.11 show both fault-parallel and fault-perpendicular stress distribution are affected by mechanical properties; Increasing in ν results significant increase in the magnitude of the fault-parallel and fault-perpendicular stresses and widens the area under tension.

Figure 3.12-a,b depict fault-strike-perpendicular stress distribution on a plane *25 m* below the upper tip-line of fault, *Z=-3425 m*, assuming $\nu = 0.25$ and 0.1 respectively. Figures show fault-strike-parallel joint development in a zone of tensile stress concentration adjacent to the upper tip-line is very likely and mechanical property doesn't significantly affect fault-strike-perpendicular stress concentration. Figure 3.13-a and 3.13-b represent fault-strike-parallel stress distribution along the same plane. Fault-parallel stress has less concentration compared with fault-perpendicular stress, and mechanical property is more effective on fault-strike-parallel stress distribution. Extensive magnitude of fault-perpendicular tensile stress concentrated around upper and lower tip-lines would explain why fault-parallel joints are more common.

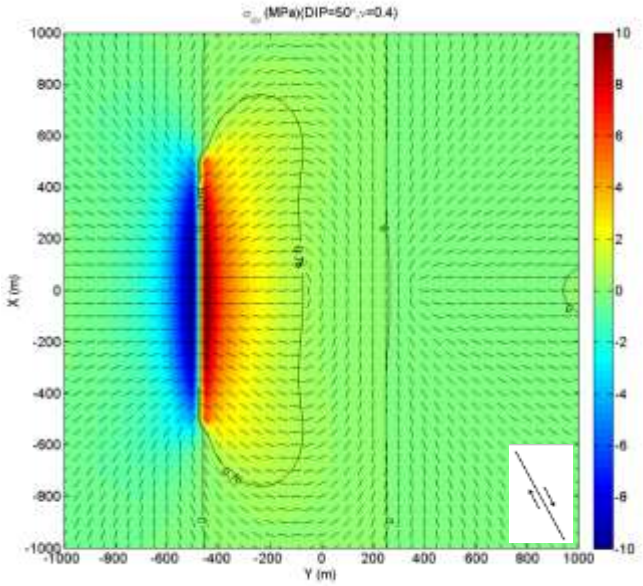

3.10-a: v=0.4

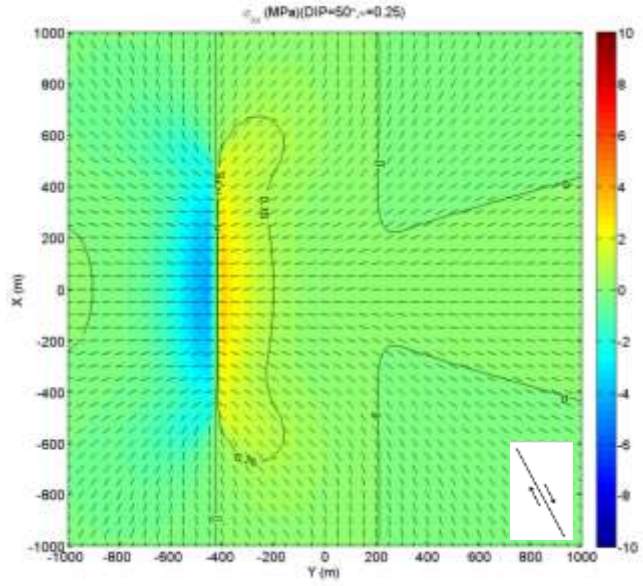

3.10-b: v=0.25

Figure 3.10: Effect of mechanical properties on fault-strike-parallel stress distribution on a horizontal plane of observation, Z=-3500 m.

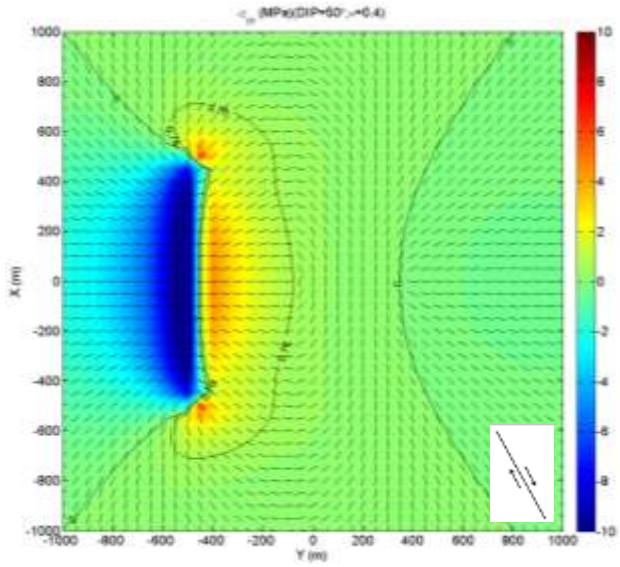

3.11-a: ν=0.4

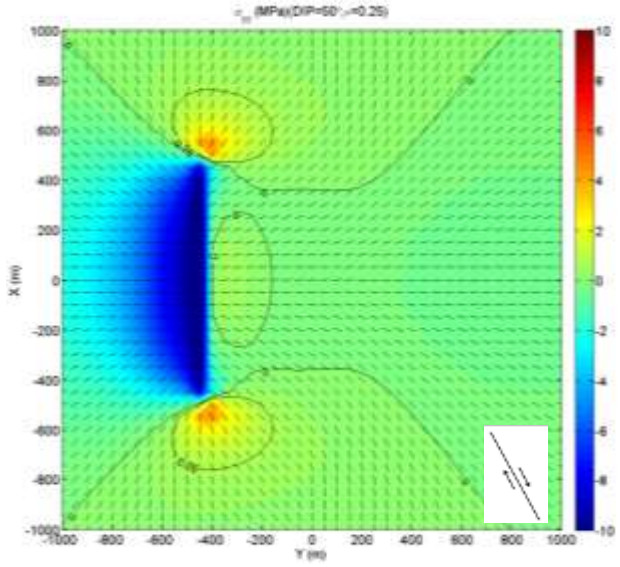

3.11-b: ν=0.25

Figure 3.11: Effect of mechanical properties on fault-strike-perpendicular stress distribution on a horizontal plane of observation, Z=-3500 m.

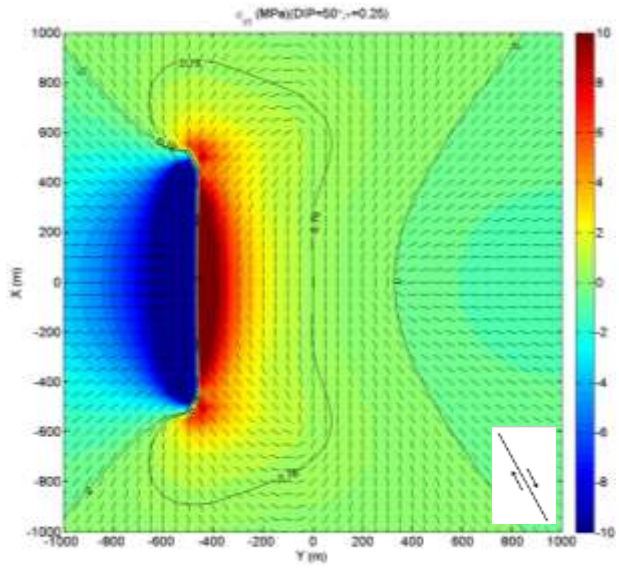

3.12-a: v=0.25

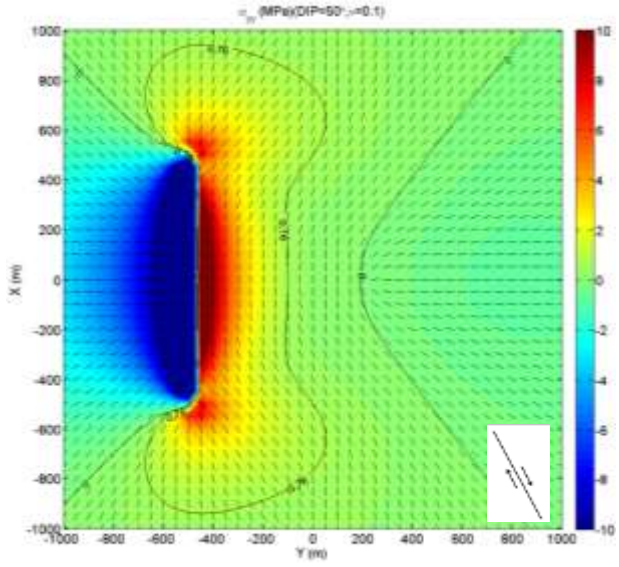

3.12-b: v=0.1

Figure 3.12: Effect of mechanical properties on fault-strike-perpendicular stress distribution on a horizontal plane of observation, Z=-3425 m.

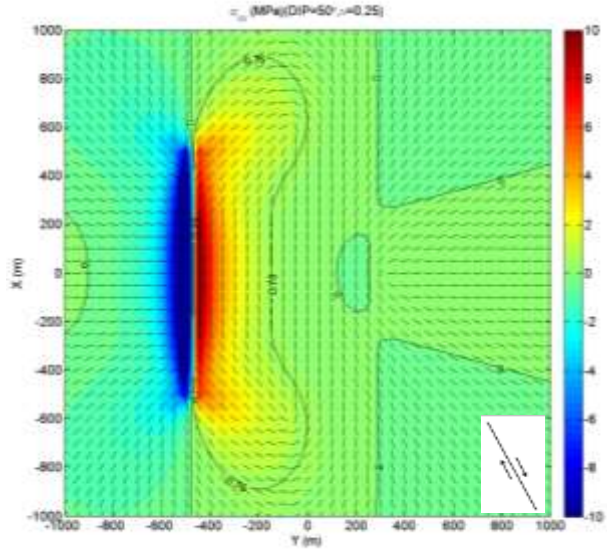

3.13-a: ν=0.25

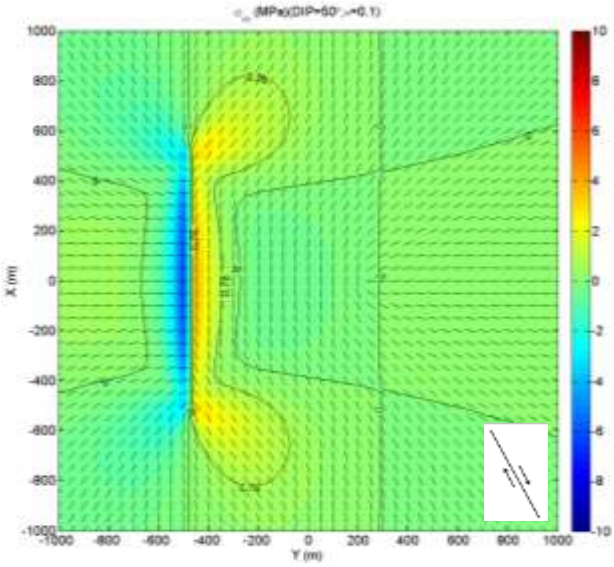

3.13-b: ν=0.1

Figure 3.13: Effect of mechanical properties on fault-strike-parallel stress distribution on a horizontal plane of observation, Z=-3425 m.

Area adjacent to upper (or lower) part of the fault is not the only zone that fault-strike-parallel stress might be generated in a restively broad zone. Figure 3.14-a shows how mid-depth fault-strike-parallel tension would be generates around an isolated fault. Figures 3.14-a, b depict the

effect of Poisson's ratio on fault-strike-parallel stress distribution along a horizontal plane of observation small distance above the fault center assuming $\nu = 0.1$ and 0.25 respectively. Figures 3.14-a, b convey Poisson's ratio significantly changes the pattern of mid-depth fault-strike-parallel tensile stress distribution. Significantly broader area of tension is generated with lower Poisson's ratio ($\nu = 0.1$). Contrary to Figure 3.14-a, Figure 3.14-b shows using medium value of Poisson's ratio ($\nu = 0.25$), only a narrow zone adjacent to the fault experiences fault-parallel tension. Figure 3.15-a and b depict the effect of mechanical properties on fault-strike-perpendicular stress distribution on the same plane. In contrast with fault-strike-parallel stress distribution, Figures 3.15-a, b show mechanical property doesn't change the pattern of fault-strike-perpendicular stress distribution pattern, although increasing in Poisson's ratio magnifies its magnitude.

Lateral process zones or areas right ahead of lateral tip-line of the fault are another area of tensile stress concentration as depicted in Figures 3.15-a and 3.15-b. Within lateral process zones, trajectories are almost fault-parallel which means joints would form parallel to the fault strike and may provide a mechanism of fault elongation (lateral propagation) and shear failure promoted by extensional fractures (this mechanism was described before and schematically was depicted in Figure 3.1-c).

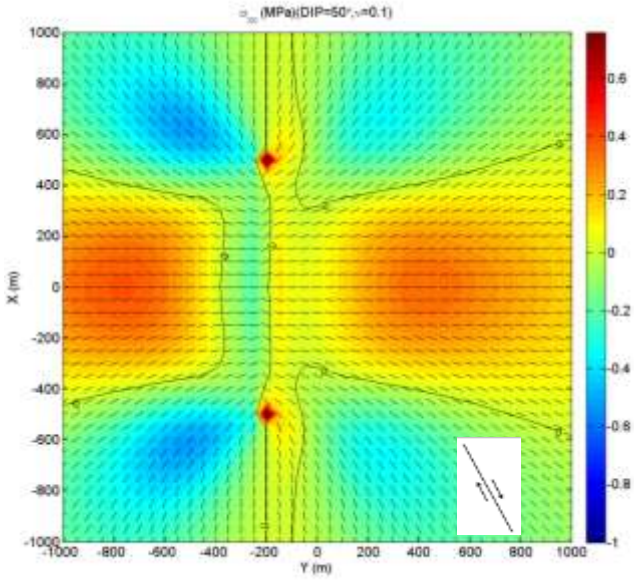

3.14-a: v=0.1

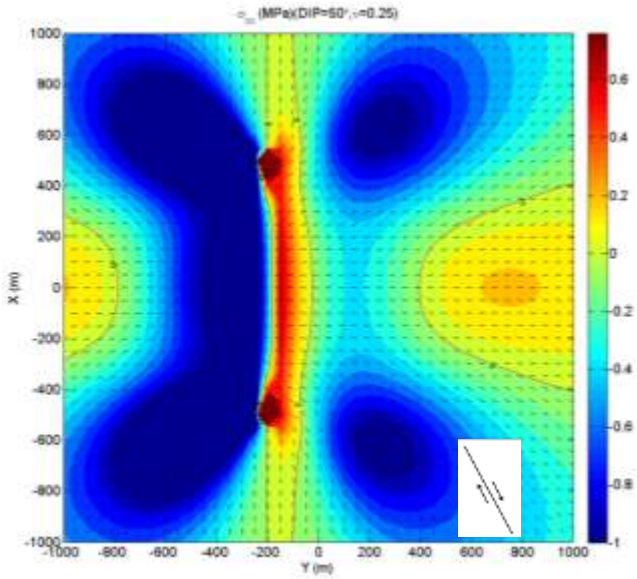

3.14-b: v=0.25

Figure 3.14: Effect of mechanical properties on fault-strike-parallel stress distribution on a horizontal plane of observation small distance above the fault center, Z=-3755 m**.**

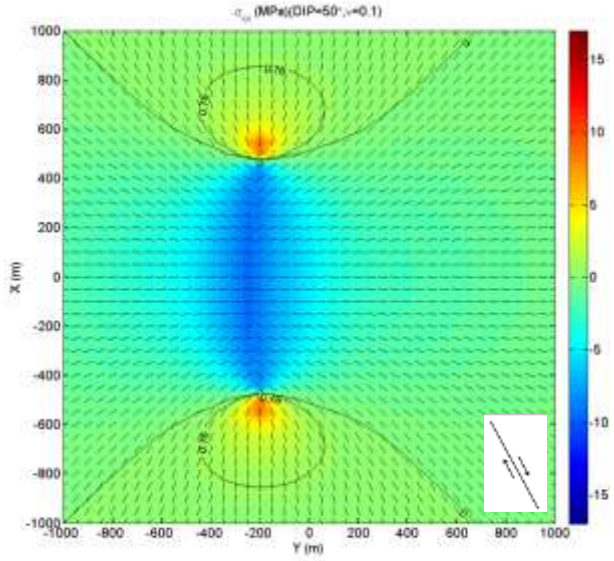

3.15-a: v=0.1

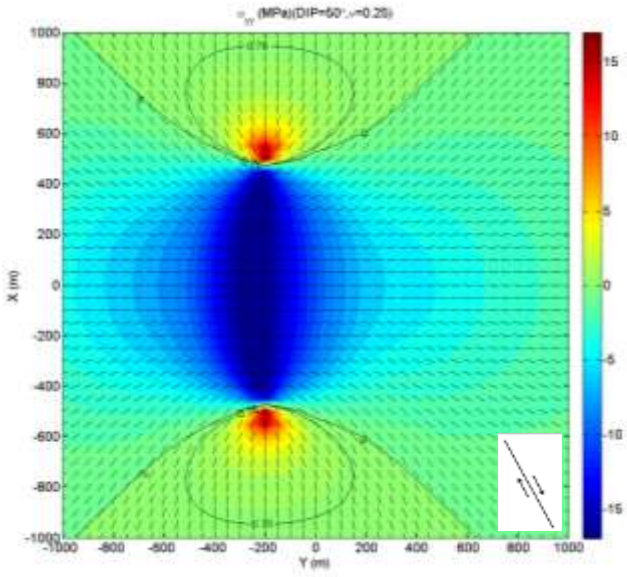

3.15-b: v=0.25

Figure 3.15: Effect of mechanical properties on fault-strike-perpendicular stress distribution on a horizontal plane of observation small distance above the fault center, Z=-3755 m.

2.3.4.2 Effect of Fault Height

Fault slip is proportional to the deference of overburden and minimum horizontal stress magnitudes, and increases with depth assuming all remote stresses are linearly dependent on depth. Therefore increasing in depth should increase slip movement on the surface of the fault and magnifies stress perturbation around the fault. Figure 3.16-a & b represent the effect of fault height on fault-strike-parallel stress distribution on the plane parallel to the fault and 50 meters offset into the hanging wall. Poisson's ratio equals 0.1 for both cases. Both faults are square but dimension of the first fault (Figure 3.16-a) is two times of the second one (Figure 3.16-b). Comparing these two figures shows that fault-parallel stress distribution increases by a factor of 2 and is proportional to fault height. Figures 3.17-a and 3.17-b show the effect of fault height on fault-strike-parallel stress distribution along a horizontal observation plane small distance above the fault center for aforementioned faults. Comparing Figures 3.17-a and 3.17-b shows fault-strike-parallel stress is proportional to fault depth as well.

2.3.4.3 Effect of Burial Depth

Figure 3.18-a and 3-18-b show fault-strike-parallel stress distribution on different plane of observation. The plane of observation is parallel to the fault and 50 meters offset into the hanging wall for Figure 3.18-a, and is a horizontal plane small distance above the fault center for Figure 3.18-b. Poisson's ratio equals 0.1 for both cases and buried depth is 6.8 km (two times of the buried depth used in Figures 3.16 and 3.17). Comparing Figure 3.18-a with 3.18-a, and Figure 3.18-b with Figure 3.17-a confirms that buried depth affects the perturbation of stress filed around a normal fault in the same manner as fault height does. It can be inferred that development of joints at the vicinity of normal faults would be more likely to be observed around taller and deeper faults.

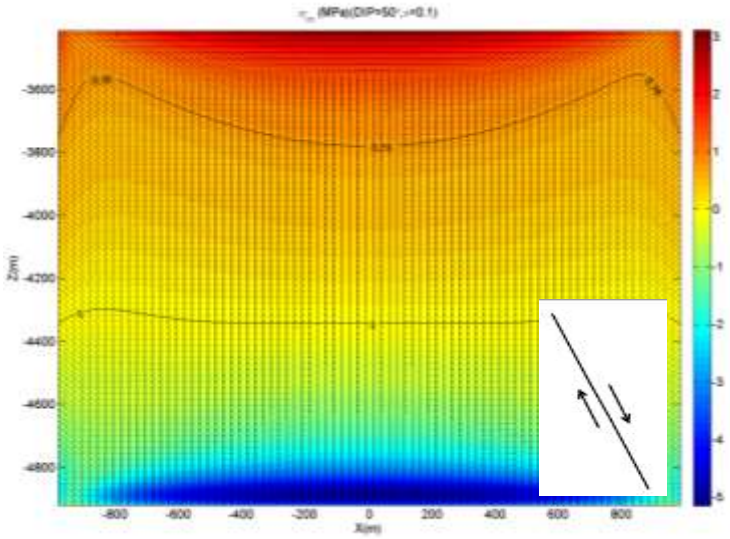

3.16-a: Height = Length = 2 km

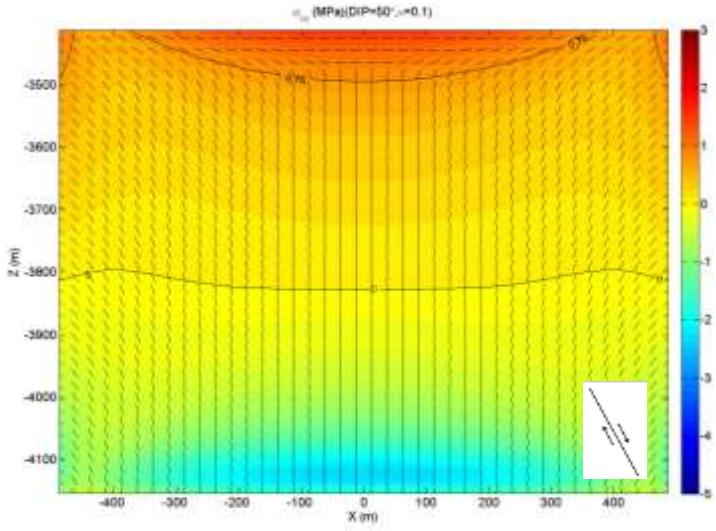

3.16-b: Height = Length = 1 km

Figure 3.16: Effect of fault dimensions on fault-strike-parallel stress distribution on the plane parallel to the fault and 50 meters offset into the hanging wall

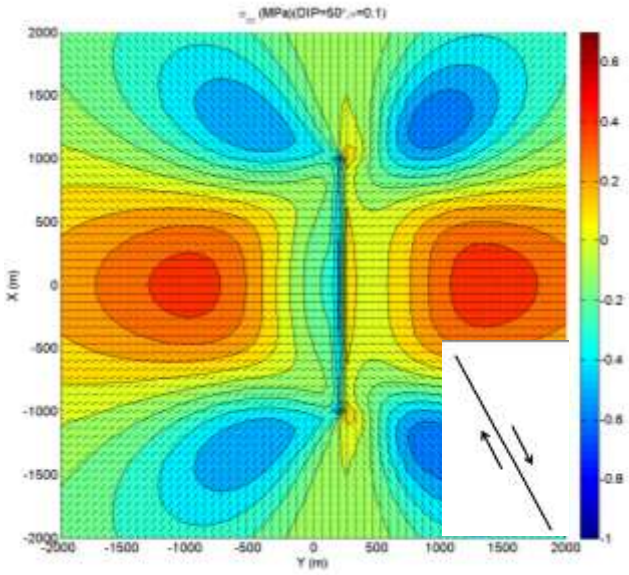

3.17-a: Height = Length = 2 km, Z=-4250 m

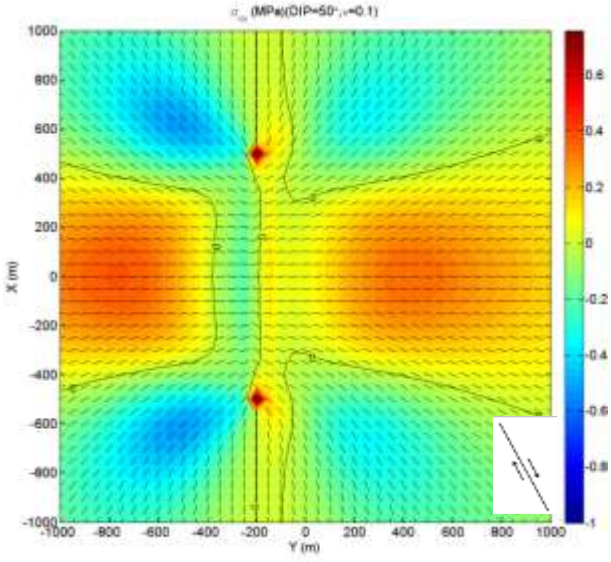

3.17-b: Height = Length = 1 km, Z=-3755 m

Figure 3.17: Effect of fault dimensions on fault-strike-parallel stress distribution on a horizontal plane of observation small distance above the fault center.

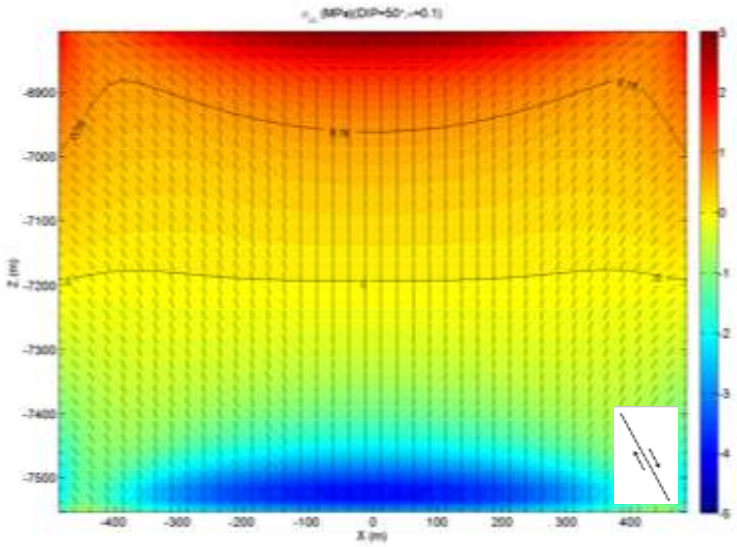

3.18-a: Fault-strike-parallel stress distribution on a plane parallel to the fault and 50 meters offset into the hanging wall

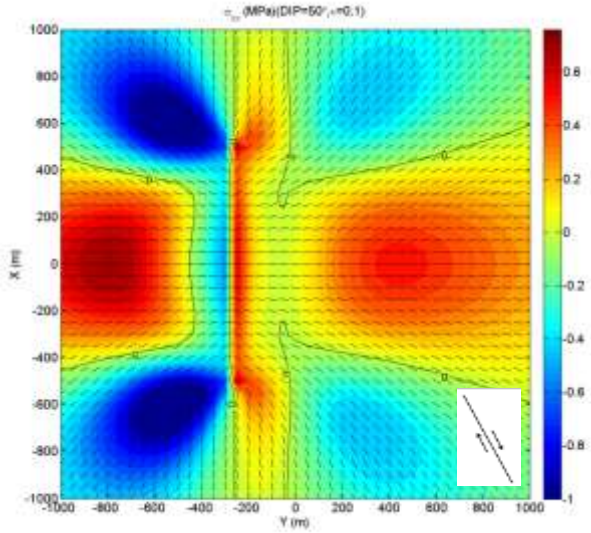

3.18-b: Fault-strike-parallel stress distribution on a horizontal plane of observation small distance above the fault center, Z=-7150 m

Figure 3.18: Effect of buried depth on fault-strike-parallel stress distribution. Buried depth = 6.8 km, two times of the reference case.

2.3.4.4 Effect of Fault Interaction

As discussed before, Figures 3.14-a, 3.17-a and 3.18-b show for low value of Poisson's ratio ($\nu = 0.1$), a broad area of tension at mid-depth is generated in both hanging-wall and foot-wall of an isolated normal fault. The magnitude of tension increases by increasing in fault height or buried depth. Comparing Figures 3.17-a and 3.17-b show the maximum tensile stress in both side of the fault occurs in a distance proportional to the fault height from the fault strike. This conveys that successive parallel fault interaction should intensify tensile stress distribution in this zone. Figures 3.19-a, b examine the optimum distance between two parallel normal faults that causes increasing in the fault-strike-parallel tensile stress distribution. Buried depth is assumed to be 6.8 km, ν=0.1, and the length of square fault is 1.0 km (same condition as the case represented in Figure 3.18-b). The spacing between normal faults is 750m and 500m in Figures 3.19-a and 3.19-b respectively. Comparing Figure 3.19-a with Figure 3.19-b shows the optimized distance is about three quarters of 1 fault height. This distance between normal faults increase the magnitude of fault-strike-parallel or fault-strike-perpendicular stresses about 50 % compared with isolated fault (Figure 3.18-b). Increasing in spacing more than 1 fault height results in decreasing in interaction between adjacent faults. Fault-strike-perpendicular stress distribution for these two configuration of normal faults are depicted in Figures 3.20-a and 3.20-b respectively. Compressive stress adjacent to faults is magnified for both cases compared with the single fault (Refer to Figure 3.15-a). The magnification is due to the combined effect of increasing in overburden in terms of buried depth as well as fault interaction. Tensile stresses around fault tips are intensified making a relatively big influenced area outside of their tips where joint would form sub-parallel to the fault strike. The process of fault-parallel joint development in these zones might occur repeatedly as the fault grows, making a configuration of parallel joints and normal fault. This mechanism is related to stress concentration around lateral tip-line of faults. Comparing Figure 3.20-a and b with the case of single fault shown in Figure 3.15-a and b suggests that the stress concentration adjacent to lateral tips is intensified by interaction between normal faults, but is less influenced by mechanical properties

Figure 3.21-a and 3.21-b show fault-strike-parallel and fault-strike-perpendicular stress distribution due to for a combination of three faults. Figure 3.21-a shows combination of three successive parallel faults increases tension in both sides of the middle fault. The longer the array of successive parallel normal faults, the broader the area of fault-strike-parallel tension. Number of faults and spacing between faults in the controls the length of the array, and the length of fault dictates the width of the array. Distribution of tensile stress in such a big zone suggests a mechanism of joint development due to overburden acting on a series of normal faults. Another interesting stress distribution pattern is depicted in Figure 3.21-b showing fault-strike-perpendicular stress everywhere outside of the array is tensile providing a mechanism for cross-joint development. While fault-parallel joints would form ahead of fault tips outside of this array during lateral growth of faults, joints would extend perpendicular to the fault strike in a zone

inside of the array resulting in cross-joints configuration development. Fault-parallel joint development between normal faults would increase fault-perpendicular tensile stress inside the array and helps fault-strike-perpendicular joint development (Bai *et al.* 2002; Olson, 2007).

Further decreasing in Poisson's ratio results in higher level of fault-strike-parallel tensile stress distribution inside the array; Comparison between Figure 3.22-a and 3.22-b shows tensile stress in this zone increases up to 33% by decreasing Poisson's ratio from 0.1 to 0.05. Comparing Figure 3.22-b with the reference case (Figure 3.14-a) shows by decreasing Poisson's ratio from 0.1 to 0.05, doubling the buried depth (from 3.4 km to 6.8 km), and doubling fault height and length from 1.0 km to 2.0 km, the magnification factor exceeds 6.0.

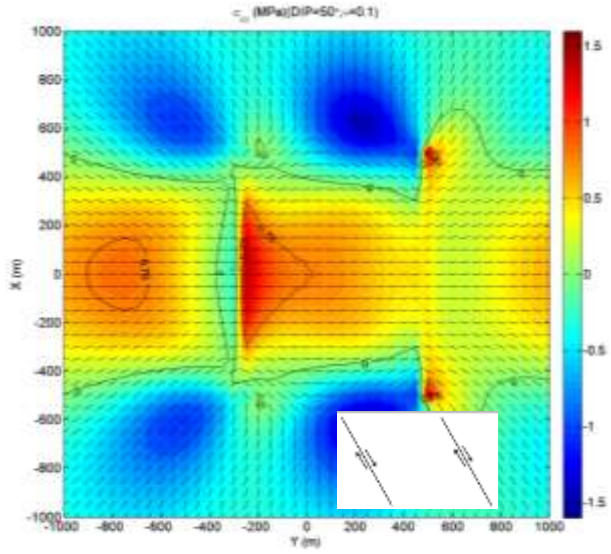

3.19-a: Distance between normal faults equals three quarters of 1 fault height

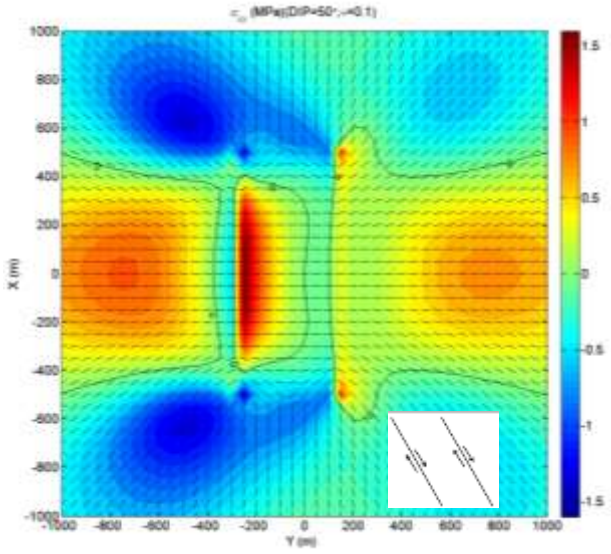

3.19-b: Distance between normal faults equals half of 1 fault height

Figure 3.19 Effect of Interaction between successive parallel normal faults on fault-strike-parallel stress distribution (ν=0.1, buried depth=6.4 km, fault height=1.0 km).

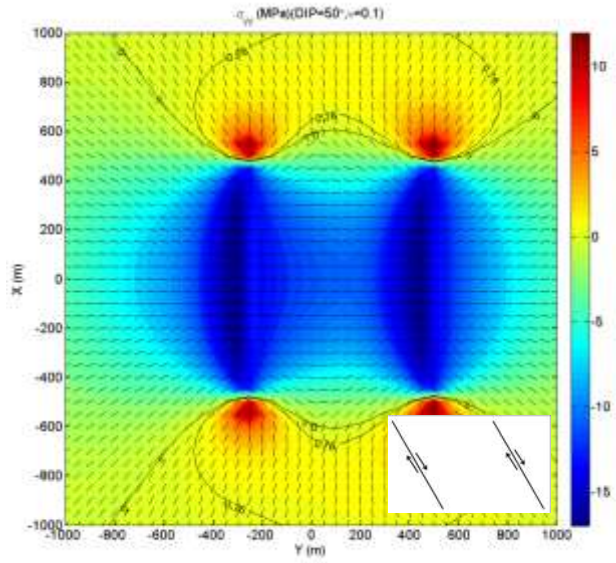

3.20-a: Distance between normal faults equals three quarters of 1 fault height

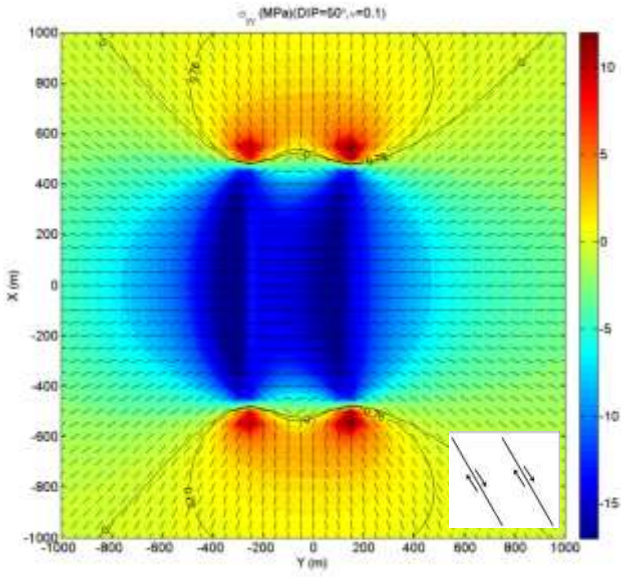

3.20-b: Distance between normal faults equals half of 1 fault height

Figure 3.20: Effect of Interaction between successive parallel normal faults on fault-strike-perpendicular stress distribution (ν=0.1, buried depth=6.4 km, fault height=1.0 km).

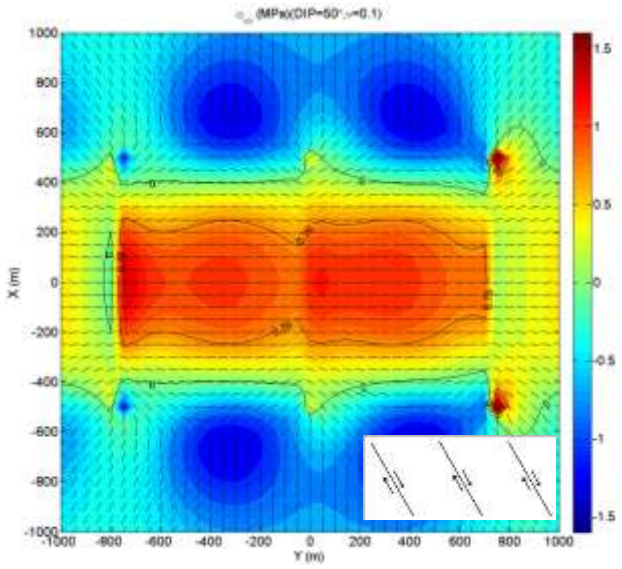

3.21-a: Fault-strike-parallel stress distribution.

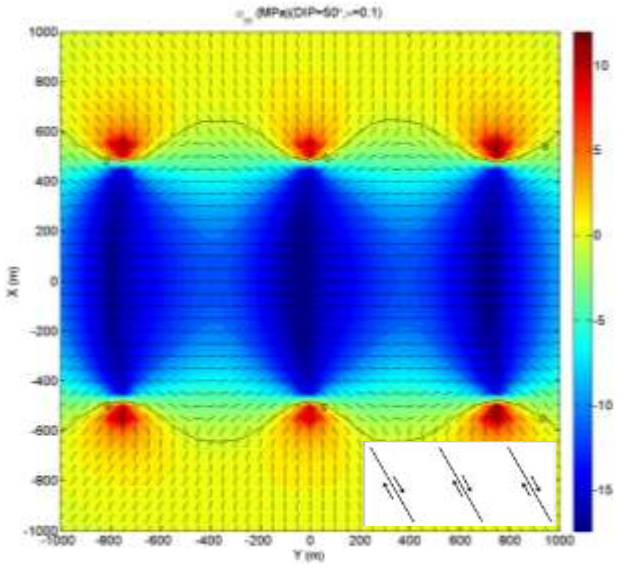

3.21-b: Fault-strike-perpendicular stress distribution

Figure 3.21: Stress perturbation inside and outside of an array of successive parallel normal faults (ν=0.1, buried depth=6.4 km, fault height=1.0 km).

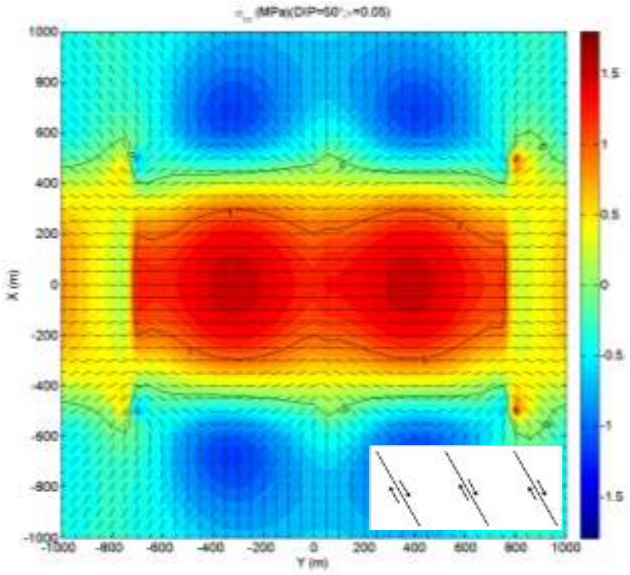

3.22-a: Fault height=fault length=1.0 km

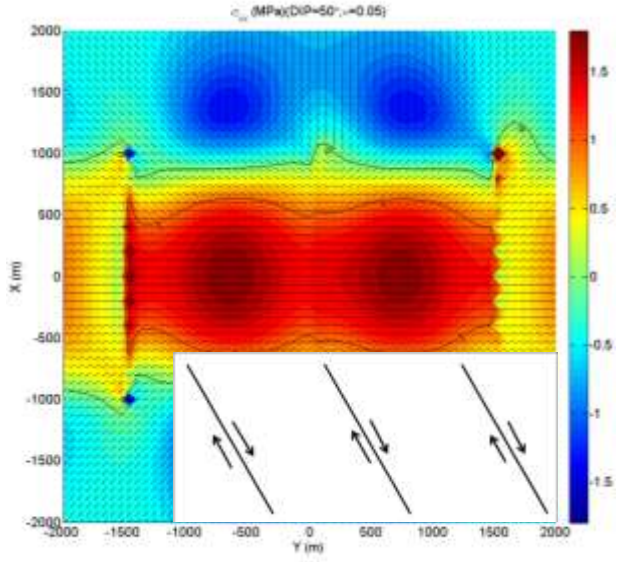

3.22-b: Fault height=fault length=2.0 km

Figure 3.22: Array of successive parallel normal faults and fault-strike-parallel tensile stress distribution inside the array (ν=0.05, buried depth=6.4 km).

2.3.4.5 Effect of Horizontal Remote Stresses

All contours mentioned before represented effective stress distribution assuming internal fluid pressure in joints approaches S_{hmin} and the state of remote stress was isotropic. In fact, isotropic remote stress condition is rare in the nature especially in the normal faulting regime. Davatzes *et al.* (2005) compared fault throw measurements with calculated values obtained from the numerical modeling and estimated differential remote stresses as 5.0 MPA at the time of faulting in Rough and Rocky Mesa.

Figure 3.23-a and 3.23-b show σ_{yy} (fault-strike-perpendicular stress) and σ_{xx} (fault-strike-parallel stress) distribution along a horizontal observation plane a small distance below the upper tip-line. Fault-parallel differential compressive remote stress doesn't resolve on the surface of the fault and therefore doesn't affect fault slip. It only reduces σ_{xx} (tension is positive). Difference between σ_{yy} and σ_{xx} for a point locates 200m away from the fault strike (shown in Figures 3.23-a & b) is about 4.0 MPa (σ_{yy}-σ_{xx} ≈4.0 MPa). Fault-parallel differential compressive remote stress (equals 5.0 MPA) doubles that difference; therefore, it neither affects stress trajectories, nor reduces σ_{xx}. That means fault-parallel joints would develop adjacent to the top and bottom tip-line of faults and up to few hundreds away from the fault strike regardless of the magnitude of differential compressive remote stress. That might explains why fault-parallel joints are commonplace.

Figure 3.24-a and b depict σ_{xx} and σ_{yy} stress distribution along a horizontal observation plane 100 m below the upper front of the fault where the effect of stress concentration is attenuated. Trajectories show the possibility of fault-perpendicular joint development around the normal fault. However, the difference between σ_{xx} and σ_{yy} for the same point is about σ_{xx}-σ_{yy} =1.16 MPa, means small value of fault–parallel differential compressive remote stress more than 1.16 MPa removes the fault-parallel tension and changes the direction of trajectories. That means fault-perpendicular joint development few hundreds away from the fault strike in layers at depth comparable to upper part of normal faults in hanging-walls (or lower part in footwalls) is not very likely, as small value of induced fault-perpendicular tensile stress and trajectories are very sensitive to fault–parallel differential compressive remote stress. On the other hand, stratigraphic column depicted in Figure 3.7 supports the assumption of joint generation in a level about 100 m below the upper tip-line of normal faults. If we accept this assumption, then according to the numerical modeling, we would conclude the isotropic state of stress in Rough and Rocky Mesa at the time of jointing.

Figure 3.25-a & b depict σ_{xx} and σ_{yy} stress distribution along a horizontal plane of observation cutting the fault at mid-depth. The magnitude of σ_{xx} and σ_{yy} for the same point are represented in figures. Although fault–parallel differential compressive remote stress of magnitude as small

as 1.0 MPa is enough to remove fault-parallel tension almost everywhere inside the array of normal faults, but a large value of differential remote stress as high as 12 MPA is necessary to change the direction of trajectories. Lack of resultant tensile stress could be compensated with extra pore pressure more than minimum horizontal stress (which even might exceed overburden according to Fyfe *et al.* 1978; Engelder and Fischer, 1996), or other mechanism of joint development such as regional tectonic strains during and subsequent to faulting. It can be concluded that joint development perpendicular to the fault strike is more likely to happen between successive normal faults in mid-depth layers for rocks with low value of Poisson's ratio.

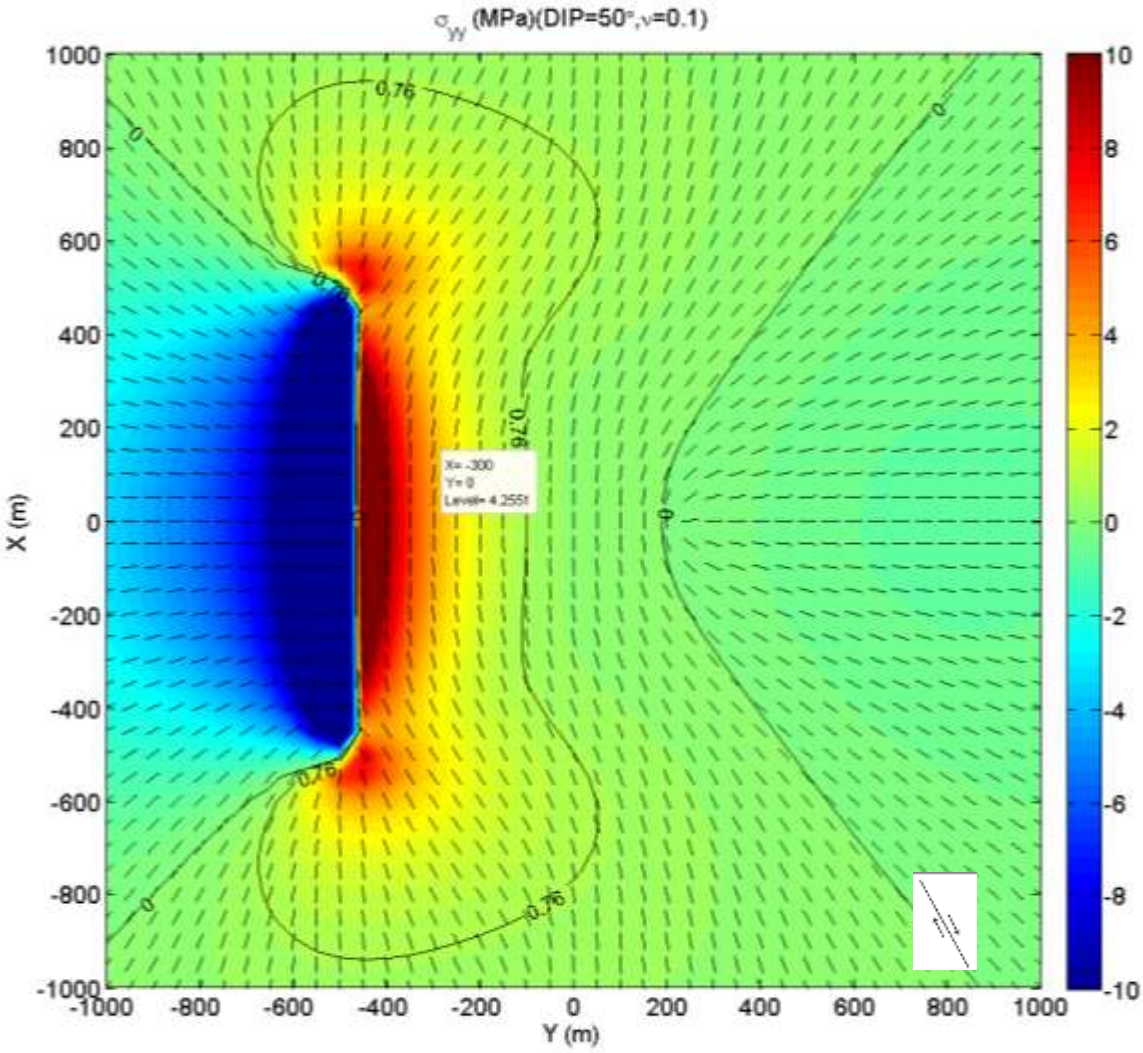

Figure 3.23-a: Fault-strike-perpendicular stress distribution on a horizontal plane of observation small distance below the upper tip-line. Fault-strike-parallel joint development is likely as fault–parallel differential compressive remote stress doesn't affect fault-perpendicualr tensile stress distribution and trajectories around the fault.

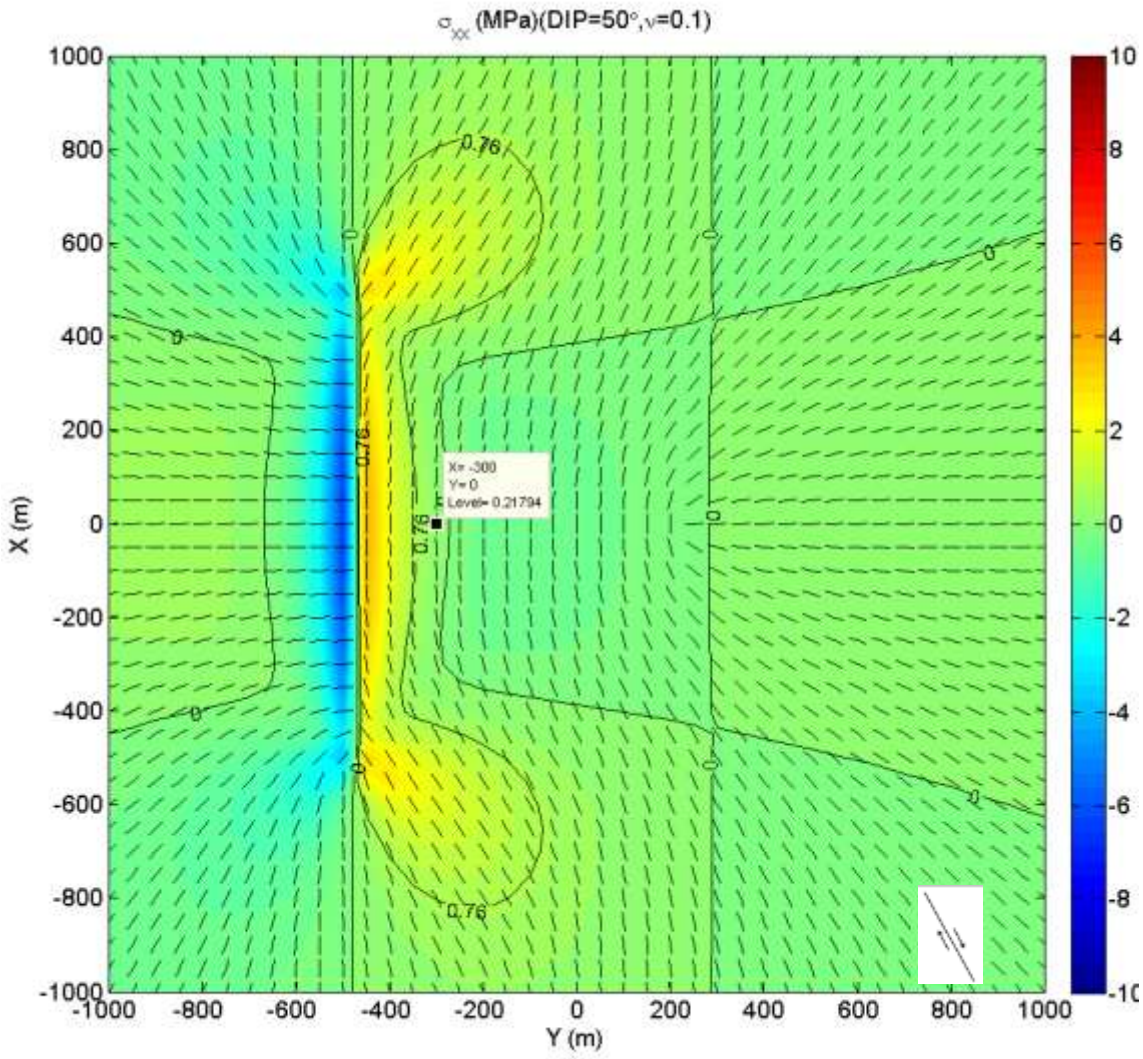

Figure 3.23-b: Fault-strike-parallel stress distribution on a horizontal plane of observation small distance below the upper tip-line

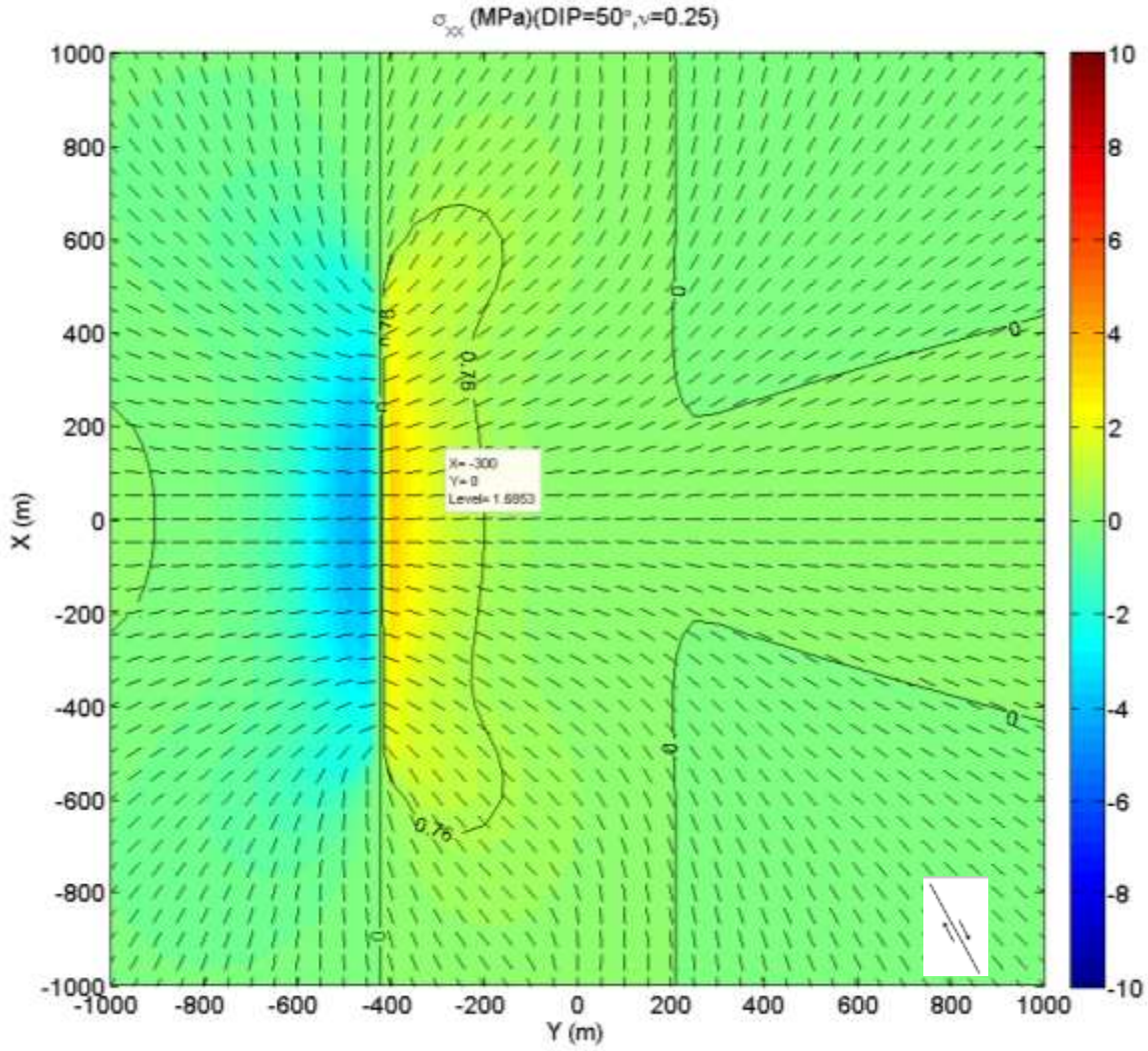

Figure 3.24-a: Fault-strike-perpendicular stress distribution on a horizontal plane of observation 100 m below the upper tip-line. Fault-strike-perpendicular joint development is less likely as fault–parallel differential compressive remote stress affect fault-parallel tensile stress distribution as well as trajectories around the fault.

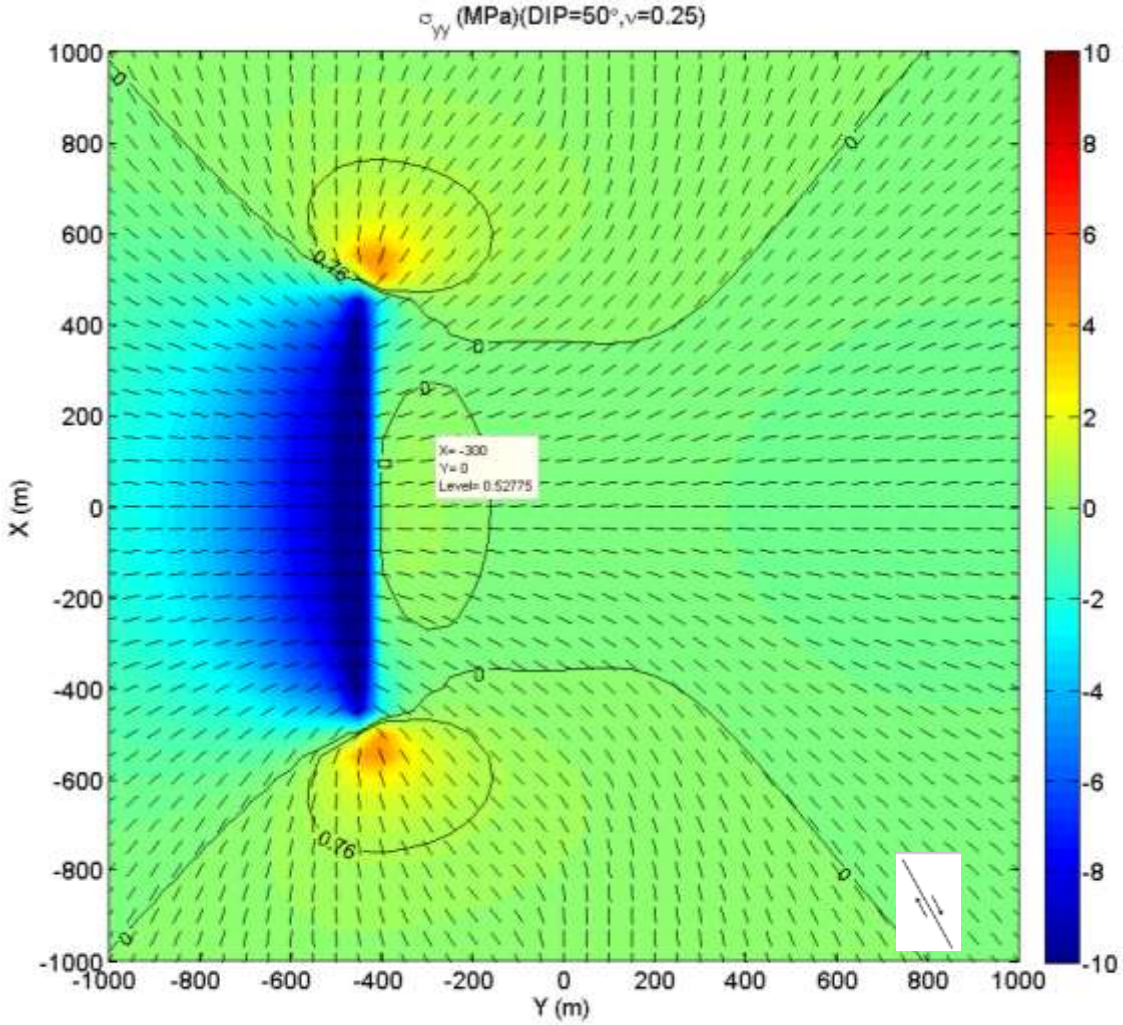

Figure 3.24-b: Fault-strike-parallel stress distribution on a horizontal plane of observation 100 m below the upper tip-line**.**

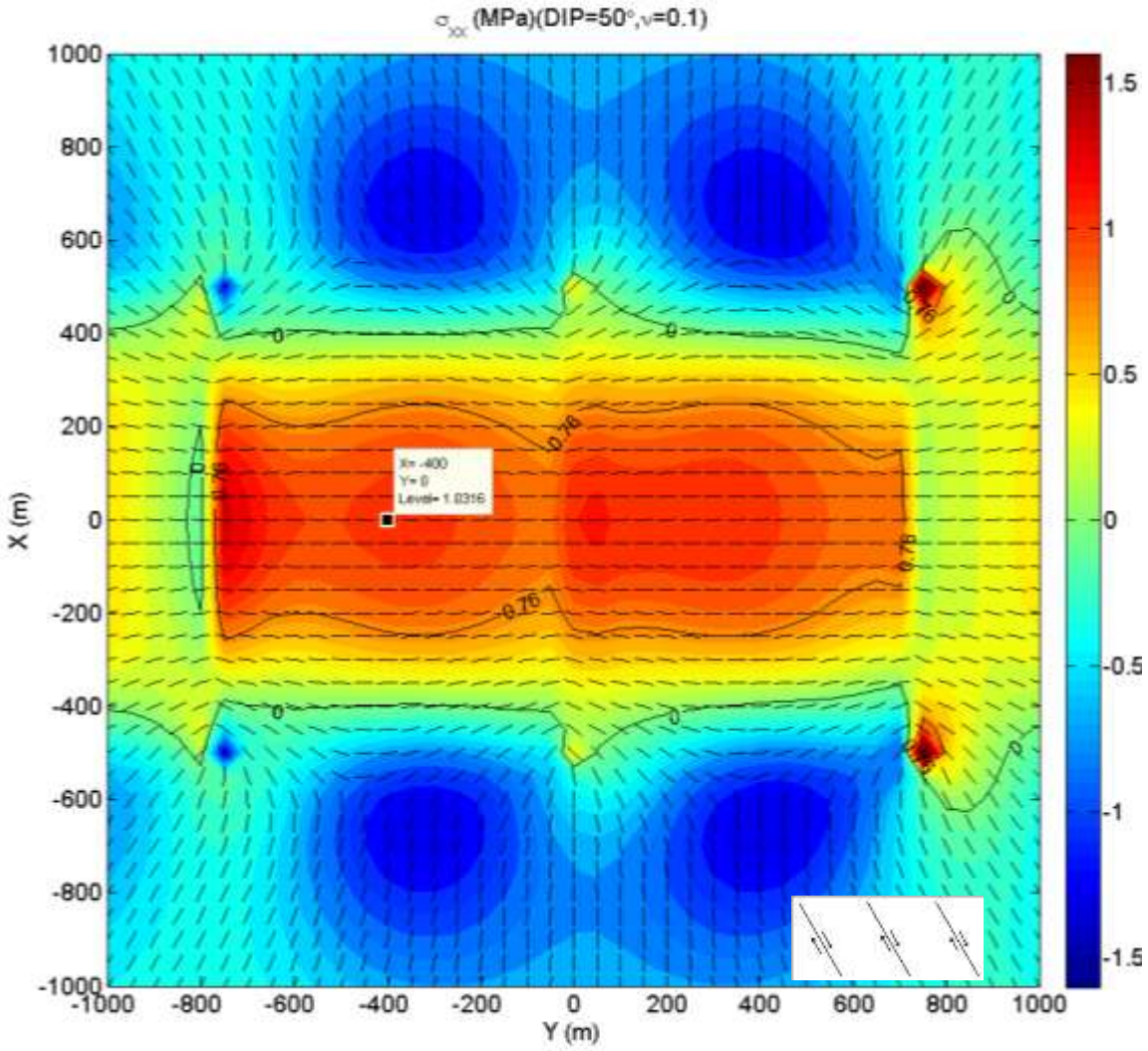

Figure 3.25-a: Array of three successive parallel normal faults and Fault-strike-parallel stress distribution. Fault-strike-parallel joint development is likely inside the array. Trajectories inside the array is unlikely to rotate due to the effect of fault–parallel differential compressive remote stress

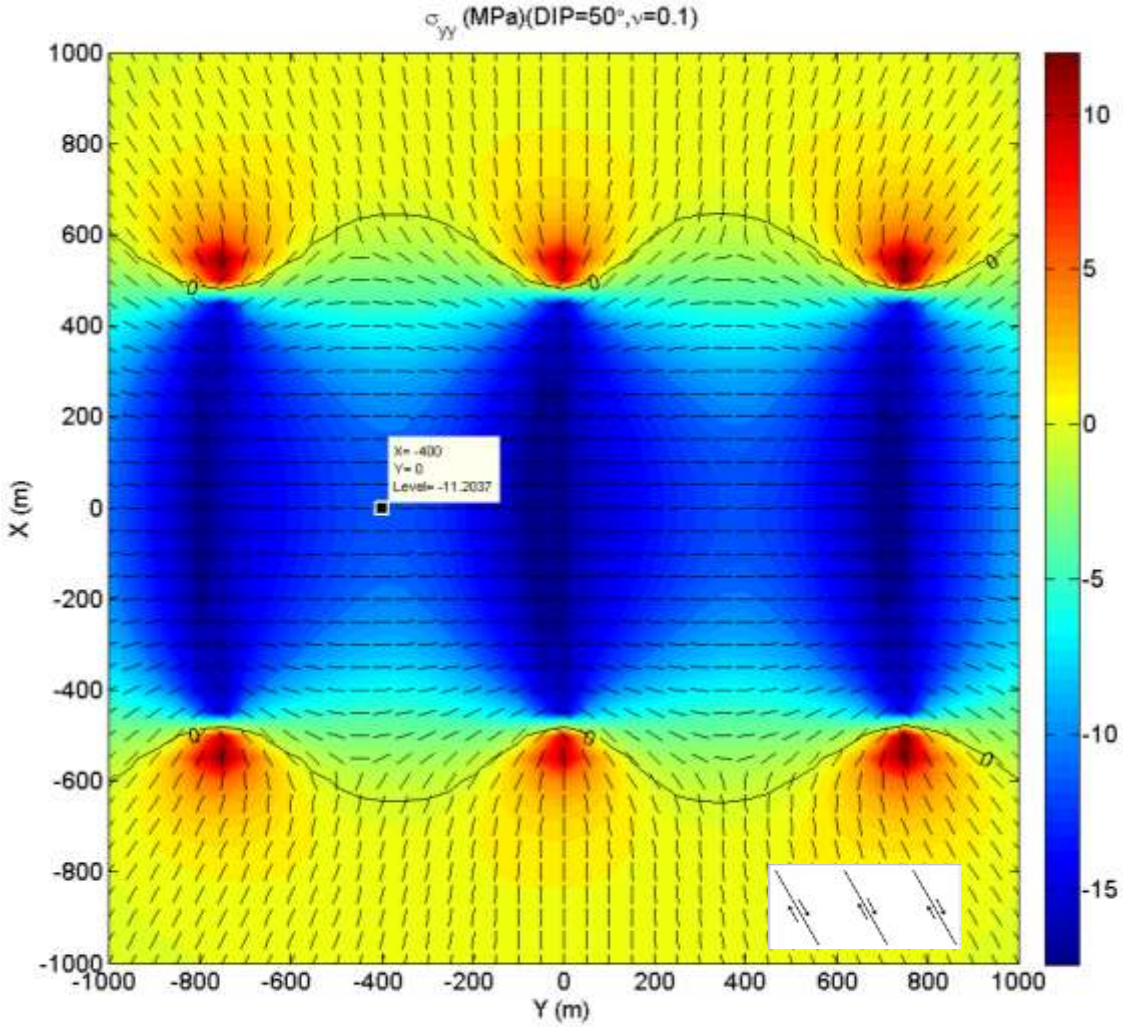

Figure 3.25-b: An array of three successive parallel normal faults and Fault-strike-perpendicular stress distribution. Cross-joints configuration is likely. Trajectories outside the array don't rotate due to the effect of fault–parallel differential compressive remote stress.

2.3.5 Conclusion

Results show joint orientation is dependent on its vertical position with respect to the normal fault. In hanging-wall, normal slip causes fault-parallel tension above the middle depth of the fault and compressive stress below the mid-depth. This distribution flips over in foot-wall. Ignoring lateral tip and regions outside the lateral tips, there is only a narrow layer adjacent to upper tip-line (in hanging wall) and bottom tip-line (in footwall) that experiences fault-perpendicular tensile stress. The magnitude of fault-perpendicular tensile stress around upper or lower tipl-lines is extensive and the corresponding trajectories are parallel to the fault strike. That implies the possibility of fault-parallel joint development at depth comparable to the very top or bottom of the fault; the magnitude of tensile stress and the direction of trajectories are not sensitive to the magnitude of fault-parallel differential compression remote stress. That explains why fault-parallel joints maybe the most probable to occur around normal faults. There is a thicker zone around normal fault below the mentioned layer that fault-parallel tensile stress is distributed but its magnitude is small and is more sensitive to fault-parallel differential compressive remote stress. Mechanical properties significantly affect the pattern of tensile stress distribution. While high value of Poisson's ratio increases the magnitude of both fault-parallel and fault-perpendicular tension around the tip-lines, Low value ($\nu \approx 0.1$) completely changes fault-perpendicular tensile stress distribution pattern in mid-depth along an isolated fault. Low value of Poisson's ratio causes fault-perpendicular tensile stress being distributed in a broad zone which covers both footwall and hanging-wall adjacent to middle part of the fault. The magnitude of the tensile stress in that region is small and very sensitive to even small value of fault-parallel differential compressive remote stress; however, increasing in buried depth, increasing in fault height and the interaction between successive normal faults increase the magnitude of tension. Trajectories inside the array of normal faults are not affected by increasing fault-parallel differential compressive remote stress. This situation suggests a mechanism of opening mode fracture extension in a relatively wide area induced by overburden.

In general, normal fault can cause regional stress rotation, but the generated tension is not enough to exceed compressive remote horizontal stresses except a small zone very close to the fault tip-line. For joint propagation, this deficiency in tension might be compensated with extra pore pressure more than S_{hmin} (or even S_v in normal faulting regime), regional tectonic strains during and subsequent to fault generation or propagation, or fault-perpendicular remote tension induced by bending effects.

2.4 Hydraulic Fracture Height Growth and Non-planar Propagation Paths[3]

2.4.1 Overview

Hydraulic fractures may not necessarily start perpendicular to the minimum horizontal remote stress because of the lack of alignment between the wellbore and the principal stresses, local stress perturbation, or natural fracture adjacent to a horizontal well. The 3-D boundary element displacement discontinuity model is used to explain how fracturing from misaligned horizontal wellbores might results in non-uniform height growth of the hydraulic fracture by evaluating of SIF distribution along the upper front of the fracture. Results show the misalignment affect lateral extension and this nonplanar propagation has an impact on height growth and might result in restriction in fracture height and fracture width.

2.4.2 Introduction

Figure 4.1 shows the ideal alignment of horizontal well and longitudinal hydraulic fracture system where the horizontal well is perpendicular to the minimum remote horizontal stress $S_{hmin} = S_3$ and the wellbore lies in the principal remote stress plane, parallel to $S_{Hmax} = S_2$. However, hydraulic fractures may not necessarily start perpendicular to the minimum horizontal remote stress because of the lack of alignment between the wellbore and the principal stresses, local stress perturbation, or natural fracture adjacent to a horizontal well (Olson, 2008). The geometry of a hydraulic fracture could be further complicated by lateral propagation which is non-planar and height growth that is non-uniform. The non-planarity of the fracture path and its resultant near-wellbore width restriction and excessive treating pressure were considered by Olson (1995) and Olson & Wu (2012) using 2-D and pseudo 3-D displacement discontinuity modeling, respectively. In this section, The effect of misalignment angle on the possibility of irregular height growth as well as fringe fracture generation are considered by contemplating the stress intensity factor distribution around the periphery of misaligned hydraulic fracture. Wellbore stress effects are not considered in this study.

[3] The material of this section was used for presenting and proceeding in: Sheibani F., J.E. Olson. 2013. Stress intensity factor determination for three-dimensional crack using the displacement discontinuity method with applications to hydraulic fracture height growth and non-planar propagation paths. In The International Conference for Effective and Sustainable Hydraulic Fracturing, Brisbane, Australia, 20-22 May 2013.

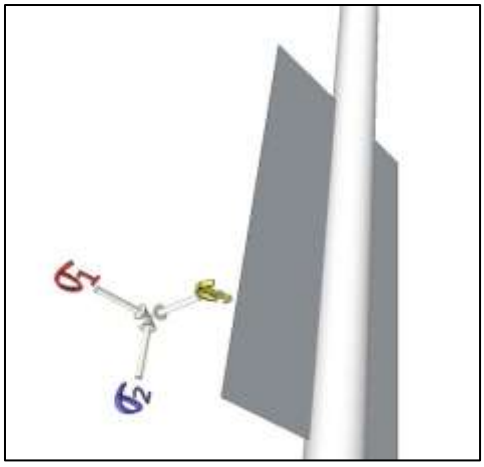

Figure 4.1: Ideal longitudinal fractured horizontal well with hydraulic fracture perpendicular to σ_{hmin}.

2.4.3 Theoretical Background

Lateral kinking propagation of the vertical hydraulic fracture is modeled based on maximum circumferential stress criteria (Erdogan & Sih, 1963) as discussed previously. The model takes into account the height growth as pure Mode I propagation. Any contribution of Mode III or out of plane shear on vertical propagation is neglected; however, the possibility of fringe crack generation based on Mode I+III combination will be studied by Mode III SIF evaluation along the upper front of the fracture. As discussed in previously, the angle of twisting is dependent on the magnitude of Mode III and Mode I SIF as well as mechanical properties (Pollard *et al.* 1982) is calculated using Equation 2.5. Higher values of Mode III SIF (or lower opening mode) result in bigger twisting angle.

Fracture front propagation velocity defines which edge extends first. Charles power law (Atkinson, 1984) is used to relate the equivalent opening Mode stress intensity factor at the tip of the crack to the propagation velocity as the following (Atkinson, 1984):

$$V = AK_{eq}^{n} \tag{4.1}$$

2.4.4 Numerical Modeling

For the propagation cases that follow, it is assumed $S_{hmin} = S_{xx}^{r}$ = 15 MPa (where r denotes remote stresses), P_{frac} is constant and equal to $20.0\ MPa$, the remote compression differential stress is $(\sigma_{yy}^{r} - \sigma_{xx}^{r}) = 2.0\ MPa$, the propagation velocity exponent is $n = 2$, $\nu = 0.25$ and $E = 30.0\ GPa$. The initial fracture length and height are assumed to be 3 meters (a square crack), subdivided by 9 DDM elements. The fracture is assumed to remain rectangular during the

propagation (i.e., the height is uniform along the entire length, but the crack path in plan-view can be non-planar).

2.4.5 Results and Discussion

To examine the effect of horizontal well misalignment angle on fracture propagation (Figure 4.2), first it is assumed the differential compression in y direction($S^r_{yy} - S^r_{xx}$) is 40% of the net injection pressure, ($P_{frac} - S^r_{xx}$). Fracture path non-planarity is strongly affected by the initial misalignment angle, β, especially for extreme cases. The starter fracture is centered at $(0,0)$ and is rotated counterclockwise by β. The smallest misalignment $\beta = 10°$ is the closest to planar fracture and $\beta = 89°$ is the most curved path.

Non-planar propagation has an impact on height growth (Figures 4.3 and 4.4). For the smaller misalignment cases (β<=45°), crack height keeps pace with crack length growth for our imposed rectangular shape (Figure 4.2). For the stronger misalignment cases of β >45°, the crack height growth is somewhat hindered to only ~80% of the length. Looking at the opening mode SIF (K_I) distribution along the top edge of the fracture is more interesting, however, since our propagation algorithm responds only to the average crack tip SIF. The more severe the fracture reorientation, the lower the K_I for the initial fracture segment, where for the 89° misalignment case, the K_I at the center of the crack is 50% lower than it would be for a planar fracture. This implies that at the wellbore, there could be a restriction in fracture height because of the non-planar propagation that might also restrict width and hinder infectivity.

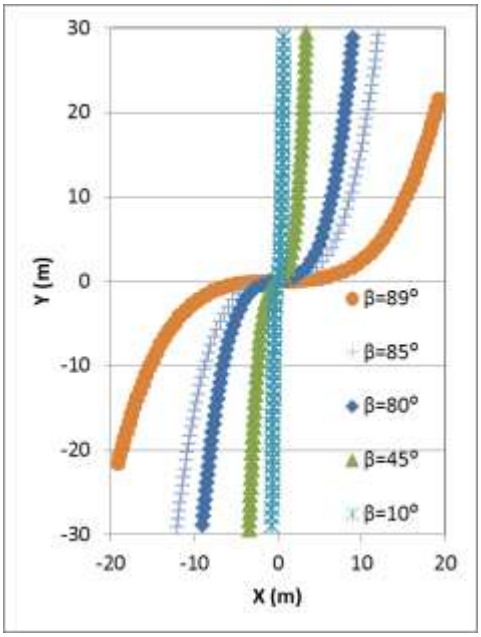

Figure 4.2: Map view of non-planar fracture paths (upper front propagation, $\frac{\Delta H}{2} = \mathbf{25.0}\ \boldsymbol{m}$)

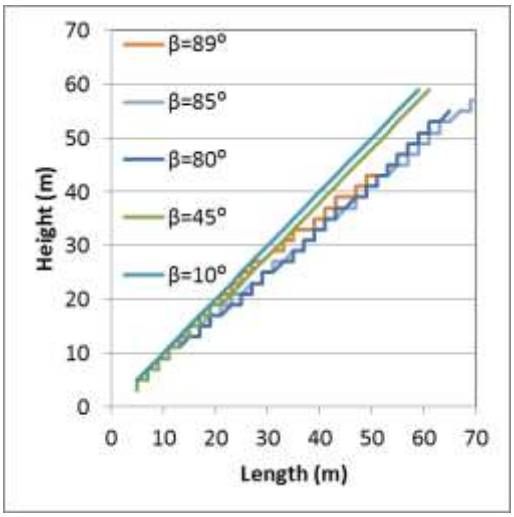

Figure 4.3a: Vertical versus lateral growth of the hydraulic fracture

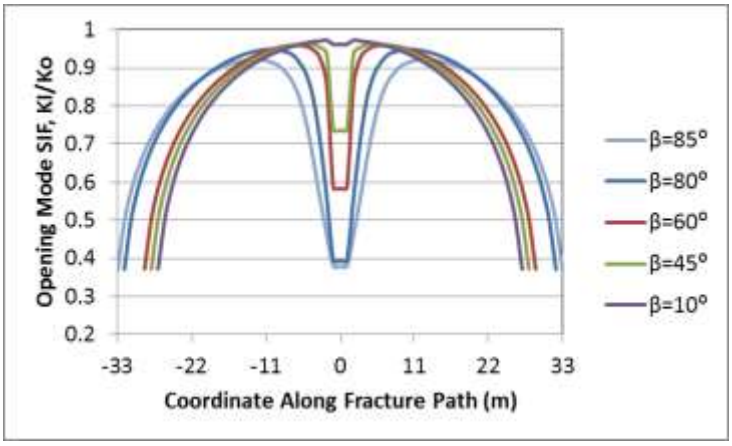

Figure 4.3b: K_I along the upper front of hydraulic fracture implying height growth restriction around the wellbore due to misalignment normalized to SIF of planar fracture at $\boldsymbol{x = 0}$ (upper front propagation, $\frac{\Delta \boldsymbol{H}}{\boldsymbol{2}} = \boldsymbol{25.0\ m}$)

The time progression of the K_I variation along the top fracture front is displayed in Figure 4.4 for the case $\beta = 80°$. The K_I at the initial fracture location (the injection location) grows very slowly in comparison to the curving wings of the fracture.

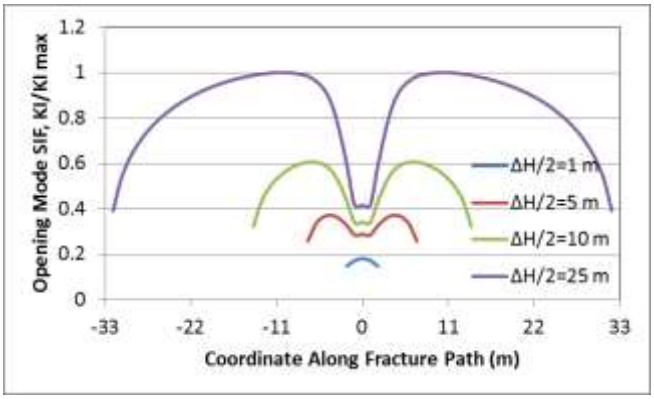

Figure 4.4: K_I distribution variation normalized by the absolute maximum opening mode SIF during propagation along the upper front of a hydraulic fracture perforated from a misaligned horizontal wellbore. Misalignment angle, $\boldsymbol{\beta = 80°}$.

Although K_I is restricted in the misaligned portion of the fracture, Mode III or out of plane shear SIF(K_{III}) is accentuated. This twisting SIF could cause the fracture to break down into several en echelon cracks, causing further propagation hindrance in the vertical direction. Figure 4.5 depicts the distribution of K_{III} for varying fracture misalignment based on the simulation of Figure 4.3.

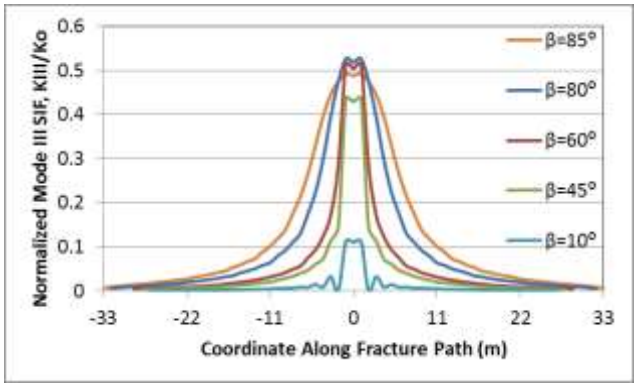

Figure 4.5: Mode III SIF along the upper front of hydraulic fracture normalized to SIF of planar fracture at $\boldsymbol{x = 0}$, implying height growth restriction around the wellbore due to misalignment (upper front propagation, $\boldsymbol{\frac{\Delta H}{2} = 25.0\ m}$)

As discussed previously (Equation 2.1), Fracture path is affected by remote stresses as well as near-tip stress distribution and is quantifies by ratio R (Cruikshank *et al.* 1991). The magnitude of R shows how fast the misaligned fracture will be aligned with maximum horizontal stress. Figure 4.6 present the bigger the magnitude of R ratio, the faster the fracture will be rotated to be aligned perpendicular to minimum horizontal stress. Because the differential remote stress is kept constant for these 3 cases, smaller magnitude of ratio R means the dominance of fracture driving stresses results in a straighter fracture path.

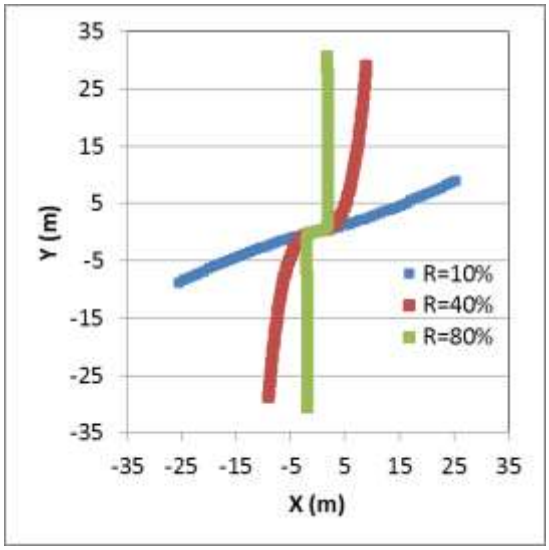

Figure 4.6: R ratio effect on fracture path. Upper front propagation, $\frac{\Delta H}{2} = \mathbf{25.0}\ \boldsymbol{m}$, $\boldsymbol{\beta} = \mathbf{80}°$ and $(\boldsymbol{\sigma_{yy}^{r}} - \boldsymbol{\sigma_{xx}^{r}}) = \mathbf{2.0}\ \boldsymbol{MPa}$.

2.4.6 Conclusion

Lack of alignment between the wellbore and the principal stresses, local stress perturbation, or natural fracture adjacent to a horizontal well might results in misalignment in hydraulic fracture. In this section longitudinal hydraulic fracture propagation irregularities from misaligned horizontal wellbore was considered. Results show lateral propagation of misaligned hydraulic fracture is non-planar, fracture path non-planarity is strongly affected by the initial misalignment angle, and non-planar propagation results in fracture width and height growth around horizontal wellbore. In addition, Mode III distribution and fringe crack generation is accentuated in the misaligned portion of the wellbore causing further propagation hindrance in the vertical direction.

2.5 References

Acocella, V., A. Gudmundsson, and R. Funiciello. 2000. Interaction and linkage of extension fractures and normal faults: examples from the rift zone of Iceland. Journal of Structural Geology. 22: 1233-1246.

Anderson, E.M. 1951. The dynamics of faulting. Oliver & Boyd, Edinburgh.

Atkinson B.K. 1984. Subcritical crack growth in geological materials. Journal of geophysical research. 89(B6): 4077-4114

Atkinson, B.K. and P.G. Meredith. 1987. The theory of subcritical crack growth with applications to minerals and rocks, In. Fracture Mechanics of Rocks ed. B.K. Atkinson B, 111-166.

Aydin, A, R.A. Schultz. 1990. Effect of mechanical interaction on the development of strike-slip faults with echelon patterns. Journal of Structural Geology. 12(1): 123-129.

Bahat, D. 2004. Eight distinct fault-joint geometric/genetic relationships in the Beer Sheva syncline, Israel.

Bahorich, B., J.E. Olson, and J. Holder. Examining the effect of natural fractures on hydraulic fracture propagation in hydrostone block experiments. In SPE Annual Technical Conference and Exhibition, San Antonio, 8-10 October 201

Bai, T., D.D. Pollard, and H. Gao. 2000. Explanation for fracture spacing in layered materials. Nature. 403: 753-756.

Bai, T, L. Martin, M.R. Gross, and A. Aydin. 2002. Orthogonal cross joints; do they imply a regional stress rotation?. Journal of Structural Geology. 24: 77-88.

Barsoum, R.S. 1976. On the use of isoparametric finite elements in linear fracture mechanics, International Journal for Numerical Methods in Engineering. 10(1): 65-88.

Belayneh, M. 2004. Paleostress orientation inferred from surface morphology of joints on the southern margin of the Bristol Channel Basin, UK. Geological Society of London Special Publication. 231: 243-255.

Benzley, S.E. 1974. Representation of singularities with isoparametric finite elements. , International Journal for Numerical Methods in Engineering. 8(3): 537-545.

Blenkinsop, T.G. 2008. Relationships between faults, extension fractures and veins, and stress. Journal of Structural Geology. 30: 622-632.

Brogi A. 2011. Variation in fracture patterns in damage zones related to strike-slip faults interfering with pre-existing fractures in sandstone (Calcione area, southern Tuscany, Italy.) Journal of Structural Geology. 33: 644-661.

Caputo, R. 2005. Stress variability and brittle tectonic structures. Earth-Science Reviews. 70: 103-127.

Caputo, R. 2010. Why joints are more abundant than faults. A conceptual model to estimate their ratio in layered carbonate rocks. Journal. of Structural. Geology. 32: 1257–1270.

Chan, H.C.M. 1991. Equivalent crack formation by propagating cracks under tension. Engineering Fracture Mechanics. 39(2): 433-441.

Chan, S.K., I.S. Tuba, and W.K. Wilson. 1970. On the finite element method in linear fracture mechanics. Engineering Fracture Mechanics. 2: 1-17.

Chang, C.C., M.E. Mear. 1995. A Boundary Element Method for Two Dimensional Linear Elastic Fracture Analysis. International Journal of Fracture. 74: 219-25.

Chen, Y.M. 1975. Numerical computation of dynamic stress intensity factors by a Lagrangian finite-deference method (THE HEMP CODE). Engineering Fracture Mechanics. 7(4): 653:660.

Conard, R.E., M. Friedman. 1976. Microscopic feather fractures in the faulting process. Tectonics. 33: 187-198.
Cooke, M.L., and D.D. Pollard. 1996. Fracture propgation paths under mixed mode loading within rectangular blocks of polymethyl methacrylate. Journal of Geophysical research. 101(B2): 3387-3400.
Cottrell, B., J.R. Rice. 1980. Slightly curved or kinked cracks. International Journal of Fracture. 16: 155-169.
Crawford, A.M., and J.H. Curran. 1982. Higher-order functional variation displacement discontinuity elements. International Journal of Rock Mechanics and Mining Sciences & Geomechanics Abstract. 19(3): 143-148.
Crouch, S.L. 1976. Solution of plane elasticity problems by the displacement discontinuity method. International Journal for Numerical Methods in Engineering. 10(2): 301-343.
Crouch, S.L., and A.M. Starfield. 1983. Boundary element methods in solid mechanics. London: George Allen & Unwin.
Cruikshank, K. M. G. Zhao, and A.M. Johnson. 1991. Analysis of minor fractures associated with joints and faulted joints. Journal of Structural Geology, 13(8): 865-886.
Davatzes, N.C., P. Eichhubl, and A. Aydin. 2005. Structural evolution of fault zones in sandstone by multiple deformation mechanism: Moab fault, southeast Utah. GSA Bulletin. 117(1-2): 135-148.
Delaney P.T., and D.D. Pollard. 1981. Deformation of host rocks and flow of magma during growth of Minette dikes and breccia-bearing intrusions near Ship Rock, New Mexico. Geological Survey professional paper No. 1202.
Dong, C.Y., and C.J. de-Pater. 2001. Numerical implementation of displacement discontinuity method and its application in hydraulic fracturing. Computer Methods in Applied Mechanics Engineering. 191(8-10) 745-760.
Dyer, R. 1988. Using joint interaction to estimate paleostress ratios. Journal of Structural Geology. 10: 685-699.
Engelder, T. 1985. Loading paths to joint propgation during a tectonic cycle: an example from the Appalachian plateau, U.S.A. Journal of Structural Geology. 7(3/4): 459-476.
Engelder, T. 1992. Stress regimes in the lithosphere. Princeton University Press. Princeton, NJ. 457.
Engelder, T., and M.P. Fischer. 1996. Loading configuration and driving mechanisms for joints based on the Griffith energy-balance concept. Tectonophysics. 256: 253-277.
Engelder T., and D. Peacock. 2001. Joint development normal to regional compression during flexural-flow folding: the Lilstock buttress anticline, Somerset, England. Journal of Structural Geology. 23: 259-277.
Erdogan, F., and G.C. Sih. 1963. On the crack extension in plates under plane loading and transverse shear. ASME Journal of Basic Engineering. 85: 519-527
Fischer, M.P., and M.S. Wilkerson. Predicting the orientation of joints from fold shape: results of pseudo-three-dimensional modeling and curvature analysis. Geology. 28(1): 15-18.
Fossen H. 2010. Deformation bands formed during soft-sediment deformation: Observation from SE Utah. Marine and Petroleum Geology. 27: 215-222.
Frid, V., D. Baht, and A. Rabinovich. 2005. Analysis of en echelon/hackle fringes and longitudinal splits in twist failed glass sample by means of fractography and electromagnetic radiation. Journal of Structural Geology. 27: 145-159

Fyfe, W.S., N.J. Price, and A.B. Thompson. 1978. Fluids in the Earth's Crust. Elsevier, New York.
Gercek, H. 2007. Poisson's ratio for rocks. International Journal of Rock Mechanics and Minim Science. 44: 1-13.
Gross, M.R., D. Bahat, A. Becker. 1997. Refashions between jointing and faulting based on fracture-spacing ratios and fault-slip profile: A new method to estimate strain in layered rocks. Geology. 25(10) :887-890.
Guidi G.D., R. Caputo, and S. Scudero. 2013. Regional and local stress field orientation inferred from quantitative analysis of extension joints: case study of southern Italy. Tectonics. 32: 1-13.
Gupta, S., P.A. Cowie, N.H. Dawers, and J.R. Underhill. 1998. A mechanism to explain rift-basin subsidence and stratigraphic pattern through fault-array evolution. Geology. 26: 595-598.
Hancock, P.L. 1985. Brittle microtectonics: principles and practice. Journal of Structural Geology. 7:437-457.
Henshell, R.D., K.G. Shaw. 1975. Crack tip finite elements are unnecessary. International Journal for Numerical Methods in Engineering. 9: 495-507.
Homberg C., J.C. Hu, J. Angelier, F. Bergerat, and O. Lacombe. 1997. Characterization of stress perturbations near major fault zones: insights from 2-D distinct-element numerical modeling and field studies (Jura mountains). Journal of Structural Geology. 19(5): 703-718.
Horri, H., and S. Nemat-Naser. 1985. Compression-induced microcrack growth in brittle solids: axial splitting and shear failure. Journal of Geophysical Research. 90: 3105-3125.
Hussain, M.A., S.L. Pu, and J.H. Underwood. 1974. Strain energy release rate for crack under combined Mode I and Mode II. Fracture Analysis, ASTM STP 560, 2.28
Irwin, G..R. 1957. Analysis of stress and strain near the end of a crack traversing a plate. Journal of Applied Mechanics. 24: 361-364.
Irwin, G.R. 1962. Crack-extension force for a part-through crack in a plate. Journal of Applied Mechanics. 29(4): 651-654.
Isida, M., T. Yoshida, and H. Noguchi. 1991. A rectangular crack in an infinite solid, a semi-infinite solid and a finite-thickness plate subjected to tension. International Journal of Fracture. 52: 79-90.
Jiang S., Z. Ying, and C. Du. 2010. The optimal XFEM approximation for fracture analysis. IOP Conference Series: Materials Science and Engineering 10 (1).
Jordan P.D., C.M. Oldenburg, J.-P. Nicot. 2011. Estimating the probability of CO2 plumes encountering faults. Greenhouse Gases: Science and Technology, 1: 160-174.
Jourde, H., P. Fenart, M. Vinches, S. Pister, and B. Vayssade. 2007. Relationship between the geometrical and structural properties of layered fractured rocks and their effective permeability tensor. A simulation study. Journal of Hydrology. 337: 117-132.
Kassir, M.K. 1981. Stress intensity factor for a three-dimensional rectangular crack. Journal of Applied Mechanics. 48(2): 309-313.
Kassir, M.K. 1982. A three-dimensional rectangular crack subjected to shear loading. International Journal of Solids and Structures 18(12): 1075-1082.
Kattenhorn, S.A. 1998. A 3D mechanical analysis of normal fault evolution and joint development in perturbed stress field around normal faults. PhD Dissertation. Stanford University.

Kattenhorn S.A., and D.D. Pollard. 1999. Is lithostatic loading important for the slip behavior and evolution of normal fault in the Earth's crust? Journal of Geophysical Research: Solid Earth. 104(B12): 28879-28898.
Kattenhorn, S.A., A. Aydin, and D.D. Pollard. 2000. Joints at high angles to normal fault strike: an explanation using 3-D numerical models of fault-perturbed stress field. Journal of Structural Geology. 22: 1-23.
Krantz, R.L. 1979. Crack-crack and crack-pore interactions in stressed granite. International Journal of Rock Mechanics and Mining Sciences & Geomechanics Abstracts. 16: 37-47.
Lange, F.F. 1968. Interaction between overlapping parallel cracks; a Photoeleastic study. The International Journal of Fracture Mechanics. 4: 287-294.
Laubach, S.E., P. Eichhubl, C. Hilgers, and R.H. Lander. 2010. Structural diagenesis. Journal of Structural Geology. 32: 1866-1872.
Lawn, B.R. and T.R. Wilshaw. 1993. Fracture of Brittle Solids, 2nd ed. New York: Cambridge University Press.
Lazarus, V., J.B. Leblond, and S. Mouchrif. 2001. Crack front rotation and segmentation in mixed Mode I+III or I+II+III. Part II: comparison with experiments. Journal of the Mechanics and Physics of Solids. 49: 1421-1443
Lin B., M.E. Mear, and K. Ravi-Chandar. 2010. Criterion for initiation of cracks under mixed-mode I + III loading. International Journal of Fracture. 165: 175-188.
Lin X., and J. Ballmann. 1993. Re-consideration of Chen's problem by finite difference method. Engineering Fracture Mechanics. 44(5): 735-739.
Macdonald, K.C., J.C. Sempere, and P.J. Fox. 1984. East pacific rise from the Siqueiros to the OroZco fracture zone: Along-strike continuity of the neovolcanic zone and the structure and evolution of overlapping spreading centers. Journal of Geophysical Research. 89: 6049-6069.
Maerten, L., P. Gillespie, and D.D. Pollard. 2002. Effects of local stress perturbation on secondary fault development. Journal of Structural Geology. 24: 145-153.
Maerten, L., P. Gillespie, and J.M. Daniel. 2006. Three-dimensional geometrical modeling for constraint of subseismic fault simulation. AAPG Bulletin. 90(9): 1337-1358.
Martel, S.J., and W. Boger. 1998. Geometry and mechanics of secondary fracturing around small three-dimensional faults in granitic rock: Journal of Geophysical Research, 103: 21299-21314.
Mastrojannis, E.N., L.M. Keer, and T.A. Mura. 1979. Stress intensity factor for a plane crack under normal pressure. International Journal of Fracture. 15(3): 101-114.
Mear, M.E., G.J. Rodin. 2011. An isolated Mode I three-dimensional planar crack: The stress intensity factor is independent to elastic constant. International Journal of Fracture. 172(2): 217-218.
Mériaux, C., J.R. Lister. 2002. Calculation of dyke trajectories from volcanic centers. Journal of Geophysical Research. 107(B4): 2077-2087.
Min, K.B., L. Jing, and O. Stephansson. 2004. Determining the equivalent permeability tensor for fractured rock masses using a stochastic REV approach: Method and application to the field data from Sellafield, UK. Hydrogeology Journal. 12: 497-510.
Murakami, Y., M. Endo. 1983. Quantitative evaluation of fatigue strength of metals containing various small defects or cracks. Engineering Fracture Mechanics. 17(1): 1-15.
Murakami, Y., S. Kodama, and S. Konuma. 1989. Quantitative evaluation of effects of non-metallic inclusions on fatigue strength of high strength steels. I: Basic fatigue mechanism and

evaluation of correlation between the fatigue fracture stress and the size and location of non-metallic inclusions. International Journal of Fatigue. 11(5): 291-298.
Mutlu, O., and D.D. Pollard. 2006. A complementarity approach for modeling fractures. In: Yale D, Holtz S, Breeds C, and Ozbay U. (eds.) 50 years of Rock Mechanics-Landmarks and Future Challenges: The 41st U.S. Symposium on Rock Mechanics, Paper No: ARMA/USRMS 06-1058, June 17-21 2006, Golden, CO, USA.
Nicot, J.P., and S.D. Hovorka. 2009. Chapter 17. Leakage pathways from potential CO2 storage sites and importance of open traps: case of the Texas Gulf Coast, in Grobe, M., Pashin, J.C., and Dodge, R.L., eds., Carbon dioxide sequestration in geological media—state of the science: AAPG Studies in Geology, 59: 321–334.
Nisitani, H., and Y. Murakami. 1974. Stress intensity factor of an elliptical crack and semi-elliptical crack in plates subjected to tension. International Journal of fracture. 10(3): 353-368.
Noda, N.A., and T.A. Kihara. 2002. Variation of the stress intensity factor along the front of a 3-D rectangular crack subjected to mixed-mode load. Archive of Applied Mechanics. 72: 599:614.
Okada, Y. 1992. Internal deformation due to shear and tensile faults in a half-space. Bulletin of the Seismological Society of America. 82(2): 1018-1040.
Olson, J., D.D. Pollard. 1989. Inferring paleostresses from natural fracture patterns: A new method. Geology. 17: 345-348.
Olson, J. E., D.D. Pollard. 1991. The initiation and growth of en-echelon veins. Journal of Structural Geology. 13(5): 595-608.
Olson, J.E. 1991. Fracture mechanics analysis of joints and veins. PhD Dissertation. Stanford University.
Olson, J.E., 1993. Joint pattern development: effects of subcritical crack-growth and mechanical crack interaction. Journal of Geophysical Research. 98: 12252-12265.
Olson, J.E. 1995. Fracturing from highly deviated and horizontal wells: Numerical analysis of non-planar fracture propagation. SPE Rock Mountain Regional/Low Permeability Reservoir Symposium, Paper No. SPE 29573, March 20-22 1995, Denver, CO, USA.
Olson, J.E. 2003. Sublinear scaling of fracture aperture versus length: An exception or the rule. Journal of Geophysical Research. 108(B9): 2413-2424.
Olson, J.E. 2004. Predicting fracture swarms-the influence of subcritical crack growth and the crack-tip process zone on joint spacing in rock. Geological Society of London Special Publication. 231: 73-88.
Olson, J.E., 2007. Fracture aperture, length and pattern geometry development under biaxial loading: a numerical study with application to natural, cross-jointed systems. Geological Society Special Publication. 289: 123-142.
Olson, J.E. 2008. Multi-fracture propagation modeling: Application to hydraulic fracturing in shales and tight gas sands. The 42st U.S. Symposium on Rock Mechanics and 2nd U.S.-canada Rock Mechanics Symposium, Paper No: ARMA 08-327, June 29-July 2 2008, San Francisco, CA, USA.
Olson J.E, K. Wu. 2012. Sequential versus simultaneous multi-zone fracturing in horizontal wells: Insight from a non-planar, multi-frac numerical model. SPE Hydraulic Fracturing Technology Conference, Paper No: SPE 152602-PP, February 6-8 2012, The Woodland, TX, USA.

Pande, G.N., G. Beer, and J.R. Williams. 1990. Numerical Methods in Rock Mechanics. West Sussex: John Wiley & Sons Ltd.
Peacock, D.C.P. 2001. The temporal relationship between joints and faults. Journal of Structural Geology. 23: 329-341.
Peirce A., and E. Detournay. 2008. An Eulerian moving front algorithm with weak-form tip asymptotic for modeling hydraulically driven fractures.
Philip, Z.G., J.W. Jennings, J.E. Olson, S.E. Laubach, and J. Holder. 2005. Modeling coupled fracture-matrix fluid flow in geomechanically simulated fracture networks. SPE Reservoir Evaluation & Engineering. 8: 300-309.
Pollard D.D., P. Segall, and P.T. Delaney. 1982. Formation and interpretation of dilatant echelon cracks. Geological Society of America Bulletin. 93: 1291-1303.
Pollard, D.D., A. Aydin. 1984. Propagation and linkage of oceanic ridge segments. Journal of Geophysical Research, 89(B12): 10,017-10,028.
Pollard, D.D., P. Segall. 1987. Theoretical displacement and stress near fracture in rock: with application to faults, joints, veins, dikes and solution surfaces. In: Atkinson BK. (ed.) Fracture Mechanics of Rock. London: Academic Press. 277-350.
Pollard, D.D., A. Aydin. 1988. Progress in understanding jointing over the past century. Geological Society of America Bulletin, 100(8): 1181-1204.
Pollard, D.D., S. Zeller, J. Olson, and A. Thomas. 1990. Understanding the process of jointing in brittle rock masses. In Proceedings: 31st US Symposium on Rock Mechanics (USRMS),Golden, CO, 18-20June 1990, eds. 447-454. Rotterdam: A.A. Balkema.
Pons, A.J., A. Karma. 2010. Helical crack-front instability in mixed-mode fracture. Nature. 464: 85-89
Qiu, Y. 2002. Natural Fracture Modeling and characterization. PhD dissertation. University of Texas at Austin.
Rawnsley, K.D., T. Rives, and J.P. Petit. 1992. Joints development ion perturbed stress fields near faults. Journsal of Structural Geology. 14(8-9): 939-951.
Renshaw, C.E. D.D. Pollard. 1994. Are large differential stress required for straight fracture propagation paths?. Journal of Structural Geology. 16(6): 817-822.
Ritz, E., and D.D. Pollard. 2011. Closure of circular arc cracks under general loading: effects on stress intensity factors. International Journal of Fracture. 167(1): 3 -14.
Rizzo, F.J. 1967. An integral equation approach to boundary value problems of classical elastostatics. Quarterly of Applied Mathematics. 25: 83-95.
Rotevatn A., H. Fossen, J. Hesthammer, T.E. Aas, and J.A. Howell. 2007. Are relay ramps conduit for fluid flow? Structural analysis of relay ramp in Arches National Park, Utah. Special Publication, Geological Society, London. 270: 55-71.
Scavia, C. 1991. The displacement discontinuity method on the analysis of open cracks. Meccanica. 26(1): 27-32.
Schultz, R.A. 1988. Stress intensity factor for curved cracks obtained displacement discontinuity method. International Journal of Fracture 37(2): R31-R34.
Secor, D.T. 1969. Mechanics of natural fracturing extension at depth in the earth's crust, In: Bear, A.J., D.K. Norris, eds. Research in tectonics. Geological Survey of Canada Special Paper. 68-52: 3-47.
Sempere, J.C., K.C. Macdonald. 1986. Overlapping spreading centers: implication for crack growth simulation by the displacement discontinuity method. Tectonics. 5(1): 151-163.

Sheibani F., J.E. Olson. 2013. Stress intensity factor determination for three-dimensional crack using the displacement discontinuity method with applications to hydraulic fracture height growth and non-planar propagation paths. In The International Conference for Effective and Sustainable Hydraulic Fracturing, Brisbane, Australia, 20-22 May 2013.

Sheibani F., J.E. Olson. 2013. Impact of Fracture Height on Mixed Mode Fracture Propagation: Insights from 3D Displacement Discontinuity Modelling. ARMA, 47th U.S. Rock Mechanics / Geomechanics Symposium, San Francisco, 23-26 June 2013.

Shou K.J., and S.L. Crouch. 1995. A higher order displacement discontinuity method for analysis of crack problems. International Journal of Rock Mechanics and Mining Sciences & Geomechanics Abstract. 32 (1): 49-55.

Sih, G.C. 1974, Strain-energy-density factor applied to mix-mode crack problems. International Journal of fracture Mechanics. 10: 305-321

Simon, J.L., A.E. Arlegui, C.L. Liesa, and A. Maestro. 1999. Stress perturbations registered by jointing near strike-slip, normal, and reverse faults: Examples from the Ebro Basin, Spain. Journal of Geophysical Research. 104(B7): 15141-15153.

Sneddon, I.N. 1946. The distribution of stress in the neighborhood of a crack in an elastic solid. Proceedings of the Royal Society of London. Series A, Mathematical and Physical Sciences. 187(1009): 229-260.

Soliva, R., A. Benedicto, and Laurent Maerten. 2006. Spacing and linkage of confined normal faults: Importance of mechanical thickness. Journal of Geophysical Research. 111(B01402): 1-17.

Swain, M.V., J.T. Hagan. 1978. Some observations of overlapping interacting cracks. Engineering Fracture Mechanics. 10: 299-304.

Tarancon, J.E., A. Vercher, E. Giner, and F.J. Fuenmayor. 2009. Enhanced blending elements for XFEM applied to linear elastic fracture mechanics. International Journal for Numerical Methods in Engineering. 77(1): 126-148.

Thomas, A.L., and D.D. Pollard. 1993. The geometry of echelon fractures in rock-implication from laboratory and numerical experiments. Journal of Structural Geology. 15(3-5): 323-334.

Tuckwell, G.W., L. Lonergan, and R.J.H. Jolly. 2003. The control of stress history and flaw distribution on the evolution of polygonal fracture networks. Journal of Structural Geology. 25: 1241-1250.

Vermilye, J.M. and C.H. Scholz. 1998. The process zone: a microstructural view of fault growth. Journal of Geophysical Research. 103: 12223-12237.

Wang, Q., N.A. Noda, M.A. Honda, and M. Chen. 2001. Variation of stress intensity factor along the front of a 3D rectangular crack by using a singular integral equation method. International Journal of Fracture. 108: 119-1431.

Weaver, J. 1977. Three dimensional crack analysis. International Journal of Solids and Structures. 13(4): 321-330

Wen, P.H., M.H. Aliabadi, and D.P. Rooke. 1994. A fictitious stress and displacement discontinuity method for dynamic crack problems. In: Brebbia CA. (ed.) Boundary Element Method XVI. Southampton: Computational Mechanics Publications. 469-476.

Willemese, J.M. 1997. Segmented normal faults: correspondence between three-dimensional mechanical models and field data. Journal of Geophysical Research. 102: 675-692.

Willemse, E.J.M., and D.D. Pollard. 2000. Normal Fault growth: Evolution of tipline shapes and slip distribution. In: Lehner FK, Urai JL. (ed.) Aspects of Tectonic Faulting. NY: Springer. 193-226.

Wilson, J.E., J.S. Chester, F.M. Chester. 2003. Microfracture analysis of fault growth and wear processes, Punchbowl Fault, San Andreas System, California. Journal of Structural Geology. 25: 1855-1873.
Withhjack, M., J. Olson, and E. Peterson. 1990. Experimental Models of Extensional Forced Folds. The American Association of Petroleum Geologist Bulletin. 74(7): 1038-1054.
Wu, H., and D.D. Pollard. 1995. An experimental study of the relationship between spacing and layer thickness. Journal of Structure Geology. 17: 887-905.
Wu, R. 2006. Some fundamental mechanism of hydraulic fracturing. PhD dissertation, Georgia Institute of Technology.
Yan, X. 2005. Stress intensity factors for cracks emanating from a triangular or square hole in an infinite plate by boundary elements. Engineering Failure Analysis. 12(3): 362-375.
Younes, A.I., and T. Engelder. 1999. Fringe cracks: Key structures for the interpretation of the progressive Alleghanian deformation of the Appalachian plateau. Geological Society of America Bulletin. 111(2): 219-239.
Zoback, M.D. 2011. Reservoir Geomechanics. 5th edition, University Press, Cambridge, United Kingdom. 140-145.

CHAPTER 3
GEOLOGIC CALIBRATION

3.1 Seismic Calibration from Fracture Patterns in Outcrops and Core – Geologic Observations and Techniques

3.1.1 Background and Motivation

This research addresses uncertainty and difficulty in measuring natural fracture attributes, which is a central impediment to effective exploration and development of low-permeability gas formations. Fluid flow in fractured rock is an increasingly central issue in recovering water and hydrocarbon supplies and geothermal energy, in predicting flow of pollutants underground, in engineering structures, and in understanding large-scale crustal behavior (National Research Council, 1996; Nelson, 2001; Narr, 2006). Successful imaging and prediction of open fractures is essential to gas production from low-permeability reservoirs. For example, we have shown that in some tight formations contrasts in degree of fracture cementation can be the difference between producers and dry holes (Laubach, 2003). In these rocks, differences in fracture length distribution profoundly affect the magnitude and pattern of permeability (Philip et al., 2005). Together with the well-known challenges of obtaining meaningful samples of fractures using boreholes (see, for example, Narr, 1996) the need for information on these hard-to-measure attributes makes fracture prediction, detection, and characterization a central challenge in successfully accessing the resources in tight formations.

Seismic methods offer the promise of measuring key fracture attributes away from borehole samples. Most seismic data analysis techniques currently practiced are based on equivalent or effective media theories that map fracture sets into a set of anisotropic elastic coefficients. Unfortunately most of these analytical developments make use of fracture distributions that are unrealistic, and of seismic measurements that are indirect (Marrett, 1997; Grechka and Tsvankin, 2002; Marrett et al, 2007). A direct fracture response in the recorded seismic data is present in seismic diffraction scattering patterns (Willis et al, 2006). The objective of our research was to:

- develop new seismic diagnostics and imaging methods based on diffraction detection,
- to test the response of the new methods when applied to representative realistic fracture patterns generated by numerical models, or found in core or in outcrop reservoir analogs, and

- to develop new geological methods and concepts to guide the development of geophysical techniques toward seismic imaging of regional fracture sets.

Our goal was to overcome limitations of the commonly practiced seismic analysis tools and to improve processing and analysis of seismic data for characterizing low permeability gas formations where natural opening-mode fractures and small faults may be essential to producibility, a substantial part of the resource base.

Another limitation of the current state of the art in seismic fracture detection and characterization is a lack of robust site-specific data from the subsurface that allows the seismic data to be tested, verified, and calibrated. Our work on new seismic methods was supplemented with studies designed to fill this gap by demonstrating methods that can overcome the limitations imposed by sampling bias on current industry methods for characterizing fractures in low-permeability formations. This approach built on the use of indirect and diagenetic proxies as guides to fracture attributes, allowing small rock samples, such as, for example, those that can be retrieved with wireline methods, (Ortega et al., 2006; Gomez and Laubach, 2006; Laubach and Gale, 2006) to accomplish fracture characterization.

Our research plan included a research and development phase (Phase I) and a validation phase (Phase II). The tasks in Phase I were conducted concurrently because of the benefit from the interplay and feedback between seismic methodology development (Task 4), creation of realistic numerical fracture patterns for code testing and sensitivity analysis (Task 5), and rigorous quantification of fractures in outcrop analogs (Task 6). This play successfully provided fracture patterns for code testing and sensitivity analysis, tests of the geomechancial code, and an opportunity to perfect microstructural surrogate methods for validation and testing. We generated realistic fracture patterns with a geomechanical model and with geostatistical techniques guided by the geomechanical model and outcrop examples. We verified geomechancial modeling results through measurement of fracture patterns in outcrops that are reservoir analogs and core with the aim of also providing input for seismic model development.

Our study was conducted in close collaboration with the industry and benefited from collaboration of the PI's with operators. Cost sharing was provided through a combination of industry in-kind contributions, industry cash contributions, and university foundation funds

3.1.2 Approach

Fractures significant to production are generally considered below the detection limit of conventional reflection seismic techniques. We approached this limitation along four lines of research: 1. Investigate novel techniques in diffraction seismic techniques that may provide the

opportunity to shrink the observation gap between conventional seismic techniques and fracture size distributions that can be observed in core and image logs; 2. Develop new approaches to fracture network modeling; 3. Investigate proxy techniques that allow predictions of fracture occurrence based on characteristics of the fracture population that can be observed using seismic techniques; and 4. Investigate aspects of fracture populations that make them more or less conducive to detection by seismic techniques. This section of the report addresses line 3. and 4. Proxy techniques investigated here include fracture aperture scaling, used in conjunction with characterization of fracture spatial organization (fracture clustering). Aspects controlling seismic detection include fracture clustering and the diagenetic attributes of fractures and hostrock.

3.1.3 Fracture Aperture Scaling

Outcrops can provide an inventory of the seismically significant features we should expect in the subsurface, but it is essential to select outcrops having fractures that are really representative of the subsurface. We have developed a set of criteria for identifying such outcrops (Laubach, 2003; Laubach et al., 2004; Laubach and Ward, 2006). Among seismically important attributes, fracture orientation may controls direction of diffracted p-waves as well as s-wave anisotropy, fracture openness could determine whether fractures will have a first-order seismic signature, and fracture size distribution could control magnitude of seismic signature (Marrett, 1997). Aperture, spacing, shape (aperture to length ratio), and size-spacing patterns will affect diffraction of p-waves propagating through fractured rock. Open fracture length, which may be related to magnitude of velocity anisotropy for elastic shear waves propagating through fractured rock, could also affect diffraction patterns of p-waves propagating through fractured rock. We described and analyzed outcrops having these attributes (Hooker, 2012; Hooker et al., 2012; 2013, in review).

Because individual fractures in fracture systems vary across a tremendous range of sizes and follow power-law scaling (Marrett et al., 1999; Ortega et al., 2006 and references therein), simple averages of attributes are not useful (Marrett, 1996). Fracture openness also varies greatly as a function of diagenetic state and fracture size (Marrett and Laubach, 1997; Laubach, 2003) and fracture opening rate (Olson et al, 2007; Lander et al., in preparation). Our core and outcrop studies documented these attributes.

We performed fracture aperture-scaling studies of sandstone formations exposed in outcrop that share fracture structural and diagenetic characteristics in common with producing tight-gas reservoirs. Figure 1 summarizes aperture-scaling distributions from several unconventional sandstone reservoirs in the Rocky Mountains, including the Mesaverde Group tight-gas sandstone reservoirs of the Piceance Basin. We collected kinematic aperture data from core samples in Mesaverde Group sandstone along 1D scanlines on consecutive thin sections

imaged under scanning electron microscopy cathodoluminescence (SEM-CL). Kinematic aperture refers to the fracture aperture measured from wall to wall, without regard to fracture cement lining the fracture walls. SEM-CL resolves fractures on the micron scale, thus allowing the collection of a statistically significant fracture population over the width of a core in several of the analyzed core depths. Size distributions are here quantified by plotting fracture-size rank (cumulative number) versus fracture aperture (e.g., Marrett et al., 1999). Combined macroscopic and microscopic scanline measurements allow data from different scales of observation from the same body of rock to be compared on the same graph. Because microscopic scanlines are shorter than those for large fractures, such a comparison requires normalizing the cumulative number of fractures to the scanline length by dividing cumulative number by scanline length, the result being the cumulative frequency. Such data represent the number of fractures encountered per unit length of rock rather than per scanline. Therefore, not only does the technique facilitate observation of fractures at different scales, but it also controls for scanlines of different length collected at a single scale of observation. Details of the technique are given in Hooker et al., 2013.

Aperture scaling results from the southern Piceance Basin, shown in Figure 1 in comparison with other data sets, demonstrate that fracture aperture tend to follow a power-law scaling relationship. Among the 22 outcrop and slant-core fracture-size datasets reported in Hooker et al., (2013), 19 are best fit by power-law equations, three are best fit by exponential or log-normal size distributions. No observed fracture set is best fit by a normal size distribution. Power-law size-distribution curves have a coefficient a and exponent b. The a coefficient of the power-law equation represents the y-intercept of the line in log-log space (with the y-axis at $\log(x) = 0$); the b parameter represents the line's slope. It can be qualitatively appreciated (Figure 1) that variation in a among individual datasets is greater than variation in b. Power-law exponents b in these datasets have values of -0.8 ± 0.1.In general, less variation in b exists among populations containing more fractures, suggesting that some variation of b can be attributed to statistically inadequate sampling. The fairly uniform power-law exponent for aperture frequency distributions can be used to estimate the spatial variation in fracture spacing (frequency) of subseismic fractures from the frequency of large seismically detectable fractures provided the site-specific coefficient a can be obtained from core-based micro-scanline results in control wells (Eichhubl et al., in preparation). Such predictions identify the characteristic spacing of fractures of a specified size class, generally the smallest aperture found to be conductive in a reservoir (Laubach, 2003). In the Piceance basin, the highest fracture frequencies are observed in the deepest parts of the Mesaverde Group (Figure 2), consistent with fracture formation driven by gas generation (Fall et al., in review). Figure 2 also illustrates the sample-to-sample variation in fracture frequency in the reservoir, increasing with depth. This variation may reflect fracture clustering. Preliminary results of scaling analyses for fracture clusters of tight-gas sandstone outcrop analogs suggest systematic variations in both coefficients a and b within and outside clusters (Figure 3).

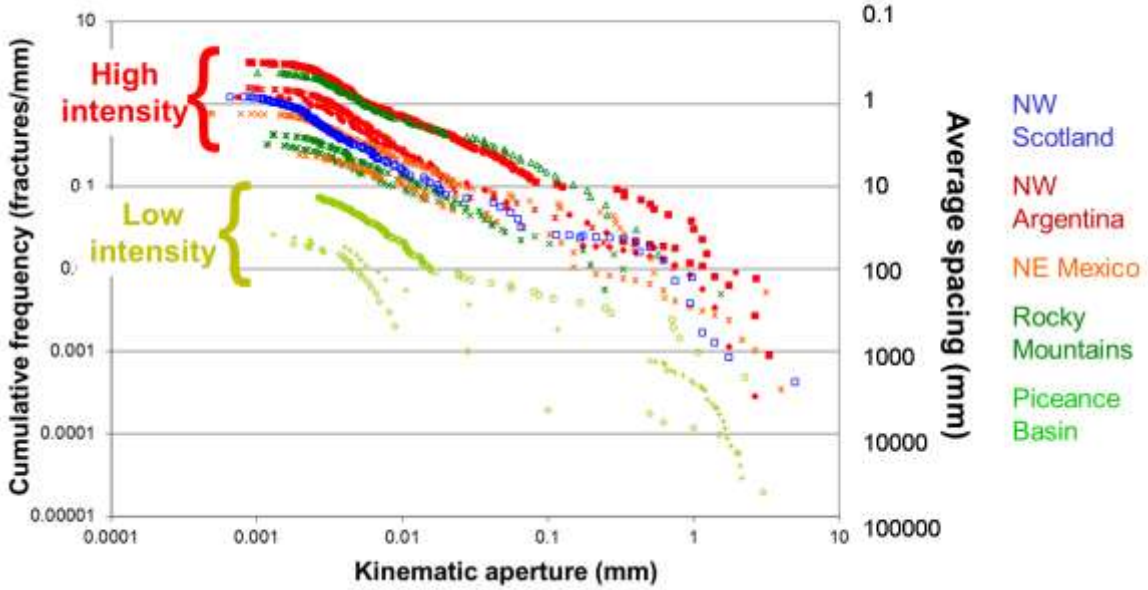

Figure 1. Kinematic aperture versus cumulative frequency of fractures for several unconventional sandstone reservoirs and selected outcrop analog sandstone formations. Different fracture populations share similar power-law distributions (slope) but differ in intensity. Outcrop fracture populations (Scotland, Argentina, Mexico) are generally higher than core-based populations (Rocky Mountains, Piceance Basin).

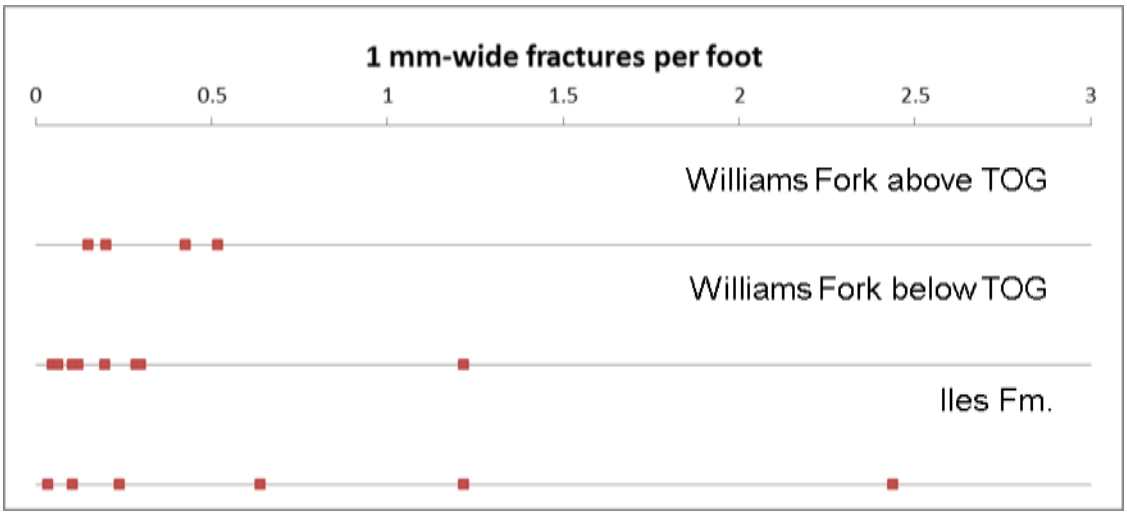

Figure 2. Frequency (number of fractures per linear foot of scanline) for three different horizons for 1-mm wide fractures in the Mesaverde Group of the southern Piceance basin. Highest fracture frequencies are observed in the producing intervals of the Williams Fork Formation below the top of continuous gas (TOG) and the Iles Formation.

Figure 3. Cluster of opening-mode fractures in sandstone of the Cambrian Eriboll Formation, Scotland. Fractures are lined with quartz cement resembling fractures in producing unconventional reservoirs.

3.1.4 Fracture Diagenetic Attributes

Diagenesis affects host rock and fracture attributes. Contrary to widely held views, for many rocks diagenetic state is a much more important control on which fractures are open than orientation of fractures with respect to in situ stress (Laubach et al., 2004a). Diagenetic fluid-

mineral reactions result in fracture cement that, in some cases, completely fills fracture space resulting in fractures that are effectively stiffer than the surrounding medium and less permeable to fluid flow. On the other hand, in many cases in cored tight gas formations we have observed fractures are only partially filled by cement bridges (Figures 5 and 6) (Laubach et al., 2004b). These cement bridges prop fractures open potentially enhancing fluid flow relative to uncemented fractures, but are also likely to reduce the compliance of the fractured rock relative to rock containing uncemented fractures, and enhancing the seismic signature. Yet, in other cases, most dominant in diagenetic settings <80°C, fractures remain uncemented. Uncemented fractures are prone to closing upon changes in loading conditions thus reducing their effect on elastic wave scattering and p-wave diffraction, as well as their contribution to fluid flow. Changes in loading conditions may be induced by hydrocarbon production from fractured reservoirs. Recognition of, and distinction among, uncemented fractures, partially cemented fractures containing cement bridges, and completely cemented fractures is essential in effective reservoir characterization. Our investigations quantified the abundance of open, partially cemented, and completely cemented fractures in the Mesaverde Group of the Piceance basin and other selected reservoirs and reservoir analogs, and assessed mechanism that control type and extent of fracture mineral cements. We focused on the prediction of carbonate fracture cement because carbonate cement is frequently observed to occlude fractures to completion, whereas quartz cement, in the absence of carbonate cement, tends to line fracture walls and to preserve fracture porosity.

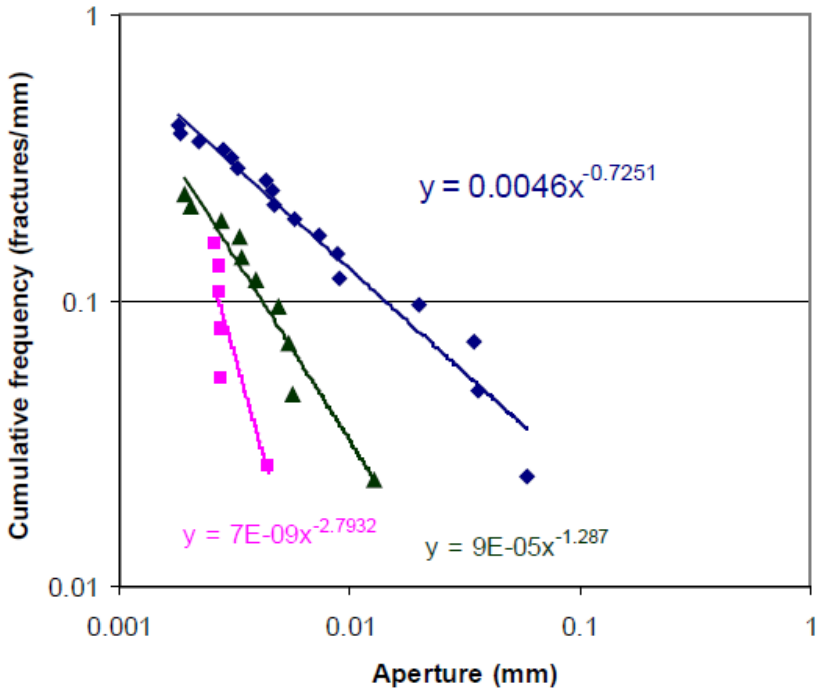

Figure 4. Fracture aperture scaling analysis of a fracture cluster in Cambrian Eriboll Formation, an outcrop analog for a tight-gas sandstone. Squares: outside cluster; triangle: margin of cluster, diamonds: within cluster.

3.1.4.1 Textural Relationships

Mesaverde sandstones in our study wells are extensively cemented by quartz cement overgrowth and clay cements (chlorite, illite, illite/smectite), consistent with previous petrographic studies (Pitman et al. 1989; Crossey and Larsen 1992; Klimentidis and Welton 2008; Ozkan et al. 2011). These diagenetic phases predate carbonate cement with exception of siderite pore cement that formed locally prior to quartz overgrowth.

Carbonate pore cement includes calcite, ferroan-dolomite, ankerite, and siderite whereas calcite is the only carbonate mineral phase in fractures (Figures 5-7). Fracture calcite cement occurs both as banded crack-seal and as sparry cement. Absolute abundance of carbonate pore cement and the relative abundance of different carbonate species are highly variable within the study wells. Iron- and magnesium-bearing carbonate pore cement occurs only in the presence of detrital dolomite, with the proportions of ferroan-dolomite and ankerite being variable. Ferroan-dolomite and ankerite preferentially occur with detrital dolomite as substrate, less commonly with feldspar (albite). In general, the iron content increases in these carbonate phases with growth. Authigenic ferroan-dolomite and ankerite precipitated on detrital dolomite is observed to penetrate and to replace what appears to be a 'pre-existing' phase, preferentially albite resembling similar replacement textures described elsewhere by Milliken (2003).

Siderite cement is a minor component of the sandstone only occurring in deeper samples as small (<40 μm) rhombs rimming detrital grains. This siderite cement is enveloped by quartz overgrowths and therefore predates quartz overgrowth cement indicating that siderite formed early in the diagenetic history and prior to fracture opening and cementation.

Calcite pore cement occurs in both detrital dolomite bearing and dolomite-free stratigraphic units. Based on point count analyses, calcite pore cement content is higher in shallower samples and decreases with increasing depth. This decrease correlates with an increase in ferroan-dolomite cement. Similar trends were observed by Pitman et al. (1989) in the MWX wells in the Rulison Field.

Where present, ferroan-dolomite and ankerite cement are the dominant cement phases and calcite only a minor component in the Mamm Creek and MF31-19G wells. Where calcite pore cement occurs together with detrital dolomite and ferroan-dolomite/ankerite, textural relations indicate that calcite is the youngest carbonate generation (Figure 7).

Cross-cutting relations demonstrate that calcite cemented fractures postdate ferroan-dolomite and ankerite pore cement (Figure 7). The timing relations between calcite pore cement and calcite fracture cement are ambiguous. Pore and adjacent fracture cement in optical continuity do not exclude that both generations were formed contemporaneously. On the other hand, calcite pore-cement crosscut by quartz-lined fractures indicates that some calcite pore cement formed prior to quartz fracture cement, which predates fracture calcite. Calcite cement shows leaching textures and generates secondary porosity. Porous albite, K-feldspar, and calcite appear in a patchy texture that is characteristic of albitization of detrital feldspar (Figure 8). Furthermore, muscovite hosted in albite indicates sericitization of primary feldspar. Albitization thus provides a source for Ca2+ available for carbonate precipitation. Although calcite is observed to be the dominant Ca-species that is associated with albite, ferroan-dolomite is also observed in textural association with albite. However, ferroan dolomite cement occurs only in the presence of detrital dolomite. The presence of detrital dolomite thus controls which carbonate forms during albitization.

In contrast to quartz which lines fracture and which tends to preserve fracture porosity, calcite tends to seal fractures completely. Several fractures lined with euhedral calcite crystals and kinematic apertures >8 mm were observed in well MF31-19G.

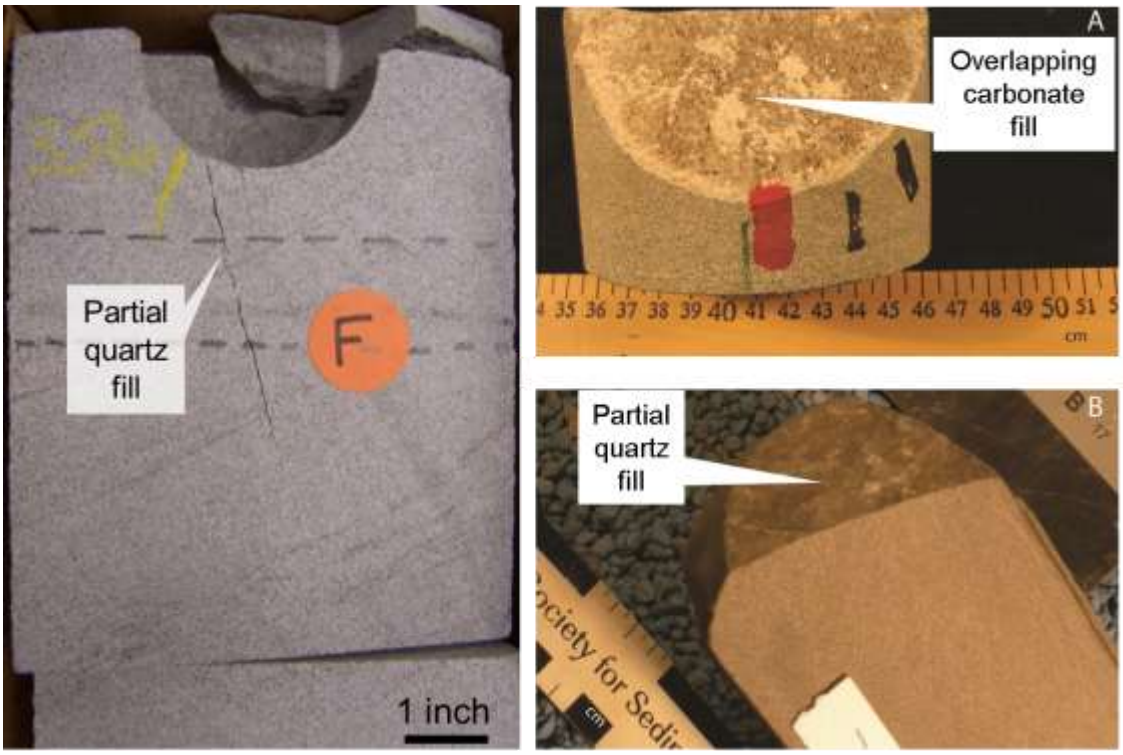

Figure 5. Natural fractures in core of Mesaverde Group sandstones in the Piceance Basin. Fractures are partially cemented with quartz and carbonate cement.

A.

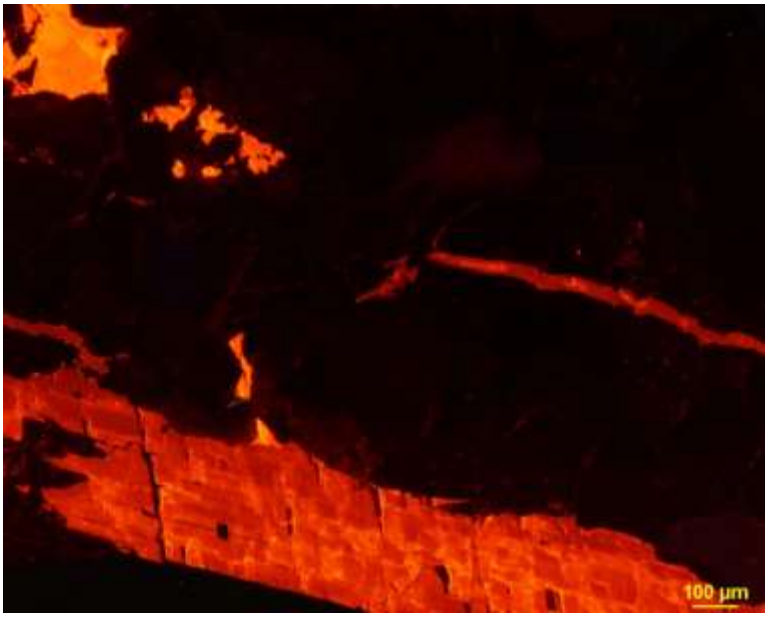

B.

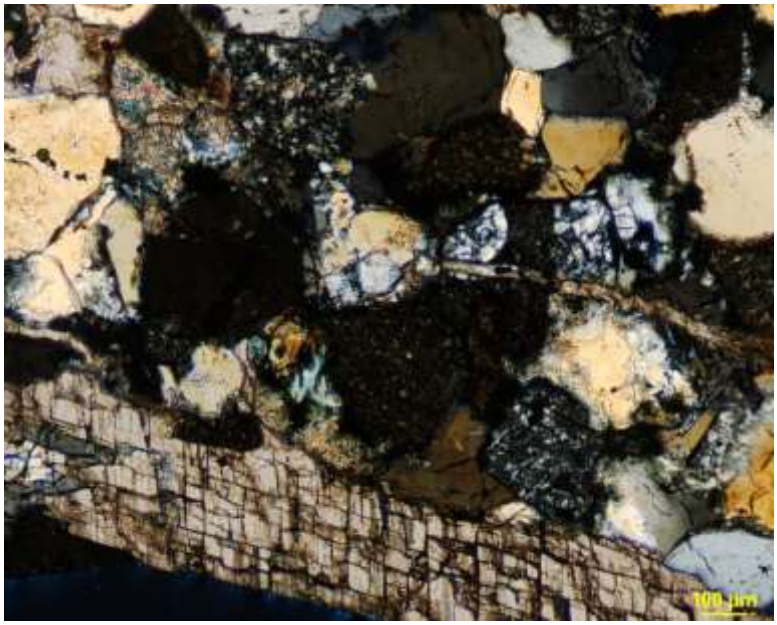

Figure 6: A. Cold cathode luminescence image of carbonate pore (top left) and fracture (bottom and center right) cement in Mesaverde Group sandstone, Piceance Basin. Pore cement appears intergrown with feldspar suggesting calcite precipitation resulting from albitization of calcic plagioclase. B. Cross-polarized transmitted light image of A.

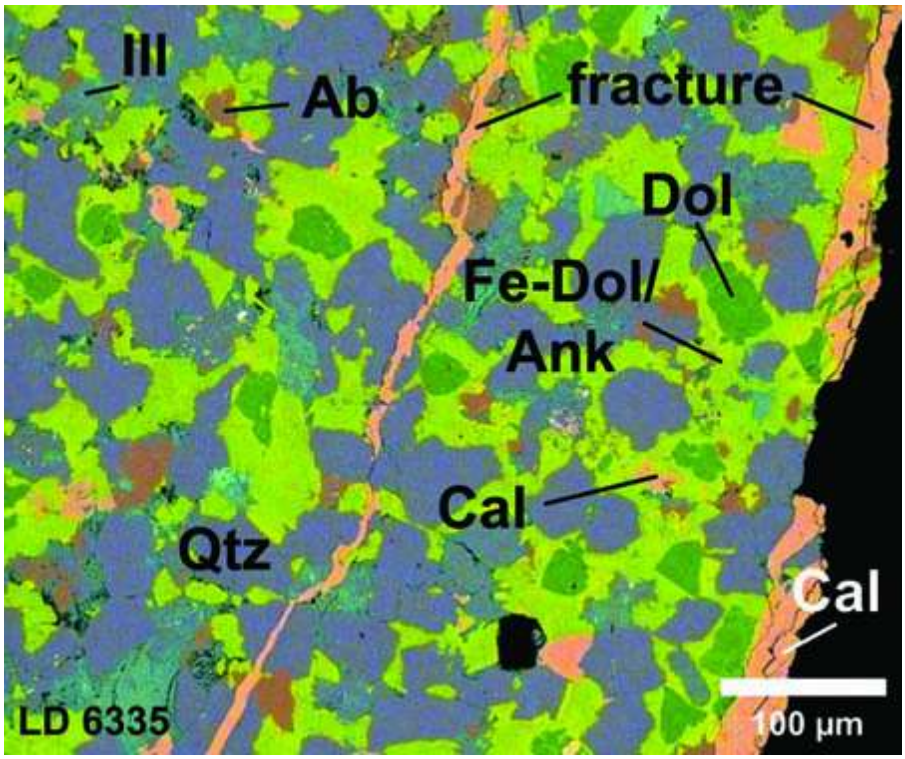

Figure 7. High magnification elemental X-ray map indicating different carbonate phases in Mesaverde sandstone, Mamm Creek field, Piceance basin. Detrital dolomite (dark green) is overgrown by pre-kinematic ferroan-dolomite/ankerite cement (light green). Calcite (orange) occurs as later formed carbonate phase filling interstitial cement porosity. Syn- and/or post-kinematic calcite precipitates in open fracture porosity.

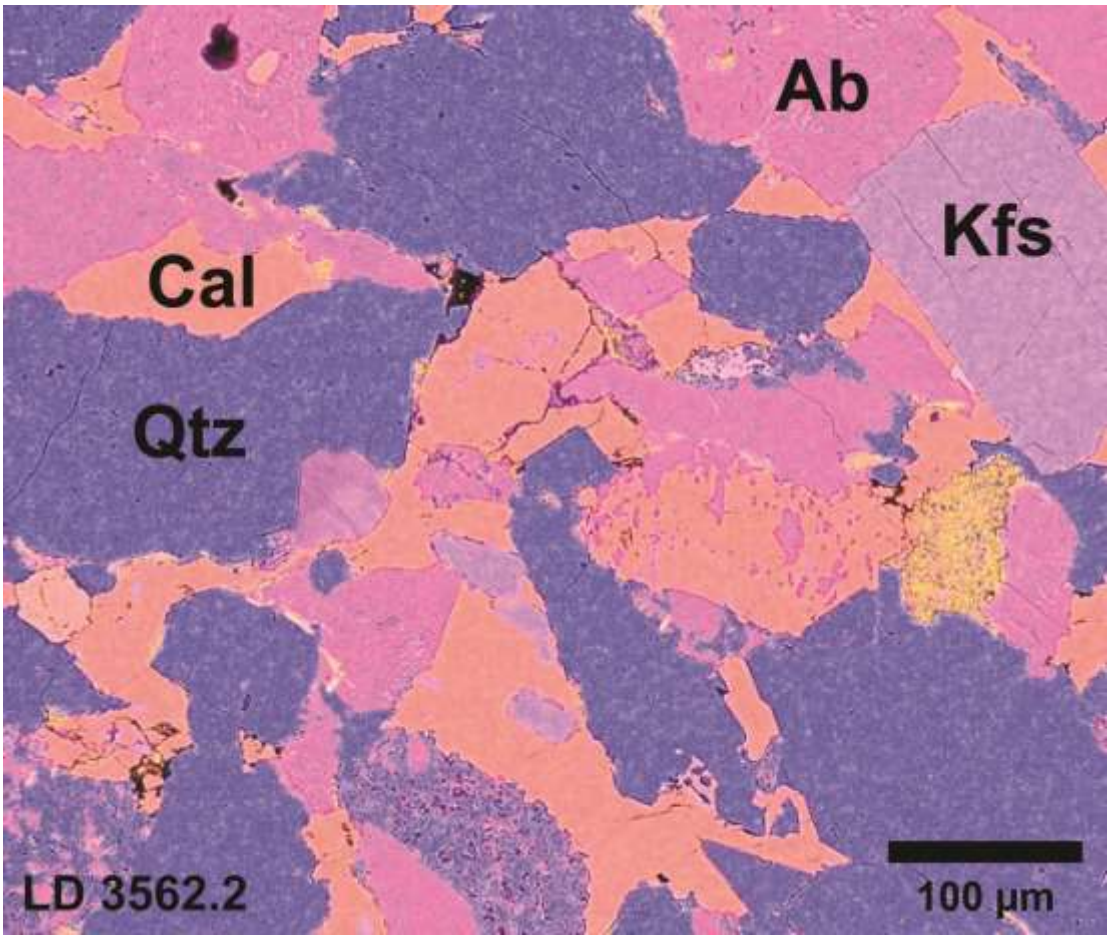

Figure 8. High magnification X-ray map showing calcite cement in Mesaverde sandstone, Mamm Creek. Patchy albite (red) and calcite (orange) replace feldspar.

3.1.4.2 Fluid Inclusion Analyses

Fluid inclusions microthermometry was performed on fracture carbonate cements in well MF31-19G to determine the temperature conditions under which the cements formed. Both primary and secondary fluid inclusion assemblages (FIAs) were observed. Primary inclusions appear in small 3D clusters and as isolated negative-crystal shaped inclusions. The secondary inclusions occur as short, healed microfractures. The shape of the inclusions varies from irregular to negative crystal shapes; sizes range from ~1 to ~20 µm in diameter. Calcite cements contain fluid inclusion assemblages of coexisting two-phase aqueous and single-phase hydrocarbon gas inclusions, similar to inclusions trapped in quartz cements (Fall et al. 2012, see also Becker et al., 2010). The coexistence of these two fluid phases indicates that the inclusions were trapped in an immiscible fluid system (aqueous fluid + free hydrocarbon gas), and the measured homogenization temperatures (Th) of the aqueous inclusions represent true trapping

temperatures. The aqueous inclusions at room temperature contain 5-10 volume% vapor. Homogenization temperatures range from ~138°C to ~163°, with Th variation of ~1-15°C within a single FIA. These higher temperature variations are probably caused by reequilibration of inclusions in calcite due to the low hardness and cleavage of the host calcite. However, liquid-vapor phases are consistent within single FIAs. Final ice melting temperatures provided salinities ranging from ~2.0 to 3.5 wt% NaCl equivalent for inclusions in calcite, with no systematic trends in salinity with homogenization temperature.

3.1.4.3 Oxygen and Carbon Isotopes

The $\delta^{18}O_{PDB}$ isotope composition of calcite fracture and pore cement varies between -18.1‰ and -13.4‰; and $\delta^{13}C_{PDB}$ values between -17.0‰ and -2.0‰. In general, and particularly for MF31-19G, the $\delta^{18}O$ varies more for pore cement than for fracture cement. The larger spread in $\delta^{18}O$ values for pore cement may reflect a wider range of temperatures over which pore cement formed compared to fracture cement. The $\delta^{13}C$ composition of calcite cements generally becomes more positive with increasing core depth. This increase in $\delta^{13}C$ with depth has also been reported for fracture cement by Pitman and Dickinson (1989).

3.1.4.4 Strontium Isotopes

Strontium isotopic values of carbonate fracture cement show a wide spread with highly radiogenic ratios (Figure 9). These Sr-isotope ratios >0.7123 are distinctly higher than the seawater ratio during Late Cretaceous times (0.7078, McArthur et al., 2001). $^{87}Sr/^{86}Sr$ values for the M31-19G well shows a range from 0.71261 to 0.71739. Two shallow samples have a ratio of 0.7127, whereas three deeper samples sampled within 1' (0.3 m) show a range of 0.7126 to 0.7174. $^{87}Sr/^{86}Sr$ values for the shallower Mamm Creek samples are comparable to the shallower fracture cements in the MF31-19G well.

$^{87}Sr/^{86}Sr$ ratios suggest that albitization of detrital feldspar is the primary source of Ca^{2+}. During albitization the anorthite component is dissolved, with albite remaining as a porous daughter phase. Released Ca^{2+} drives precipitation of carbonate cements. The petrographic observations (Figure 8) are consistent with this interpretation. Differences in CL color and cross-cutting relations between pore- and fracture-filling calcite cement (Figure 10) suggest, however, that both types of calcite formed as different cement generations at different times, with pore calcite cement perhaps serving as the precursor calcite phase for subsequent fracture calcite cement precipitation involving pore cement dissolution, mass transfer into the fracture, and fracture cement precipitation Fracture carbonate cement is thus predicted to be most abundant in areas of carbonate pore cement.

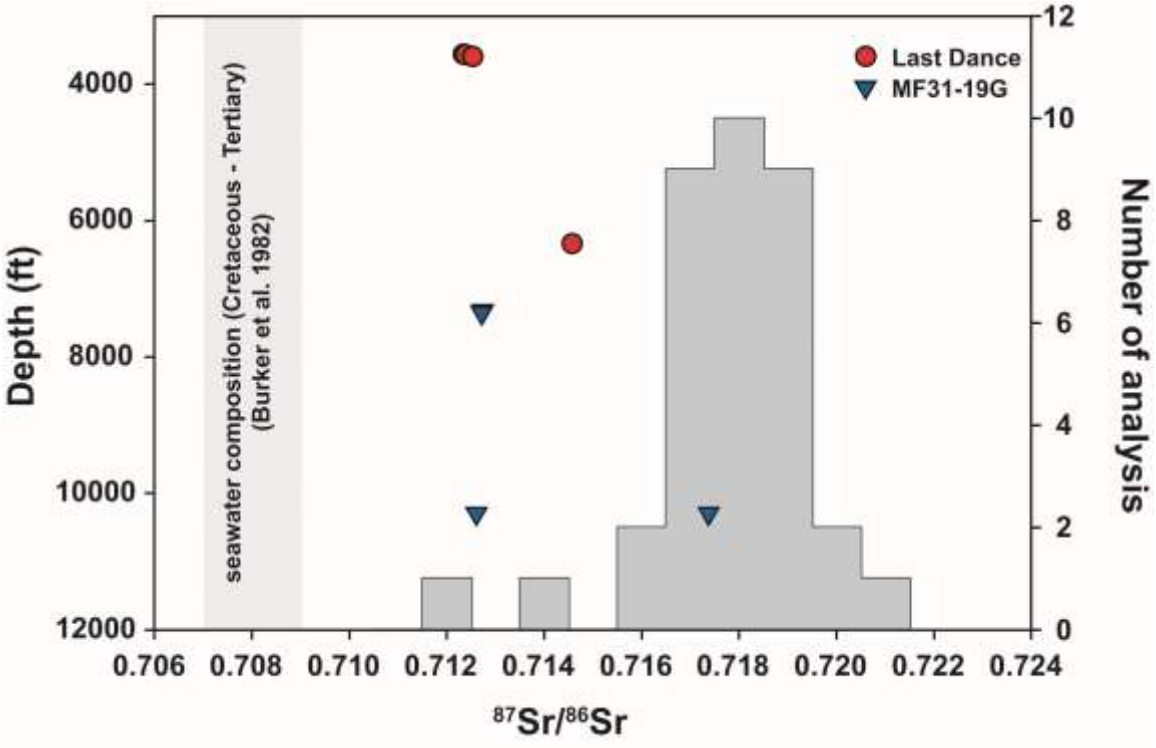

Figure 9. $^{87}Sr/^{86}Sr$ values of calcite fracture cement along two wells from the Piceance Basin. The range of present formation water of the Mesaverde Sandstone and the seawater Sr-isotope ratio during Cretaceous and Tertiary times are shown for comparison.

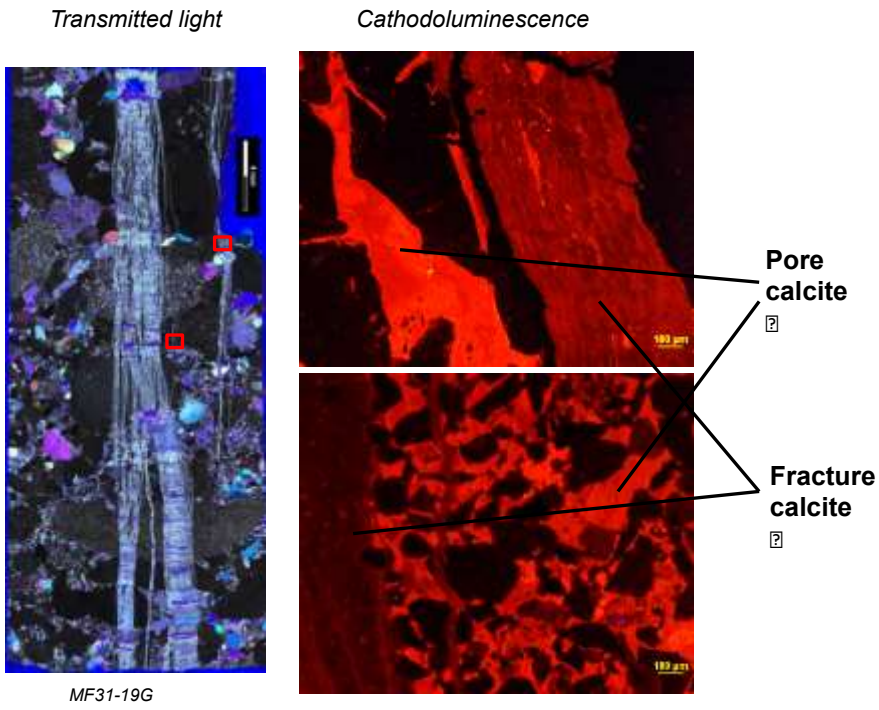

Figure 10. Transmitted light and cold-cathode luminescence images of carbonate fracture cement in Mesaverde sandstones, Piceance Basin. Differences in luminescence color are indicative of compositional differences between fracture and pore cement, suggesting multiple stages of carbonate cementation.

3.1.4.5 Fracture Degradation

We tested this assumption for Mesaverde sandstone in a Piceance basin well and for Jurassic-Cretaceous Cotton Valley Formation (Taylor sandstone) in the SFE 3 well, Harrison County, east Texas, by calculating the degradation index as defined by Laubach (2003) (Figure 11). The degradation index is defined as the ratio of pore cement formed during and after fracture opening (syn- and postkinematic cement) to preserved porosity in the host rock. Laubach (2003) proposed that this index can be determined based on petrographic analysis of conventional or sidewall core in the absence of direct fracture observations, thus serving as a predictor for fracture degradation. Degradation of 100% indicates that all pore space is filled by syn- to postkinematic cement whereas 0% degradation implies no syn- to postkinematic pore cement while remaining porosity is still present. Degradation index values for routine point-count analyses are plotted in Figure 11 as green and red circles for samples with ≤50% and >50% degradation, respectively. In the Mesaverde well, we find that, out of 44 fractures,

degradation of 35 fractures (80%) was predicted correctly (Weisenberger et al., in prep.). This observation is in support that fracture calcite cement tracks pore calcite cement closely.

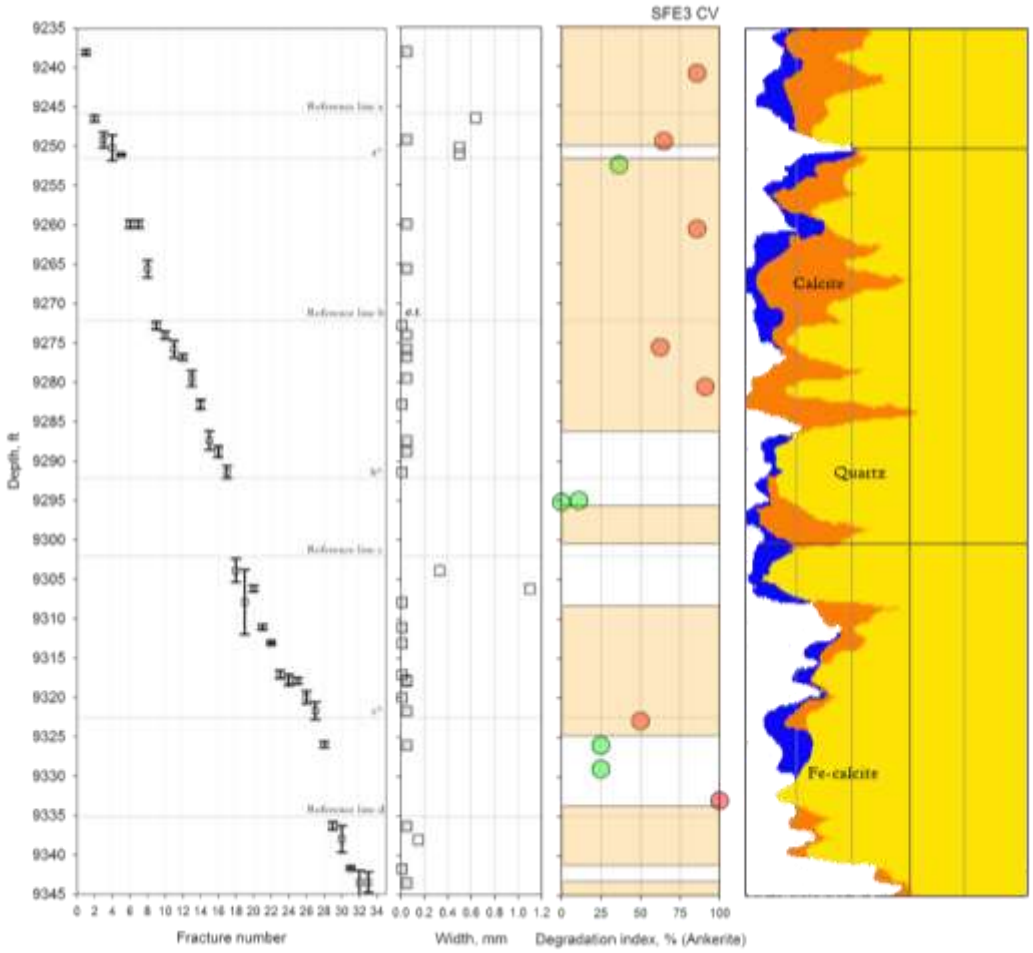

Figure 11. Fractures observed in core, fracture widths, degradation index as an indirect indicator of sealed or open fractures. Values near 100 percent indicate sealed fractures. Example is from Jurassic-Cretaceous Cotton Valley Formation (Taylor sandstone), SFE 3 well, Harrison County, east Texas.

3.1.5 Discussion and Impact

Our results demonstrate that, while fracture diagenesis is frequently heterogeneous in reservoirs, aspects essential to the reservoir seismic response such as degree of cement infill and fracture cement mineral composition, are predictable using proxy techniques such as the degradation index and applying a fundamental understanding of reservoir diagenetic processes during burial. It is our expectation that **t**he widely applicable techniques that we developed will have an impact on effective targeting of zones of potentially good producibility in tight

formations. Philip et al. (2005) showed that fracture attributes such as fracture length distribution and clustering, which are currently not accounted for in either seismic or well-log based fracture analysis, can have order of magnitude impacts on effective permeability. In fact, core and production data show that fracture attributes such as degree of diagenetic overprint on fractures, leading to locally sealed or partly sealed fractures, can be the difference between productive (economic) wells and dry holes (Laubach, 2003). Such fracture attributes cannot currently be distinguished using currently available seismic techniques even under the most favorable circumstances. Yet this is the type of information our project and the resulting technology was designed to delineate. Our approach has the potential for reducing exploration and finding costs, increasing the success of exploration, and overcoming limitations in existing technologies.

In addition to anticipated economic benefits, improved technologies in targeting naturally fractured reservoirs may increase the efficiency and reach of hydraulic fracture treatments. Improved targeting technologies can provide direct environmental benefits by, for examples, optimizing water use for hydraulic fracture treatments and reducing the footprint of well sites.

3.2 References

Becker, S.P., Eichhubl, P., Laubach, S.E., Reed, R.M., Lander, R.H., and Bodnar, R.J., 2010, A 48 m.y. history of fracture opening, temperature, and fluid pressure: Cretaceous Travis Peak Formation, East Texas basin: Geological Society of America Bulletin, v. 122, p. 1081-1093.

Crossey, L.J., and Larsen, D., 1992, Authigenic mineralogy of sandstones intercalated with organic-rich mudstones: integrating diagenesis and burial history of the Mesaverde Group, Piceance Basin, NW Colorado, in Houseknecht, D.W., and Pittman, E.D., eds., Origin, Diagenesis, and Petrophysics of Clay Minerals in Sandstones, Special Publication 47. SEPM Society for Sedimentary Geology, p. 125-144.

Fall, A., Eichhubl, P., Cumella, S.P., Bodnar, R.J., Laubach, S.E., and Becker, S.P., 2012, Testing the basin-centered gas accumulation model using fluid inclusion observations: Southern Piceance Basin, Colorado: AAPG Bulletin, v. 96, p. 2297-2318.

Fomel, S., 2003, Time-migration velocity analysis by velocity continuation: Geophysics, v.68, 1662-1672.

Fomel, S., 2007a, Local seismic attributes: Geophysics, v. 72, A29-A33.

Fomel, S., 2007b, Velocity-independent time-domain seismic imaging using local event slopes:Geophysics, v. 72, S139-S147.

Fomel, S., Landa, E., and Taner, M. T., 2007, Post-stack velocity analysis by separation and imaging of seismic diffractions: Geophysics, v. 72, U89-U94.

Gomez, L. G., and Laubach, S. E, 2006, Rapid digital quantification of microfracture populations. Journal of Structural Geology, v. 28, 408-420.

Grechka, V., Tsvankin, I., 2002, Feasibility of seismic characterization of multiple fracture sets. Geophysics 68, 4, 1399-1407.

Holder, J., J. E. Olson, & Z. Philip, 2001, Experimental determination of subcritical crack growth parameters in sedimentary rock: Geophysical Research Letters, v. 28, 599-602.

Hooker, J.N., Gale, J.F.W., Gomez, L.A., Laubach, S.E., Marrett, R., and Reed, R.M., 2009, Aperture-size scaling variations in a low-strain opening-mode fracture set, Cozzette Sandstone, Colorado: Journal of Structural Geology, v. 31, p. 707-718.

Hooker, J.N., Laubach, S.E., Gomez, L., Marrett, R., Eichhubl, P., Diaz-Tushman, K., and Pinzon, E., 2011, Fracture size, frequency, and strain in the Cambrian Eriboll Formation sandstones, NW Scotland. Scottish Journal of Geology, v. 47, no. 1, 45-56.

Hooker, J. N., 2012, Fracture scaling and diagenesis, PhD Dissertation, Jackson School of Geosciences, The University of Texas at Austin, 694 p.

Hooker, J.N., Gomez, L.A., Laubach, S.E., Gale, J.F.W., and Marrett, R., 2012, Effects of diagenesis (cement precipitation) during fracture opening on fracture aperture-size scaling in carbonate rocks: Geological Society, London, Special Publications, v. 370.

Khaidukov, V., E. Landa, and T. Moser, 2004, Diffraction imaging by focusing-defocusing: An outlook on seismic superresolution: Geophysics, 69, 1478–1490.

Klem-Musatov, K., 1994, Theory of Seismic Diffractions: Soc. of Expl. Geophys.

Klimentidis, R.E., and Welton, J.E., 2008, Advances in Reservoir Quality Assessment of Tight-Gas Sands - Links to Producibility, AAPG Annual Convention: San Antonio, Texas, Search and Discovery Article #40395.

Landa, E., Fomel, S., and Reshef, M., 2008, Separation, imaging, and velocity analysis of seismic diffractions using migrated dip-angle gathers: 78th Annual International Meeting, Soc. Expl. Geophys., 2176-2180.

Laubach, S.E., 2003, Practical approaches to identifying sealed and open fractures: AAPG Bulletin, v. 87 (4), 561-579.

Laubach. S.E., Reed, R., Olson, J.E., Lander, R.H., & Bonnell, L.M., 2004, Coevolution of crack-seal texture and fracture porosity in sedimentary rocks: cathodoluminescence observations of regional fractures: Journal of Structural Geology v. 26, no. 5, 967-982.

Laubach, S.E., and Ward, M., 2006, Diagenesis in porosity evolution of opening-mode fractures, Middle Triassic to Lower Jurassic La Boca Formation, NE Mexico. Tectonophysics. v. 419, p. 75-97.

Laubach, S.E., Marrett, Randall, and Olson, J., 2000, New directions in fracture characterization: The Leading Edge, v. 19, no. 7, 704–711.

Laubach, S.E., Olson, J.E., & Gale, J.F.W., 2004a, Are open fractures necessarily aligned with maximum horizontal stress? Earth & Planetary Science Letters, v. 222, no. 1, 191-195.

Laubach, S.E., Reed, R. M., Olson, J. E., Lander, R. H., and Bonnell, L. M., 2004b, Coevolution of crack-seal texture and fracture porosity in sedimentary rocks: cathodoluminescence observations of regional fractures: Journal of Structural Geology, v. 26, no. 5, p. 967-982.

Laubach, S.E., and Gale, J.F.W., 2006, Obtaining fracture information for low-permeability (tight) gas sandstones from sidewall cores: Journal of Petroleum Geology, v. 29 (2) (April 2006), 147-158.

Mcarthur, J.M., Howarth, R.J., and Bailey, T.R., 2001, Strontium Isotope Stratigraphy: LOWESS Version 3: Best Fit to the Marine Sr-Isotope Curve for 0–509 Ma and Accompanying Look-up Table for Deriving Numerical Age: The Journal of Geology, v. 109, p. 155-170.

Marrett, R., 1996, Aggregate properties of fracture populations: Journal of Structural Geology, v. 18, nos. 3/4, 169-178.

Marrett, R., 1997, Permeability, porosity, and shear-wave anisotropy from scaling of open-fracture populations. RMAG Fractured Reservoirs: Characterization and Modeling Guidebook, p. 217-226.

Marrett, R., Ortega, O., & Kelsey, C., 1999, Extent of power-law scaling for natural fractures in rock: Geology, v. 27, no. 9, 799-802.

Marrett, R., Laubach, S.E. Olson, J.E., 2007, Anisotropy and beyond: geologic perspectives on geophysical prospecting for natural fractures. The Leading Edge, vol. 26, no. 9, 1106-1111.

Marrett, R., Gale, J.F.W., Gomez, L.A., in press, Spatial arrangement of fracture arrays. Journal of Structural Geology.

Milliken, K.L., 2003, Late Diagenesis and Mass Transfer in Sandstone-Shale Sequences, in Heinrich, D.H., and Karl, K.T., eds., Treatise on Geochemistry: Oxford, Pergamon, p. 159-190.

Montoya, P., Fisher, W., Marrett, R., and Tatham, R., 2002, Estimation of fracture orientation and relative intensity using azimuthal variation of P-wave AVO responses and oriented core data in the Tacata Field, Venezuela, SEG Expanded Abstracts, 2002, AVO2 Case History, Salt Lake City, 261-264.

National research Council, 1996, Rock Fractures and Fluid Flow: Contemporary Understanding and Applications: National Academy Press, 551 p.

Narr, W., 1996, Estimating fracture spacing in subsurface rock: AAPG Bulletin, vol. 80, p. 1565-1586.

Narr, W., Schechter, D. W., and Thompson, L. B., 2006, Naturally fractured reservoir characterization: Society of Petroleum Engineers, Richardson, TX, 112 p.

Nelson, R. A., Geologic Analysis of Naturally Fractured Reservoirs, 2nd ed., Gulf Professional Publishing, 332 p.

Olson, J. E., 2003, Sublinear scaling of fracture aperture versus length: An exception or the rule? Journal of Geophysical Research (American Geophysical Union), v. 108, no. B9, 2413, doi:10.1029/2001JB000419.

Olson, J. E., 2007, Fracture aperture, length and pattern geometry development under biaxial loading: a numerical study with applications to natural, cross-jointed systems. In: Lewis, H. & Couples, G. D. (eds) Fracture-Like Damage and Localisation, Geological Society of London, Special Publication, v. 289; p. 123-142.

Olson, J. E., Lander, R., Laubach, S., 2007, Combining diagenesis and mechanics to quantify fracture aperture distributions and fracture pattern permeability: In Lonergan, L., Jolley, R.J., Sanderson, D.J., Rawnsley, K., eds., Fractured Reservoirs, Geological Society of London Special Publication 270, 97-112.

Ortega, O. O. & Marrett, R., 2000, Prediction of macrofracture properties using microfracture information, Mesaverde Group sandstones, San Juan Basin, New Mexico: Journal of Structural Geology, 22, 571–588.

Ortega, O. J., Marrett, R., and Laubach, S. E., 2006, A scale-independent approach to fracture intensity and average fracture spacing: AAPG Bulletin, v. 90, no. 2 (February 2006), 193-208

Ozkan, A., cumella, S.P., milliken, K.L., and laubach, S.E., 2011, Prediction of lithofacies and reservoir quality using well logs, Late Cretaceous Williams Fork Formation, Mamm Creek field, Piceance Basin, Colorado: AAPG Bulletin, v. 95, p. 1699-1723.

Philip, Z. G., Jennings, J. W. Jr., Olson, J. E., Laubach, S. E., and Holder, J., 2005, Modeling coupled fracture-matrix fluid flow in geomechanically simulated fracture networks: SPE Reservoir Evaluation & Engineering, v. 8, no. 4 (August 2005), p. 300-309

Pitman, J.K., and Dickinson, W., 1989, Petrology and Isotope Geochemistry of Mineralized Fracture in Cretaceous Rocks - Evidence for Cementation in a Closed Hydrological System, Geology of Tight Gas Reservoirs in the Pinedale Anticline area, Wyoming, and the Multiwell Experiment Site, Colorado, U.S. Geological Survey Bulletin, p. J1-J15.

Pitman, J.K., Spencer, C.W., and Pollastro, R.M., 1989, Petrography, Mineralogy, and Reservoir Characteristics of the Upper Cretaceous Mesaverde Group in The East-Central Piceance Basin, Colorado: U.S. Geological Survey Bulletin, v. 1787-G, p. G1-G31.

Sayers, C. M., Dahi Taleghani, A., and Adachi, J., 2008, The effect of mineralization on the ratio of normal to tangential compliance of fractures: Geophysical Prospecting, doi: 10.1111/j.1365-2478.2008.00746.x

Sen, M.K., Lane, F.D., and Foster, D. J., 2007, Anomolous reflection amplitudes from fractured reservoirs—Failure of AVOA: The Leading Edge, v. 26, p. 1148-1152.

Taner, M.T. and Landa, E., 2005, Method for detecting earth formation fractures by seismic imaging of diffractors, U.S. patent #20050219949.

Taner, M.T., Fomel, S., and Landa, E., 2006, Prestack separation of seismic diffractions using plane-wave decomposition: 76th Ann. Internat. Mtg, submitted, Soc. of Expl. Geophys.

Willis, M.E., Burns, D.R., Rao, R., Minsley, B., Toksöz, M.N., and Vetri' L., 2006, Spatial orientation and distribution of reservoir fractures from scattered seismic energy: Geophysics, 71, O43-O51.

Wilson, C., 2004, Predicting fracture degradation in the Piceance Basin, Colorado: Can a surrogate measurement guide the way to open fractures and highly productive wells? A geology, engineering and value-of-information study. The University of Texas at Austin Department of Petroleum & Geosystems Engineering, M.A. thesis, 150 p.

CHAPTER 4
TECHNOLOGY TRANSFER

Technology transfer was provided through three annual meetings with industry stakeholders, direct interaction with producers, our research web site http://www.beg.utexas.edu/frac/geophysics.php, presentation and sessions chaired at national meetings, and publication of results in international journals. Industry meetings were held in Austin, TX (September, 2013), Houston, TX, Santa Barbara (CA, September 2011), and Rochester, NY (September 2012), involving industry experts in unconventional resources from the following companies: Anadarko, Apache, BHP Billington, BP, Cairn India, CGG, Chevron, ConocoPhillips, Devon, Encana, ExxonMobil, Hess, Kuwait Oil, Marathon, Newfield, Nexen, Pace, Pemex, Petrobras, Repsol, Saudi Aramco, Schlumberger, Shell, Statoil, Southwestern, Total, Weatherford, and YPF. Number of industry participants ranged from 30-40 attendees per meeting.

Peer-reviewed journal publications that came out of this project include the following:

- W. Burnett and S. Fomel, 2011, Azimuthally anisotropic 3D velocity continuation: **International Journal of Geophysics**, Article ID 484653.
- L. Casasanta and S. Fomel, 2011, Velocity-independent tau-p moveout in a vertically-varying VTI medium: **Geophysics**, v. 76, U45-U57.
- A. Klokov and S. Fomel, 2012, Separation and imaging of seismic diffractions using migrated dip-angle gathers: **Geophysics**, v. 77, S131-S143.
- A. Klokov and S. Fomel, 2013, Selecting an optimal aperture in Kirchhoff migration using dip-angle images: **Geophysics**, v. 78, S243-S254.

Presentations of the results of this project at international scientific meetings include the following:

- W. Burnett and S. Fomel, 2010, Azimuthally anisotropic 3D velocity continuation: **80th Annual International Meeting, SEG**, 307-312.
- W. Burnett and S. Fomel, 2011: Diffraction imaging using 3D azimuthally-anisotropic velocity continuation, **EAGE 73rd Conference and Exhibition**, B026.
- L. Decker, A. Klokov, and S. Fomel, 2013, Comparison of seismic diffraction imaging techniques: plane wave destruction versus apex destruction: **83rd Annual International Meeting, SEG**, 4054-4059.
- P. Eichhubl, J. F. Gale, J. E. Olson, S. E. Laubach, J. N. Hooker, A. Fall, T. B. Weisenberger, and E. Ukar, 2012, What can outcrop and core based observations tell us about natural fractures in unconventional reservoirs?: **AAPG Annual Convention and Exhibition**, abstract 1236894, Theme 5: Shale Play Characterization Techniques and Methods.
- J. N. Hooker, P. Eichhubl, G. Xu, H. Ahn, A. Fall, P. Hargrove, S. E. Laubach, and E. Ukar, 2012, Effects of fracture reactivation and diagenesis on fracture network evolution: Cambrian Eriboll Formation, NW Scotland, **AGU Fall Meeting** abstract H21B-1097.

- J. N. Hooker, A. Fall, G. Xu, A. L. Kaylor, H. Ahn, P. Eichhubl, and S. E. Laubach, 2011, Predicting open natural fractures in unconventional sandstone reservoirs: Spatial distribution, diagenesis, timing, and opening rates: **AAPG Annual Convention and Exhibition** Abstracts, vol. 20, p. 85-86.
- A. Klokov and S. Fomel, 2013, Seismic diffraction imaging, one migration dip at a time: **83rd Annual International Meeting, SEG**, 3697-3702.
- F. Sheibani and J. E. Olson. 2013. Stress intensity factor determination for three-dimensional crack using the displacement discontinuity method with applications to hydraulic fracture height growth and non-planar propagation paths: **The International Conference for Effective and Sustainable Hydraulic Fracturing**, Brisbane, Australia, 20-22 May 2013.
- F. Sheibani and J.E. Olson. 2013. Impact of Fracture Height on Mixed Mode Fracture Propagation: Insights from 3D Displacement Discontinuity Modelling: **ARMA, 47th U.S. Rock Mechanics / Geomechanics Symposium**, San Francisco, 23-26 June 2013,
- T. B. Weisenberger, P. Eichhubl, A. Fall, and S. E. Laubach, 2012, Fracture degradation by carbonate cement in tight-gas sandstones, Piceance Basin, Colorado. Proceedings of the **34th International Geological Congress**, 5-10 August 2012, Brisbane, Australia, 2681.
- T. B. Weisenberger, A. Fall, J. N. Hooker, P. Eichhubl, S. E. Laubach, and J. S. Davis, 2012, Predicting fracture porosity degradation by calcite cement in Mesaverde Group sandstones, Piceance Basin, Colorado: **AAPG Annual Convention and Exhibition** abstract 1232574 Theme 5: Tight Gas P44.

The presentation by Decker et al. at the 83rd Annual International Meeting of SEG in Houston in 2013 was awarded the SEG Best Student Poster award.

LIST OF ACRONYMS

Page

CHAPTER 1

CHAPTER 2

CHAPTER 3